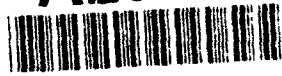WHOI-92-40

# Woods Hole Oceanographic Institution

# Massachusetts Institute of Technology

### Joint Program
### in Oceanography/
### Applied Ocean Science
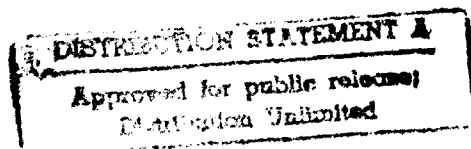### and Engineering

## DOCTORAL DISSERTATION

## Interaction of an Eddy with a Continental Slope

by

Xiaoming Wang

September 1992

DTIC
ELECTE
MAR 0 2 1993
S B D

93-04229

93 3 1 006

**WHOI-92-40**


Interaction of an Eddy with a Continental Slope

by

Xiaoming Wang

Woods Hole Oceanographic Institution
Woods Hole, Massachusetts 02543

and

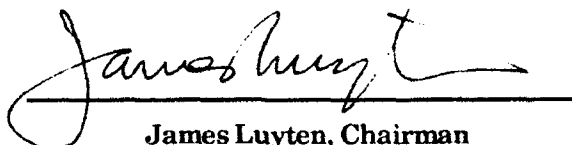The Massachusetts Institute of Technology
Cambridge, Massachusetts 02139

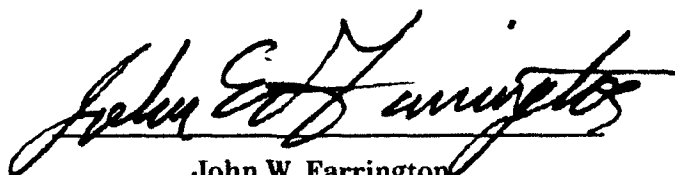September 1992

**DOCTORAL DISSERTATION**

**Approved for Distribution:**


**James Luyten, Chairman**
Department of Physical Oceanography


**John W. Farrington**
Dean of Graduate Studies

# INTERACTION OF AN EDDY WITH A CONTINENTAL SLOPE

by

## Xiaoming Wang

B.S. Shandong College, China
(1982)
S.M. MIT-WHOI
(1989)

Submitted in partial fulfillment of the
requirements for the degree of

Doctor of Philosophy

at the

MASSACHUSETTS INSTITUTE OF TECHNOLOGY

and the

WOODS HOLE OCEANOGRAPHIC INSTITUTION

September 1992

© Xiaoming Wang 1992

Signature of Author.............................................
Joint Program in Physical Oceanography
Massachusetts Institute of Technology
Woods Hole Oceanographic Institution

Certified by.............................................
Glenn R. Flierl                    Paola Malanotte-Rizzoli
Professor                          Professor
Thesis Co-Supervisor               Thesis Co-Supervisor

Accepted by.............................................
Lawrence J. Pratt
Chairman, Joint Committee for Physical Oceanography
Massachusetts Institute of Technology
Woods Hole Oceanographic Institution

To My Motherland

2

# INTERACTION OF AN EDDY WITH A CONTINENTAL SLOPE

by

Xiaoming Wang

## Abstract

This study concerns the barotropic interactions between a mesoscale eddy and a straight monotonic bottom topography. Through simple to relatively complicated modeling effort, some of the fundamental properties of the interaction are investigated.

In chapter two, the fundamental aspects of the interaction are examined using a simple contour dynamics model. With the simplest model configuration of an ideal vortex and a step topography, the basic dynamical features of the observed oceanic eddy-topography interaction are qualitatively reproduced. The results consist of eddy-induced cross-topography exchange, formation of topographic eddies, eddy propagation and generation of topographic waves.

In chapter three, a more complicated primitive equation model is used to investigate a mesoscale eddy interacting with an exponential continental shelf/slope topography on both $f$ and $\beta$-planes. The $f$-plane model recasts the important features of chapter two. The roles of the eddy size and strength and the geometry of topography are studied. It is seen that the multiple anticyclonic eddy-slope interactions strongly affect the total cross-slope volume transport and the evolution of both the original anticyclone and the topographic eddy. Since a cyclone is trapped at the slope and eventually moves on to the slope, it is most effective in causing perturbation on the shelf and slope. The responses on the shelf and slope are mainly wavelike with dispersion relation obeying that of the free shelf-trapped wave modes. On the $\beta$-plane, the problem of an eddy colliding onto a continental shelf/slope from a distance with straight or oblique incident angles is investigated. It is found that the straight eddy incident is more effective in achieving large onslope eddy penetration distance than the oblique eddy incident. The formation of a dipole-like eddy pair consisting of the original anticyclone and the topographic cyclone acts to suppress the eddy decay due to long Rossby wave radiation. A weak along-slope current near the edge of the slope is found, which is part of a outer slope circulation cell originated from the Rossby wave wake trailing the propagating eddy.

3

Model-observation comparisons in chapter four show favorable qualitative agreement of the model results with some of the observed events in the eastern U.S. continental margins and in the Gulf of Mexico. The model results give dynamical interpretations to some observed features of the oceanic eddy-topography interactions and provide enlightening insight into the problem.

Thesis Supervisors:
Drs. Glenn R. Flierl, Professor, and Paola Malanotte-Rizzoli, Professor
Massachusetts Institute of Technology

# Acknowledgments

I would like to thank my advisors, professors Glenn Flierl and Paola Malanotte-Rizzoli, for their guidance, support and encouragement throughout this thesis study. Their advice not only contributed to this research, but also helped my professional growth as a scientist.

The members of my thesis committee, Drs. David Chapman, Terry Joyce and Larry Pratt, made useful suggestions and provided timely information which improved this study. Discussions with Larry Pratt were especially helpful in improving some of the results in chapter two. I am also grateful to Dr. Ken Brink for being chairman of the defense and for correcting this thesis.

Many people lent me helping hands along the way. Dr. Roberta Young helped me through the initial confusion of using the NCAR Cray-YMP and shared with me generously her expertise and knowledge. Dr. Steve Meacham provided the basic contour dynamics computer program used in chapter two, and exchanged torpedos with me during many late-night star-war games. My fellow students at MIT and in the Joint Program made my life as a graduate student more joyful and challenging, and I am very proud of being one of them.

Special thanks go to Dr. Rui-Xin Huang, for many delightful conversations about a wide range of topics, from oceanography to being a good scientist. The memory of fishing over WHOI dock and swimming behind Clark Lab will endure.

My wife, Ying, shared with me every moment of ups and downs in our life, and kept my spirit up with her love and wit. My daughter, Aileen, contributed by messing up my manuscript at home and helped type unrecognizable words into my computer, which were, of course, full of fun and love.

5

# Contents

7

# Chapter 1

# Introduction

Strong and localized mesoscale eddies are among the most dominant features in oceanic flows. Their dynamic properties and role in the general oceanic circulation have been investigated extensively.. Great attention has been given to these eddies concerning their evolution, propagation and dissipation when they are in isolation. Much understanding has been achieved during the last two decades of study. The results are summarized in a collection of research papers edited by Robinson (1983) and in a review by Flierl (1987). *Now it is fair to say that the properties of the eddies in isolation are fairly well understood.* The attention is shifting to nonisolated eddies and eddies in a variable ambient field, for example, the existence of shear flow or large bottom topography near the eddy field. A typical example of the importance of such effects arises in the study of warm-core and cold-core rings formed by the detachment of a portion of a Gulf Stream meander due to hydrodynamic instability processes. The proximity of these highly energetic eddies to the Gulf Stream and continental boundary allows them to interact with the Stream and the bottom topography. The present study will focus on one of these important issues, i.e., the interaction between an eddy and topography.

Existing evidence shows that the eddy interaction with bottom topography can influence the speed and direction of the eddy propagation (Evans et al, 1985; Kirwan et al,1984), the eddy shape (Cheney and Richardson, 1976; Kennelly et al, 1985), and the rate of eddy dissipation (Cheney and Richardson, 1976). On the other hand an

eddy encountering continental topography will radiate topographic Rossby waves (Louis and Smith, 1982; Ramp, 1989; Shaw and Divakar, 1991), cause cross-isobath fluid motion (Morgan and Bishop, 1977; Smith, 1978; Churchill et al, 1986; Joyce et al 1992) and possibly induce topographic eddies (Kennelly et al, 1985). All these are important processes that affect at least the regional circulation and water mass structure. Due to frequent occurrence of the eddy-topography interactions over length scales much larger than a single eddy scale, the interactions are likely to have a strong impact on the basin scale ocean circulation, especially on the volume and property exchanges between deep ocean and continental shelf and slope waters. For example, the Mid-Atlantic Bight shelf receives an average 157 $km^3/year$ fresh water from river runoff. To conserve the salinity on the shelf, Wright (1976) estimated that about 2400 $km^3/year$ ($6.8 \times 10^4$ $m^3/s$) of shelf water must be transported offshore. The observations show that the eddy induced offshelf transport can account for a significant portion of it (Morgan and Bishop, 1977; Smith, 1978; Churchill et al, 1986).

Due to the complexity of the eddy-topography interaction, theoretical investigation has been limited to study of the translation of an isolated eddy on a sloping bottom. Nof (1983) found that a cold (dense) eddy over a uniformly sloping bottom will translate at 90° to the right of the downslope direction. The translation speed depends only on the stratification, Coriolis parameter and the bottom slope. It is independent of the intensity and size of the eddy. With a rather different dynamic approach, Swaters and Flierl (1990) investigated the propagation of ventilated coherent cold eddies on a sloping bottom. Their leading-order solution corresponds to a solitary baroclinic monopole which propagates along shelf at the same speed as that of Nof (1983). The features in these models are, however, not quite at the level of strength and the size of bottom slope as the Gulf Stream ring-continental shelf and slope interactions. Therefore the important nonlinear propagation tendency is not included in their models. Smith and O'Brien (1983) were able to study nonlinear eddy-finite topography interaction using a two layer numerical model. They showed the important difference between an anticy-

clone and a cyclone when interacting with a shallowing topography in the lower layer: the anticyclone tends to move downslope and the cyclone tends to move upslope under the strong influence of nonlinear self-advection associated with the topographic $\beta$-effect. However Smith and O'Brien (1983) did not investigate the response of the fluid over the topography or the cross topography transport processes, and the topography in their model was fully contained in the lower layer below a depth of 3000 meters. Later work focused on the topographic Rossby waves generated by a nearshore eddy and their subsequent onshelf propagation. There are two different assumptions for wave generation mechanisms. Louis and Smith (1982) investigated the barotropic radiation by an eddy over a slope and found that the topographic Rossby waves generated in such a system agree fairly well with the observed velocity from the Scotian Shelf break. With a series of numerical experiments, Shaw and Divakar (1991) argued that the density advection by a warm-core ring is responsible for generating large wave-like velocity oscillations near shelf break. Their results show better amplitude agreement with the observations than that of Louis and Smith (1982). In both studies the waves are generated by a source on the continental rise or slope, and propagate shoreward onto the shelf. Since the waves so generated are fairly barotropic and the steep slope is an excellent insulator to low frequency waves, the onslope penetration by the topographic waves requires the source be located on the mid or upper slope (Shaw and Peng, 1987). Therefore the shelf water may be subject to the direct perturbation of the eddy forcing. Other studies involve the responses on the shelf and slope due to an offshore eddy forcing, such as the work of Chapman and Brink (1987) and Qiu (1990). In these studies the offshore forcing is prescribed as a boundary forcing and is allowed to translate along the offshore boundary. The shelf and slope responses and their dependence on the forcing frequency and stratification are examined. The treatment of the offshore eddy as a boundary forcing in these studies is a crude approximation. One can examine shelf and slope responses to the eddy forcing in such models but not the feedback from the variation of eddy field and the property exchange between the slope and deep ocean.

10

A better approach to the eddy-topography interaction problem must involve actively both the process on the topography and the evolution of the eddy field. The simplest model of this kind is a system containing an eddy and a step-like topography without stratification, friction and external forcing. This model is investigated in chapter two using the method of contour dynamics. As the potential vorticity interface separating the fluid in the deep and shallow regions is perturbed by the eddy, relative vorticity is generated due to the vortex stretching or compression as the fluid column moves across the step topography. The perturbation velocity field in turn influences the evolution of the interface itself and the motion of the eddy. The theoretical development of this process is similar to the eddy-shear current interaction problem investigated by Stern and Flierl (1987) and Bell (1990). The wavelike interface perturbation can be solved analytically for weak or linear interactions. The perturbation grows with increasing nonlinearity and large interface deformation takes place. Such cases are investigated with a numerical contour dynamics model for various strength of nonlinearity and size of the topography. The fundamental features observed in real oceanic situations are qualitatively reproduced and the interpretation of these results is simple and straightforward. The basic processes captured by the model are: (1) the eddy-induced cross topography volume transport; (2) the formation of a topographic eddy and streamer; (3) the generation of topographic waves and a residual along-topography current; and (4) the eddy propagation. The dependence of these features on the variable model parameters is also investigated. The propagation of the eddy under the influence of the interface perturbation and the topographic eddy are discussed. The results from this simple model study indicate that the model contains some of the fundamental physics of the eddy-topography interaction, though most finer points are beyond its scope.

This leads naturally to chapter three, the study of eddy-topography interaction with a barotropic primitive equation (PE) model. A more realistic topography and eddy as well as friction are included in the model. For simplicity and easy comparison with the results in chapter two, the density is still assumed uniform. The topography is assumed

to be a single exponential function of the offshore distance. It has the same form used by Buchwald and Adams (1968), for purpose of being able to compare directly the dispersion relationship of the eddy-induced topographic waves and that of free continental shelf waves. These restrictions can be easily relaxed in the model. The model experiments are performed on both the $f$-plane and the $\beta$-plane. The former allows a direct comparison with the contour dynamics (CD) results. The PE model results, though complicated, can be qualitatively interpreted using the simple CD results for comparison. The most important changes occur to the cross topography volume transport and the waves over the topography. Unlike the step topography case, the cross topography volume transport over a continuous topography profile will originate from different part of the slope, depending on the topography and penetration distance by the eddy forcing. In the CD case the interfacial wave excited by the eddy forcing is monochromatic, due to the topographic restriction. The topographic waves on a continuous monotonic depth profile, according to Huthnance (1975), will have an entire set of barotropic trapped modes. The eddy forcing will excite a subset of these modes at different frequencies and wave numbers. On the planetary $\beta$-plane, an isolated eddy will propagate due to the effect of planetary wave dispersion. This allows the eddy to be initialized away from the topography. Therefore the collision of an eddy with continental topography at different incident angles can be investigated. The oblique incidence and straight collision of an eddy onto a slope topography are studied. These experiments represent more realistically the observed oceanic eddy-topography interactions. The major results from the CD study are still qualitatively applicable to explain the $\beta$-plane interactions, but the latter results are general enough that direct model-observation comparisons are possible.

Chapter four contains the comparison study of the model results with observations. The Gulf Stream ring-shelf and slope interactions are examined first. Since the existing observations are limited, no single interaction event is able to illustrate all the important features revealed by the model results. The comparisons are made to different events with emphasis on the appearance of certain interesting features. The Loop Current eddy

12

interactions with the Western Gulf of Mexico slope are also examined. Both comparisons show not only the qualitative similarities but also some limited quantitative agreement with the model. The results provide useful insight into the complicated eddy-topography interaction processes.

Finally the limitations of the model results are discussed and future improvements and further investigations are proposed.

# Chapter 2

# Vortex-Escarpment Interactions

## 2.1 Introduction

The problem of eddies interacting with a continental shelf/slope is rather complex as it involves a density front, external forcing, irregular bottom topography, mixing, etc. In this chapter we shall study this problem in a much idealized framework; i.e, we examine the interaction process of a vortex with a step-like topography in a homogeneous fluid. The simplified system contains an isolated eddy and topography. All external forcings are dropped. Density is assumed homogeneous over the entire domain, and in this chapter, there is no mixing or friction of any kind. Furthermore, the topography is taken as an infinitely long and straight escarpment with the rest of the bottom flat, and the eddy is represented by either a point vortex or a constant vorticity patch that is initially some distance away from the escarpment. The initial field therefore consists only of a vortex and a potential vorticity (PV) front, which is due to and coincident with the escarpment. As the system evolves in time, the front deforms and interacts with the vortex. We will explore, at various strengths of interaction, the motion of the eddy, the time evolution of the PV front, the excitation of frontal waves and the generation of eddies. The purpose of this study is to model the eddy-topography interaction, to identify major control mechanisms and parameters, and to understand qualitatively the evolution of the front-eddy system and its time and space scales of variation. This will pave the way for a series of more complicated modeling experiments that follows in the next chapter. The study

14

is limited on $f$-plane in this chapter and will be expanded to include $\beta$-effect in Chapter 3. The $f$-plane approximation suppresses planetary waves, while the flat bottom/step topography means that the only topographic Rossby waves are "escarpment waves" due to the depth discontinuity.

Longuet-Higgins (1968) studied wave trapping by such a step bottom. He found that wave motions could exist which propagated along the discontinuity and whose amplitude decayed exponentially to either side. The period of the waves is always greater than the inertial period.

Gill $et$ $al$ (1986) examined the classic Rossby adjustment over a step topography running perpendicular to the line of the initial jump in surface pressure. They found that double Kelvin waves were generated and propagated along the step and the flow diverted parallel to the step, $i.e.$, perpendicular to the initial surface discontinuity (compared to a flow along the line of the initial discontinuity in the classic Rossby adjustment problem). There is no mass flux across the step since the adjustment is strictly geostrophic.

With the present formulation, our problem is to study interaction between a vortex and a PV front. Such a problem is analogous to interaction of a vortex with a shear flow, which has been addressed previously by a number of researchers (Hedstrom 1986, Stern and Flierl 1987, Nof 1988, Bell 1990, Stern 1991 and Bell and Pratt 1991). In those studies the vortex is represented by either a patch of uniform vorticity or a point vortex, while the PV front is usually associated with a given shear flow. The authors investigated a wide range of possible scenarios, such as front meadering and waves, formation and propagation of "streamers", the motion of the eddy and eddy entraining into a shear flow. There are certain similarities between the current studies and those listed here, so it is relevant to review them in some detail.

Stern and Flierl (1987) studied interactions between a point vortex and various kinds of shear flows on the $f$-plane, where the shear flow was stable to small perturbations and was represented by a potential vorticity interface. They recognized the importance

of the signs of the vortex and of the shear in the interaction process and showed that an anticyclone to the north of a region of cyclonic shear (resembling the situation of a warm core ring and the Gulf Stream) would generate a localized northward perturbation on the interface. The resulting interaction between the vorticity anomaly created by this displacement and the vortex resulted in westward propagation of both the disturbance and the vortex. In the like-signed case the point vortex moved in the same direction as the shear flow. This would excite a resonant lee wave at the interface, resulting in the vortex moving toward the interface. In the like-signed case the capture of the vortex by the shear flow was seen. On the other hand, in the opposite-signed case, the vortex might capture a segment of the interface by winding it up around itself if the two were initially close enough.

Hedstrom (1986) extended the study of Stern and Flierl (1987) to a two layer system with PV fronts in both layers. The eddy was far enough from the front so that linear dynamics could be assumed. She found that adding a finite lower layer to the one layer problem did not qualitatively change the results of Stern and Flierl unless the lower layer also had changes in potential vorticity. The character of the solution was affected mostly by the ratio of the dominant scale to the deformation radius, since it basically determines the barotropicity or baroclinicity of the solution. She also verified previous findings that in the linear regime the shear flow-vortex interaction draws the eddy toward the flow through the mechanism of either resonant interaction between eddy and frontal waves or interaction between heton-like eddies.

Bell (1990) studied a vortex-potential vorticity interface problem similar to Stern and Flierl (1987) with emphasis on interface waves at small amplitude limit. He interpreted that the resonant lee wave at the interface was due to a radiative transfer of momentum from the vortex to the interface. Thus, from momentum conservation, he was able to derive a simple solution of vortex drift which was only based on the shape of interface.

Since jet currents arising in geophysical problems are often unstable and asymmetric, Bell and Pratt (1991) investigated the same type of eddy-shear flow interaction problem as Stern and Flierl (1985), but using unstable jet profiles. For long range interactions they found that in the barotropic case the jet instability broke the jet up into eddies which caused the forcing cyclonic (anticyclonic) eddy south of the jet to move southwestward (northeastward); while in the equivalent barotropic case a steady lee wave was triggered by the forcing eddy which induced a propagation of the eddy in the opposite direction from the barotropic case. Their numerical results for short range interactions showed that the forcing eddy could strip fluid from the edge of the jet and the detached fluid and eddy propagated as a vortex pair away from the jet. They also related this latter phenomenon to the Gulf Stream warm outbreaks.

Nof (1988) studied an eddy-induced streamer and its propagation as the eddy comes into contact with a shear flow. He suggested that the formation of streamers was a result of eddy geometry rather than advection by the eddy's circulating velocity. The main reason for this was that the interaction process had been treated as a shear flow intrusion along a rotating solid boundary, and both the shape and the position of the eddy were not allowed to change. The rate of streamer propagation was found to be independent of the eddy radius and rotation, and was always one half of the particle speed along the upstream front of the shear flow.

Stern (1991) attacked a different problem of the strong interaction between an eddy and a semi-infinite current. Under certain condition satisfied by the eddy and the flow, the interaction caused the eddy to move towards the edge and into the shear flow. Eventually entrainment of the eddy into the flow took place. His calculation showed that the average entrainment velocity was proportional to the square root of the product of the eddy circulation and the relative vorticity of the shear flow.

In general the interaction can alter the motion of an eddy and induce a frontal wave, which interacts with the eddy as well as with itself and results in increasing ampli-

17

tude. As the feedback from the interface (front) couples with its own evolution, a series of new phenomena appears, such as interface meander and eddy pinch-off (Pratt and Stern, 1985), and capture of the eddy by the shear flow (Stern and Flierl, 1987).

The relation of the above work to the present problem is that they all deal with interactions between eddies and vorticity fronts. The frontal waves owe their existence to the vorticity change, which provides a restoring mechanism. In this study it is the change in water depth rather than shear that is responsible for an initial PV front. As the interaction evolves, the flow field develops from an initially motionless front. The fluid displaced from shallow to deep water generates cyclonic vorticity due to vortex stretching, while the fluid displaced from deep to shallow water generates anticyclonic vorticity due to vortex compression.

In this chapter we examine first a point vortex interacting with a small escarpment under the quasi-geostrophic approximation. Then we study the same problem with a finite escarpment as well as a finite vortex. The study will concentrate on processes such as the generation of a topographic eddy, excitation of escarpment-trapped waves, vortex movement and cross-escarpment volume transport. The effects of continuous bottom topography and planetary $\beta$ are left to later chapters.

## 2.2   Governing Equations and Matching Conditions

The governing equations for a barotropic, frictionless fluid in a rotating coordinate system with the rigid lid assumption are

$$u_t + uu_x + vu_y - fv = -p_x \tag{2.1a}$$

$$v_t + uv_x + vv_y + fu = -p_y \tag{2.1b}$$

$$(uh)_x + (vh)_y = 0 \tag{2.1c}$$

where the $x$-axis is along the escarpment towards east and the $y$-axis is across the escarpment towards north; $u$ and $v$ are the velocity components in $x$ and $y$ directions,
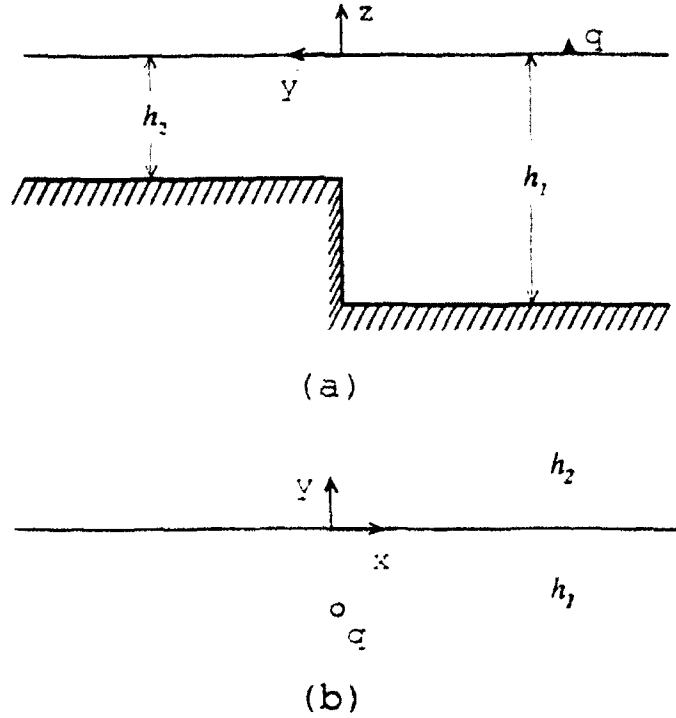
Figure 2.1: Schematic illustration of the model considered in this chapter. (a) A cross escarpment section. (b) $x$-$y$ plane view.

$p$ is the pressure and $h$ is the water depth. The system is illustrated in figure 2.1 with a step-like topography and an eddy located in the deep water. The step is aligned with $x$-axis and described by

$$h = \begin{cases} h_1, & y < 0 \\ h_2, & y > 0 \end{cases} \tag{2.2}$$

For scaling purpose we may define a velocity scale using the vortex circulation $\Gamma_0$ and the height of the topographic step $\Delta h = h_1 - h_2$: $U = (\Gamma_0 f_0 \Delta h / h)^{\frac{1}{2}}$. A length scale can be defined as $L = (\Gamma_0 h / f_0 \Delta h)^{\frac{1}{2}}$. A physical length of this system is the distance between the vortex and the topography $d$, which itself can be nondimensionalized by $L$. We scale $x$ and $y$ by $d$, perturbation velocity $u$ and $v$ by $U$. $t$ by $(f_0 \Delta h / h)^{-1}$. $p$ by $fUd$ and $h$ by $H$, and the equations (2.1) in dimensionless form are

$$u_t + \epsilon(u u_x + v u_y) - fv = -p_x \tag{2.3a}$$

$$v_t + \epsilon(u v_x + v v_y) + fu = -p_y \tag{2.3b}$$

$$(uh)_x + (vh)_y = 0 \tag{2.3c}$$

19

where $\epsilon = \Delta h L / h d$ is the Rossby number. It is seen that $\epsilon$ is proportional to the ratio of the relative height of the topography $\Delta h / h$ and the dimensionless distance $d/L$. Since $L$ is defined as a function of both $\Delta h$ and $\Gamma_0$, it can be considered as a length scale of perturbation induced by the vortex $\Gamma_0$ over the topography $\Delta h$. The nonlinearity becomes important if the topography is large and/or the distance $d/L$ is small. Also for the rigid lid assumption to be valid, it requires that $f_0 L / \sqrt{gH} \ll 1$, *i.e.*, the length scale of motion is much smaller than the barotropic deformation radius.

Introducing a transport stream function $\Psi$ such that $uh = -\Psi_y$ and $vh = \Psi_x$ gives conservation of potential vorticity in the following form,

$$\frac{d}{dt}\left(\frac{\epsilon \nabla \cdot \frac{\nabla \Psi}{h} + f}{h}\right) = 0. \tag{2.4}$$

Equation (2.4) will be solved for a localized initial disturbance. It requires that velocity vanish far away from the disturbed area,

$$u, \quad v \to 0 \qquad as \quad x, y \to \infty \tag{2.5}$$

For finite topography, continuity at the escarpment shows that the normal velocity has a jump there. If we obtain solutions to (2.4) in regions $y > 0$ and $y < 0$, then they have to satisfy certain matching conditions at $y = 0$. We first integrate (2.3a) over the depth, which yields

$$hu_t + \epsilon((hu^2)_x + (huv)_y) - fhv = -hp_x. \tag{2.6}$$

(2.3b), (2.3c) and (2.6) are integrated over a finite interval $(-\Delta y, \Delta y)\,(\Delta y > 0)$ across the escarpment and then we let $\Delta y \to 0$. All integrations which do not contain $y$-derivatives of the integrands are zero and we are left with

$$[hv] = 0 \tag{2.7a}$$

$$[\epsilon huv] = 0 \tag{2.7b}$$

$$[\tfrac{1}{2}\epsilon v^2 + p] = 0 \tag{2.7c}$$

where the square brackets denote the jump of the value inside across $y = 0$.

20

These three equations represent in order the conservation of mass, momentum and energy of the fluid crossing the escarpment. Equation (2.7a) shows a change in normal velocity at escarpment inversely proportional to the depth change; it corresponds in (2.7c) a discontinuity in pressure. We recognize (2.7c) is actually the Bernoulli integral for a steady flow; therefore the Bernoulli function $B = v^2/2 + p$ is conserved even though both normal velocity and pressure are discontinuous across the escarpment. As a result, no singularity arises in equations (2.3). The infinite pressure gradient across the escarpment is cancelled by the jump in normal velocity and therefore does not result in an infinite tangential velocity there. In fact the tangential velocity $u$ is continuous across the escarpment from (2.7a and b),

$$[u] = 0 \tag{2.8}$$

This is, however, applicable only to nonlinear cross escarpment flow. It states that the cross escarpment flux of tangential momentum must be conserved. The conditions (2.7) are frequently encountered in studying flow over abrupt topography (Grimshaw and Yi, 1990; Thompson, 1990; Spitz and Nof, 1991).

If equations (2.1) are linearized, the matching conditions will be altered from those in (2.7). By letting $\epsilon = 0$ in (2.7), we end up with matching conditions for linearized cross escarpment flow,

$$[hv] = 0 \tag{2.9a}$$

$$[p] = 0. \tag{2.9b}$$

Thus, unlike the nonlinear case, the linear matching condition requires continuity of pressure across the escarpment, even though the normal velocity is still discontinuous across the escarpment. The linear matching condition, however, does not impose any constraint on the velocity component tangential to the topography. For example, in section 2.4, the linearized solution shows that the tangential velocity component is discontinuous across the escarpment. However, the linear matching condition is a special case of equation (2.7), and therefore both matching conditions (2.7) and (2.9) will be

21

consistent in producing the same correct results at linear limit. An example is given in Appendix A to show they both result in the same dispersion relationship for small amplitude escarpment waves.

## 2.3 Solution Methodology

In the case where the depth is given by equation (2.2), a velocity stream function can be defined, $\psi = \Psi/h$. The flow field which advects the potential vorticity is the solution of the Poisson equation,

$$\nabla^2 \psi = q(x,y), \tag{2.10}$$

where $q(x,y)$ represents the relative vorticity in the entire solution domain. The value of the vorticity and its initial distribution are known everywhere, and the successive vorticity distribution can be calculated by marching the system forward in time. The stream function can be sought via the Green's function method, i.e., finding the field $\psi$ caused by a distributed source $q(x,y)$. This is done by integrating the source strength and the Green's function over the entire source space $A$,

$$\psi(x,y) = \iint_A q(\xi,\eta)\, G(x,y;\xi,\eta)\, d\xi d\eta, \tag{2.11}$$

and velocity at any point $(x,y)$ is obtained by taking partial derivatives of $\psi$ with respect to $x$ or $y$,

$$(u,\ v) = (-\frac{\partial}{\partial y},\ \frac{\partial}{\partial x}) \iint_A q(\xi,\eta)\, G(x,y;\xi,\eta)\, d\xi d\eta, \tag{2.12}$$

where $G(x,y;\xi,\eta)$ is the Green's function at location $(x,y)$ due to source at $(\xi,\eta)$, vorticity $q$ is assumed to be piecewise constant in $A$. Assuming $\partial A$ is the boundary of $A$, and is variable in both space and time, equation (2.12) can be written in the form of contour integrals along $\partial A$. For different forms of Green's function, the contour integral will be formed differently. Assuming that the Green's function consists of two monopoles located at $(\xi, \eta)$ and $(\xi, -\eta)$, and has the form $G(x,y;\xi,\eta) = c_1 \ln r + c_2 \ln r_0$, where $r = \sqrt{(x-\xi)^2 + (y-\eta)^2}$ and $r_0 = \sqrt{(x-\xi)^2 + (y+\eta)^2}$, and $c_1$ and $c_2$ are constant co-

22

efficients to be determined. Applying the matching condition (2.7), the Green's function is found to have the following form,

$$G(x,y;\xi,\eta) = \frac{1}{2\pi} \begin{cases} \begin{cases} \ln r - \frac{h_1-h_2}{h_1+h_2} \ln r_0, & y < 0 \\ \frac{2h_1}{h_1+h_2} \ln r, & y > 0 \end{cases} & \eta < 0 \\ \begin{cases} \frac{2h_2}{h_1+h_2} \ln r, & y < 0 \\ \ln r + \frac{h_1-h_2}{h_1+h_2} \ln r_0, & y > 0 \end{cases} & \eta > 0 \end{cases}$$ (2.13)

This Green's function represents the flow field at $(x, y)$ caused by a point vortex at $(\xi, \eta)$. $h_1$ and $h_2$ are the water depths given by equation (2.2). This is a general form of Green's function on an infinite plane with a step depth change at $y = 0$. If $h_1 = h_2$, it is the Green's function on an infinite plane with flat bottom. If $h_2 = 0$, it becomes the Green's function on a semi-infinite plane ($y < 0$) with a vertical wall at $y = 0$. For $h_1 \neq h_2 \neq 0$, the escarpment can be regarded as a partial wall at $y = 0$, and appears in 2.13 as a partial image effect to the velocity field.

To write equation (2.12) in terms of contour integrals, we must turn $x$ and $y$ derivatives into $\xi$ and $\eta$ and then we can invoke the divergence theorem. As an example, consider the expression for the eastward flow at a point north of the escarpment. From (2.12) and (2.13) we have

$$u_+ = -\frac{\partial}{\partial y} \iint_{A_-} \frac{q_-}{2\pi} \frac{2h_1}{h_1+h_2} \ln r \, d\xi d\eta - \frac{\partial}{\partial y} \iint_{A_+} \frac{q_+}{2\pi} \left( \ln r + \frac{h_1-h_2}{h_1+h_2} \ln r_0 \right) d\xi d\eta.$$

Bringing the constants outside the integral and using

$$\frac{\partial}{\partial y} \ln r = -\frac{\partial}{\partial \eta} \ln r$$

$$\frac{\partial}{\partial y} \ln r_0 = \frac{\partial}{\partial \eta} \ln r_0$$

gives

$$u_+ = \frac{q_-}{2\pi} \frac{2h_1}{h_1+h_2} \iint_{A_-} \frac{\partial}{\partial \eta} \ln r \, d\xi d\eta + \frac{q_+}{2\pi} \iint_{A_+} \frac{\partial}{\partial \eta} \ln r \, d\xi d\eta$$

$$- \frac{q_+}{2\pi} \frac{h_1-h_2}{h_1+h_2} \iint_{A_+} \frac{\partial}{\partial \eta} \ln r_0 \, d\xi d\eta,$$

which yields

$$u_+ = \frac{q_-}{2\pi} \frac{2h_1}{h_1 + h_2} \oint_{\partial A_-} \ln r \, d\xi + \frac{q_+}{2\pi} \oint_{\partial A_+} \left(\ln r - \frac{h_1 - h_2}{h_1 + h_2} \ln r_0\right) d\xi, \qquad (2.14\text{a})$$

where $r$ and $r_0$ are evaluated at $y = \eta$ on the boundary $\partial A$. Similar manipulations give

$$v_+ = \frac{q_-}{2\pi} \frac{2h_1}{h_1 + h_2} \oint_{\partial A_-} \ln r \frac{\partial \mathcal{L}}{\partial \xi} \, d\xi + \frac{q_+}{2\pi} \oint_{\partial A_+} \left(\ln r + \frac{h_1 - h_2}{h_1 + h_2} \ln r_0\right) \frac{\partial \mathcal{L}}{\partial \xi} \, d\xi \quad (2.14\text{b})$$

$$u_- = \frac{q_-}{2\pi} \oint_{\partial A_-} q_- \left(\ln r + \frac{h_1 - h_2}{h_1 + h_2} \ln r_0\right) d\xi + \frac{q_+}{2\pi} \frac{2h_2}{h_1 + h_2} \oint_{\partial A_+} \ln r \, d\xi \qquad (2.14\text{c})$$

$$v_- = \frac{q_-}{2\pi} \oint_{\partial A_-} \left(\ln r - \frac{h_1 - h_2}{h_1 + h_2} \ln r_0\right) \frac{\partial \mathcal{L}}{\partial \xi} \, d\xi + \frac{q_+}{2\pi} \frac{2h_2}{h_1 + h_2} \oint_{\partial A_+} \ln r \frac{\partial \mathcal{L}}{\partial \xi} \, d\xi, \quad (2.14\text{d})$$

where $\partial A_-$ and $\partial A_+$ are closed integration paths along the boundaries of $A$ for $\eta < 0$ and $\eta > 0$, $q_-$ and $q_+$ are the vorticity anomalies in these regions, respectively, and $\mathcal{L}$ denotes the $\eta$ coordinate of $\partial A$. As a general statement, we can turn (2.12) into contour integrals as long as the Green's function can be written as a sum of terms each of which is either symmetric or antisymmetric with respect to $x$ vs. $\xi$ or $y$ vs. $\eta$ derivatives.

Now we have to evaluate a set of contour integrals (2.14) to get $u$ and $v$. To be able to do this, $\partial A$ must be known. In contour dynamics method, $\partial A$ is evolved in a Lagrangian way by calculating velocity on $\partial A$ and time stepping it forward. In the present problem, $\partial A$ consists of both the potential vorticity interface and the topography; only the former, also referred as potential vorticity contour, needs to be updated. The $y$ coordinate of the contour, $\mathcal{L}$, evolves according to

$$\frac{\partial \mathcal{L}}{\partial t} + u_{\mathcal{L}} \frac{\partial \mathcal{L}}{\partial x} = v_{\mathcal{L}} \qquad (2.15)$$

where $u_{\mathcal{L}}$ and $v_{\mathcal{L}}$ are the along and across-escarpment velocity components on the contour. Equation (2.15) shows explicitly the nonlinearity and time dependency of this system. The problem of solving for the nonlinear evolution of the system defined by equations (2.1) and condition (2.7) is thus reduced to that of performing contour integrals along $\partial A$ for $u$ and $v$, and time stepping $\mathcal{L}$ in (2.15) for new $\partial A$.

The advantage of this method in solving the present problem is multiple: it is simple in mathematical approach, straightforward in physical interpretation and efficient

in numerical computation. It avoids the conventional grids of the finite difference method and therefore avoids diffusion of any type. The contour dynamics method has been used widely in studying geophysical flows, such as vortex dynamics (Polvani, 1988), finite perturbation of shear flow (Pratt and Stern, 1986), eddy-shear flow interaction (Hedstrom, 1986; Stern and Flierl, 1987; Bell, 1990; Stern 1991) and topographic eddy generation (Thompson, 1991). More about the contour dynamics method can be found in recent reviews by Dritschel (1989) and Pullin (1992). The numerical implementation of this method will be discussed briefly in a later section. First we will examine the fundamental linear behavior of waves trapped at an escarpment and linear interaction of a vortex with an escarpment.

## 2.4 Linear Analysis of Vortex Interaction with Finite Escarpment

The equations (2.14) and (2.15) are usually difficult to solve analytically and therefore numerical solutions are often sought. But for certain linearized cases, it is possible to integrate the contour dynamics equations analytically and to obtain solutions for small amplitude perturbation over a finite escarpment. Small amplitude means that the ratio of amplitude of contour deformation $\mathcal{L}$ to its lateral length scale is of order of Rossby number $\epsilon$, which itself is small. The vorticity equation in the presence of a point vortex at location $(X, Y)$ is now written as

$$\nabla^2 \psi = q + \Gamma \delta(x - X) \delta(y - Y), \tag{2.16}$$

with $q$, the vorticity anomaly given by

$$q = \begin{cases} \Delta q h_1, & \mathcal{L} < y < 0 \\ -\Delta q h_2, & 0 < y < \mathcal{L} \\ 0, & other \end{cases} \tag{2.17}$$

where $\Delta q = \Delta h/(\epsilon h_1 h_2)$, $\Delta h = h_1 - h_2$, and $\Gamma$ is the dimensionless strength of the vortex and will be scaled so that $|\Gamma| = 1$ in later study.

25

The velocity field is decomposed into two portions, the perturbation velocity due to the contour deformation and the velocity due to the point vortex. The former is given by equations (2.14) and the latter can be obtained by taking proper $x$ or $y$ derivative of (2.13). The linearization is based on the assumption of small amplitude perturbations of the potential vorticity interface. The velocity at the interface due to the point vortex at $Y < 0$ is approximated by that at $y = 0$,

$$u_v = \frac{\Gamma}{2\pi} \frac{2h_1}{h_1 + h_2} \frac{Y}{r_v^2} \tag{2.18a}$$

$$v_v = \frac{\Gamma}{2\pi} \frac{2h_{3-j}}{h_1 + h_2} \frac{x - X}{r_v^2}, \tag{2.18b}$$

where $j = 1$ for $\mathcal{L} < 0$ and $j = 2$ for $\mathcal{L} > 0$ and $r_v = \sqrt{(x - X)^2 + Y^2}$. To linearize the perturbation velocity (2.14), we take the Taylor series expansion of the integrands about the small parameter $\mathcal{L}$ and reduce the integrals along closed path to line integrals, which yield

$$u = \frac{\Delta q}{2\pi} \frac{2h_{3-j}}{h_1 + h_2} \int_{-\infty}^{\infty} \frac{y}{(x - \xi)^2 + y^2} \hat{\mathcal{L}} \, d\xi \tag{2.19a}$$

$$v = \frac{\Delta q}{2\pi} \frac{2h_{3-j}}{h_1 + h_2} \int_{-\infty}^{\infty} \frac{x - \xi}{(x - \xi)^2 + y^2} \hat{\mathcal{L}} \, d\xi, \tag{2.19b}$$

where $\hat{\mathcal{L}}$ is equal to $\mathcal{L}$ rescaled by local water depth to make the areas contained by $\hat{\mathcal{L}} < 0$ and $\hat{\mathcal{L}} > 0$ the same: $\hat{\mathcal{L}} = h_1 \mathcal{L}_-$ for $\mathcal{L} < 0$ and $\hat{\mathcal{L}} = h_2 \mathcal{L}_+$ for $\mathcal{L} > 0$,

The contour evolution equation (2.15) is linearized and becomes

$$\frac{\partial \hat{\mathcal{L}}}{\partial t} - \bar{u} \frac{\partial \hat{\mathcal{L}}}{\partial x} = h_j \{v(x, 0, t) + v_v(x, 0)\}. \tag{2.20}$$

where we have let the $x$ coordinate translate with the point vortex in a speed $\bar{u} = X_t$ (perturbation induced velocity excluded due to linearization). The vortex translation speed is now due to both the perturbation advection and the image of the point vortex,

$$X_t = \frac{\Delta q}{2\pi} \frac{2h_2}{h_1 + h_2} \int_{-\infty}^{\infty} \frac{Y}{(X - \xi)^2 + Y^2} \hat{\mathcal{L}}(\xi, t) \, d\xi + \frac{\Gamma}{4\pi Y} \frac{h_1 - h_2}{h_1 + h_2} \tag{2.21a}$$

$$Y_t = \frac{\Delta q}{2\pi} \frac{2h_2}{h_1 + h_2} \int_{-\infty}^{\infty} \frac{X - \xi}{(X - \xi)^2 + Y^2} \hat{\mathcal{L}}(\xi, t) \, d\xi. \tag{2.21b}$$

26

Equations (2.18), (2.19), (2.20) and (2.21) form a complete set for unknowns $\hat{\mathcal{L}}$, $X$ and $Y$. Similar equations were also obtained in the study of vortex-shear flow interaction problems by Stern and Flierl (1987) and Bell (1990). The present formulation differs from theirs in the existence of a finite escarpment, which, unlike a shear flow, introduces an image effect in the velocity field and causes the asymmetry in unscaled front $\mathcal{L}$.

### 2.4.1 Free Escarpment-Trapped Waves

In the absence of the vortex, we solve the linearized system of equations (2.19) and (2.20). We intend to derive a free wave solution and its dispersion relation. Assuming sinusoidal interface waves of the form $\hat{\mathcal{L}} = e^{ik(x-ct)}$ with $k$ and $c$ being wave number and phase speed, respectively, and substituting it into equations (2.19), we can obtain

$$u = sgn(y) \frac{h_{3-j}}{h_1 + h_2} \Delta q \; e^{-k|y| + ik(x-ct)} \tag{2.22a}$$

$$v = \frac{h_{3-j}}{h_1 + h_2} \Delta q \; e^{-k|y| + ik(x-ct)+i\pi/2} \tag{2.22b}$$

where $j = 1$ for $y > 0$ and 2 for $y < 0$, and $sgn(y) = 1$ for $y > 0$ and $-1$ for $y < 0$. It is seen that $u$ is $180°$ out of phase at two sides of the escarpment and both $u$ and $v$ are discontinuous across the escarpment.

Substituting $\hat{\mathcal{L}}$ and $v$ into contour evolution equation (2.20), and letting $\bar{u}$ and $v_v$ be zero, it is easy to obtain a dispersion relation for escarpment trapped waves,

$$kc = -\Delta q \frac{h_1 h_2}{h_1 + h_2} = -\frac{\Delta h}{\epsilon (h_1 + h_2)}, \tag{2.23}$$

where the wave number $k$ is required to be positive to satisfy the amplitude decay as $|y| \to \infty$ in equation (2.22). The trapped wave always propagates in the direction with shallow water on the right side (northern hemisphere). For a given frequency, long waves travel faster than short waves. No matter what the wave numbers are, the trapped waves take only the natural frequency of the escarpment, which depends on the size of

27

the topography only and is always less than the inertial frequency $f$. If the escarpment is small, i.e., $h_1 = h$, $h_2 = h - \Delta h$ and $\Delta h/h \ll 1$, the wave speed is approximately $c = -\Delta q/2k$ with $\Delta q = f\Delta h/h$ the change in vorticity across the wave front. It is interesting to compare this escarpment wave dispersion relation with that for a barotropic shear flow front over a flat bottom. In such a case, the PV front is due to the variation of the velocity shear: $u_0 = U - \alpha y$ for $y > 0$ and $U$ for $y < 0$, where $U$ is a constant mean current and $\alpha > 0$ is the shear in the region $y > 0$. The dispersion relation for waves at this shear interface is $c - U = -\alpha/2k$. Except the background mean current which advects the interface wave in the direction of $U$, this dispersion relation is similar to that of the escarpment waves. Both dispersion relations are dependent on the value of vorticity jump across the interface and have zero group velocity. Finally the above discussed interface waves can be compared to one dimensional Rossby wave which has a dispersion relation $c = -\beta/k^2$. They have an important similarity: they are vorticity waves and owe their existence to the background vorticity variation.

## 2.4.2 Small Amplitude Vortex-Escarpment Interaction

Equations (2.18)–(2.21) can be integrated to give the results for small amplitude vortex-escarpment interaction. Before the interface between the two different vorticity regions is disturbed, $\mathcal{L}$ is zero everywhere and coincident with the escarpment. After vortex is switched on, the interface is forced to deform. Fluid moving across the escarpment gains relative vorticity due to stretching or compression. Now velocity at any point has two parts, one due to the vortex field and the other due to interface perturbation. As the contour evolves, the perturbed interface will influence both its own motion and that of the vortex.

In order to linearize the interface equation, we examine the momentum balance of a perturbed interface. Once the interface is perturbed away from its equilibrium position, both the vortex and the perturbation affect interface evolution. For the perturbation to

28

remain at small amplitude, these two forcings must roughly balance at the interface. In terms of the momentum balance, this means that the velocity components at the interface induced by the vortex and by the perturbation are of the same order of magnitude. Since the length scale of the interface perturbation is of the same order of magnitude as the distance between the interface and the vortex, the same argument suggests that the vortex translation velocity is of the same order of magnitude as the perturbation velocity. Thus the advection term on the left hand side of equation (2.20) can be neglected at the order of perturbation magnitude squared, provided the interface perturbation is small everywhere. As a result the equations (2.20) and (2.21) are uncoupled. They can be written as follows,

$$\hat{\mathcal{L}}_t - \frac{\Delta q}{2\pi} \frac{2h_1 h_2}{h_1 + h_2} \int_{-\infty}^{\infty} \frac{\hat{\mathcal{L}}}{x - \xi} \, d\xi = \frac{\Gamma}{2\pi} \frac{2h_1 h_2}{h_1 + h_2} \frac{x}{x^2 + R^2} \tag{2.24a}$$

$$X_t = -\frac{\Delta q}{2\pi} \frac{2h_2}{h_1 + h_2} \int_{-\infty}^{\infty} \frac{R}{\xi^2 + R^2} \hat{\mathcal{L}}(\xi, t) \, d\xi - \frac{\Gamma}{4\pi R} \frac{h_1 - h_2}{h_1 + h_2} \tag{2.24b}$$

$$Y_t = -\frac{\Delta q}{2\pi} \frac{2h_2}{h_1 + h_2} \int_{-\infty}^{\infty} \frac{\xi}{\xi^2 + R^2} \hat{\mathcal{L}}(\xi, t) \, d\xi. \tag{2.24c}$$

The initial conditions are $(X, Y) = (0, -R)$ and $\hat{\mathcal{L}}(x, 0) = 0$.

Taking the Fourier transform of (2.24a) in $x$ results in a simple first order ordinary differential equation, which is solved to yield

$$\tilde{\mathcal{L}}(k, t) = -\frac{\Gamma}{\Delta q} \begin{cases} \left(e^{-i\Delta \bar{q} t} - 1\right) e^{-kR} & k \geq 0 \\ \left(e^{i\Delta \bar{q} t} - 1\right) e^{kR} & k < 0 \end{cases}, \tag{2.25}$$

where $\tilde{\mathcal{L}}(k, t)$ is the Fourier transform of $\hat{\mathcal{L}}$ in $k$ space and $\Delta \bar{q} = \Delta h / \epsilon (h_1 + h_2)$. (2.25) can be inverted to give

$$\hat{\mathcal{L}}(x, t) = \frac{\Gamma}{\pi \Delta q} \left\{ \frac{R}{x^2 + R^2} (1 - \cos \Delta \bar{q} t) + \frac{x}{x^2 + R^2} \sin \Delta \bar{q} t \right\} \tag{2.26}$$

This result is the same as that for the linear eddy-shear flow interaction solved by Bell (1990). Substituting $\hat{\mathcal{L}}$ into (2.24b and c) yields

$$X_t = -\frac{\Gamma}{2\pi R} \frac{h_2}{h_1 + h_2} (1 - \cos \Delta \bar{q} t) - \frac{\Gamma}{4\pi R} \frac{h_1 - h_2}{h_1 + h_2} \tag{2.27a}$$

$$Y_t = \frac{\Gamma}{2\pi R} \frac{h_2}{h_1 + h_2} \sin \Delta \bar{q} t \tag{2.27b}$$

29

Equation (2.26) shows that the interface perturbation consists of three parts. The first is a stationary bump. For $\Delta\bar{q} > 0$, $\Gamma < 0$ and $Y < 0$, the bump is toward the vortex and the fluid in it is of cyclonic vorticity. It advects the vortex towards the positive $x$-direction at a constant speed $-\Gamma h_2/2\pi R(h_1 + h_2)$. The second and third parts are oscillatory. The part symmetric about $x$ contributes to the oscillation of $X_t$, and the asymmetric part causes the interface to tilt periodically, and thus is responsible for the vortex oscillation in $y$-direction. The symmetric oscillation of the interface is $180°$ out of phase with the vortex and has frequency $\Delta\bar{q}$, which we already know is the frequency for free escarpment trapped waves. The asymmetric oscillations are in phase. There is also an image induced vortex translation, together with the advection of the stationary cyclonic bump, toward the positive-$x$ direction. The trajectory of the vortex is described by

$$(X + \frac{\Gamma}{4\pi R}t)^2 + (Y - R)^2 = (\frac{\Gamma}{2\pi R\Delta q}\frac{h_2}{h_1 + h_2})^2.$$

It is noted for this kind of problem, vortex-escarpment or vortex-shear flow alike, a dipole-like structure, containing the vortex and the interface perturbation, will always form with oscillatory parts superposed on it. This can be verified for present case by integrating over entire bump area; it is found it has exactly the same amount but opposite circulation as the point vortex. The possible dipole-like structures are shown in figure 2.2 for $Y < 0$. This figure illustrates the important behavior of interaction between an eddy and an escarpment. It is seen from equations (2.27) that the height of the escarpment, the strength of the vortex and the vortex-escarpment distance all affect the vortex propagation, it is the escarpment size that determines the fact that which motion tendency, the perturbation induced or the image induced, will dominate the direction of vortex motion. In figure 2.2, the cases (a) and (c) correspond to the oceanic situation of an anticyclone or a cyclone interaction with a continental slope, which will be discussed in more detail in the later sections.
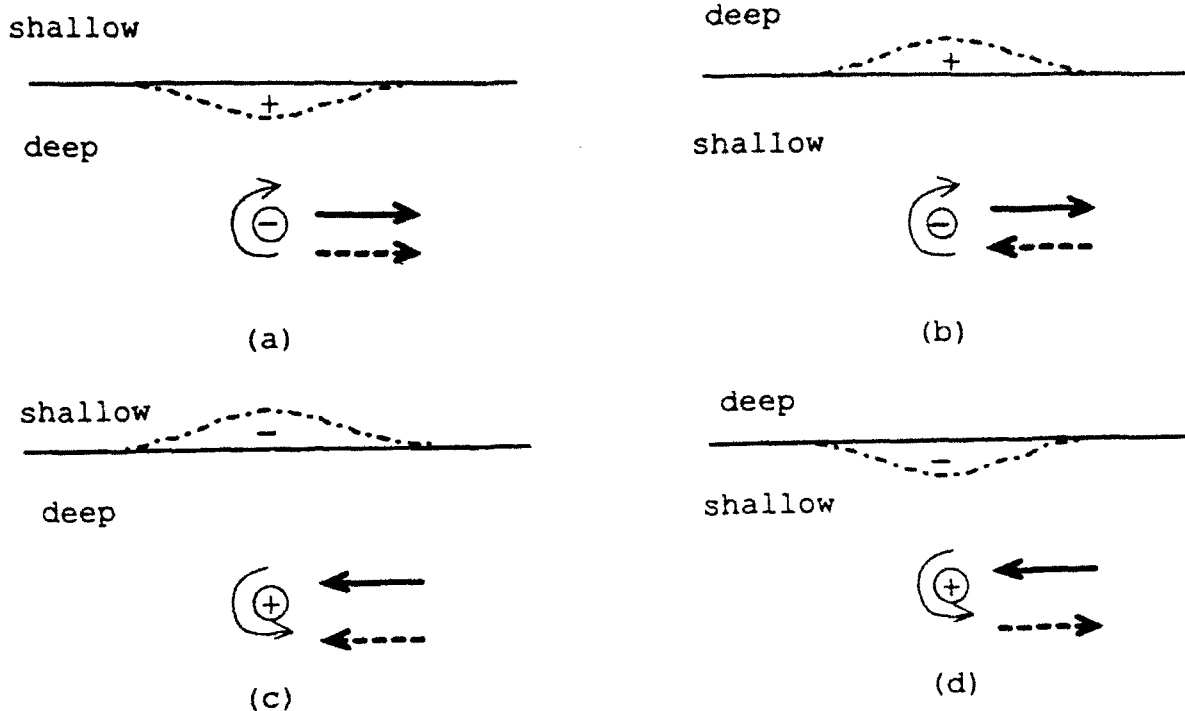
Figure 2.2: Schematic dipole structure of the interface displacement at an escarpment induced by a cyclonic or anticyclonic eddy and the eddy motion tendency. (a) Anticyclone in deep water, (b) anticyclone in shallow water, (c) cyclone in deep water, and (d) cyclone in shallow water. The vortex motion induced by the perturbation is in solid arrow and the image induced in dashed arrow.

It is illuminating at this point to examine some of the conservation properties associated with above discussed problem. First of all, the mass conservation in the present context has the following form

$$\int_{-\infty}^{\infty} h_j \mathcal{L}(x,t)dx = constant.$$

Due to the lack of friction and dissipation, the total momentum, energy and potential vorticity are all conserved. Multiplying the vorticity equation (2.16) by $yh_j$ and integrating it over the entire space, after some simple manipulations we get

$$M = h_i \Gamma Y - \frac{1}{2}\Delta q \int_{-\infty}^{\infty} \mathcal{L}^2(x,t)\,dx$$

where $h_i$ is the fluid depth on the same side as the vortex, and $M = \iint_S yh_j \nabla^2 \psi\, dxdy$, the integration being over the entire fluid domain $S$. Taking the time derivative of $M$ and making use of equations (2.26), (2.27b) and mass conservation, it is easy to show that $M$ is invariant. The quantity $M$, often defined as pseudomomentum, is therefore conserved. For more discussions on pseudomomentum, the readers are referred to Dritschel

31

(1988) and Bell and Pratt (1992), where they proved that the pseudomomentum for a nonlinear stratified system with multiple contours and a flat bottom is conserved. In the present case, if $Y = -R$ and $\mathcal{L}(x,t) = \mathcal{L}_0(x)$ are given at $t = 0$, the pseudomomentum conservation can be written as

$$Y = -R + \frac{1}{2}\frac{\Delta q}{h_i \Gamma} \left\{ \int_{-\infty}^{\infty} h_j^2 \, \mathcal{L}^2(x,t) \, dx - \int_{-\infty}^{\infty} h_j^2 \, \mathcal{L}_0^2(x) \, dx \right\}.$$

It shows that since the pseudomomentum is conserved, the $y$ position of the vortex can be calculated from the displacement of the interface. The pseudomomentum equation shows the vortex must approach the interface if the interface is flat originally and if $\Delta q/\Gamma$ is positive.

## 2.5 Finite Amplitude Interaction of a Vortex with a Small Escarpment

### 2.5.1 Numerical Scheme

The nonlinear terms in equation (2.3) enter the balance at order $O(\epsilon)$, as we expand unknowns in power of $\epsilon$. This is the case when the interface deformation reaches finite amplitude. The direct cause of this is that the vortex gets very close to the escarpment, and the advective effect dominates the momentum transfer. The interface, the$\leftarrow$ ore, is drawn to a large deformation by the vortex as strongly nonlinear interaction follows. This will be discussed in this section. The condition of a small escarpment will be used. The definition of small topography here is that the depth change divided by the mean depth of the fluid $\Delta h/h$ is on the order of Rossby number $\epsilon = U/f_0 L$, where $U$ is the velocity scale and $L$ is the length scale of motion. Under this condition, the quasi-geostrophic approximation will be made, and the stream function of the flow field satisfies a Poisson equation, given by equation (2.16), but the vorticity anomaly now is

$$q = \begin{cases} \Delta q, & \mathcal{L} < y < 0 \\ -\Delta q, & 0 < y < \mathcal{L} \,, \\ 0, & other \end{cases} \qquad (2.28)$$

where $\Delta q = \Delta h / \epsilon h$. Then in (2.7) we can approximate $[h] = 0$ and resulting matching conditions are $[v] = 0$ and $[p] = 0$, *i.e.*, the discontinuities across the escarpment are on the order of the Rossby number. We may readily use the Green's function from (2.13) by setting $h_1 = h_2$ and calculate velocity according to

$$u = -\Delta q \int_{-\infty}^{\infty} \ln \sqrt{\frac{(x - \xi)^2 + (y - \mathcal{L})^2}{(x - \xi)^2 + y^2}} \, d\xi \qquad (2.29\text{a})$$

$$v = -\Delta q \int_{-\infty}^{\infty} \ln \sqrt{(x - \xi)^2 + (y - \mathcal{L})^2} \, \frac{\partial \mathcal{L}}{\partial \xi} \, d\xi \qquad (2.29\text{b})$$

but solve the nonlinear contour evolution equation (2.15).

The numerical contour dynamics model will be used. We outline briefly its numerical implementation. There is a wide range of applications of this technique; readers are referred to Polvani (1988) and Meacham (1991) for more details on its geophysical fluid dynamics application and implementation. From a known position of the contour at a given time, the velocity field is calculated by evaluating contour integrals (2.29) along the interface and escarpment. The contour is then stepped forward to new positions according to (2.15) using a second order Runge-Kutta scheme. As the contour deforms with time, the points on the contour may become dense in one area and sparse in other areas; the spacing of the points on the contour is therefore rearranged according to required resolution as well as local contour curvature. In addition, points are added and removed as needed during contour evolution. The contour may be multivalued. Pinch-off and coalescence of a portion of the contour are allowed. At the extreme case a closed contour may deform to a thread and thus be removed, provided there is essentially no loss of potential vorticity.

For single escarpment problem, there are only two distinctive values of constant relative vorticity induced as $\mathcal{L} \neq 0$. The fluid moving across the escarpment into region $y > 0$ $(0 < y < \mathcal{L})$ gains negative vorticity due to vortex compression, and that moving into $y < 0$ $(\mathcal{L} < y < 0)$ gains positive vorticity due to vortex stretching. In the quasi-geostrophic approximation the positive and negative vorticity so induced are
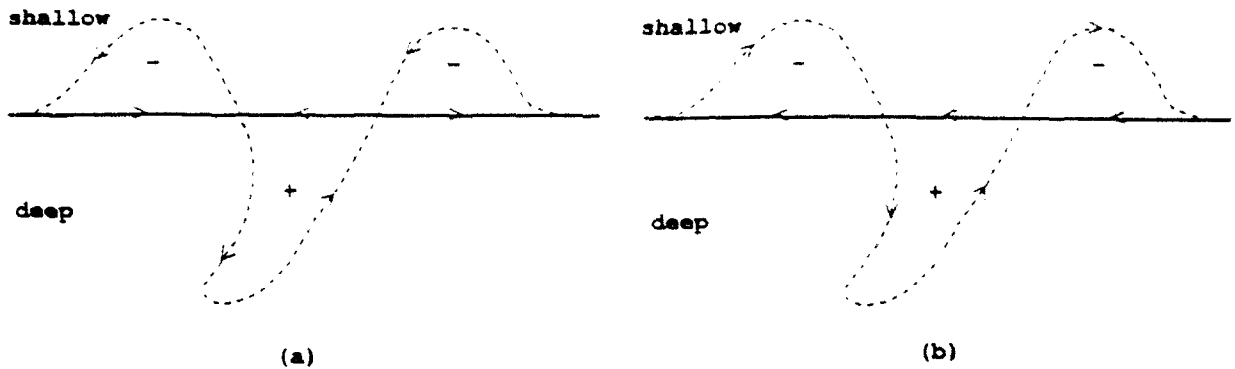
33

Figure 2.3: A schematic illustration of the contour integration. (a) The contour integrals along individual contour enclosing perturbed area and (b) along interface and escarpment as a whole.

equal numerically. In figure 2.3 a portion of the deformed contour is shown. Nonzero vorticity anomalies are only contained in area enclosed by contour $\mathcal{L}(x,t)$ and escarpment $y = 0$. We only need to evaluate contour integrals along paths that encircle nonzero $\nabla \psi$ as shown in figure 2.3a, in which positive path is defined as counter-clockwise along the contour with $\nabla \psi \neq 0$ on the left. This can be easily rewritten as two contour integrals, one along the interface from left to right and the other along escarpment from right to left as shown in figure 2.3b. To do this one only needs to add a minus sign to the integrand which is in $y > 0$. This sign cancels the negative sign for the anomaly strength.

## 2.5.2 Solutions and Discussions

### Overview of Numerical Experiments

The process of quasi-geostrophic vortex-escarpment interaction is studied in this section. The circulation of the vortex is fixed at $\Gamma = -1$, except otherwise mentioned. In following sections we will concentrate on the cases which initially involve only one vortex. It may

34

be anticyclonic or cyclonic, and a point or finite vortex. In the quasi-geostrophic system, only two parameters can be chosen independently, the topographic strength $\Delta q = \Delta h / \epsilon$ and the initial distance between the vortex and the escarpment, $Y_0$. A periodic boundary condition in $x$ direction is used at the two ends of the contour to avoid using a very long contour.

First, a free escarpment-trapped wave experiment is performed which gives the same dispersion relationship as that given in equation (2.23). The model is then applied to the case that can be described by the previous linear solution (such as $\Delta q = 1$ and $Y_0 = -4$). The numerical solution agrees with the analytical solution in predicting interface deformation and wave dispersion with a discrepancy less than two to three per cent. The model is then used to perform a series of experiments with large interface deformation under strongly nonlinear conditions. In these experiments, we will examine processes of cross-topography volume exchanges, interface waves, eddy formation and vortex movement, etc.. It is impossible to cover the whole parameter space; only typical *responses* within the parameter range close to geophysical processes such as oceanic mesoscale eddies are to be discussed here. Table 2.1 lists the cases to be studied in this section. In general they can be considered as advection dominated ($|Y_0|$ small) or radiation dominated ($|Y_0|$ large). The linear interaction studied in the previous section is an example of the radiation dominated case. In this section we will focus on advection dominated strong interactions.

## Numerical Results

We first look at a case where the vorticity due to topography has equal strength as that of the point vortex, $\Delta q = 1$, which is initially located at $(X_0, Y_0) = (\pi, -0.75)$. The interface evolution is shown in figure 2.4. The contour is initially coincident with the escarpment at $y = 0$. The water is deeper in $y < 0$. The vortex is switched on at $t = 0$. The clockwise-rotating vortex velocity field initially causes antisymmetric contour

35

# Table 2.1

Barotropic Quasi-Geostrophic Experiments ($\epsilon = 0.1$)

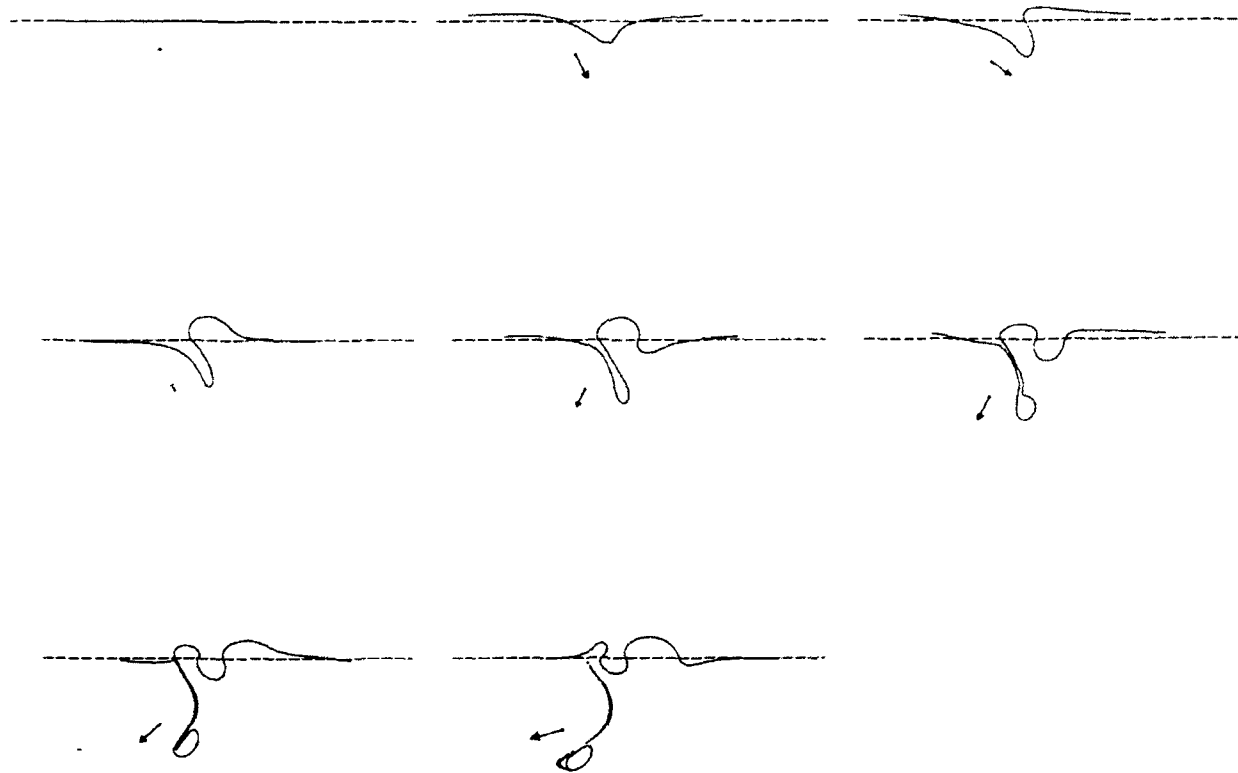| Cases | $\Delta q$ | $Y_0$ | Streamer | Cyclonic Eddy | Volume Exchange |
|-------|------------|-------|----------|---------------|-----------------|
| 1 | 1.0 | $-2.0$ | No | No | 0.1 |
| 2 | 1.0 | $-1.25$ | No | No | 0.5 |
| 3 | 1.0 | $-1.0$ | Yes | Yes | 0.75 |
| 4 | 1.0 | $-0.75$ | Yes | Yes | 0.8 |
| 5 | 1.0 | $-0.5$ | Yes | Yes | 0.9 |
| 6 | 1.0 | $-0.25$ | Yes | No | 1.0 |
| 7 | 0.5 | $-1.0$ | Yes | Yes | 1.5 |
| 8 | 0.5 | $-0.75$ | Yes | Yes | 1.6 |
| 9 | 0.25 | $-1.0$ | Yes | No | 4.0 |
| 10 | 3.0 | $-0.75$ | No | Yes | 0.3 |

Figure 2.4: Time evolution of the interface and vortex for case 4 in table 2.1, $\Delta q = 1$ and $Y_0 = -0.75$. The solid contour stands for the interface and the dashed line for the escarpment. The vortex is marked by a solid dot at the beginning of an arrow, which represents the velocity vector of the vortex translation. The time sequence of evolution starts from $t = 0$ with increment $\Delta t = 4$ at upper-left corner and continues with time increasing to the right and downward.

deformation toward $y > 0$ for $x < \pi$ and $y < 0$ for $x > \pi$. The antisymmetry is soon broken as the vortex starts moving eastward due to its closeness to the cyclonic interface perturbation. Unlike the linear perturbation problem where the interface as well as the vortex simply oscillates stably, the perturbation continues to grow and forms a cyclonic lobe to the east of the vortex. This lobe in turn advects the vortex southward. The shear of the vortex and the perturbation velocity together force more fluid into the head of the lobe. The neck is stretched to form a thin streamer around the vortex. As the system evolves, the head detaches from the neck and becomes an eddy. It pairs with the point vortex to form a dipole-like structure and propagates along an arc path farther southwestward. The shape of the eddy is approximately elliptical and its longer axis is almost tangential to its arc path. It is also noted that the distance between the eddy and the vortex is almost the same as the initial vortex-escarpment distance. Since cyclonic vorticity is advected away from the interface, there is more anticyclonic vorticity than cyclonic vorticity near the escarpment. This vorticity imbalance has two important dynamic effects: first it, together with the new cyclonic eddy, induces a weak westward along-escarpment current; second the interface has larger crests ($\mathcal{L} > 0$) than troughs ($\mathcal{L} < 0$). The perturbation velocity field (velocity field excluding that induced by point vortex) indeed shows a time dependent, weak westward current developed near the escarpment during the interaction. This current is mainly in between the escarpment and the topographic cyclone and decays outside this range. There is no such unidirectional current formed on the shallow side, and the velocity is also much weaker (figure 2.5).

The main interface at the escarpment feels less influence from the point vortex after it drifts away southward. The interface waves are observed to propagate westward along the escarpment, with period about 15 dimensionless time; for comparison the corresponding linear wave for $\Delta q = 1$ has period of 12.6 dimensionless time. Nonlinear steepening of wave front can be seen from figure 2.4. The wave speed is also slower than the linear wave speed. It should be noted that the interface wave in figure 2.4 propagates against the vortex velocity field, which advects whole interface eastward.
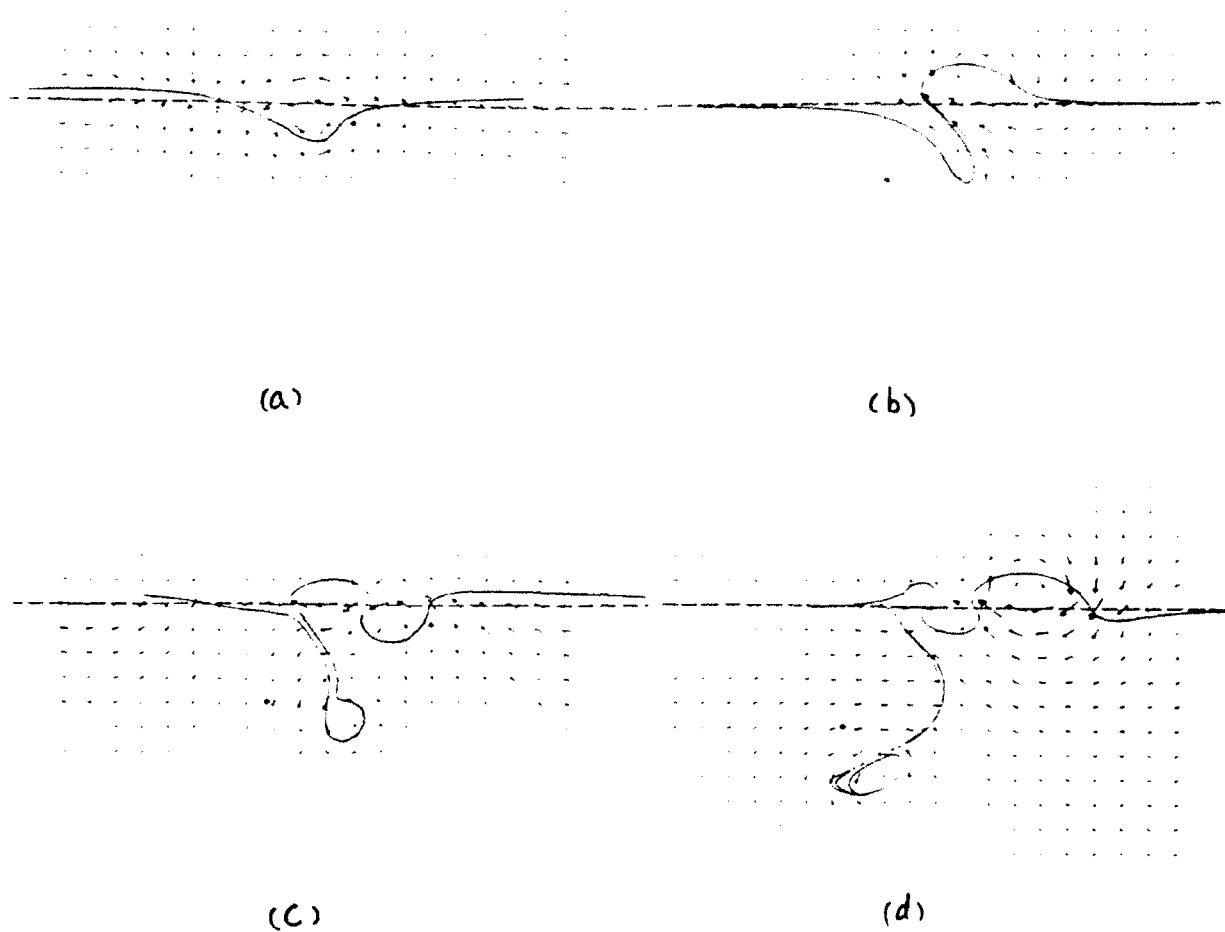
38

(a)

(b)

(c)

(d)

Figure 2.5: Perturbation velocity field for the case shown in figure 2.4 at time $t =:$ (a) 4, (b) 12, (c) 20 and (d) 28.
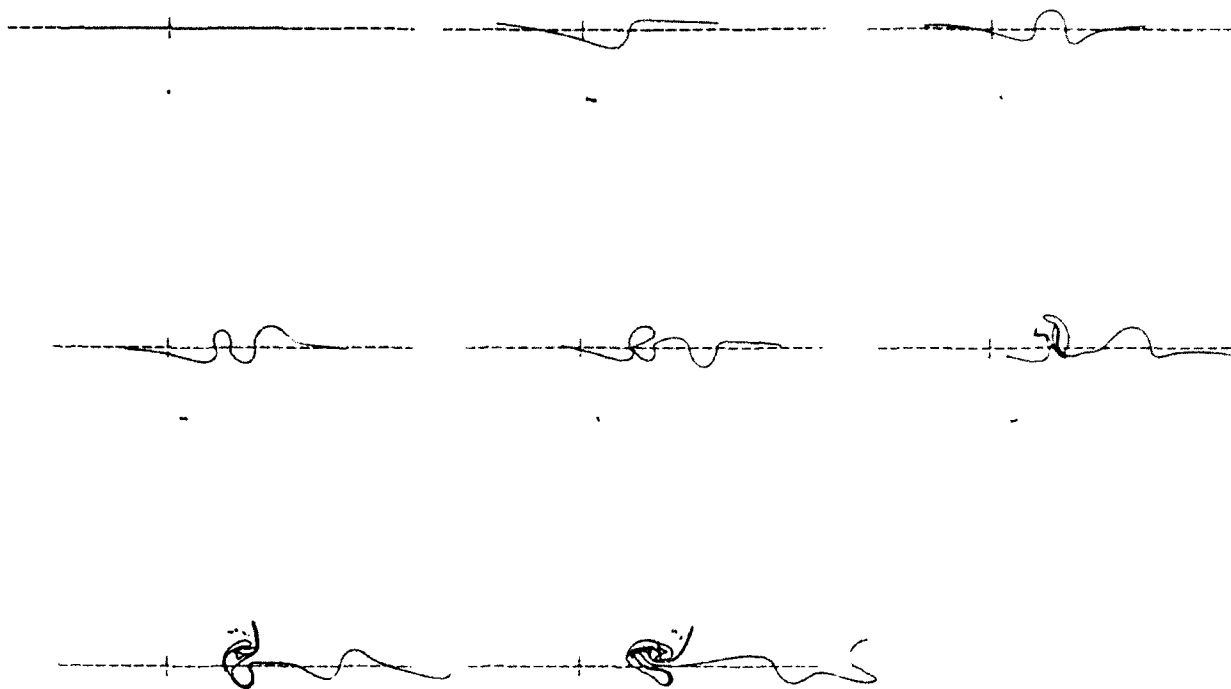
Figure 2.6: Time evolution of the interface and vortex for case 2 in table 2.1, $\Delta q = 1$ and $Y_0 = -1.25$. The time sequence of evolution starts from $t = 0$ with increment $\Delta t = 8$. Other notations are the same as that shown in figure 2.4. Notice that the cross-escarpment scale is enlarged.

The strength of interaction also depends on the distance between the vortex and the escarpment. By fixing the size of the topography and the circulation of the vortex, we can perform a series of experiments probing the dependence of interaction on initial vortex position $Y_0$. The parameters and typical behavior of the system are listed in table 2.1. The results for large $|Y_0|$ (e.g. $|Y_0| > 3$) fall into the linear radiative interaction as described by the analytical solution in the previous section. Since the interface wave generated in this system has zero group velocity, it does not propagate energy away from the perturbed region. Thus the energy and momentum transfer is entirely confined to the radiation between the interface and the vortex. The interface and the vortex are locked in a state of resonant oscillation. This process has already been discussed in the previous section and will not be considered here. For moderate value of $|Y_0|$ ($-3 < Y_0 < -1$) and fixed $\Delta q = 1$, the interaction shows gradually increasing nonlinear effects. An example, case 2 from table 2.1, is shown in figure 2.6. The interface perturbation has
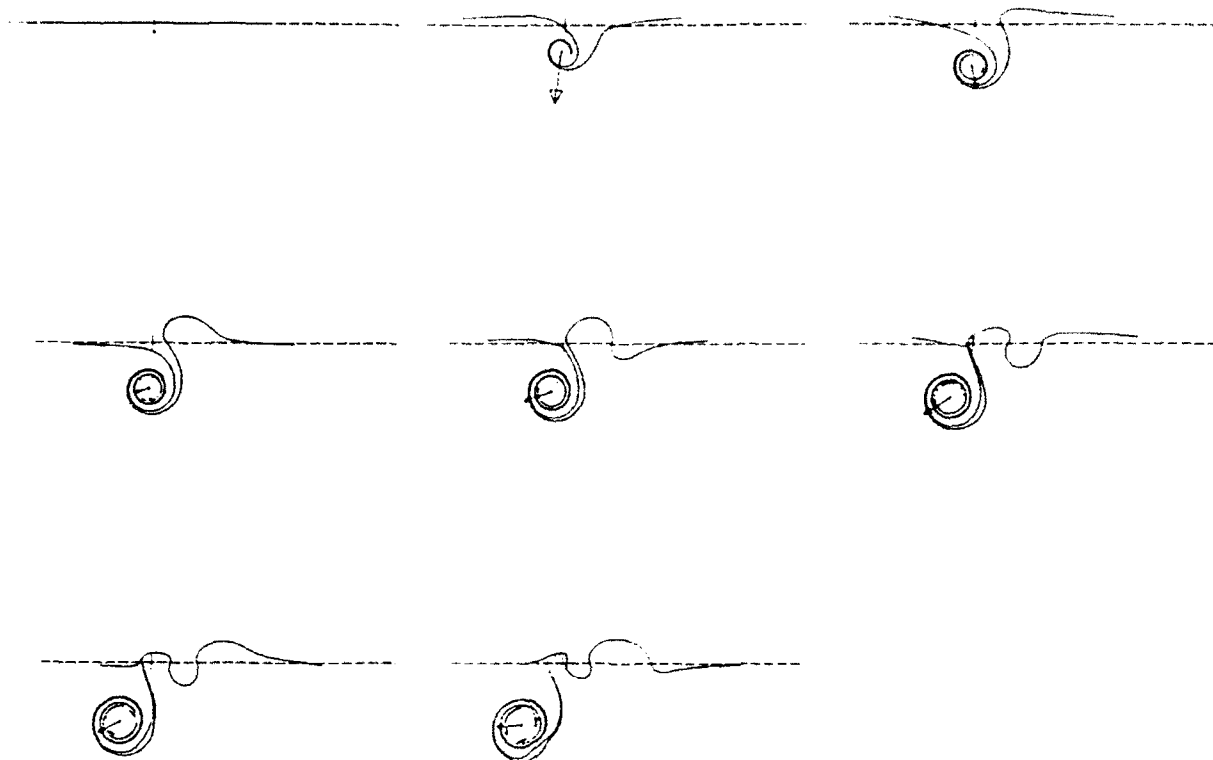
Figure 2.7: Time evolution of the interface and vortex for case 6 in table 2.1. $\Delta q = 1$ and $Y_0 = -0.25$. The time sequence of evolution starts from $t = 0$ with increment $\Delta t = 4$. Other notations are the same as that shown in figure 2.4.

finite amplitude, but never grows to form a streamer or eddy. Once reaching finite amplitude, the nonlinear self-interaction of the interface will dominate the evolution process since the vortex is relatively far away. The interface perturbation shows clearly the sign of nonlinearity with steepening and breaking of the front. The most obvious role of the vortex, after its initial perturbation of the interface, is to advect the interface and the frontal structure to the direction opposite to the escarpment wave propagation. One of the major differences between this moderately nonlinear interaction and the other stronger interactions is that no fluid is drawn away from the escarpment by the vortex during the interaction. This distinguishes it from a whole set of problems which always involves cross topography volume fluxes caused by the forcing vortex. On the other hand, for very small $|Y_0|$, such as $Y_0 = -0.25$ (case 6 in table 2.1), the vortex will have a much stronger effect on the interface evolution. Figure 2.7 shows that the streamer is quickly wrapped around by vortex and no cyclonic eddy is generated. Since it is our intention to

investigate strongly nonlinear eddy-escarpment interactions with both cross-escarpment volume exchanges and topographic eddy formation, the cases represented typically by cases 2 and 6 will not be dealt with specifically in following studies.

When topography is small, *i.e.*, $\Delta q < 1$, it is easier for fluid to cross the escarpment and therefore more cross-escarpment volume exchange occurs. This is because more fluid of weaker vorticity anomaly is needed to balance the vortex forcing. As a consequence, the eddy formed has larger area, and the interfacial wave has larger amplitude and wavelength. This is indeed the case as shown in figure 2.8 for $\Delta q = 0.5$ and $Y_0 = -0.75$. Compared with figure 2.4 the difference in contour evolution is quite obvious. On the other hand if topography is large, *i.e.*, $\Delta q > 1$, it is harder for fluid to cross the escarpment and thus less volume exchange takes place. An example is shown in figure 2.9 for $\Delta q = 3$ and $Y_0 = -0.75$ (case 10 in table 2.1). When compared with figures 2.4 and 2.8, the interface perturbation decreases as the topography increases. There are also time and space scale variations associated with varying parameters. When $\Delta q$ is even larger (larger topography or smaller $\epsilon$), such as $\Delta q = 5$ for $Y_0 = -0.75$, the interface is too rigid to detach; it only deforms in a relatively small amplitude pattern and momentum transfer is radiation-dominated.

## Formation of a Topographic Eddy

For certain parameter range, vortex-escarpment interaction shows strongly nonlinear behavior. There is progressive formation of a high PV tongue, streamer and eddy. The eddy cannot form if this distance is either too small (such as case 6, figure 2.7) or too large (such as case 2, figure 2.7) To better understand this eddy formation and detachment, we will examine in detail the structure of the contour and velocity field for case 4 ($\Delta q = 1$ and $Y_0 = -0.75$), shown in figure 2.10. At dimensionless time $t = 16$, a lobe of cyclonic vorticity extends to the east of the point vortex. The fluid is continuously pumped into the lobe and forms a cyclonic head at the tip of the lobe. The anticyclonic velocity field
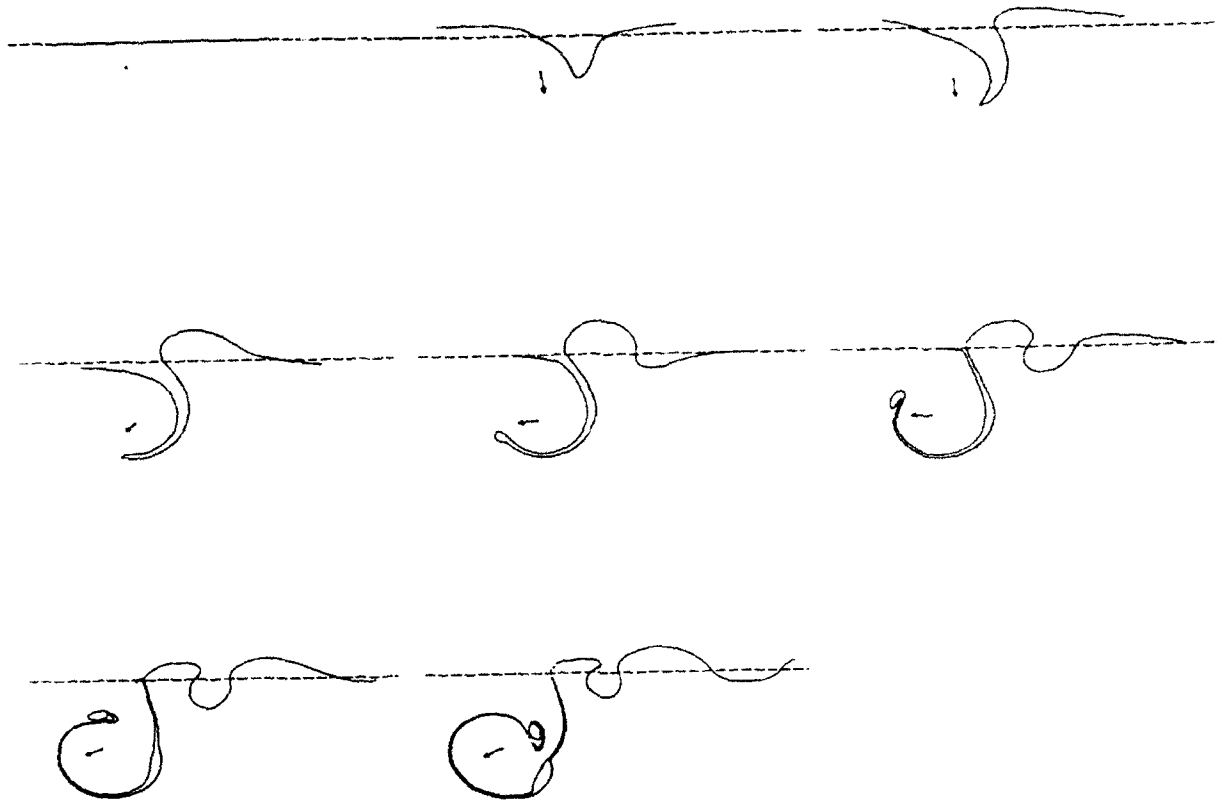
Figure 2.8: Time evolution of the interface and vortex for case 8 in table 2.1, $\Delta q = 0.5$ and $Y_0 = -0.75$. The time sequence of evolution starts from $t = 0$ with increment $\Delta t = 8$. Other notations are the same as that shown in figure 2.4.

due to the negative PV anomaly north of the lobe pushes the lobe towards the west, where it encounters the vortex velocity field in the opposite direction ($t = 18$ and $20$). Together they squeeze the lobe neck and force fluid into the head. The cyclonic velocity field of the growing head then acts to thin the neck and eventually lead to its detachment from the lobe ($t = 22$). The lobe then contains only a small amount of fluid and becomes a streamer around the vortex. On the other hand, if the streamer is advected around vortex faster than that a head can form, there will be no eddy formed. This process is compared with the detachment of single-lobe meanders studied by Pratt and Stern (1986). In their case, the meandering contour wa a shear flow interface, there was no vortex present, and the meander evolution extracted energy from the current. They found that in order for detachment to occur, the lobe must be of relatively large amplitude and small width. In that case, the basic flow and the anomaly field acted together to thin the neck and caused eddy detachment. The detached area depended upon the lobe width.
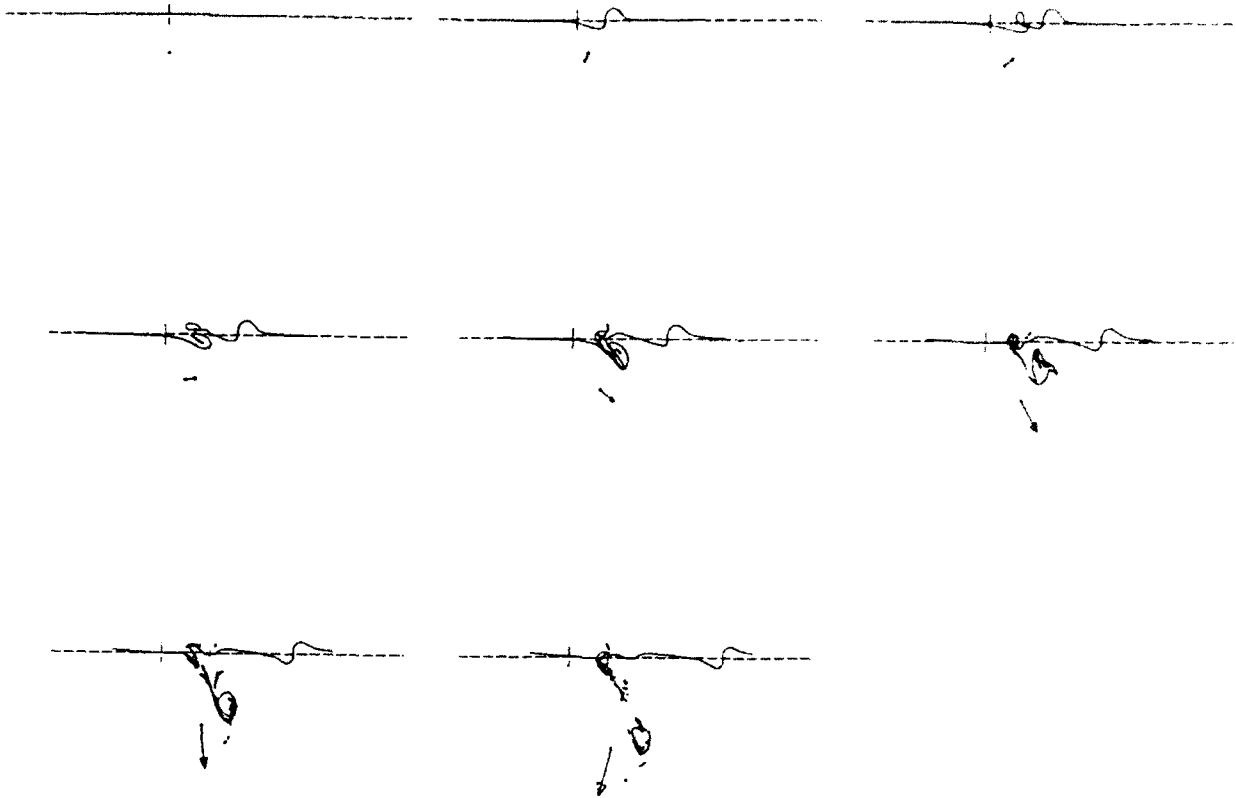
43

Figure 2.9: Time evolution of the interface and vortex for case 10 in table 2.1, $\Delta q = 3$ and $Y_0 = -0.75$. The time sequence of evolution starts from $t = 0$ with increment $\Delta t = 4$. Other notations are the same as that shown in figure 2.4.

This is quite similar to the eddy detachment in the present study. The differences are that in this study the precondition of the interface is achieved through vortex-interface interaction and the vortex provides shear and momentum for the eddy formation.

We again study figure 2.8, which corresponds to case 8 in table 2.1 and has a topography smaller than that in case 4. Since the interface is less rigid due to weaker topography, the vortex advection dominates the evolution. In contrast to figure 2.4, which has larger topography, a large volume of fluid of weak PV anomaly is drawn across the escarpment and wrapped around the vortex faster than it could form a sizable head. Only in later stage of interaction is a small eddy formed. There is a lobe formed in the middle of the thinning streamer, which is in between the vortex and a cyclonic interface perturbation northeast of it. The condition for this lobe formation is very similar to the head formation process in figure 2.10.
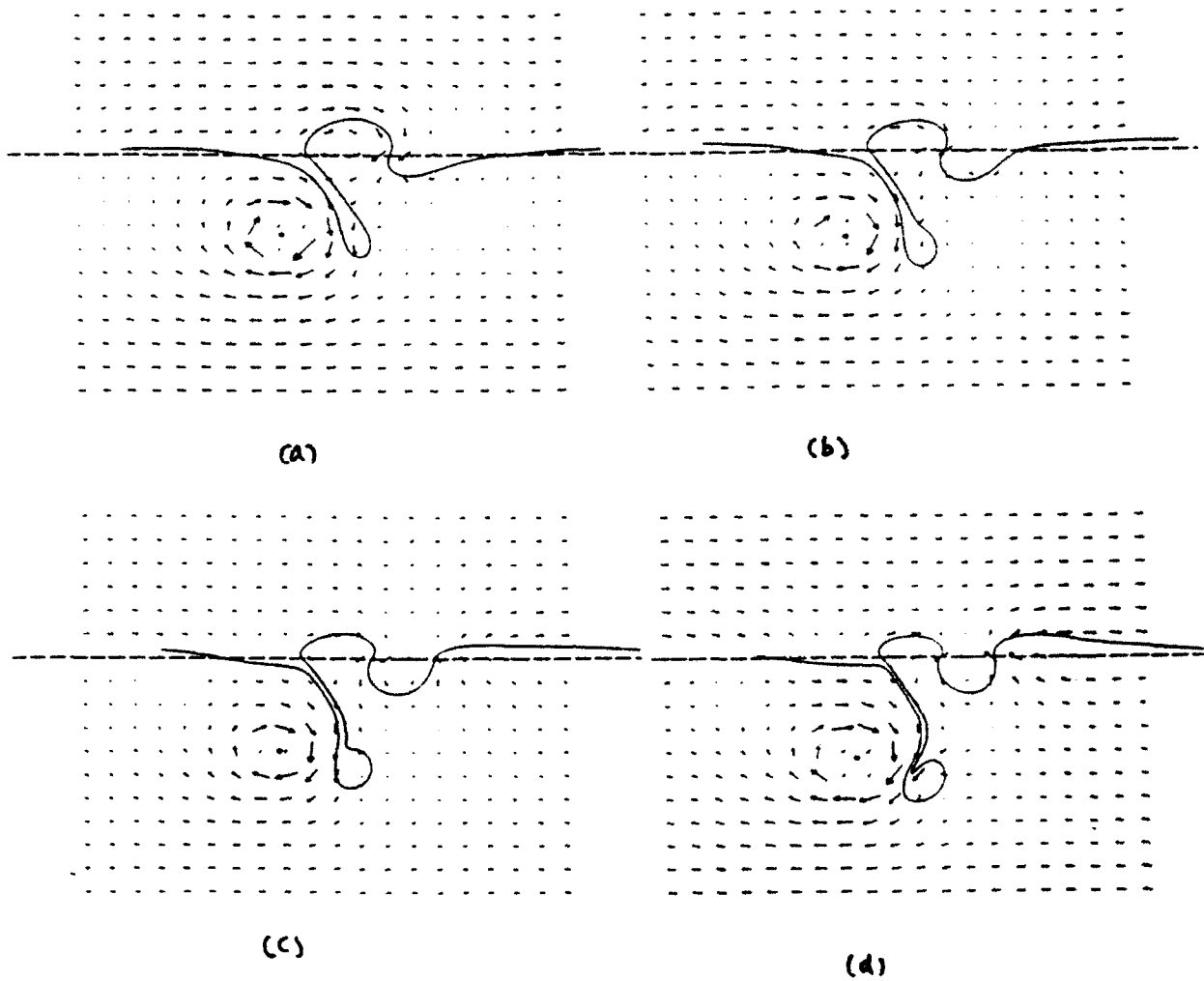
Figure 2.10: Full velocity field for the case shown in figure 2.4 at time $t =$ (a) 16, (b) 18, (c) 20 and (d) 22.

The eddy formation over a large escarpment shown in figure 2.9 is quite different from those over small escarpment. Due to large $\Delta q$, thus strong self-interaction, the disturbance develops quickly into a cyclonic eddy close to the main interface, where it is subject to strong perturbation shear and vortex advection. The eddy is then advected away from the main interface by the vortex. At the opposite extreme, for very small $\Delta q$ (for example, case 9 in table 2.1), the fluid is easily advected across topography and wrapped around the vortex. Little shear is provided by the perturbation field to generate a sizable cyclonic pool which could balance the vortex field. In such a situation, there is no eddy formed during entire interaction process.

In general, eddy formation requires a proper balance between the vortex and the perturbation field in both strength and distance. These conditions also decide the size of the eddy formed. Taking eddy formation in case 3 ($\Delta q = 1$ and $Y_0 = -1$) as the standard, eddy formation in cases where $\Delta q < 1$ is in favor of larger $|Y_0|$, and eddy formation in cases where $\Delta q > 1$ is in favor of smaller $|Y_0|$.

### Forced Escarpment Waves

The comparison of figures 2.4, 2.8 and 2.9 also reveals that it appears there are two active time scales in this system. One is an advection time scale, in which the streamer is advected around vortex; the other is a topographic time scale, in which the interface wave evolves. It can be seen from figures 2.4, 2.8 and 2.9, the advective process is slower and the interfacial waves evolve faster as the topography becomes larger. The only factor that is responsible for these changes is the different $\Delta q$ in these cases.

The wave periods are listed in table 2.2 for three different values of $\Delta q$. In the table, the observed wave period is the wave period seen at a fixed location. It also contains influences from processes other than the escarpment wave, such as the point vortex and topographic eddy. For example, north of the vortex, the velocity due to the anticyclonic point vortex is eastward, opposite to the direction of escarpment waves.

## Table 2.2

QG Escarpment Waves ($\epsilon = 0.1$)

| $\Delta q$ | $\Delta h$ | Linear Period | Observed Period | Corrected Period |
|------------|------------|---------------|-----------------|------------------|
| 0.5 | 0.05 | 25.1 | 34 | 24.7 |
| 1.0 | 0.1 | 12.6 | 15 | 12.6 |
| 3.0 | 0.3 | 4.2 | 5 | 4.5 |

Therefore, at a fixed point there, the observed wave period is somewhat larger than the true period; while south of the vortex, the observed period is smaller. Since it is difficult to remove the influences due to the topographic eddy and the streamers, we will only use the information north of the escarpment and calculate the wave period by removing only the influence due to the point vortex. Let $T_c$ and $T_0$ be the corrected and observed wave periods, respectively, $U$ be the average velocity at the observation point due to the point vortex, and $c_0$ the observed wave speed ($c_0 = T_0/\lambda$, $\lambda = 2\pi$ is wave length), then

$$T_c = \frac{T_0}{1 - U/c_0}$$

The results are listed in table 2.2. The observation point is one fourth wave length away from the topography. It is seen that the corrected wave period is very close to the linear escarpment wave period calculated using equation 2.23. In the present case of step topography, only one wave mode per interaction is excited, which is the resonant mode associated with the given escarpment size. The observed velocity as a function of time

47

at the observation point is shown in figure 2.11 for three cases tabulated in table 2.2 (figure 2.11 a, b and c). The evolution of the escarpment wave clearly follows an internal time scale, depending mainly on the topography; while the interface itself is affected by a combination of both topography and nonlinear advection. The detached parts of the interface, i.e., the topographic eddy and streamers, evolve on an advection time scale defined by external process such as the point vortex here.

The waves on the deep side ride on a developing along-escarpment current as shown in figure 2.11d for case 4. Away from the topography, $u$ at two sides of the escarpment is $180^\circ$ out of phase. However near the escarpment nonlinearity enters at the lowest order and $u$ is continuous across the escarpment.

The wave amplitude depends on the size of topography and decays to both sides of the escarpment (figure 2.11 a, b, c, e and f). In general a fixed vortex forcing will generate larger interface perturbation over small topography than over large topography, but the total perturbation vorticity tends to remain the same. As a result, large interface change is induced over small topography, i.e., large volume of weak vorticity anomaly, as compared to small volume of strong vorticity anomaly over large topography.

The dependence of wave amplitude on $Y_0$ is weak within the strong interaction range of $Y_0$. Results show that from case 3 to case 5, $Y_0$ is halved, but the amplitude of the escarpment wave at $y = \pi$ increases only by less than ten per cent. The wave frequency is independent of $Y_0$. This is an expected result since the wave dispersion relation is determined only by the internal scales, such as topography, and not by the external forcing.


**Vortex Motion**

Once the interface is perturbed from its equilibrium position, it affects the motion of the point vortex. Figure 2.12 shows the vortex trajectories for the cases listed in table 2.1. With the exception of one case, in which the vortex is initially too far away from
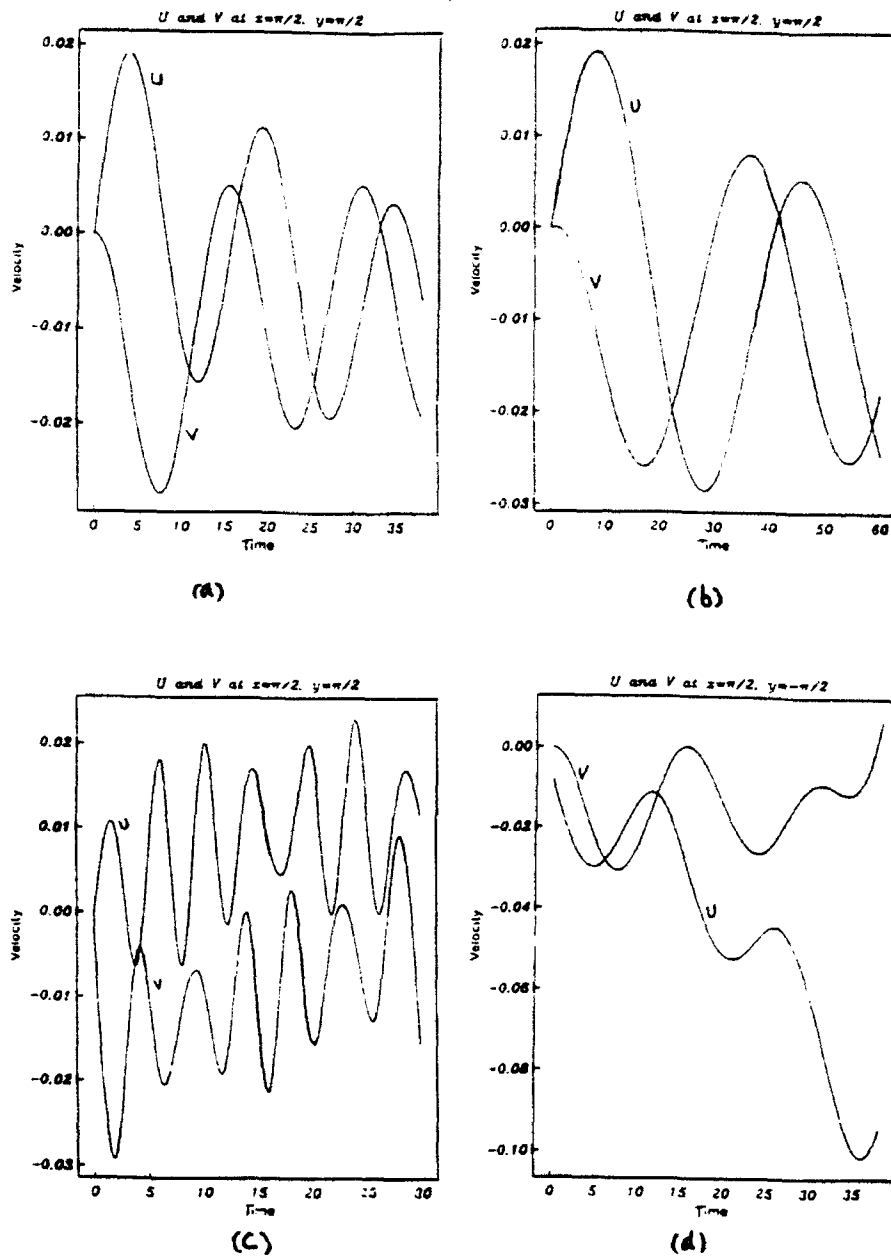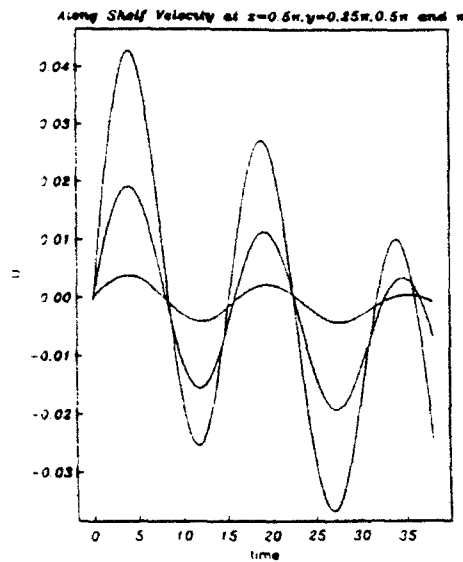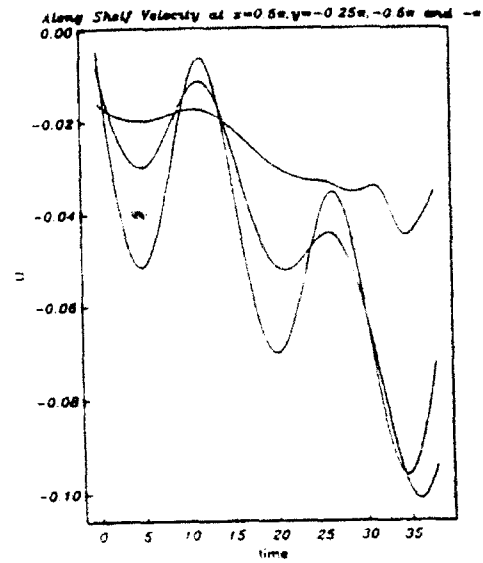
48

Figure 2.11: Along and across escarpment velocity components vs. time for (a) case 4, (b) case 8, (c) case 10 at $(x, y) = (\pi/2, \pi/2)$, and (d) case 4 at $(x, y) = (\pi/2, -\pi/2)$; along escarpment velocity vs. time for case 4 at (e) $x = \pi/2$, $y = \pi/4$, $\pi/2$ and $\pi$, and (f) $x = \pi/2$, $y = -\pi/4$, $-\pi/2$ and $-\pi$.

Figure 2.11: (continued)

the interface, all other cases show large southward excursions regardless the details of interaction.

The cyclonic perturbation formed to the northeast of the vortex expels the vortex away from the escarpment. The stronger the perturbation, the larger the southward excursion of the vortex. Subsequent formation and detachment of a cyclone in some cases causes further southwestward vortex translation in the form of a dipole-like structure. It may eventually drift northward and re-interact with the escarpment. This implies that interaction of an anticyclone with topography is intermittent, and multiple interactions may happen, resulting in a net westward vortex drift. Since the contours become very complicated before reaching this stage, only one example will be shown here to illustrate this process. Figure 2.13 shows the contour evolution following figure 2.4 from time $t = 36$ to 96. The eddy trajectory is shown in figure 2.14. The vortex is advected mainly by the topographic cyclone in a dipole-like structure and drifts back to reinteract with the escarpment. During the second interaction, the topographic cyclone, together with the interface perturbation, causes the vortex to move along a cycloid trajectory, and results
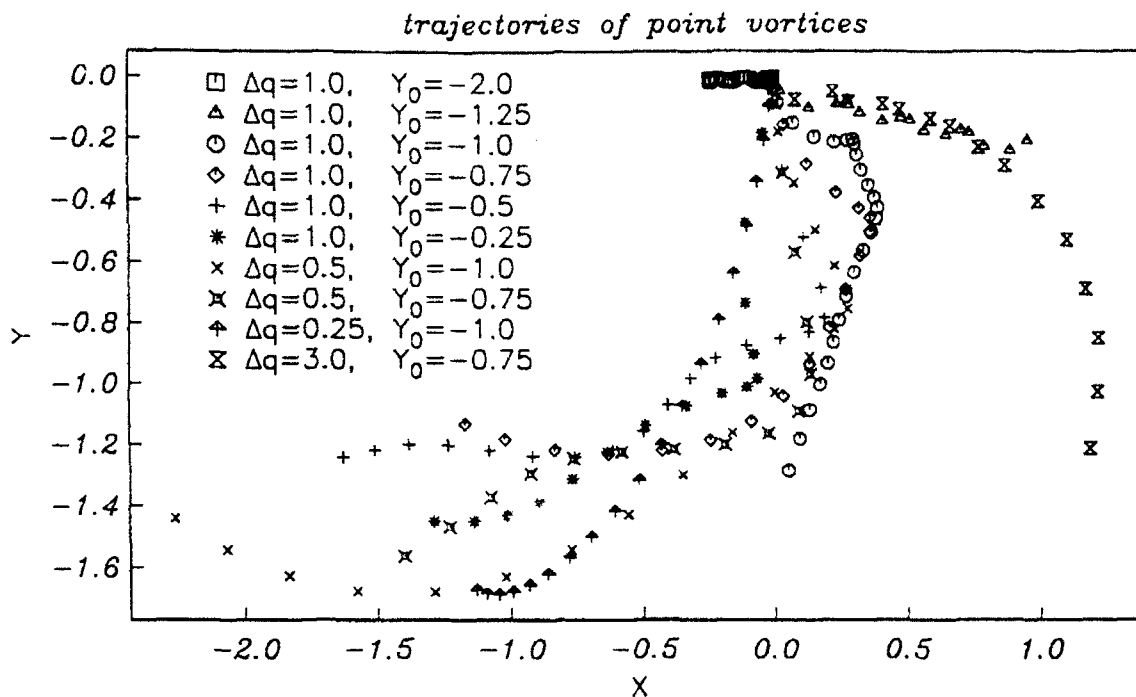
Figure 2.12: The trajectories of the point vortices for quasi-geostrophic cases.
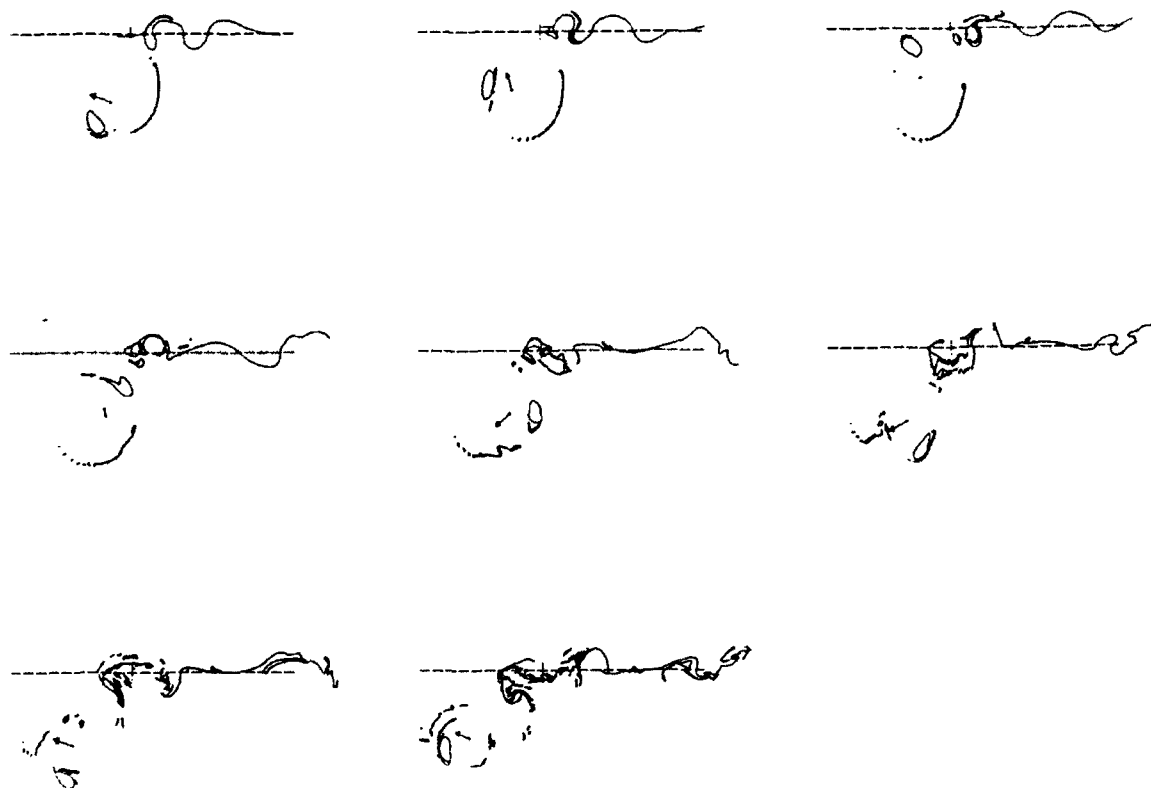


Figure 2.13: Time evolution of the interface and vortex for case 4 in table 2.1, $\Delta q = 1$ and $Y_0 = -0.75$. The time sequence of evolution follows figure 2.4 and starts from $t = 36$ with increment $\Delta t = 8$. Other notations are the same as that shown in figure 2.4.
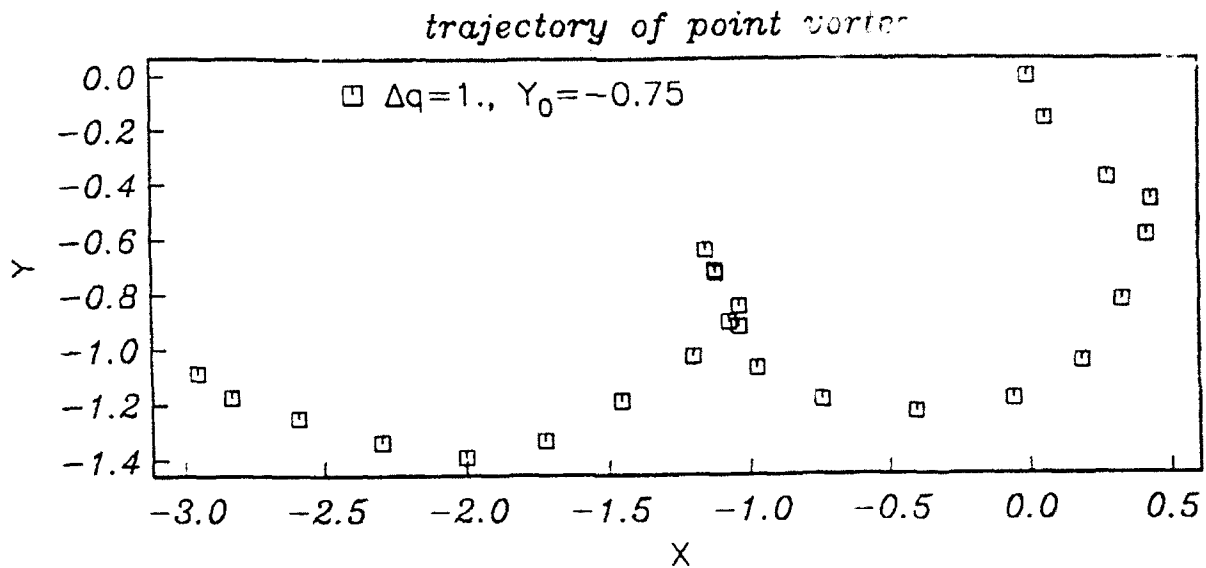
Figure 2.14: The trajectory of the point vortex for case shown in figure 2.13.

in a net westward vortex drift. Also the topographic cyclone is greatly perturbed when it passes through in between the point vortex and the escarpment. It deforms in shape and spins off fluid filaments. The effect from the unrealistically complicated contours at large time does not distort the trajectory seriously, indicating that the vortex motion is not dominated by the interface perturbation during the second interaction.

## Cross-Escarpment Volume Exchange

The conserved potential vorticity is used as a tracer for mass movement. The cross-escarpment volume exchange is defined as the volume of fluid with anomalous potential vorticity at one side of the escarpment. This includes both the volume of interface waves and that detached from the interface. This volume is plotted against time in figure 2.15 for the deep side. In general, cross-escarpment volume transport increases as either distance $|Y_0|$ decreases or topography $\Delta q$ weakens. The change of $\Delta q$ has the most dominant effect on the volume exchange. Comparing the transported volume for cases 4, 8 and 10, it is seen that the volume exchange roughly increases linearly with the decrease of $\Delta q$. For most cases (except the case $\Delta q = 0.25$ and $Y_0 = -1$), the cross escarpment
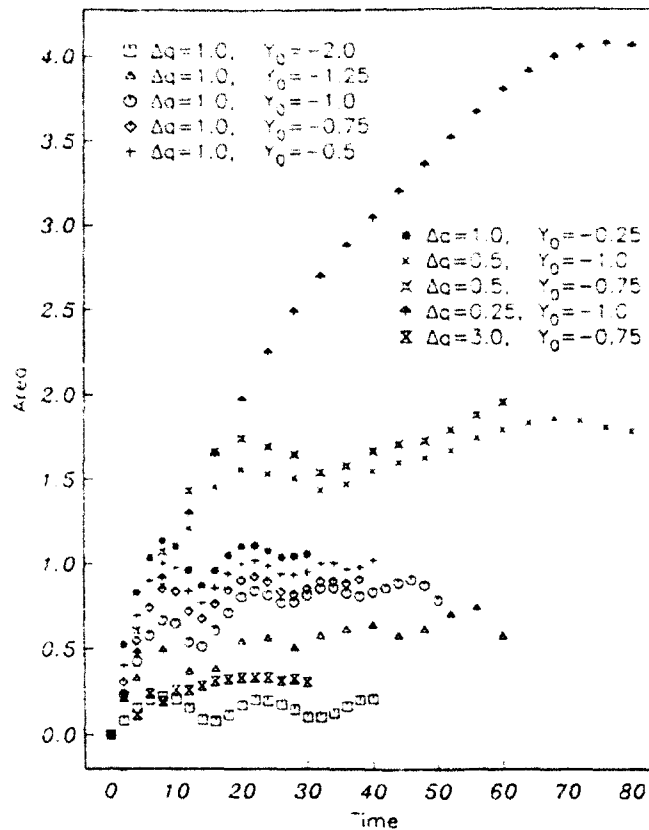
Figure 2.15: Cross escarpment transported volume for quasi-geostrophic cases.

volumes reach stationary values in less than one corresponding linear wave period. The volumes then oscillate around these values. The frequency of the volume oscillation is close to that of the corresponding escarpment wave, and depends mostly on the value of $\Delta q$. The variation of $Y_0$ affects the value of the transport more than its frequency of oscillation. From $Y_0 = -2$ to $Y_0 = -1$, the frequency of area oscillation shown in figure 2.15 only increases slightly, and then stays almost unchanged through $Y_0 = -0.25$; while the net area increases several fold for the same parameter range, the amplitude of the area oscillation is relatively constant. The oscillation is due to the existence of a standing oscillation of the interface, similar to that shown in the linear solution of equation (2.26). In fact the cross topography volume transport approaches an asymptotic value 1 if $\Delta q = 1$ is held fixed and $Y_0$ goes to zero. This is because that the vortex tends to generate an interface perturbation that can only have a total vorticity not larger than that of the vortex itself, which is $-1$. A unit volume of perturbation in the case $\Delta q = 1$ contains the same amount of vorticity but with opposite sign. The nonlinearity is important only near the interface, where it contributes to maintain a nonzero average cross-escarpment

volume and affect the wave frequency. Since cross-topography motion is stronger with the increase of nonlinearity, the decrease of $|Y_0|$ results in the increase of nonlinearity, and thus the increase of net cross-escarpment transport. At large time, multiple eddy-topography interactions are possible. For the specific case shown in figure 2.13, the second interaction does not contribute to the net cross-topography volume transport.

### Summary

We have studied in this section the strong advective interaction between a point vortex and an escarpment under the quasi-geostrophic assumption. As the vortex is initially close enough to the escarpment, it can advect fluid across it. This volume transport increases as the vortex gets closer to the escarpment and as the size of the escarpment decreases. The cross-escarpment transported volume is in the form of interface displacement at the topography and a detached topographic eddy. This cyclonic topographic eddy pairs with the original anticyclonic vortex in a dipole-like structure and strongly influences the vortex motion. This, together with the fact that an anticyclone is expelled when approaching a shallow topography, results in a net westward vortex motion. Interface waves are generated and display a resonant response to the vortex forcing. Due to the loss of cyclonic vorticity anomaly at the interface from the detachment of topographic eddy, the net anticyclonic vorticity anomaly left at the vorticity front and the detached cyclone in the deep water combine to drive a westward along-escarpment current.

## 2.6   Vortex-Finite Escarpment Interaction

Flow over finite topography experiences horizontal divergence or convergence, which was neglected in flow over quasi-geostrophic topography. Meanwhile the discontinuities in velocity and pressure field discussed in section 2.2 arise. The Rossby number, assumed small in the quasi-geostrophic approach, can now be of order one and comparable to the topography. These, together with some other changes in parameter ranges, naturally lead

us to the investigation of interaction of a vortex with a finite escarpment. The results will be compared with that of the previous quasi-geostrophic studies. In this section, we will also study the case of a cyclone interacting with an escarpment.

## 2.6.1 Numerical Scheme

Although the vorticity anomaly $q$ in equation (2.16) is still piecewise constant on integration contours, the perturbation cyclonic and anticyclonic anomalies are no longer equal and are given by equation (2.17). There is stronger positive anomaly generated than negative anomaly. However, neither is this a contradiction to vorticity conservation nor will it cause any peculiar behavior to the system, because the circulation of the cyclonic anomaly and that of the anticyclonic anomaly are the same. It may have some effects on the system evolution due to the fact that the anticyclonic field indeed has weaker strength and is more widely spread than the cyclonic field.

The same vorticity equation 2.16 governs the stream function field of flow across both finite and quasi-geostrophic topography. But unlike the quasi-geostrophic problem, here $\Delta h/h_i$ and $\epsilon$ can be order one. The ratio $\Delta h/\epsilon h_i$ and the dimensionless vortex strength $\Gamma$, however, like those in QG problem, are finite. The interface perturbation induced by the vortex, thus the integrated vorticity, is on the same order of magnitude as the circulation of the vortex, and both are of order of Rossby number. Therefore despite some important differences discussed above, we may expect similarities between these two models of the interaction processes.

The contour integrals in (2.14) can be evaluated as two continuous contour integrations, just as in the QG case: one integral along the interface from left to right (counter-clockwise if the contour is self closed) and another along the escarpment from right to left. Due to the fact the integrand takes more than one constant value along either one of these two paths, it is necessary to keep track of the order of the path, *i.e.*, to which side of the escarpment the original path belongs. Then the proper value as well as

the Green's function is chosen. In numerical implementation, this is done by finding all the zero crossings (*i.e.*, escarpment crossing) of the interface, using the fact that no two positive (negative) zero crossings can be next to each other and they can be arranged in either ascending or descending order. The integrand is then easily decided for a portion of the contour according to its two neighboring zero crossings.

The velocity at the escarpment also requires special handling, because the sudden change of normal velocity across $y = 0$ may cause a contour point to overshoot their neighboring points. Any point that moves across $y = 0$ in given time interval $\Delta t$ must be adjusted properly. Based on continuity, an average velocity for fluid parcels flowing across $y = 0$ can be computed to an accuracy $O(\Delta h)$; readers are referred to Appendix B for details.

## 2.6.2  Solutions and Discussions

### Numerical Results

The study in this section is parallel to that of section 2.5, but emphasizes the differences between them. In order to compare this to previous results directly, the same limiting values of parameter ratios as that in section 2.5 will be used. Like the previous section, the value $\Gamma = -1$ is fixed except otherwise mentioned explicitly, and only $\Delta q$ and $Y_0$ are allowed to vary. In QG case varying $\Delta h$ or $\epsilon$ is equivalent to varying $\Delta q$ alone. This is not true for finite topography case, because the Green's function now depends on depth. In the study below $\epsilon = 1$ is always assumed except as otherwise indicated.

The model is tested first for a small amplitude wave trapped at a finite escarpment. An experiment is performed with $\Delta q = 1$ ($h_2/h_1 = 0.5$) and an initial sinusoidal interface of amplitude 0.1 (scaled by the depth to have equal PV anomaly on both sides of the escarpment). The resulting dispersion relation agrees well with that given by section 2.4.1 and the relative error is less than 3% for calculation time twice the wave period.

The parameters for numerical experiments in this section are listed in table 2.3. First we examine case 4 from the list, $\Delta q = 1$ and $Y_0 = -0.75$ (for $\epsilon = 1$, this corresponds to an escarpment height one half of the water depth). The interfaces are shown in figure 2.16 and should be compared with QG case in figure 2.4. The two cases have quite similar results qualitatively. They both show formation of a cyclonic lobe, which evolves into a thin streamer and a well defined cyclonic eddy. Nonlinear waves are generated at the escarpment and propagate westward. However there are pronounced differences between these two examples. Due to finite topography, the image effect to $x$-component of velocity field is present. It advects the point vortex eastward in addition to the same effect by interface perturbations. As a result the point vortex has a larger excursion to the east of its initial position than in QG case. This also influences the interface perturbation by pushing the cyclonic lobe closer to the main interface instead of extending directly southward in figure 2.4. Another consequence due to finite depth change is that the anticyclonic perturbation spreads over an area twice as large as that of cyclonic perturbation. Since at any point the influence due to the perturbation field depends upon the distance between them, this larger scale perturbation anomaly can make a difference for near-field evolution. In the far field, the perturbation velocity can be treated as though it were generated by a point source of vorticity, so that the dimension of the anomaly is not so important. This near-field effect of the interface perturbation has an influence on its own evolution. When part of the cyclonic perturbation is drawn away by the vortex, the interface region is left with net anticyclonic vorticity. This unbalanced vorticity will drive a westward along-escarpment current on the deep side, which is stronger than that in QG cases because of the large perturbation strength at large $\epsilon$.

Like that in figure 2.4, figure 2.16 also shows two distinct time scales for advection and interface waves. But each time scale in figure 2.16 is correspondingly slower than that of QG case in figure 2.4. The eddy formation at $t = 28$ in figure 2.16 roughly corresponds to that at $t = 20$ in figure 2.4, but occurs about 8 dimensionless time units

# Table 2.3

Barotropic Finite Topography Experiments ($\epsilon = 1$)

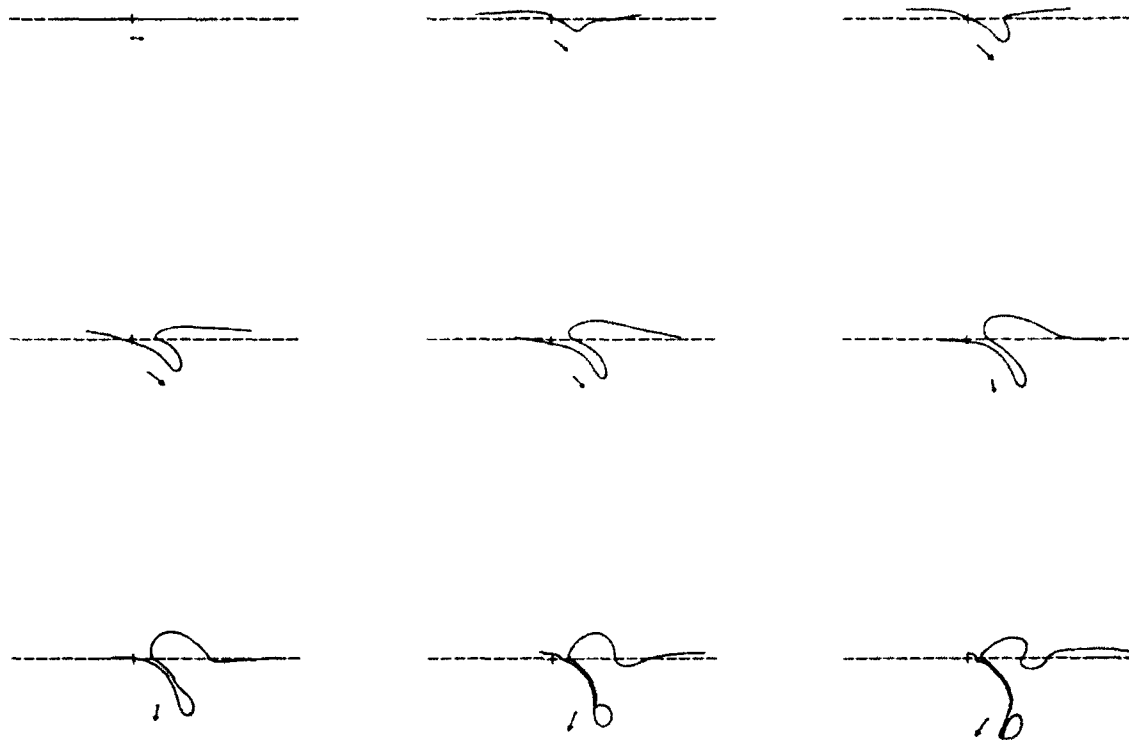| Cases | $\Delta q$ | $Y_0$ | Streamer | Cyclonic Eddy | Volume Exchange |
|-------|------|-------|----------|---------------|-----------------|
| 1 | 1.0 | $-2.0$ | No | No | 0.2 |
| 2 | 1.0 | $-1.25$ | No | No | 0.7 |
| 3 | 1.0 | $-1.0$ | Yes | Yes | 0.8 |
| 4 | 1.0 | $-0.75$ | Yes | Yes | 0.9 |
| 5 | 1.0 | $-0.5$ | Yes | Yes | 1.0 |
| 6 | 1.0 | $-0.25$ | Yes | No | 1.1 |
| 7 | 0.5 | $-1.0$ | Yes | Yes | 1.6 |
| 8 | 0.5 | $-0.75$ | Yes | Yes | 1.8 |
| 9 | 0.25 | $-1.0$ | Yes | No | 3.6 |
| 10 | 3.0 | $-0.75$ | No | Yes | 0.2 |

Figure 2.16: Time evolution of the interface and vortex for case 4 in table 2.3, $\Delta q = 1$ and $Y_0 = -0.75$. The solid contour stands for the interface and the dashed line for the escarpment. The vortex is marked by a solid dot at the beginning of an arrow, which represents the velocity vector of the vortex translation. The time sequence of evolution starts from $t = 0$ with increment $\Delta t = 4$ at upper-left corner and continues with time increasing to the right and downward.

later. This is largely due to the image effect, which causes the vortex to move parallel to the initial interface, thus hindering the perturbation from growing southward.

In figure 2.17 the perturbation velocity fields at four times are plotted. As outlined in Appendix B, the velocity of a fluid parcel moving across topography is represented by an average velocity, therefore avoiding possible numerical instability. The convergence (divergence) of velocity when crossing the escarpment from shallow to deep (from deep to shallow) can be clearly seen, which was not present in figure 2.5 of QG problem. The perturbation-induced along-escarpment flow westward in deep water is observed, similar to that described in figure 2.5.

When $\Delta q = 0.5$ (topography is 1/3 of the water depth for $\epsilon = 1$) the results (figure 2.18) show more agreement with the corresponding QG case figure 2.8. If topography is very small, then QG approximation will be valid, and the results will be essentially the same for both finite topography and QG calculations.

In figure 2.19 topography extends to 3/4 of the water depth for $\epsilon = 1$. The interface response shows large asymmetry because of the large depth change. The image effect is also stronger, which causes a rapid eastward vortex drift. The larger anticyclonic interface perturbation tends to shear off its base, and hence to form an isolated blob. For even larger topography, such as an escarpment height which takes up 4/5 of the water column ($\Delta q = 4$ for $\epsilon = 1$), the interaction is then dominated by momentum radiation and the interface and the vortex are locked in an oscillatory state. In such a case the interface deforms irregularly and the vortex drifts eastward.

Two experiments with $\epsilon = 0.5$ and 3 were performed, in which $\Delta q = 1$ and $Y_0 = -0.75$ are fixed. The results of contour evolution are plotted in figures 2.20 and 2.21. For small $\epsilon$, the escarpment is also small (since $\Delta q$ is fixed), which results in a weak image effect and a slightly faster eddy evolution than the $\epsilon = 1$ case shown in figure 2.16. The result is essentially in between figure 2.4 and figure 2.16. For larger $\epsilon$ (hence larger $\Delta h$ for fixed $\Delta q$) cases, the velocity image is stronger, and thus the distance of
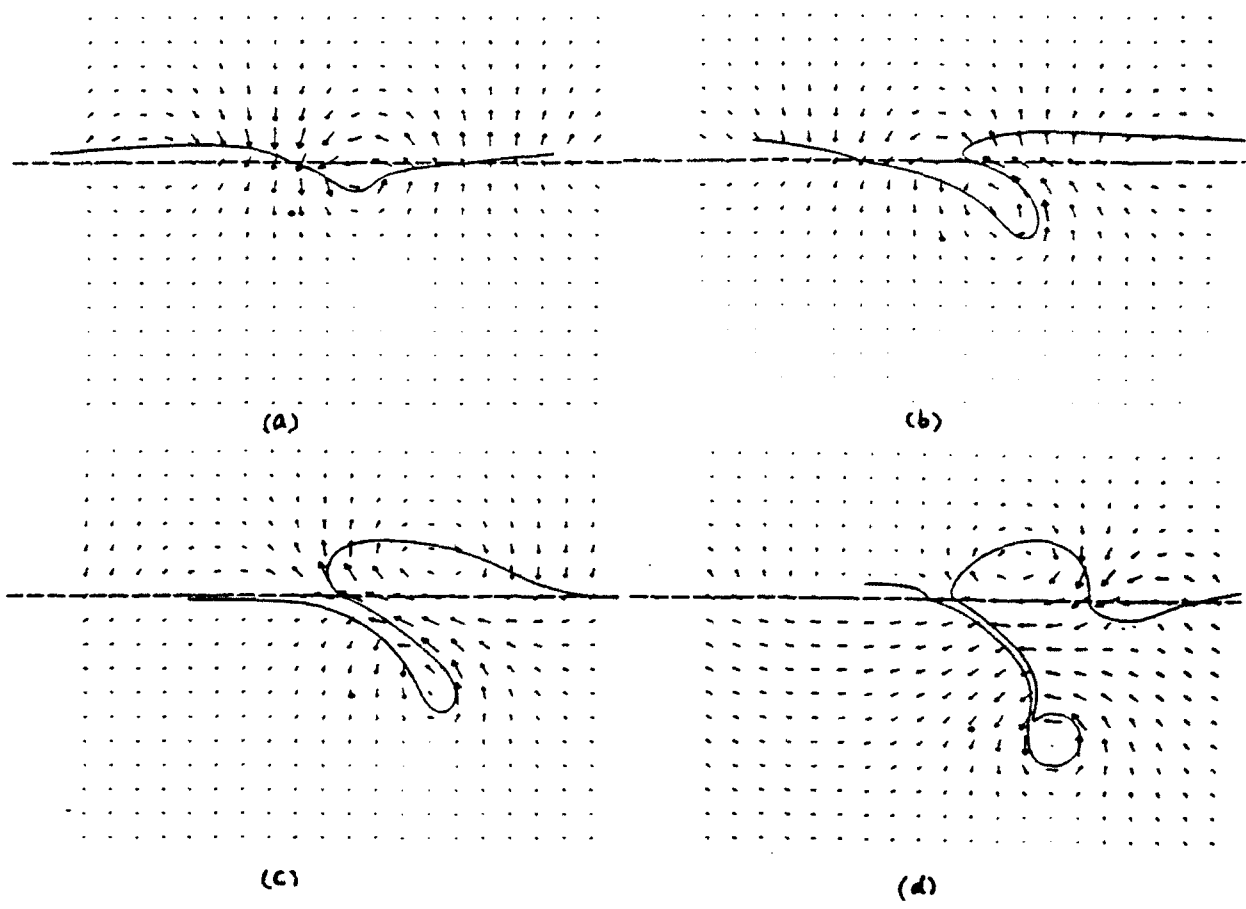
Figure 2.17: Perturbation velocity field for the case shown in figure 2.16 at time $t =$: (a) 4, (b) 12, (c) 20 and (d) 28.
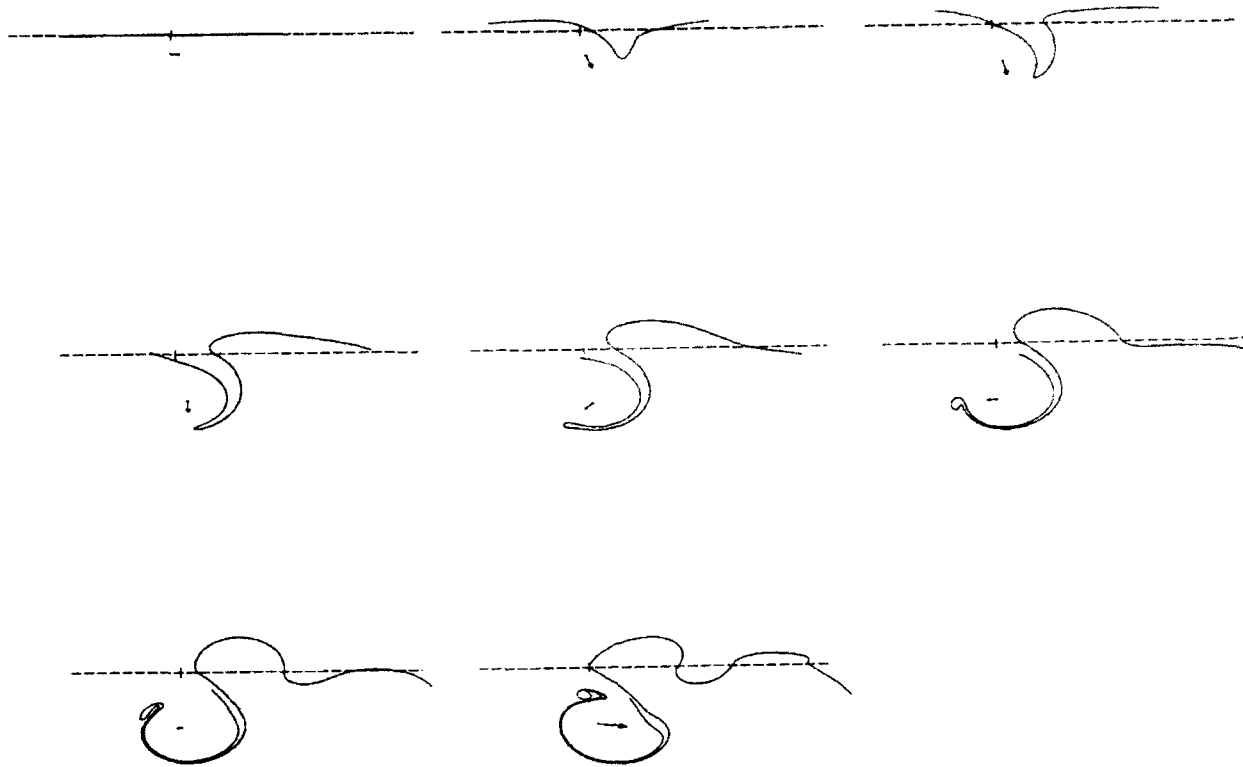
Figure 2.18: Time evolution of the interface and vortex for case 8 in table 2.3, $\Delta q = 0.5$ and $Y_0 = -0.75$. The time sequence of evolution starts from $t = 0$ with increment $\Delta t = 8$. Other notations are the same as that shown in figure 2.16.

the vortex eastward drift is larger. The result shows a pronounced difference from small $\epsilon$ cases and bears some similarities to figure 2.19, which has the same depth change.

Later in this section, we will also study the problem where the vortex has finite area or is cyclonic. The results will be compared with the corresponding point vortex or anticyclonic vortex cases.

## Formation of a Topographic eddy

For corresponding range of parameter ratios, the eddy formation processes for finite topography are similar to those in QG calculations. Compare figures 2.16, 2.18 and 2.19 with figures 2.4, 2.8 and 2.9, respectively; the eddies formed have correspondingly similar size and location. The slight difference is, as we have mentioned previously, the time that the eddy formed and detached. This is most obvious in figure 2.4 and figure 2.16, and less obvious for other cases.
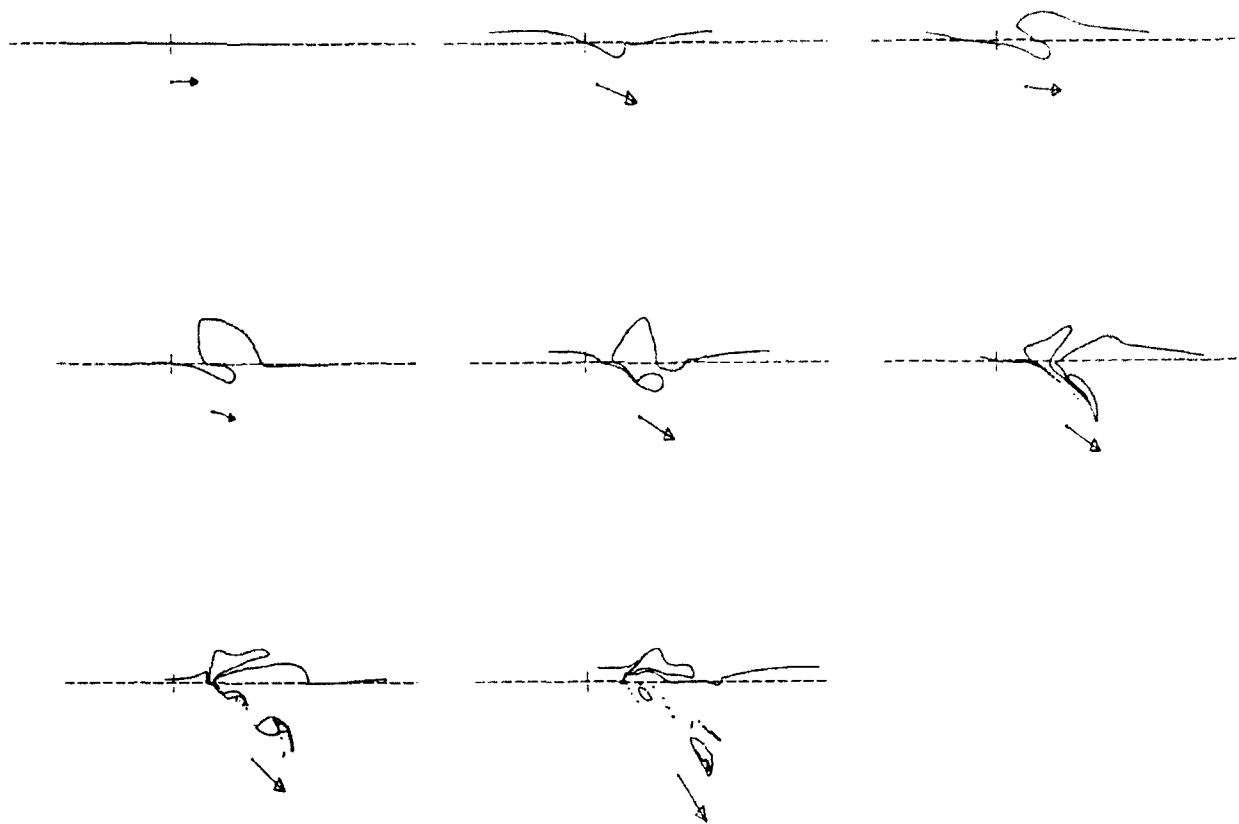
62

Figure 2.19: Time evolution of the interface and vortex for case 10 in table 2.3, $\Delta q = 3$ and $Y_0 = -0.75$. The time sequence of evolution starts from $t = 0$ with increment $\Delta t = 4$. Other notations are the same as that shown in figure 2.16.

It should be noted that the eddy strength in the present finite escarpment cases and in the QG calculation differs in order of magnitude. But it is only the ratio of this strength to the Rossby number that matters in the momentum balance; the great similarities shown here for eddy formation and evolution merely reflect this important property. With this ratio fixed, the variations in the Rossby number and topography can also affect system evolution. The influence of varying $\epsilon$ and $\Delta h$ is small when their values are small, such as QG or cases close to the QG parameter range, because at small $\epsilon$ the Green's function tends to be less dependent on depth change. For large $\epsilon$, the results are sensitive to the Rossby number and size of topography. Comparison of figures 2.16, 2.20 and 2.21 illustrates this effect. Unlike figure 2.16 and 2.20 where $\epsilon$ is relatively small, figure 2.21 shows that the eddy is formed close to the main interface in a short period of time. The eddy size is also larger than those of small $\epsilon$ case. resulting in a more balanced dipole structure with the vortex.
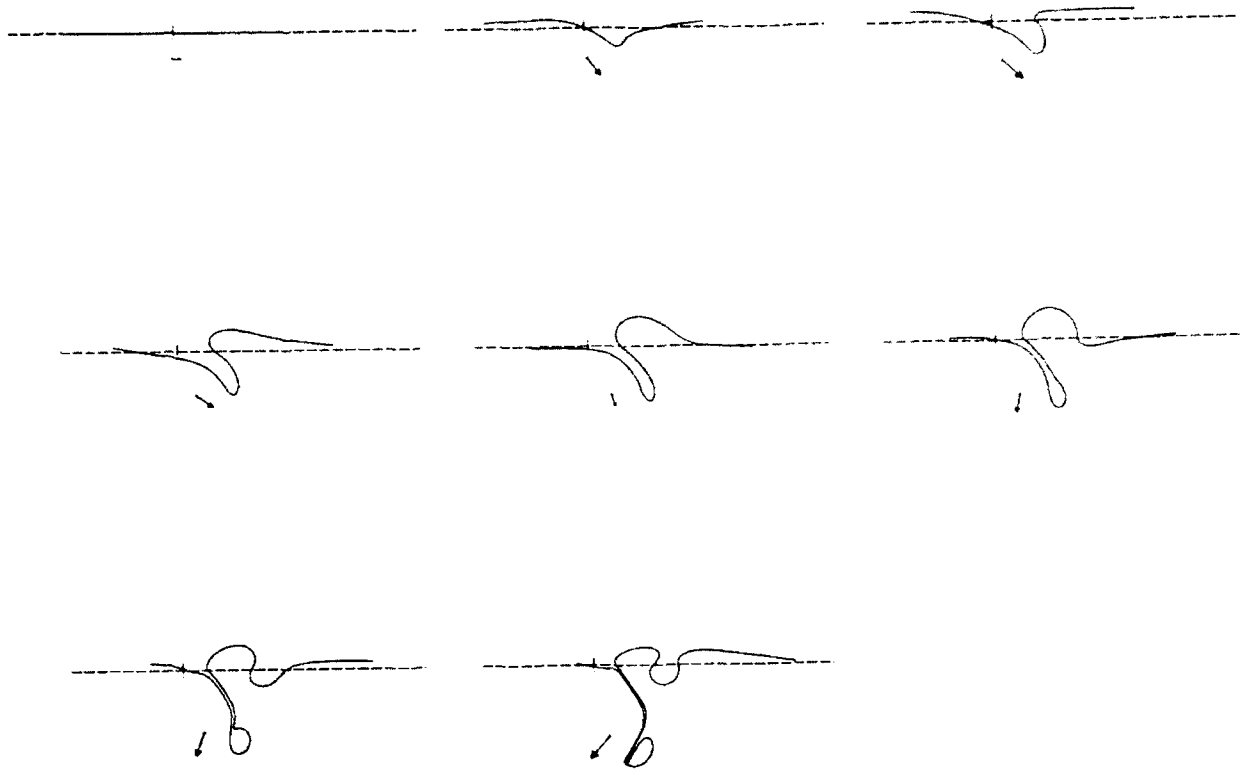
Figure 2.20: Time evolution of the interface and vortex for case $\Delta q = 1$, $\epsilon = 0.5$ and $Y_0 = -0.75$. The time sequence of evolution starts from $t = 0$ with increment $\Delta t = 4$. Other notations are the same as that shown in figure 2.16.

## Forced Escarpment Waves

Linear wave analysis in section 2.4 shows that with $\Delta q$ fixed the wave period will increase as the height of escarpment increases, but with the Rossby number fixed wave period will decrease as the height of escarpment increases. This is proved to be true also for nonlinear perturbations by the contour dynamics calculation. For example, from QG to finite escarpment, the topography varies by an order of magnitude, while $\epsilon$ also changes in proportion to keep $\Delta q$ fixed. The resulting change in escarpment waves can be seen by comparing figures 2.22a, b and c with figures 2.11a, b and c, respectively. There are two important changes seen from QG to finite escarpment. Firstly the wave period increases (compare table 2.2 with 2.4); and secondly the wave amplitude increases in the shallow side and decreases in the deep side (figure 2.22 e and f). The latter is due to the large depth change in these cases. The increase of wave period with increasing $\Delta h$ for fixed value of $\Delta q$ can be observed from figure 2.22a, g and h and table 2.5 for
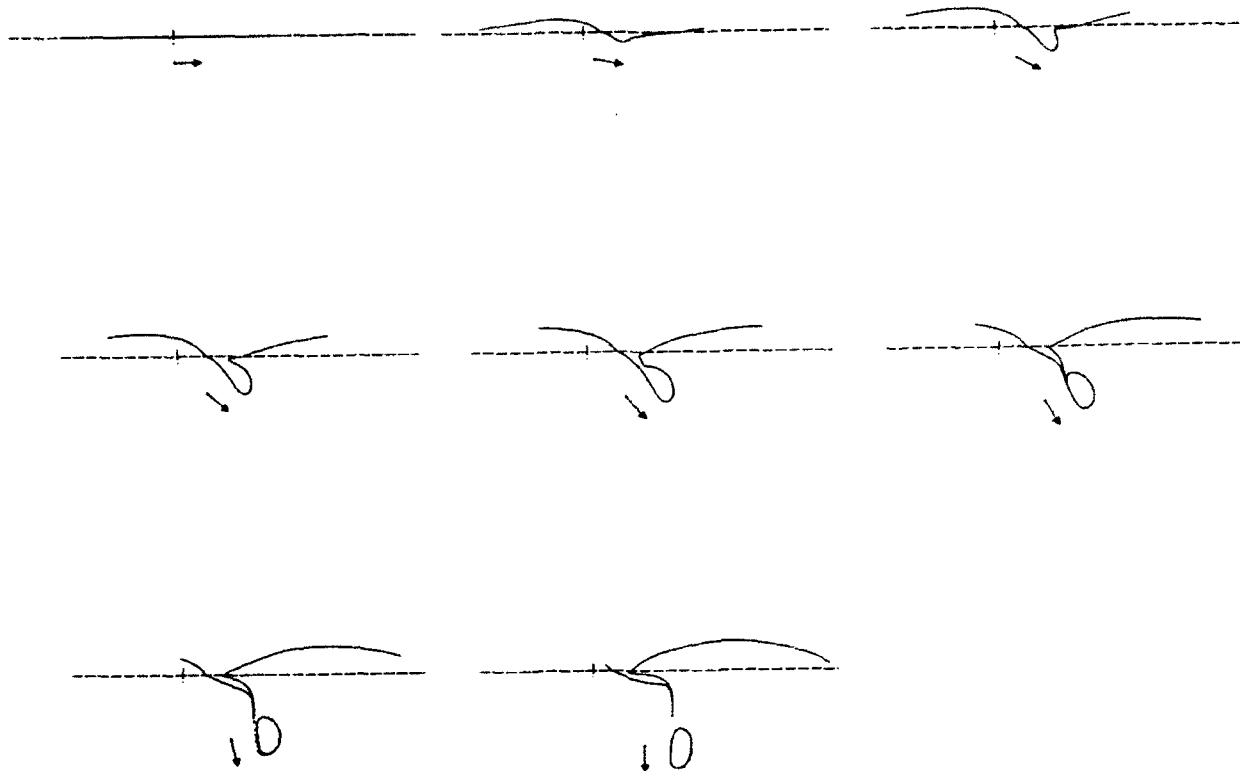
Figure 2.21: Time evolution of the interface and vortex for case $\Delta q = 1$, $\epsilon = 3$ and $Y_0 = -0.75$. The time sequence of evolution starts from $t = 0$ with increment $\Delta t = 4$. Other notations are the same as that shown in figure 2.16.

finite escarpment cases. For fixed $\Delta q$, it is seen that when $\epsilon$ is small in both table 2.2 and table 2.5, the corrected wave period is close to the linear wave period given by theoretical results. As $\epsilon$ becomes order one and larger, the nonlinearity and change in $\Delta h$ tend to have a larger effect on the escarpment waves. With the height of escarpment fixed, the variation of Rossby number has a strong influence on the interaction, because it effectively changes the vorticity anomaly and thus the momentum balance between the vortex and the perturbation. The increase of $\epsilon$ with $\Delta h$ fixed means a decrease of $\Delta q$ or weaker vorticity anomaly, and thus leads to an increase of escarpment wave period.

## Vortex Motion

The trajectories of the vortices plotted in figure 2.23 are similar to those in figure 2.12, but the vortex now has a larger eastward excursion due to the image effect. The southward vortex excursions are slightly larger for the finite topography cases. If the numerical

65

# Table 2.4

Finite Escarpment Waves ($\epsilon = 1$)

| $\Delta q$ | $\Delta h$ | Linear Period | Observed Period | Corrected Period |
|------|------|------|------|------|
| 0.5 | 1/3 | 31.4 | 58 | 31.1 |
| 1.0 | 1/2 | 18.8 | 30 | 20.3 |
| 3.0 | 3/4 | 10.5 | 14 | 11.1 |

calculations continue for a longer time, the vortex will drift westward in figure 2.23. Figure 2.24 shows the interface development following figure 2.16 from time $t = 36$ to 100, and figure 2.25 the path of the vortex. Compared with figures 2.13 and 2.14, the patterns of the dipole-like structures and vortex trajectories are both very similar, but the westward drift and the amplitude of north-south oscillation of the vortex in the finite escarpment case are about twice as large as that of the QG case.

It is noted in figure 2.23 that vortex trajectories divert clockwise with decrease of $\Delta q$ and distance $|Y_0|$. At large $\Delta q$ and $|Y_0|$, the vortex tends to have larger eastward excursions, and gradually shift southwestward at smaller $\Delta q$ and $|Y_0|$. This effect is less obvious in figure 2.12 due to the lack of image effect.
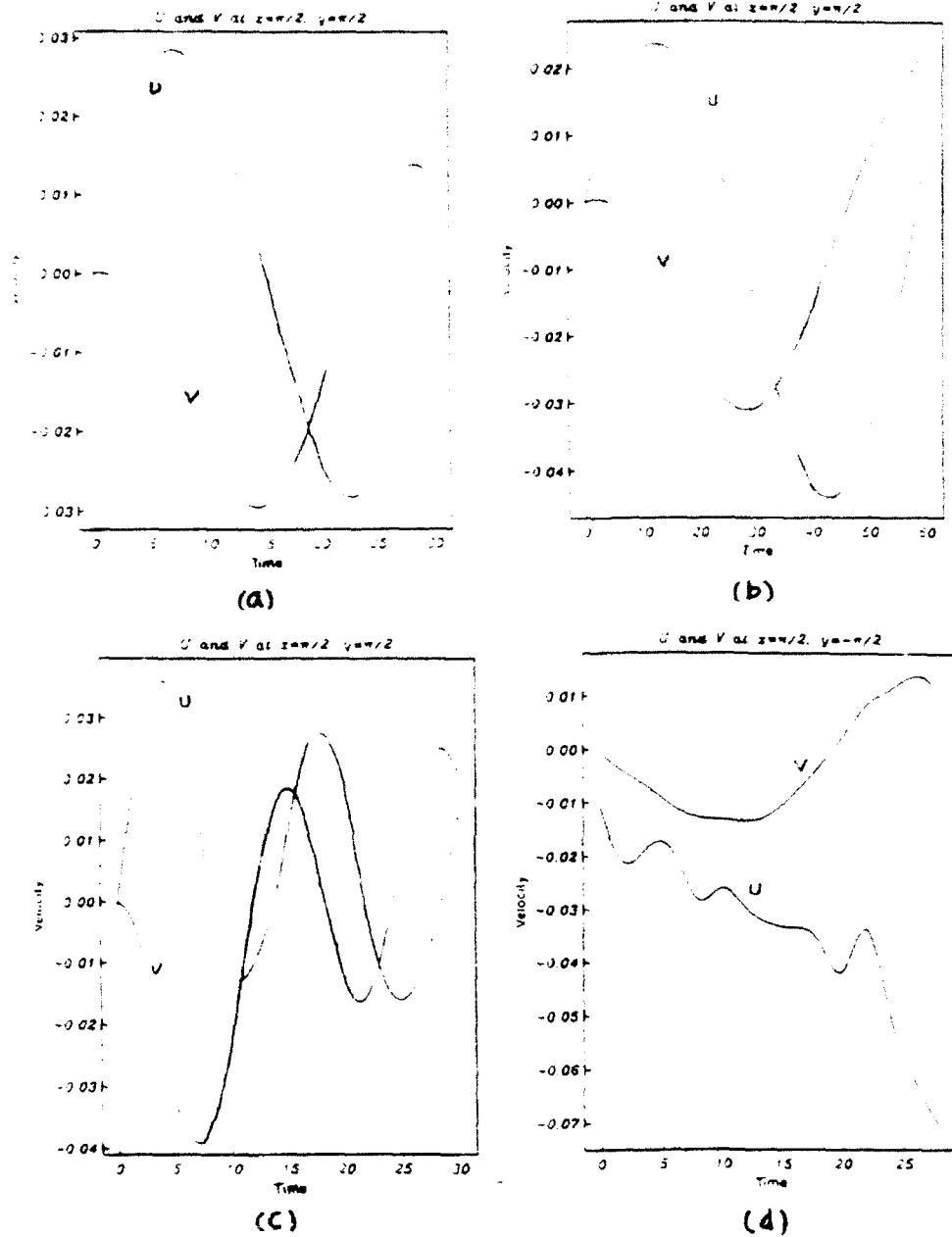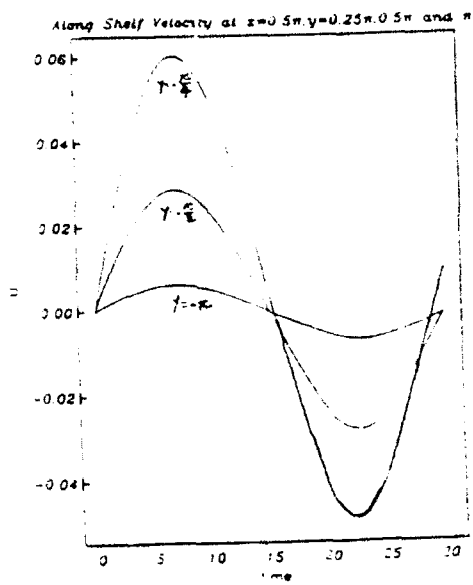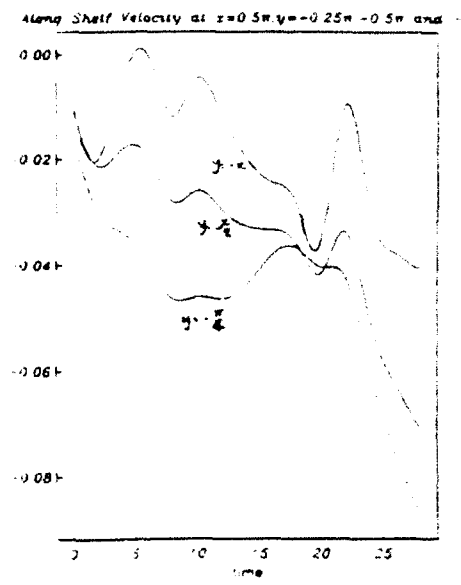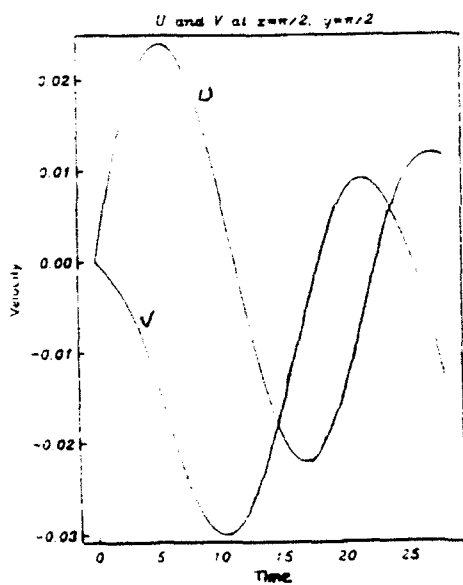
Figure 2.22: Along and across escarpment velocity components for cases in table 2.3. (a) case 4, (b) case 8, (c) case 10 at $(x,\ y) = (\pi/2,\ \pi/2)$, and (d) case 4 at $(x,\ y) = (\pi/2,\ -\pi/2)$; along escarpment velocity vs. time for case 4 at (e) $x = \pi/2$, $y = \pi/4$, $\pi/2$ and $\pi$, and (f) $x = \pi/2$, $y = -\pi/4$, $-\pi/2$ and $-\pi$; along and across escarpment velocity vs. time at $(x,\ y) = (\pi/2,\ -\pi/2)$ for cases (g) $\Delta q = 1$, $\epsilon = 0.5$, and (h) $\Delta q = 1$, $\epsilon = 3$.
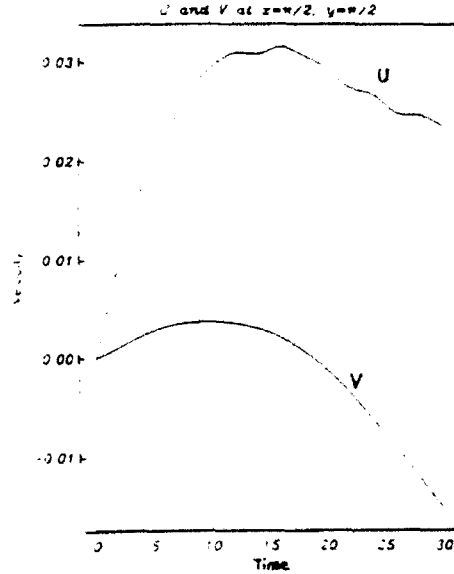
67

Figure 2.22: (continued)

# Table 2.5

Finite Escarpment Waves ($\Delta q = 1$)

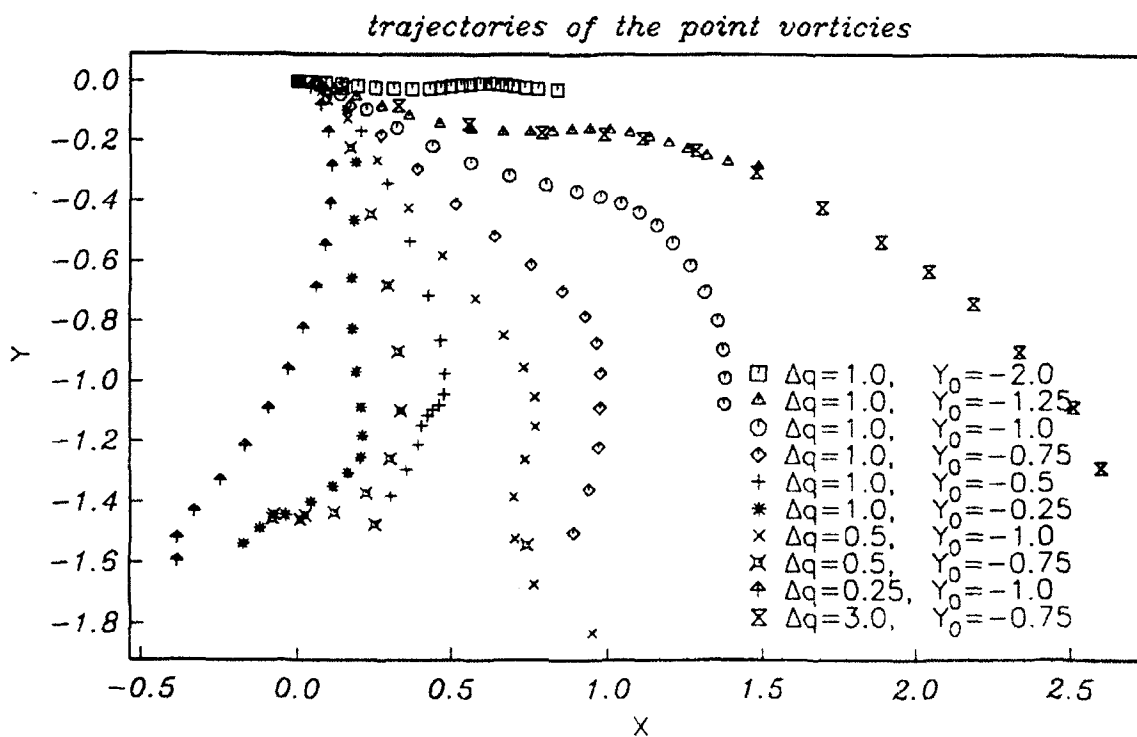| $\epsilon$ | $\Delta h$ | Linear Period | Observed Period | Corrected period |
|---|---|---|---|---|
| 0.5 | 1/3 | 15.7 | 22 | 16.5 |
| 1.0 | 1/2 | 18.8 | 30 | 20.3 |
| 3.0 | 3/4 | 31.4 | 52 | 36.3 |

## trajectories of the point vorticies



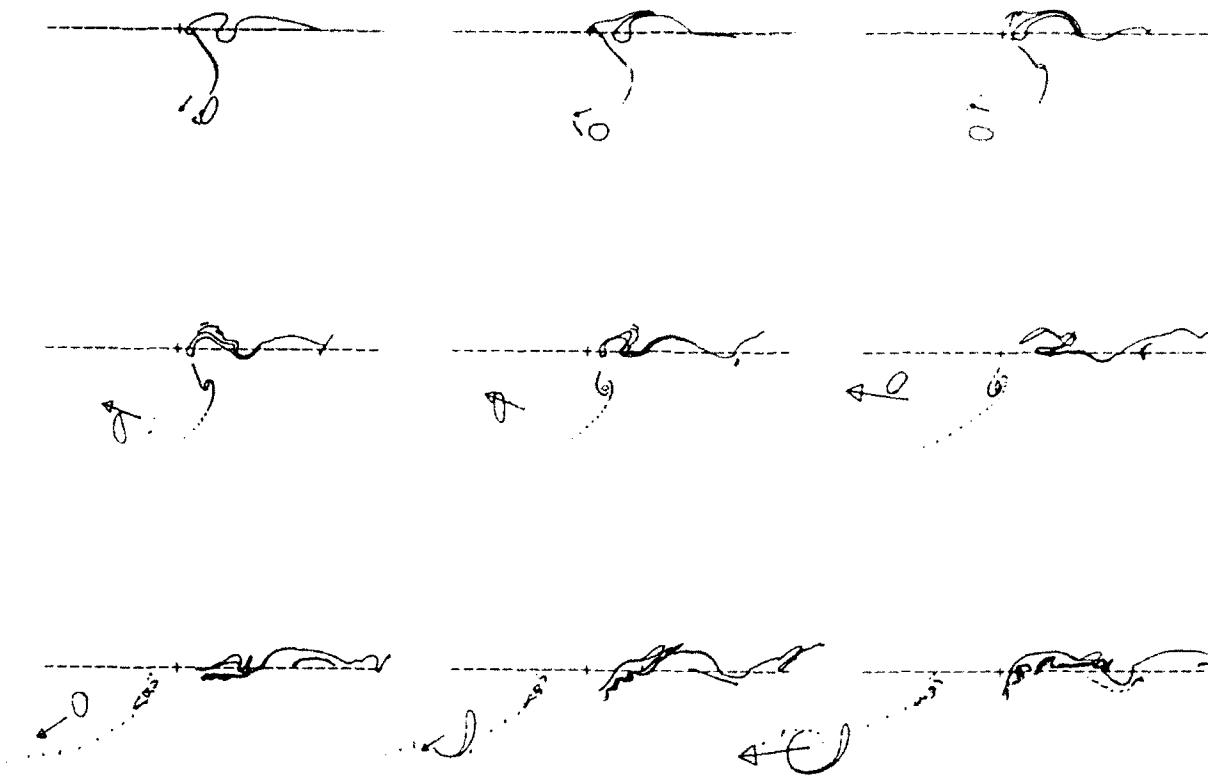Figure 2.23: The trajectories of the point vortices.

Figure 2.24: Time evolution of the interface and vortex for case 4 in table 2.3, $\Delta q = 1$ and $Y_0 = -0.75$. The time sequence of evolution follows figure 2.16 and starts from $t = 36$ with increment $\Delta t = 8$. Other notations are the same as that shown in figure 2.16.
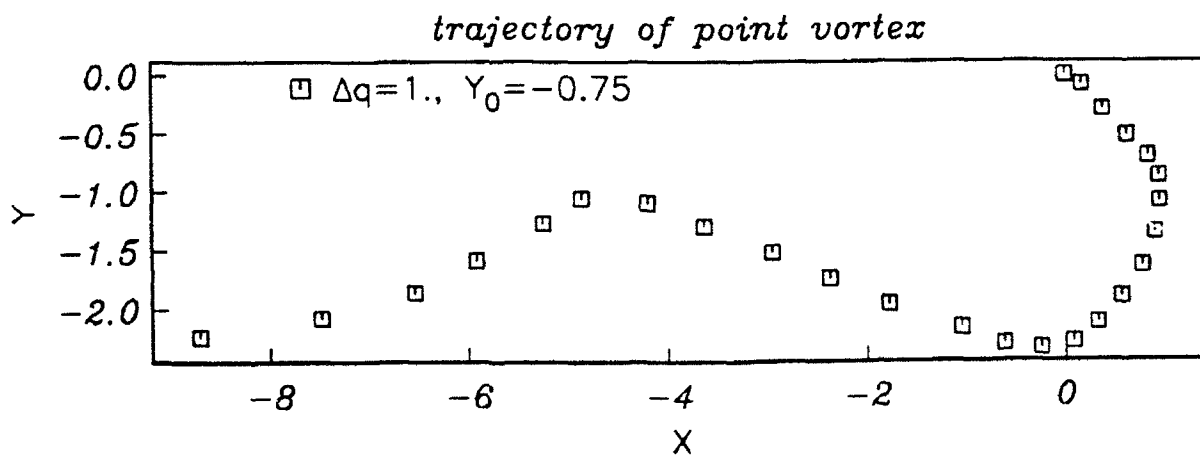


Figure 2.25: The trajectory of the point vortex for case shown in figure 2.24.
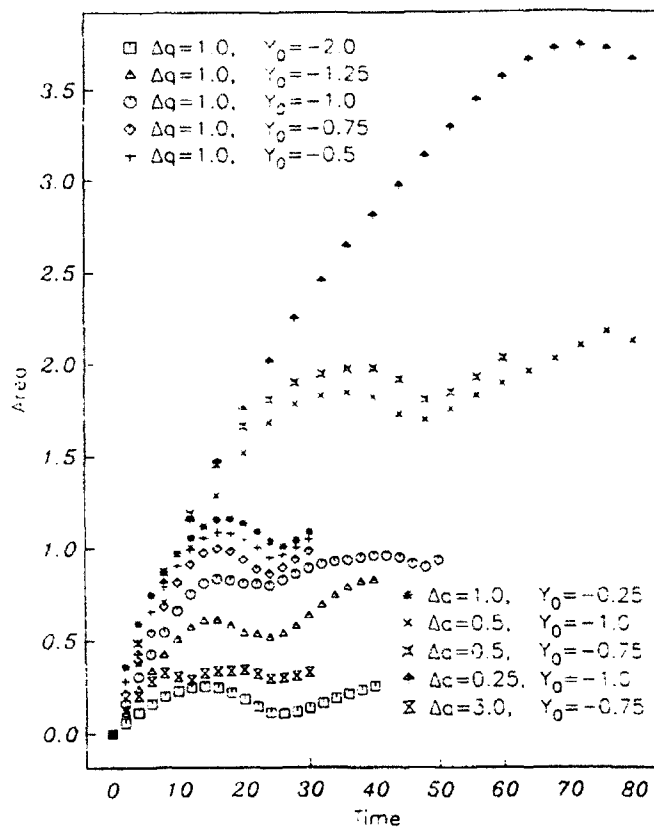
Figure 2.26: Cross escarpment transported volume.

## Cross-Escarpment Volume Exchange

Figure 2.26 shows the cross-escarpment transport verses time. The similar pattern and dependence on $\Delta q$ and $Y_0$ as that in figure 2.15 are clearly observed. A similar volume transport occurred in both models. This is because the ratio $\Delta h / \epsilon h_i$ and $\Gamma$ are comparable in both models. The time for cross-escarpment transported volume to reach its first maximum is longer than the corresponding QG case, in accordance with the finite depth change. The area oscillations for cases with $\Delta q = 1$ are all in phase, with period close to that of corresponding escarpment waves. The slight increase in volume transport (except case $\Delta q = 3$) is a reflection of the fact that vortex stayed close to escarpment for longer time, thus causing more cross escarpment volume flux. This agrees with eddy movement in figure 2.23; instead of going quickly southward like the QG cases, the vortex translated southeastward with a relatively slower southward velocity.

71

## Finite Vortex-Escarpment Interaction

In this section we will examine the consequence of a finite vortex interacting with a large escarpment. In the contour dynamics model, we only need to replace the point vortex with a circular vortex of uniform vorticity. Numerically, this means initializing a circular contour which encloses fluid of constant value of PV.

A finite vortex differs from a point vortex in several aspects. Because of its finite area, it deforms in shape and thus varies in velocity. Unlike a point vortex, a finite vortex has no singularity in its velocity field and is a more realistic approximation to a geophysical eddy.

We briefly examine three cases here, which all have the same finite vortex and initial position, but different topography. The vortex is circular with radius $1/\sqrt{\pi}$ and vorticity anomaly $-1$. The initial position of the eddy center is at $(\pi, -0.75)$. The interface evolution is shown in figures 2.27, 2.28 and 2.29 for $\Delta q = 0.5$, 1, and 3, respectively. In all the cases the Rossby number is fixed at $\epsilon = 1$.

In general the results are similar to the corresponding cases with a point vortex shown in figures 2.16, 2.18 and 2.19 (the finite vortices and the point vortices used have the same constant circulation). The cross-escarpment transported volume is about the same for each corresponding pair of cases, and so is the pattern of interface deformation. The reason is that as the finite vortex moves away from the interface, its effect on the interface can roughly be represented by a comparable point vortex of the same circulation and located at the center of vorticity of the finite vortex. There are, however, pronounced differences between the results of point vortex and finite vortex models. The biggest difference, comparing figure 2.29 to figure 2.19, is that there is no eddy detached from the interface in the former. The deformation of the finite eddy is the key to this. Firstly, deformation of the finite vortex during interaction affects momentum transfer between the interface and the vortex by altering the vortex velocity field. Secondly, when the circular vortex is enlongated to elliptical shape, its long axis always extends parallel to

72

Figure 2.27: Time evolution of the interface and finite vortex for case with $\Delta q = 0.5$, $\epsilon = 1$. The vortex has uniform vorticity of value $-1$ and radius 0.564. The solid contours stand for the interface and vortex, and the dashed line for the escarpment. The vortex center is at $(x, y) = (\pi, -0.75)$ at $t = 0$. The time sequence of evolution starts from $t = 0$ with increment $\Delta t = 8$ at upper-left corner and continues with time increasing to the right and downward.



Figure 2.28: Time evolution of the interface and finite vortex for case with $\Delta q = 1$ and $\epsilon = 1$. The time sequence of evolution starts from $t = 0$ with increment $\Delta t = 4$. The rest are the same as that in figure 2.27.
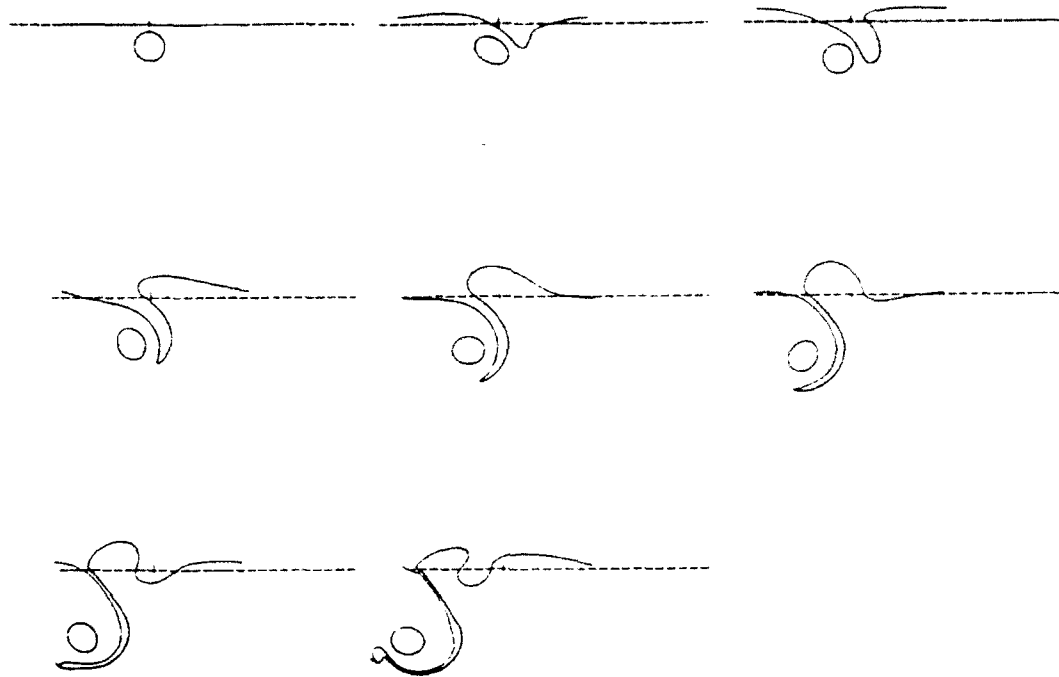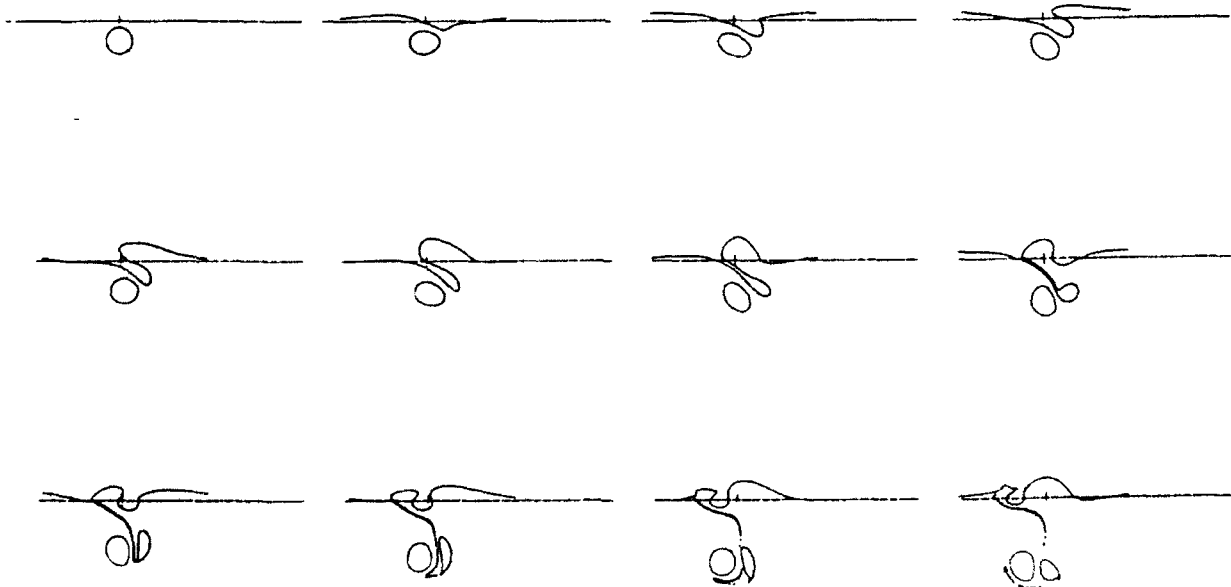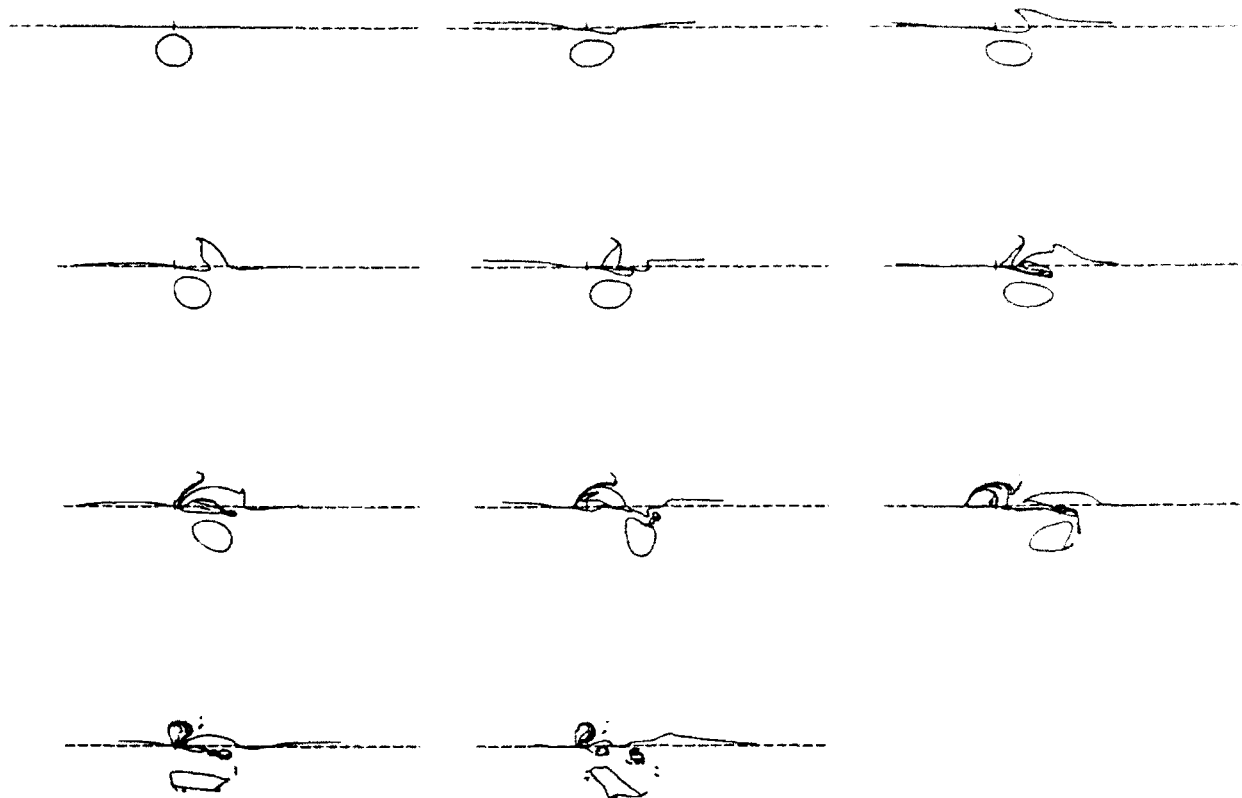
Figure 2.29: Time evolution of the interface and finite vortex for case with $\Delta q = 3$ and $\epsilon = 1$. The time sequence of evolution starts from $t = 0$ with increment $\Delta t = 4$. The rest are the same as that in figure 2.27.

the interface, and its length acts like a barrier to keep the perturbation from extending southward. In all cases, the shape of the vortex deforms periodically from circular to elliptical. As the interface evolves, the longer axis of the varying vortex rotates clockwise and always tends to align with the nearest perturbation interface. When perturbation field is strong, it may draw a filament off the deforming vortex (figure 2.29).

The escarpment waves are approximately the same for both the point vortex and the finite vortex cases. This is expected since the escarpment wave dispersion property does not depend on the forcing change. However, the wave generated by a finite vortex has slightly smaller amplitude and observed period than that by a point vortex. It is due to the fact that the periodic deformation of the finite vortex absorbs part of the the momentum, thus reduces its impact on the interface. For the same reason the finite vortex tends to have a smaller eastward excursion than the point vortex. This is especially obvious for cases of small escarpment.
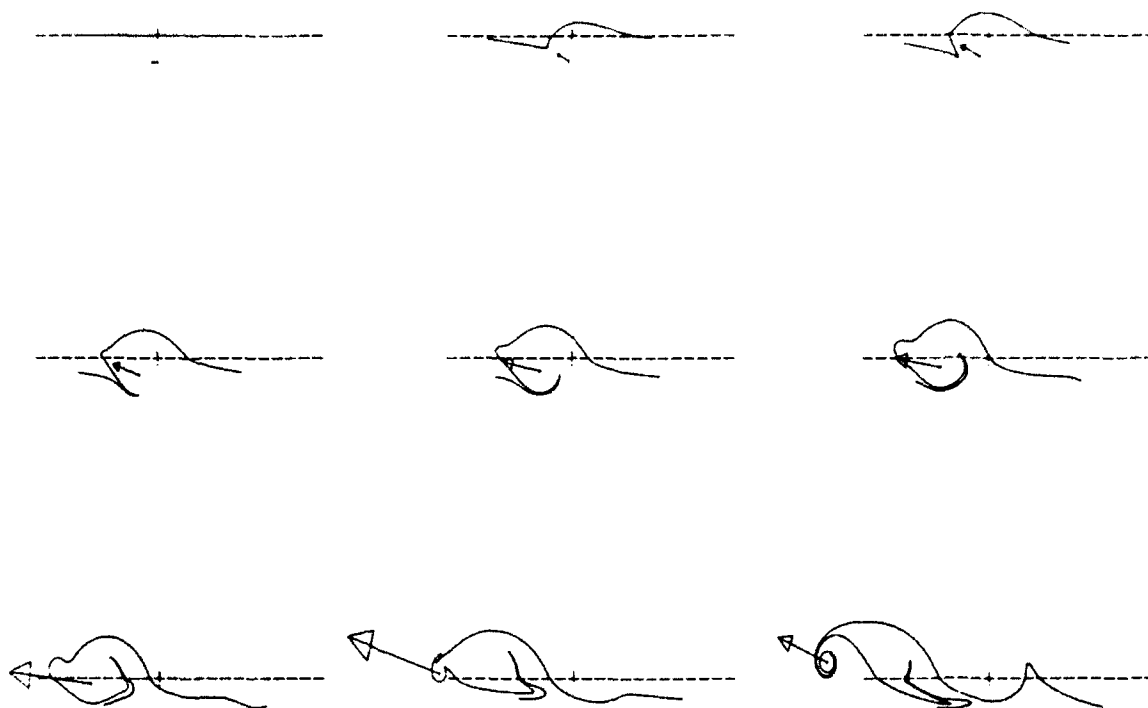
Figure 2.30: Time evolution of the interface and vortex for cyclonic vortex case $\Delta q = 0.5$, $\epsilon = 1.0$ and $Y_0 = -0.75$. The time sequence of evolution starts from $t = 0$ with increment $\Delta t = 4$. Other notations are the same as that shown in figure 2.16.

## Cyclonic Vortex-Escarpment Interaction

Unlike an anticyclone, a cyclone perturbs the interface in such a way that the perturbation velocity field initially advects the cyclone toward the topography. Thus, instead of being expelled, a cyclone is trapped to the topography. This results in a stronger vortex image and hence an enhanced westward vortex propagation during the interaction.

The results of interface evolution for interaction between a cyclonic point vortex and an escarpment are shown in figures 2.30, 2.31 and 2.32 for $\epsilon = 1$ and $\Delta q = 0.5, 1.0$ and 3.0, respectively. In these results the vortex-induced cyclonic perturbation is to the left of the vortex, and therefore advects the vortex toward the topography. The anticyclonic perturbation directly north of the vortex tends to move the vortex westward, as does the image vortex. Thus both the vortex and the interface perturbation propagate westward, while the cyclone also moves onshore. The process then varies for different values of $\Delta q$.

75

Figure 2.31: Time evolution of the interface and vortex for cyclonic vortex case $\Delta q = 1.0$, $\epsilon = 1.0$ and $Y_0 = -0.75$. The time sequence of evolution starts from $t = 0$ with increment $\Delta t = 4$. Other notations are the same as that shown in figure 2.16.

In small topography case as shown in figure 2.30, the vortex and the interface perturbation propagate at approximately the same speed. As the vortex gets closer to the topography, it also causes more cyclonic perturbation to its left. The cyclone at the leading edge of the vortex dominates its northward motion, while the contribution from the anticyclonic perturbation north of the vortex mainly contributes to the westward vortex propagation. In addition, in figure 2.30 the weakness of the topography provides less constraint for cross topography motion, and eventually the vortex is advected across the escarpment into the shallow water. The cyclonic perturbation forms a streamer, which, unlike the previous studies on anticyclone cases, does not develop into a topographic eddy.

For cases with larger topography, such as that in figures 2.31 and 2.32, the initial phase is the same as that described above. The vortex propagates westward and toward the topography. The interface perturbation now travels faster than the vortex and thus has a varying effect on vortex motion. As the anticyclonic perturbation reaches the po-
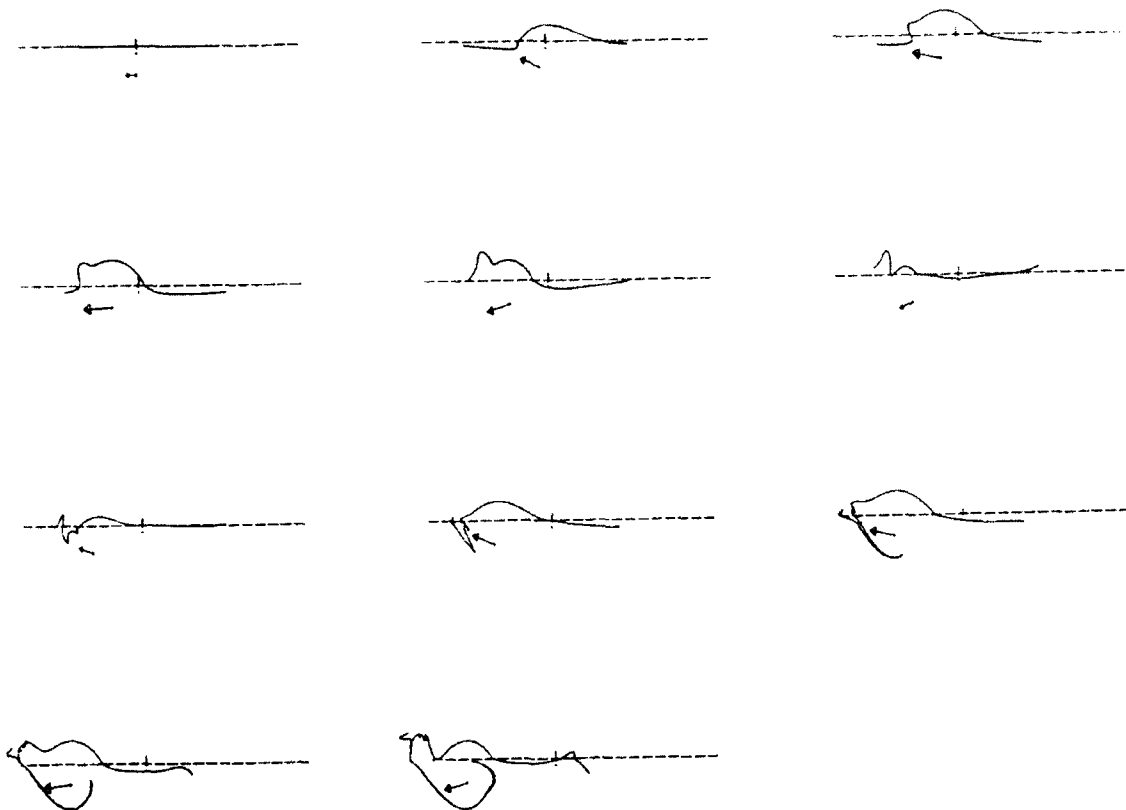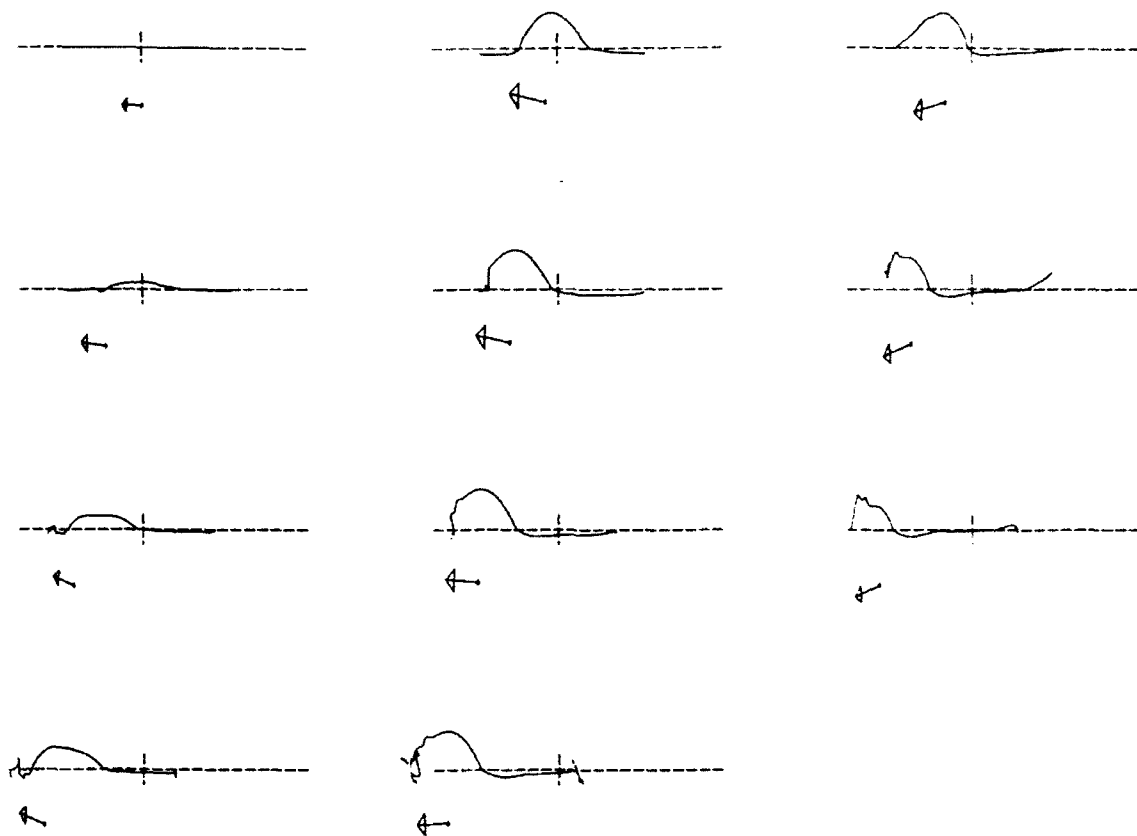
Figure 2.32: Time evolution of the interface and vortex for cyclonic vortex case $\Delta q = 3.0$, $\epsilon = 1.0$ and $Y_0 = -0.75$. The time sequence of evolution starts from $t = 0$ with increment $\Delta t = 4$. Other notations are the same as that shown in figure 2.16.

sition northwest of the point vortex, a cyclonic perturbation develops to the northeast of the vortex; they both have the effect of advecting the point vortex away from the topography. Meanwhile, the cyclonic velocity field of the vortex suppresses this interface deformation. A periodic interaction pattern develops: the interface and the vortex oscillations are coupled, and together with the image effect, this results in a net westward vortex drift at the end of each period. The net drift distance is larger for the case with larger topography due to the stronger image effect (figure 2.33, except cases such as shown in figure 2.30). It is also seen from figure 2.33 that in oscillatory cases the average position of the vortex is closer to the escarpment than the initial position. The cross-escarpment transported volume (area in two-dimensional space) is plotted in figure 2.34. The transports are correspondingly less than that of the anticyclone-escarpment interaction cases shown in figure 2.26. The volume transport oscillates with a fixed frequency the same as that of the vortex oscillation and a constant amplitude for each case
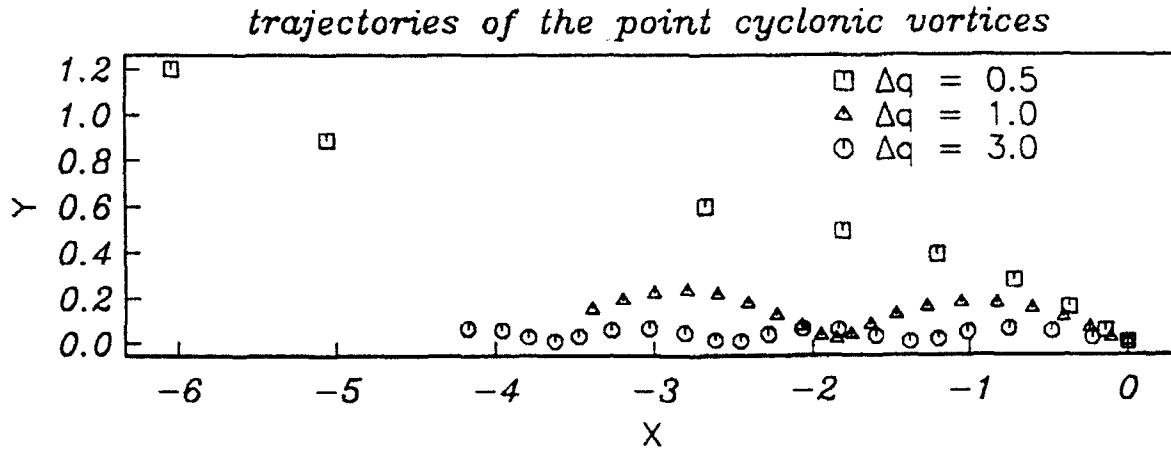
Figure 2.33: The trajectories of the cyclonic point vortices in time period length 32 for $\Delta q = 0.5$ and 40 for $\Delta q = 1$ and 3.
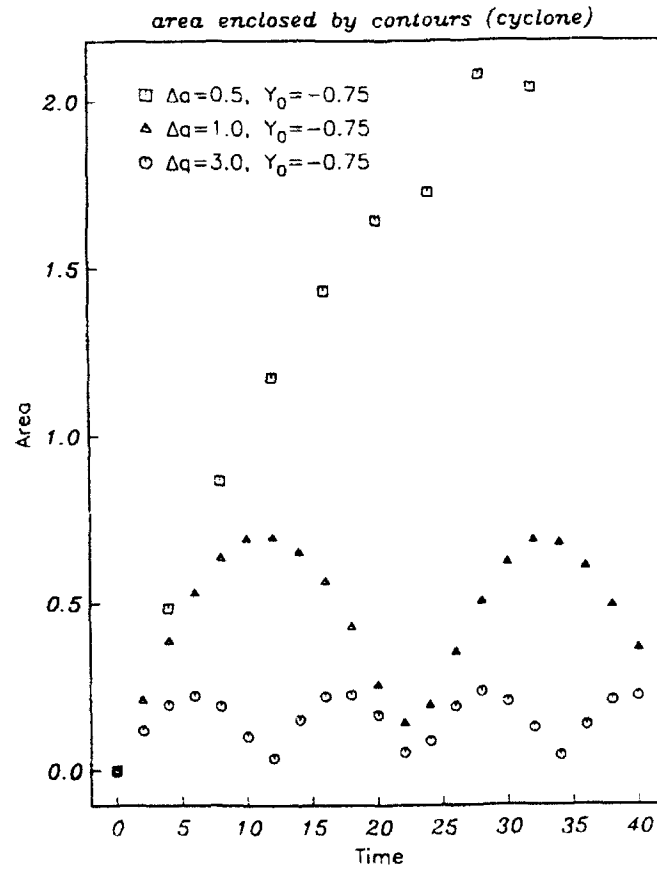


Figure 2.34: Cross escarpment transported volume induced by cyclonic vortex.

78

of $\Delta q = 1.0$ and $3.0$. As expected the smaller topography displays larger contour deformation. It is also obvious from figures 2.33 and 2.34 that the vortex and the area oscillate in phase, which results from the phase locking behavior of the interface perturbation and the vortex motion.

The studies above were repeated with finite cyclonic vortex patch replacing the point vortex in each case. The results show qualitative agreement in both the interface perturbation and the net westward eddy drift. The amplitude of north-south vortex oscillation is much smaller for the finite vortex case. Instead, the finite vortex deforms its shape periodically from circular to elliptical in accordance with the interface oscillation. In the small topography case, the finite vortex climbs onto the escarpment like the case shown in figure 2.30 but tends to ride on the escarpment instead of crossing it. In all the cases, the westward motion of the finite eddy is appreciably slower than the point vortex.

## Summary

Vortex interaction with a large escarpment in a barotropic fluid is qualitatively similar to the QG cases discussed in the previous section. The ageostrophic nonlinear advection causes fluid to cross the topography, which evolves to form the streamer and topographic eddy. Excitation of escarpment-trapped waves is seen in both. However, there are differences between them. Due to the large depth change, the stronger image effect causes a larger eastward vortex drift and thus affects the interface evolution and eddy formation. Unlike in the QG problem, the interaction depends on not only the ratio of $\Delta h$ and $\epsilon$ but also the individual values of them. In both QG and finite escarpment cases, the excitation of the escarpment waves is achieved through the mechanism of resonant oscillation, in which only one natural escarpment wave mode is excited.

There are important differences between a cyclone and an anticyclone when interacting with an escarpment. First, a cyclone is trapped at the topography and may move across the topography into shallow water; second, a cyclone tends to move faster

westward than an anticyclone and has no eastward excursion; third, a cyclone causes less cross-topography transport than the corresponding anticyclone case.

Barotropicity and the rigid lid impose strong constraints on the study in this section. They disallow any vertical change of horizontal velocity. The vertical adjustment of fluid crossing the escarpment is simplified to a vertically constant horizontal divergence or convergence, which assumes instant and uniform compression or stretching of the fluid column over the whole depth. One should be cautious when applying this model to problems where topography takes up most of the water column. The validity of the shallow water model is in question when the aspect ratio of the fluid $(h/L)$ or the depth change $(\Delta h/h)$ is not small. Thompson and Flierl (1991) have shown that the product of the Rossby number based on topographic length scale and the aspect ratio must be small for the shallow water model to be valid. In general, treating a slope as a topographic step is only appropriate for the problem in which particle excursions in one period is larger than the cross topography width.

## 2.7 Conclusions

Through simple physical arguments and modeling, we have investigated in this chapter the interaction process when an anticyclone or a cyclone encounters a step-like topography. The important processes occurring in the model include cross topography exchange, topographic eddy formation, vortex propagation and topographic trapped waves.

In the anticyclone case, the vortex is expelled away from the topography and may advect across it a volume of high PV fluid. This fluid from the shallow side may detach from its origin and evolve into a cyclonic topographic eddy, which subsequently influences the propagation of the original vortex. Due to the advection of positive vorticity away from the interface, there is more negative vorticity anomaly near the topography. This negative anomaly and the topographic eddy cause a weak westward current in the region between them. In contrast to the commonly accepted result that a steady deep forcing

can not penetrate onto a frictionless continental slope (Wang 1982, Csanady and Shaw 1983 and Vennell 1988), a varying eddy forcing in deep water is able to induce motion over a step topography by exciting topographic waves. The wave trapped at the step depends on both the topography and the Rossby number. The far field wave is linear and obeys the linear dispersion relation of free escarpment waves, which is monochromatic due to the topographic constraint. The cross-topography volume transport is dependent strongly on the size of the topography and weakly on the initial eddy position. It usually takes place within one free wave period as the vortex comes in contact with the topography. Multiple vortex-topography interactions are possible and need further investigation.

A cyclone behaves very differently from an anticyclone when interacting with a shallow topography. The interface perturbation evolves in such a way that it attracts the cyclone toward the topography. As it moves close to the topography, the cyclone drifts increasingly rapidly westward under increasing image effect. It can move across the escarpment into the shallow water. If the strength of the topography front is sufficiently large compared with that of the vortex, the cyclone will just induce a wave-like frontal perturbation and oscillate with it while propagating westward in a cycloid path. The cross-topography exchange induced by an impinging cyclonic vortex is usually much smaller than that of a comparable anticyclone.

# Chapter 3

# Mesoscale Eddy-Continental Shelf/Slope Interactions

The study in the previous chapter shows that even with a very simple model the vortex-topography interaction can produce a flow field with relatively rich dynamic structure. The mo ℄ important processes identified in the model results are (1) cross-topography volume exchange, (2) formation of a topographic eddy and (3) generation of topographic trapped waves. These processes can find their qualitative counterparts in the real ocean, and they all play important dynamic roles at least in the regional ocean near continental margins. Therefore they deserve further investigation. In a more general study, the restrictions imposed by the previous contour dynamics model, such as the step topography, idealized vortex and constant planetary rotation, must be relaxed.

In this chapter a primitive equation ocean circulation model will be used to investigate the problem of interaction between an oceanic mesoscale eddy and waters on a continental shelf and slope (shelf/slope in the following). The model incorporates major important factors that were previously simplified or neglected, except the density stratification and external forcing. According to our present knowledge in this area, even with the barotropic assumption, the model will provide us with dynamically significant and complicated structures deserving thorough investigation. The results from this study will allow some quantitative analysis and comparison with observations.

## 3.1 Introduction and Background

Although the simple model in chapter two is able to capture some important dynamic features of eddy-topography interaction, it falls short of producing details that enable quantitative model-observation comparisons. For example, the topographic wave in the previous model is monochromatic and always in resonance with the eddy forcing. This is obviously unrealistic and is an artifact due to the simplification of the model topography. The study, however, provides us with enlightening diagnosis of the fundamental interaction mechanisms. Based on the qualitative understanding of the process, further modeling effort will emphasize not only the qualitative features but also the quantitative understanding of the interaction dynamics. The increasing model complexity and sophistication will increase the degree of difficulty in interpreting the model results; thus the previous model results will be needed to shed light on the present work.

Both isolated mesoscale eddies and shelf/slope flows have received great scientific attention individually during the past two decades(see Flierl (1987), Mysak (1980) and Brink (1991) for reviews in these subjects). The theories about isolated eddies and about waves and currents on shelf/slope are now relatively well developed and understood. On the other hand, with frequent discoveries of mesoscale eddies in the continental margins and their interaction with shelf/slope waters, the knowledge on coupled eddy-shelf/slope dynamics is not yet adequate. There have been only a few modeling studies on mesoscale eddy-topography interactions. The most relevant were the work by Smith and O'Brien (1983) and Smith (1986). Smith and O'Brien (1983) examined the propagation of an isolated eddy when interacting with a western bounding topographic slope. They used a two layer primitive equation model with a linear bottom topography contained totally in the lower layer and explored the problems associated with eddy motion and its vertical structure as well as a range of parameter dependence. With a topography shallowing toward the west they found that the combination of planetary and topographic $\beta$-effects can result in very different propagation tendencies for a cyclone and an anticyclone. It

induces nonlinear self-advective motion which causes a cyclone to move upslope and an anticyclone to move downslope. In the cyclone case, the westward eddy propagation is due both to the planetary $\beta$ and the topography-induced nonlinearity, and thus the eddy can propagate at a speed faster than that on a $\beta$-plane with a flat bottom. In the anticyclonic case, the eddy may propagate eastward in the form of a vortex pair resulting from the enhancement of a trailing cyclonic dispersion center by the topographic vortex stretching effect. They also found that the barotropic eddy remains barotropic during the interaction and exhibits larger decay due to topographic wave dispersion. Due to the sloping topography, a baroclinic eddy tends to have deep compensation and a reverse nonlinear energy cascade from the barotropic to the baroclinic state is possible.

The same model as Smith and O'Brien (1983) was used by Smith (1986) to study the interaction of Loop Current eddy with topography in the Western Gulf of Mexico. The results indicate strong dependence of the eddy evolution on its lower layer amplitude. For strong lower layer flow, the topography-induced nonlinear self-advection is dominant over dispersion, and the eddy would move downslope away from the topography. A vortex pair emerges as seen by Smith and O'Brien (1983). For weak lower layer eddy strength, the fast topographic dispersion dominates the lower layer eddy evolution, allowing the upper layer eddy to propagate independently of topography. The eddy motion is thus dominated by interaction with the lateral boundary. In such a situation, the eddy is soon eroded by topographic dispersion.

The above two studies are very helpful in understanding eddy propagation and evolution when interacting with a finite bottom topography. They, however, did not explore either the responses on the shelf and slope, or the exchange across the topography induced by the strong eddy advective field. These further aspects of the eddy-topography interaction are of great importance to continental shelf/slope dynamic processes.

Partially due to the lack of reliable observations, there has not been much effort to address directly this two-way interaction process known to be common to many con-

tinental margins of the world. An alternative approach has been adopted by a number of investigators to study the shelf/slope response to an offshore forcing, in which the forcing is prescribed along an offshore boundary and is allowed to propagate along the boundary and to depend on space and time. Malanotte-Rizzoli (1984) investigated non-linear Rossby wave radiation over a quasigeostrophic topography due to a large scale propagating boundary forcing. She found that the boundary forcing acts on the interior field through a resonant mechanism, which itself is a result of nonlinear radiation and can be described by a solitary wave solution. In her study the bottom topography is on the same order as the planetary $\beta$-effect and shallows in the same direction as the planetary $\beta$. Therefore the system dynamics is not critically constrained by the presence of topography.

Chapman and Brink (1987) examined the effects of fluctuating offshore pressure forcing on a continuously stratified shelf/slope. For periodic forcing, they found that the shelf/slope response is heavily dependent on the forcing period. When the period is less than 10 days, the response is dominated by near resonance with free coastally trapped waves; for longer period forcing the response is mainly confined near the forcing field to a range about the first baroclinic Rossby deformation radius. In either case the shelf response is weak and nearly barotropic. They found that a propagating eddy forcing located near the continental slope can not penetrate onto the shelf, and the eddy velocity field is blocked by the topography. As a result, the alongshore velocity structure is squashed and has maximum on the shelf break. They also found a bottom intensified jet near the shelf break which is part of the eddy-induced circulation on the shelf.

In a recent study Qiu (1990) investigated the shelf/slope response to forcings that represent a propagating offshore eddy and a meandering western boundary current. For a traveling boundary forcing, his results show that the responses are dominated by the boundary trapped-topographic Rossby waves and are dependent strongly on the propagation speed of the forcing. When bottom friction is included, the inviscid results only hold at large propagation speeds; at small speeds the planetary $\beta$ is important. For

oscillatory forcing, the peak response is on the shelf and tends to shift from onshore to offshore as bottom friction is included.

There have been a few studies focusing on the topographic wave generation by an eddy over sloping topography. Louis and Smith (1982) investigated the mechanism of topographic wave generation by barotropic radiation from an eddy on a slope. This is basically the dispersion of the eddy constituents into barotropic topographic wave components. The theory was applied to the Scotian Slope and Rise to explain the observed velocity oscillation. Good agreement was found though the model's wave amplitude was somewhat smaller. In a recent paper Shaw and Divakar (1991) proposed a different mechanism of topographic wave generation. Using a numerical model they showed that topographic waves were generated by density advection in a baroclinic eddy over a sloping bottom. The wave amplitude is dependent on the eddy strength. Their results show that an eddy of the strength of a typical Gulf Stream warm-core ring can generate topographic waves of the observed amplitude.

The models reviewed above are linear, except Smith and O'Brien (1983) and Smith (1986). Shaw and Divakar (1991) included density advection. It appears that when the response on the shelf/slope region is considered, linear dynamics will be sufficient; when eddy propagation and dispersion are considered, regardless the size of bottom slope, the nonlinearity is dominantly important. The eddy-shelf/slope interaction borders on two different physical domains and spans different dynamic regimes. Previous research either treated processes in only one domain with others parameterized in terms of a boundary forcing, or investigated only partial dynamics over the whole domain. It is difficult to understand the interaction process without the active involvement of dynamics from both sides. The study proposed here is an effort to address the *interaction* between a mesoscale eddy and shelf/slope waters. The "forcing" field itself is also part of the dynamic field which evolves on its own and through the feedback from interaction with shelf/slope. The results will include not only the responses of the shelf/slope and eddy

evolution, but also the exchanges of mass, momentum and properties across the slope boundary.

This chapter is organized as follows: section 3.2 describes the model formulation and the numerical model; section 3.3 contains the model results and analysis of $f$-plane eddy-shelf/slope interaction; section 3.4 discusses the results of interaction on a $\beta$-plane and finally section 3.5 gives the summary of the study in this chapter.

## 3.2 Model Formulation and Numerical Method

### 3.2.1 Model Formulation

The current model is based on the incompressible Navier-Stokes equations in a rotational coordinate frame. The physical domain is a rectangular basin with continuously varying bottom topography and with a homogeneous density fluid. The dynamical equations are similar to that listed in section 2.2, but with possible internal and bottom friction terms included. The governing equations can be written as:

$$u_t + uu_x + vu_y - fv = -p_x + D_u \tag{3.1a}$$

$$v_t + uv_x + vv_y + fu = -p_y + D_v \tag{3.1b}$$

$$(uh)_x + (vh)_y = 0 \tag{3.1c}$$

where all the variables are defined in the same way as that in equation (2.1); $D_u$ and $D_v$ are the frictional terms.

The topography $h$ assumes the exponential form used by Buchwald and Adams (1968) but with different constant parameters. The topographic height is the largest at the northern boundary and decreases southward, i.e., in the negative $y$-direction, for a horizontal length $l$. After that the bottom is flat. The topography only varies in cross-channel direction as in the following:

$$h = \begin{cases} He^{2b(L-y)} + h_0, & L - l < y < L \\ He^{2bl} + h_0, & 0 < y < L - l \end{cases} \tag{3.2}$$

where $L$ is the width of the basin and $l$ the width of the topography, chosen to be 600 km and 150 km throughout this chapter, respectively. $H$, $h_0$ and $b$ are topography constants. Three sets of constants will be used in this study to represent different types of shelf/slope topography and they are:

$(A)$     $H = 50m$,   $h_0 = 0m$   $and$   $b = 10^{-5}m^{-1}$

$(B)$     $H = 4m$,   $h_0 = 46m$   $and$   $b = 1.828 \times 10^{-5}m^{-1}$

$(C)$     $H = 400m$,   $h_0 = 0m$   $and$   $b = 3.068 \times 10^{-6}m^{-1}$

These topographic profiles are plotted and shown in figure 3.1 for a north-south section. Topography A is a standard reference which the results from other cases are compared with. Its slope ranges from 0.001 on shelf to 0.017 on slope. Topography B has a longer and flatter shelf and a steeper slope. C is approximately linear. The water depth in the flat bottom ocean is about the same for all three topographies and C has a greater depth at the coast than A and B.

Since the density is homogeneous, the field will be initialized with an isolated eddy structure only. From continuity, a depth-integrated flow is horizontally nondivergent. Therefore a transport streamfunction $\psi$ is introduced and its value specified over the entire domain by

$$\psi(x,y,0) = \psi_0 e^{-(r/r_0)^\alpha}, \tag{3.3}$$

where $r = \sqrt{(x - x_0)^2 + (y - y_0)^2}$, $(x_0, y_0)$ is the initial location of the eddy center, $r_0$ is the eddy e-folding radius, $\psi_0$ is the eddy swirling transport within a unit vertical thickness. The constant $\alpha$ is a steepness parameter, specifying the radial vorticity gradient of the eddy. Equation (3.30) represents a barotropic monopole and is known to be unstable when a given barotropic instability criterion is met. Depending on the horizontal vorticity shear and on the relation to the perturbation (Pedlosky, 1979, p435), the transfer of eddy mean energy to eddy turbulent kinetic energy can happen and the eddy will break into turbulent patches. For the monopole, there exists a critical value, $\alpha_c$ such that for $\alpha < \alpha_c$, the monopole is stable to small amplitude perturbations. It has been
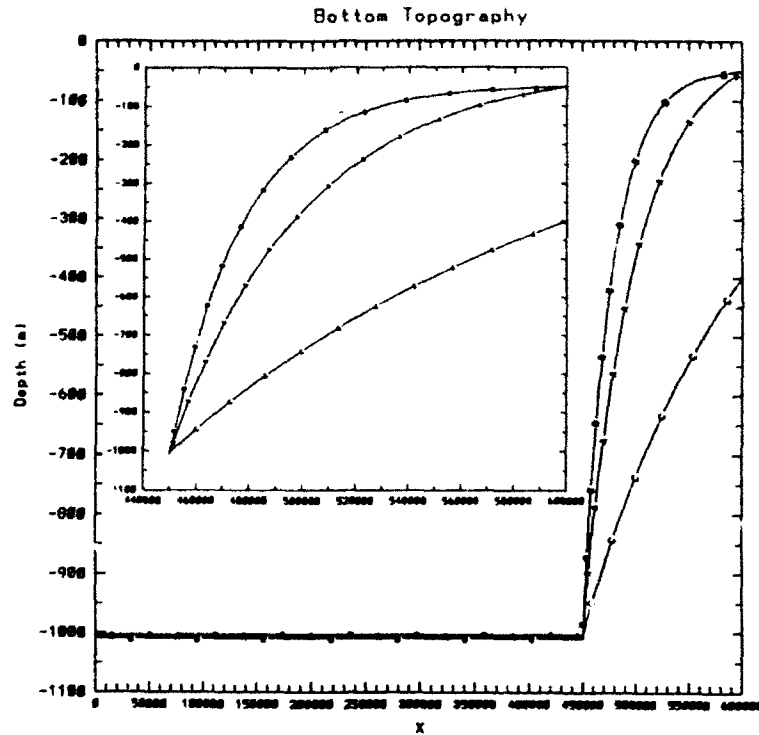
88

Figure 3.1: Three topography profiles to be used in this chapter with labels on each curve corresponding to topography (A), (B) and (C) given in the text. The inner panel shows the portion of sloping bottom of the outer panel.

shown by Carton and McWilliams (1989) that for the eddy described by equation (3.3), $\alpha_c = 1.92$. When $\alpha$ is smaller than $\alpha_c$, the steep vorticity structure holds the monopole together from being broken up through transfer of energy to turbulent flows. On the other hand, too small an $\alpha$ will result in a very steep vorticity structure, which requires higher spatial resolution to resolve the eddy and is potentially problematic numerically. A value $\alpha = 1.9$ is used throughout this study. Radial profiles of streamfunction, velocity and vorticity are shown in figure 3.2 with $r_0 = 50km$ and $\psi_0 = 0.602075r_0$.

On the two boundaries parallel to the isobaths, the no flux boundary condition is used. Fluid particles are allowed to slide along the boundaries freely.

$$v = 0, \quad \partial u/\partial y = 0 \quad on \quad y = 0, \ L \tag{3.4}$$

To choose the boundary condition at the two cross basin boundaries, the following considerations should be included: (1) no net flow through the boundaries; (2) no or small reflection from the boundary, i.e., the boundaries only absorb momentum and do not
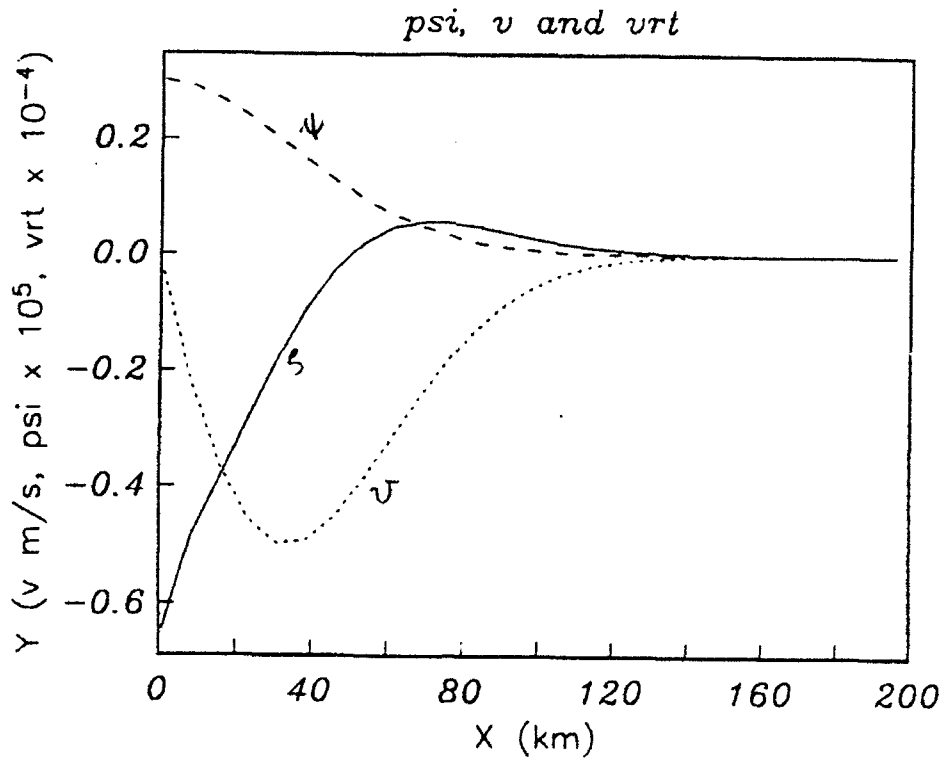
89

Figure 3.2: Profiles of (a) streamfunction $\psi$, (b) swirling velocity $v$ and (c) vorticity $\zeta$ along a radial line for $r_0 = 50km$ and $\psi_0 = 0.602075r_0$.

feedback; (3) the boundary condition should not affect the solution. The first one is a direct statement of mass conservation in the basin. The second consideration is only an approximation. Since wave generation on the topography is expected, these waves will eventually reach the boundary of the finite domain. A periodic boundary condition is not recommended because the waves will reenter the basin and thus increase the energy level of the fast-propagating components in the wave power spectrum. An open boundary condition is also not chosen, simply because the dispersive nature of the topographic waves is not known beforehand and also the third factor is involved. The boundary condition chosen for this study, though the simplest but by no means the best, is a sponge layer. Within a given distar e next to a cross basin boundary, a damping term of the form $-r_s u$ or $-r_s v$ is added to the right hand side of the $x$ or $y$ momentum equation (3.1), respectively. Here $r_s = c_0(D - d(x))/D$, and $c_0$ is a constant of the dimension of an inverse time. $0 \leq d(x) \leq D$ is the distance away from the boundary. $c_0^{-1}$ is the time scale necessary to relax the fields toward a given value (zero here). and $D$ is the thickness of the

sponge layer. For this study $c_0^{-1}$ is chosen to be one day and the layer thickness $D = 70$ km. No matter what are the choices of $c_0$ and $D$ within a given range of value, there will be a certain fraction of incoming momentum reflected by the sponge layer. In general, the sponge boundary is more effective in absorbing shorter and slower propagating waves. The fast propagating long waves may be partially reflected but re-emerge from the sponge layer with considerably weakened amplitude. Later numerical experiments show that this condition is adequate for the present problem. An improvement on this boundary condition could be the combination of a sponge and the Orlanski radiation conditions. Since the numerical experiment with a sponge condition in a domain twice the size of the one used here does not show much change, it is decided not to adopt the mixed sponge-radiation conditions.

## 3.2.2 Numerical Model

The system formed above will be solved numerically over a physical domain 720 km long in $x$ and 600 km wide in $y$. The numerical model to be used is a semispectral primitive ocean circulation model (SPEM) developed by Haidvogel et al (1991a). The model is designed for regional to basin scale ocean modeling problems and allows both irregular basin geometry and finite amplitude bottom topography. The formulation, implementation and application of SPEM can be found in detail from Haidvogel et al (1991a) and Haidvogel et al (1991b). Here only a brief summary of the model and its adaptation to the present problem are given.

The model utilizes the incompressible Navier-Stokes equations of fluid flow with the Boussineq and hydrostatic approximations. For the purposes of accommodating irregular basin geometry and finite topography, the cartesian equations are rewritten by the application of two coordinate transformations. The first is a transformation of $(x, y)$ coordinate into a boundary-fitted curvilinear, orthogonal coordinate system, $(\xi, \eta)$ (not used in the present problem of a rectangular domain). In the second transformation, a

stretched vertical $\sigma$-coordinate is adopted, where the vertical coordinate $z$ is replaced by the topography-following variable

$$\sigma = 1 + 2(z/h).$$

In the stretched coordinate, the new coordinate system spans the range $-1 < \sigma < 1$. The model equations become somewhat more complicated after these two transformations and the details can be found from Haidvogel et al (1991a). The model also assumes a rigid lid, which eliminates surface gravity waves.

A centered, second-order finite difference approximation is adopted in the horizontal. The well known Arakawa "C" grid is used for the horizontal arrangement of variables, which guarantees the conservation of the first moments of the variables u, v, w and $\rho$. The vertical dependence $(\sigma)$ of the model variables is represented as an expansion in a finite set of Chebyshev polynomials. It is restricted so that only the lowest-order polynomial has a nonzero vertical integral, which isolates the external mode (depth integrated component of the field) in the amplitude of the lowest-order polynomial. In practice, the actual variable values are taken at "collocation" points $\sigma_n$ chosen to correspond to the location of the extrema on the highest-order polynomial and are solved explicitly in the model. In the present study the density is assumed uniform and there is no vertical dependence of any kind. A minimum number of $\sigma_n$ will be used, which can not be less than three due to the model formulation. Therefore only three vertical coordinates are used. For the problem treated in this chapter, there is no stratification, and no vertically dependent boundary condition and forcing, thus an initially barotropic field will remain barotropic at all times. This is not affected by the number of vertical collocation points in the model.

The solution of the discrete equations proceeds in the following sequence of steps. First the $N$ internal modes ($N = 2$ here) of the velocity distribution (the part of the velocity which has zero depth average) are calculated by time stepping of the transformed equations (3.1a and b). A leapfrog time-stepping scheme is used in the above procedures.

To calculate the velocity components for the horizontally nondivergent, depth integrated flow, a transport streamfunction $\psi$ is introduced that

$$\bar{u} = -\psi_\eta/h, \quad \bar{v} = \psi_\xi/h. \tag{3.5}$$

By taking the curl of the depth-integrated momentum equations, the pressure terms are eliminated and a vorticity equation for $\psi$ is obtained. This vorticity equation is then time stepped as above and the streamfunction is determined by solving a generalized linear elliptical equation.

To stabilize the numerical computation an internal friction in the form of biharmonic friction is used to consume the small scale enstrophy due to the nonlinear cascade. It is desirable that this friction be as small as possible, not to affect the motion on the larger scales. It also plays an additional physical role in regulating the rate of eddy decay and flattening the eddy structure (McWilliams and Flierl, 1979). The value of the biharmonic friction coefficient used in this study is a relatively small one $\nu_4 = 10^9 m^4/s$. There is no bottom friction used in the model, except mentioned explicitly.

### 3.2.3 Model Verification

The SPEM model after being configured for the present application is tested for an isolated eddy evolution on a $\beta$-plane. Results are compared with previous work. All experiments performed here are initialized with the streamfunction given in equation (3.3) and $r_0$ and $\psi_0$ from figure 3.2. The maximum eddy swirling velocity is 0.5 $m/s$. At mid-latitude, the Coriolis parameter is about $f_0 = 10^{-4} s^{-1}$ and $\beta = 1.6 \times 10^{-11} m^{-1}s^{-1}$. The conventional Rossby number $R_0 = v_{max}/fr_0 = 0.1$ is fairly small for $f$-plane dynamics, indicating that the role of nonlinearities are fairly unimportant in the momentum balance, especially in the region away from the eddy on the shelf. For a $\beta$-plane eddy, a different measure of the ratio of nonlinearity to planetary rotation can be defined as: $Q = v_{max}/\beta r_0^2 = 12$, which indicates the dominant importance of nonlinearity for isolated eddies on the $\beta$-plane. The order of magnitude difference between $R_0$ and $Q$ separates

two different dynamical regimes that were mentioned earlier: a linear, $f$-plane regime for the shelf/slope responses and a nonlinear, $\beta$-plane regime for the eddy evolution and propagation.

First the evolution of a linear anticyclone and a nonlinear anticyclone on the $\beta$-plane in a flat bottom basin is calculated using SPEM. The results show that in the linear case the eddy translates westward at an average speed $-0.44$ cm/s for the first 60 days and leaves behind a slowly propagating weak Rossby wave wake. The meridional translating rate is identically zero. The linear propagation accelerates during the finite computational period, and the speed cited before at the end of the calculation has not reached its asymptotic limit. When nonlinearity is included, the westward propagation rate increases above the linear value and meridional propagation is seen. Over the 60 day period, the average westward and southward propagation rates are $-1.54$ cm/s and $-4.45$ cm/s, respectively. The rates are comparable with the results obtained by McWilliams and Flierl (1979), which are $-1.59$ cm/s and $-5.28$ cm/s over a period of 78 days for similar conditions. Since the eddy used here is not exactly Gaussian as that used by McWilliams and Flierl (1979), the comparison is affected slightly. Nevertheless, *above agreement indicates that the present model results are both qualitatively and* quantitatively consistent with the previous theory.

With inclusion of type A topography, a monochromatic topographic wave experiment is performed. The results show that for the initial condition of a single frequency-wave number wave (satisfying the dispersion relation of shelf waves over the topography), the wave persists in its shape during propagation until it hits the sponge boundary. The back scattering from the boundary is relatively small and the wave is hardly distorted. An estimate of wave energy density shows that the reflected waves have less than 5% of the total energy. Thus the sponge condition seems to work reasonably well in damping the incoming waves. Since there is no net flow through the boundary, the condition will be used in all later numerical experiments.
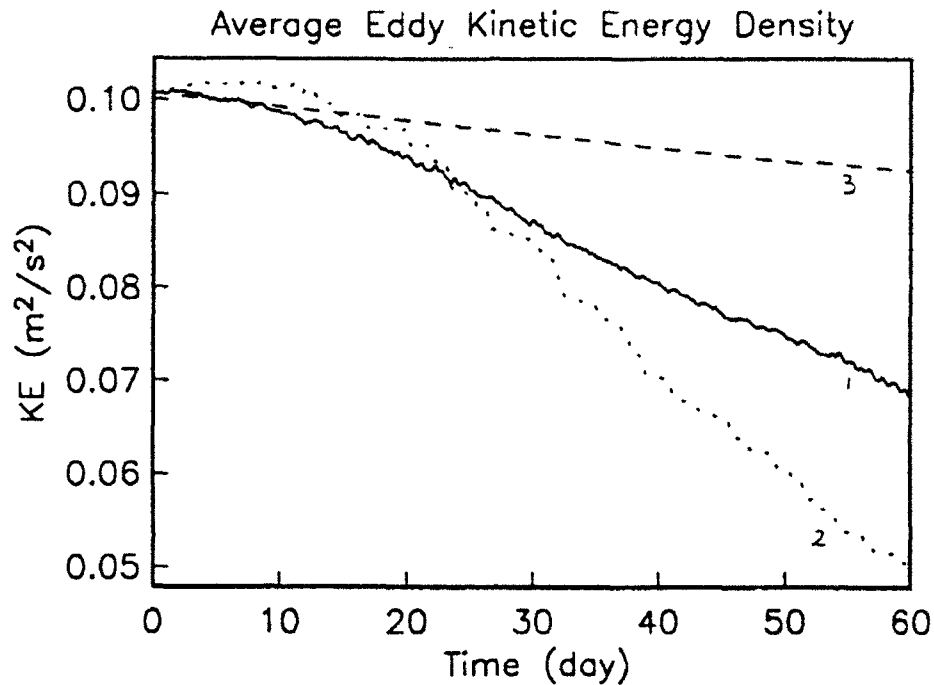
94

Figure 3.3: Eddy KE density decay: (1) nonlinear $\beta$-plane eddy with biharmonic friction, (2) linear, inviscid $\beta$-plane eddy and (3) purely frictional decay of an $f$-plane eddy.

It is desired that the internal biharmonic friction be small so that it does not cause large frictional eddy decay while stabilizing the numerical computation. The decaying of eddy kinetic energy (KE) density is examined for three cases: (1) nonlinear $\beta$-plane eddy with biharmonic friction, (2) linear, inviscid $\beta$-plane eddy and (3) purely biharmonic frictional decay of an $f$-plane eddy. The results are plotted in figure 3.3. (2) shows a quick decay of the eddy KE due to fast Rossby wave dispersion. By adding nonlinearity, the rate of eddy decay due to linear wave dispersion is significantly reduced (curve (1)). Finally it is seen from (3) the frictional effect counts less than one third of the total decay in (1). Therefore even for strong nonlinearity, Rossby wave dispersion still plays a major role in eddy decay, while the frictional decay is minor on the same time scale. These results agree well with McWilliams and Flierl (1979).

## 3.3 Eddy-Shelf/Slope Interaction on an $f$-Plane

Given the importance of planetary $\beta$-effect, it is certainly a fundamental term to be included in the model study. However, from the previous argument for the dynamic regime separation, the interaction process may be investigated to a certain extent without actually going into the $\beta$-plane. A topographic $\beta$ parameter $\beta_T = f_0 s/h$ can be defined, where $s$ is the topography slope. The ratio between topographic $\beta$ and planetary $\beta$ is: $\beta_T/\beta = 10 \sim 100$ for the topography and the parameter range of this study. Like nonlinearity, planetary $\beta$ may be neglected where the topographic control is dominant. This approximation enables us to examine the shelf process on the $f$-plane and to compare the results with the previous insights obtained from the contour dynamics calculation. The major shortcomings are related to the eddy evolution. The important planetary dispersion and decay of the eddy are suppressed, as is the associated nonlinear self-advection. However, it is felt that a better understanding of the process with complete dynamics will be achieved successively after the basic mechanisms are fully understood. The $\beta$-effect is left to next section.

Several numerical experiments are performed to model the process of eddy-shelf and slope interactions. The cases and parameters are listed in table 3.1. The study may be categorized as follows in terms of its parameter dependence: (1) different initial eddy-slope distance from the slope to the center of the eddy, (2) size and strength of the eddy (nonlinearity), (3) topography, (4) cyclone or anticyclone and (5) bottom friction. The results are discussed with reference to case F1, which is called the standard or reference case.

### 3.3.1 Standard Case

Similar to the previous contour dynamics study, the eddy is initially positioned close enough to the slope so that it starts to interact with the slope water right after time $t = 0$. In the real ocean, this initial condition may correspond to a Gulf Stream warm-core ring

## Table 3.1

| Cases | Eddy Rotation | Eddy Radius (km) | Initial Distance (km) | Topography | Comments |
|-------|---------------|------------------|-----------------------|------------|----------|
| F1 | −1 | 50 | 65 | A | Standard Case |
| F2 | −1 | 50 | 50 | A | Small Distance |
| F3 | −1 | 50 | 80 | A | Large Distance |
| F4 | −2 | 50 | 80 | A | Double Strength |
| F5 | −1 | 75 | 80 | A | Large Eddy |
| F6 | −1 | 50 | 65 | B | Steep Slope |
| F7 | −1 | 50 | 65 | C | Small Topography |
| F8 | 1 | 50 | 65 | A | Cyclone |
| F9 | 1 | 50 | 80 | A | Cyclone |
| F10 | 1 | 50 | 80 | B | Cyclone |
| F11 | −1 | 50 | 65 | A | Bottom Friction |

$f$-Plane Eddy-Topography Interaction Experiments.

spin-off onto the continental topography by a large meandering process. Since part of the eddy velocity field is initially on the topography, both vortex tube stretching caused by cross-isobath advection and topographic wave dispersion will be effective. When the eddy moves away from the topography, the eddy dispersion ceases and the eddy is subject to the influence of its own asymmetry, perturbed field and topographic eddy formation.

Figure 3.4 (case F1 of table 3.1) shows contour plots of streamfunction, relative vorticity and potential vorticity as they evolve in time. The eddy induces a large deformation of the slope potential vorticity (PV) front. A seaward disturbance develops to the northeast of the eddy which also strongly affects the eddy propagation. The slope disturbance continues to grow under the eddy advection and in turn acts on the eddy with a growing seaward moving tendency. Eventually the disturbance separates from the slope into the deep ocean and forms a cyclonic topographic eddy. The separation process takes place during day 12 to 14 and corresponds to a peak in the offshore transported volume. Immediately after the separation, the original eddy and the newly formed topographic *eddy form a vortex pair, which decides the subsequent eddy propagation. The strength* of the cyclone is much weaker than the original eddy; therefore, the resulting eddy propagation is along an anticyclonic loop in favor of the strong eddy. Figure 3.5 shows the trajectories of the positions of the spatial maximum and minimum of the eddies. It is seen that both eddies will go back to the slope and undergo a second interaction. During the second interaction, the topographic cyclone is reabsorbed by the slope and a new topographic cyclone emerges. A net drift of the eddy center about 10 km westward is seen at the end of the loop. This trend continues every time the eddy loops back to the slope and results in a persistent net westward along-slope drift. This process is weakened by the loss of eddy energy and volume and may last only a few interactions. It is seen the cyclone strength from the second interaction is only two-thirds of that of the first one.

As observed from figure 3.4, the initial circular eddy is elongated as it interacts with slope water. The radial symmetry is first perturbed by the development of a slope
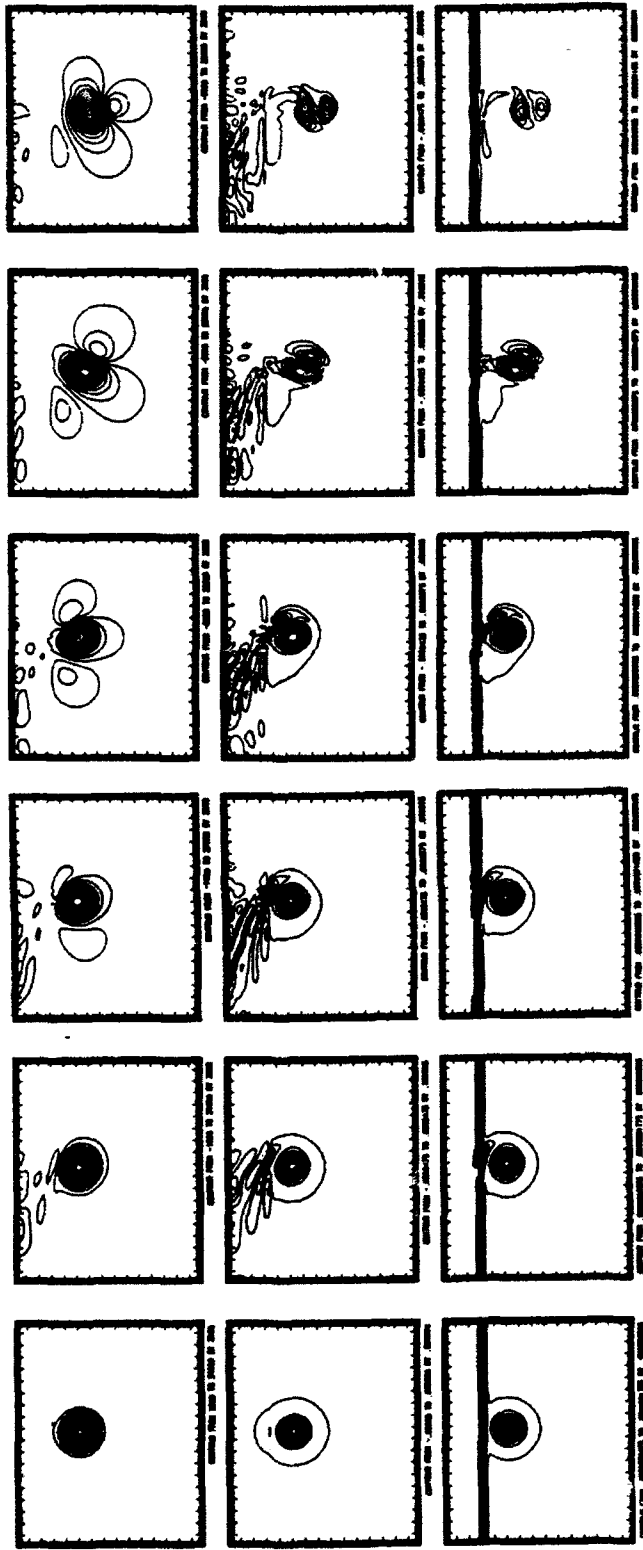
98

Figure 3.4: Contour plots of the dynamic fields. From top to bottom row: contours of streamfunction, relative vorticity and potential vorticity. Columns are ordered from left to right, starting from day 0 with time increment of 4 days. In order to emphasize the eddy and the slope perturbation field, only part of the potential vorticity contours are plotted. Case F1.
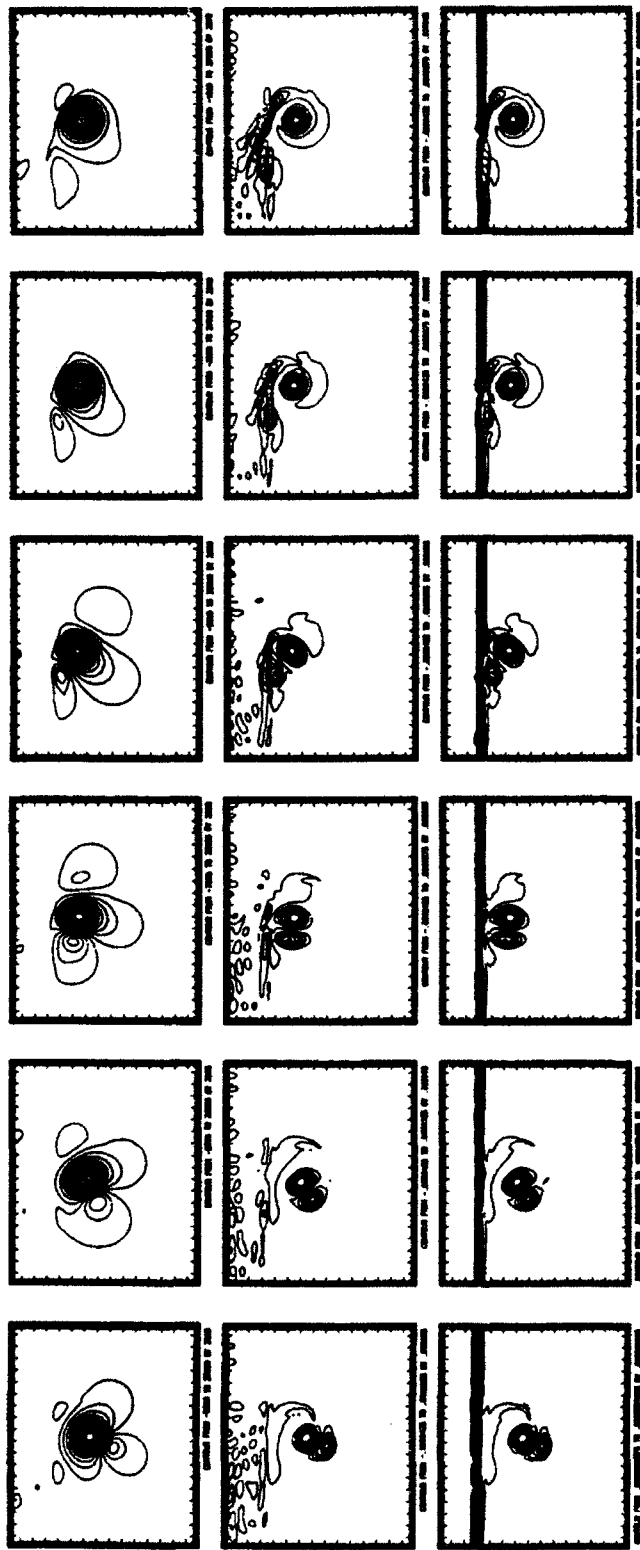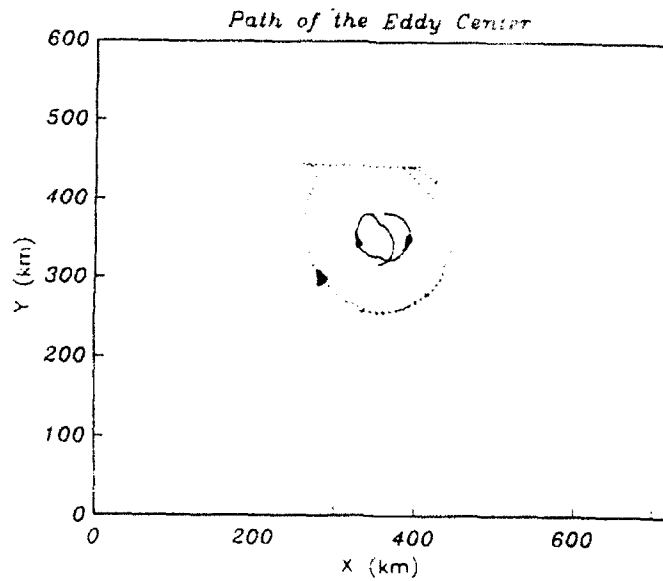
99

Figure 3.4: (continued)

Figure 3.5: The trajectories of the vorticity minimum (solid curve) and maximum (dash curve) for the original eddy and topographic eddy, respectively. The direction of motion is clockwise.

disturbance. The perturbation velocity field exerts a strong shear on the original eddy and further stretches its already elongated shape. During this period, the topographic cyclone forms and separates from the slope water. The eddy propagation speed accelerates upon the topographic eddy separation. The stretched leading and trailing edges of the original vortex are bent around the cyclone to form long streamers and are quickly dissipated by subgrid scale processes. There is a continuous loss of eddy volume around this period which is illustrated in figure 3.6a. Here the eddy volume is the eddy area multiplied by a constant depth factor. The eddy area ($A$) is defined as the area bounded by the radius of the eddy e-folding swirling transport. Meanwhile the eddy kinetic energy density (defined as $\iint_A \frac{1}{2}(u^2 + v^2) \, dx \, dy / A$) decreases for the original eddy and increases for the topographic eddy (figure 3.6b). Between day 18 and 20, both eddies experience drastic decreases in volume. This corresponds to the extreme elliptical shape and strong streamer events for both eddies after the topographic eddy separation from the slope. The original eddy
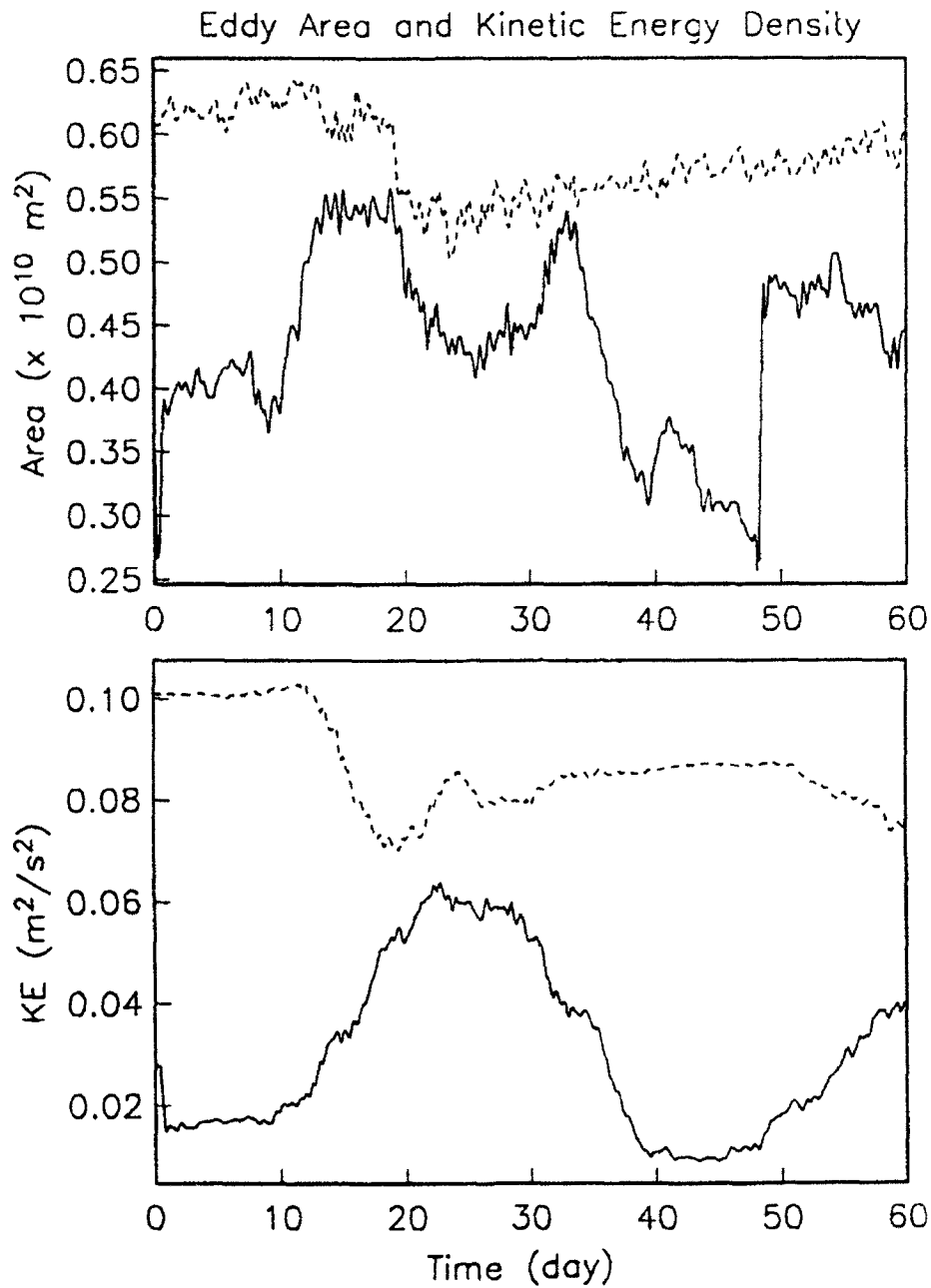
101

Figure 3.6: Upper panel: The area (the volume is the area times a constant ocean depth) of the original eddy (dash line) and the topographic eddies (solid line) vs time; lower panel: The Kinetic energy density of the original eddy (dash line) and the topographic eddies (solid line) vs time.

volume and KE remain roughly unchanged for the rest of the time. The topographic eddy undergoes the changes of birth and death. Figure 3.6 shows that during days 36 to 40, the first topographic eddy is reabsorbed by the slope water; around day 48 a new topographic cyclone emerges. The size (thus the volume) and the KE density of the second cyclone are slightly weaker than the first one, because of the decrease in original eddy strength caused by loss of the eddy volume and frictional decay.

An interesting phenomenon takes place on the shelf/slope as fluid is advected across isobath by the original eddy. The slope fluid crosses slope-deep ocean boundary at about 20° angle. It is subject to a combination of three propagation tendencies: topographic $\beta$, nonlinear self-advection and advection by the eddy. For the cyclone on the slope, topographic $\beta$ induces an along-isoba h motion tendency, which is also accompanied by a shoreward nonlinear propagation due to the steepening of the eddy vorticity gradient. These two tendencies are in the opposite direction to the motion caused by the original offshore eddy. However, the advection from the original eddy *is dominant and advects the cyclonic disturbance toward the deep ocean.* Figure 3.7 gives the accumulated volume transport across the slope associated with this advective process. This transport is defined as the total volume of fluid with the potential vorticity of slope origin but found in the region of flat bottom ocean. It is seen that most of the volume transport takes place within 10 to 12 days from the beginning of the interaction and majority of the transported volume represents the fluid originating near the edge of the slope. The upper slope water, though disturbed by the eddy, does not move off the slope. As the eddy moves away, the disturbance relaxes and causes oscillations on the shelf. This will be discussed later in this section.

Considering the cross-isobath transport process, it is well known 'h at strong ageostrophic mechanisms are needed to force fluid to cross the topographic slope. In a system without external forcing, the possible ageostrophic mechanisms are nonlinear advection, time dependence and bottom friction. Figure 3.8a shows the individual terms from momentum equation (3.1a) as functions of time at a location on the slope about
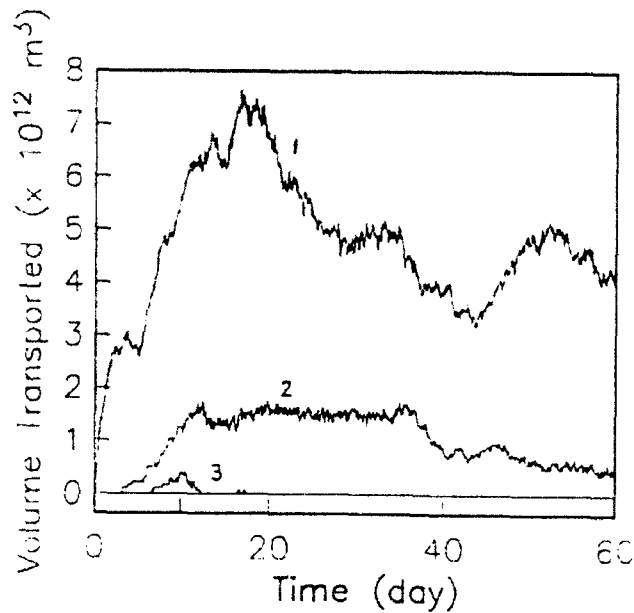
Figure 3.7: The accumulated cross-slope volume transport for case F1. The curves are (1) total volume transported; (2) volume transported from upper slope area 7.5 km away from the slope-deep ocean boundary; (3) volume transported from upper slope area 15 km away from the slope-deep ocean boundary.

81 km northeast of the eddy center. The cross-isobath velocity is initially zero at this location and grows quickly into an offslope current balanced primarily by a alongshore pressure gradient. The restoring mechanism due to the potential vorticity constraint on a sloping bottom tends to bring the disturbance to equilibrium by inducing an oscillatory motion. Instead the eddy velocity field forces a sustained continuous cross-isobath motion that lasts about eight days at this location. It is seen from figure 3.8a that terms $u\partial u/\partial x$ (curve B) and $v\partial u/\partial y$ (curve C) are substantially larger during this period. The oscillation due to the vorticity restoration can be seen superimposed on the curves of $-fv$ (curve D)and $-\partial p/\partial x$ (curve E). As expected the biharmonic friction term (curve F) is small at all time (bottom friction is not used here). After the eddy drifts away the motion at this slope location evolves into a well defined periodic oscillation. The second interaction takes place west of this location around day 34: the result can be seen from the increasing magnitude of the nonlinear advection terms in Figure 3.8b, which shows the variation of the terms at a location closer to the center of the second interaction. The
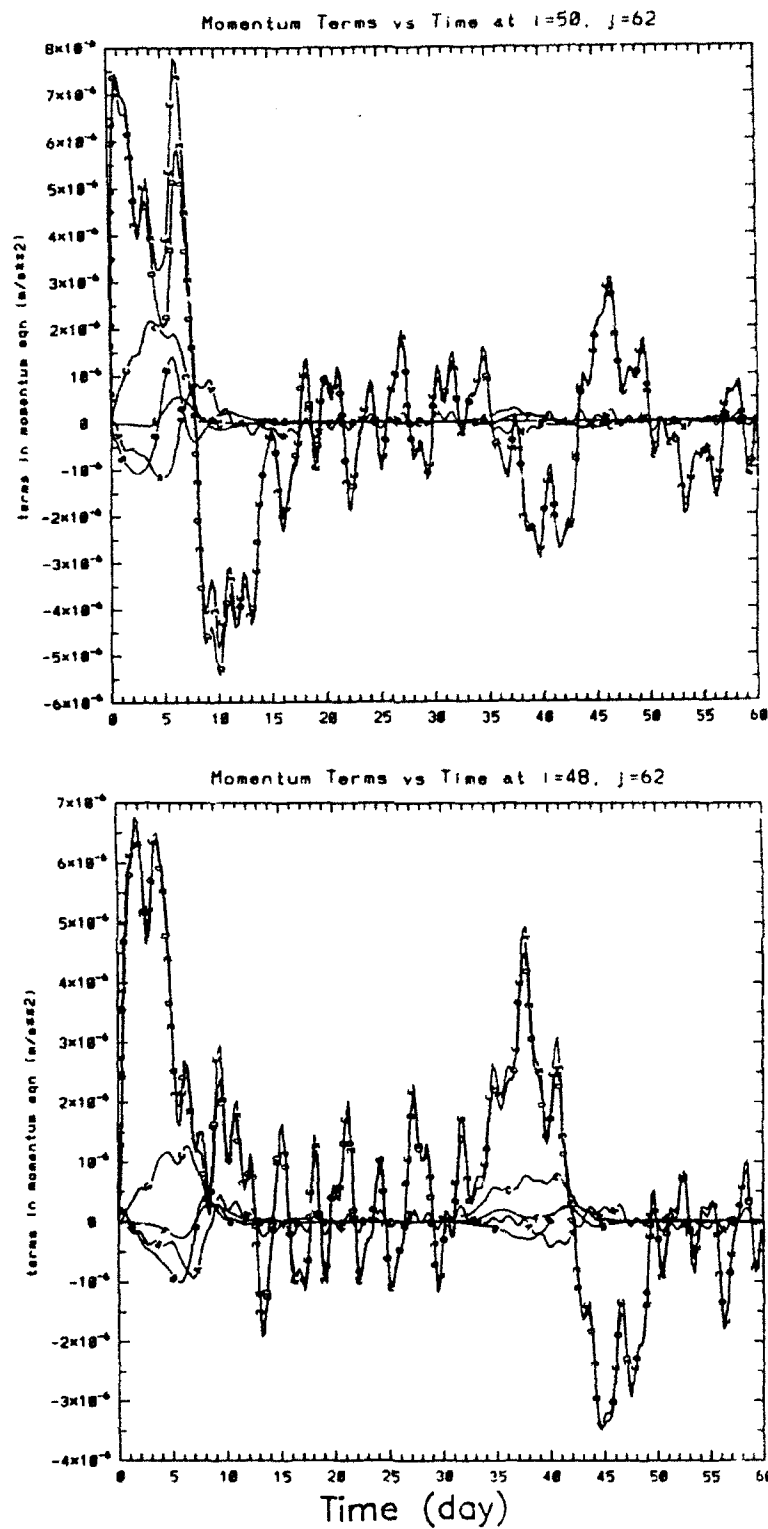
Figure 3.8: Time variation of the individual terms in equation (3.1a) at two locations. Upper panel: $(x, y) = (375, 465)$ km; Lower panel: $(x, y) = (360, 465)$ km. The legends are: (A) $u_t$, (B) $uu_x$, (C) $vu_y$, (D) $-fv$, (E) $-p_x$ and (F) $\nu_4 \nabla^4 u$.

two interactions are qualitatively the same though the second is somewhat weaker than the first and they last about the same time length. The curve $C$ for term $vu_y$ is positive, indicating slopeward momentum flux during the interaction.

To demonstrate the importance of nonlinear advection in eddy-slope interaction process, case F1 is repeated without the nonlinear terms in the momentum equations. The results differ greatly from that of F1. First, no slope volume is transported offslope into the deep ocean and there is no subsequent formation of a topographic eddy as it happens in case F1. Second, the eddy does not move. The part of the eddy that is initially on the slope radiates topographic Rossby waves. The core of the eddy within 50 km e-folding radius is, however, almost not affected by the interaction, since the eddy center is 65 km away from the topography. The slope disturbances are mainly the topographic waves from the eddy radiation and have weaker strength than that observed in case F1, due to the lack of onslope momentum flux. The results show that the nonlinearity is part of the crucial dynamics of the interaction process.

It is seen that the dynamic features observed in previous contour dynamics study are reproduced here but with richer and complicated details, such as the cross-slope volume transport, topographic eddy formation and propagation and evolution of the original eddy. The rest of this section devotes to the further analysis of these features and their variation under different parameter range.

## 3.3.2  Dependence on Initial Eddy Position

It is obvious that the strength of the interaction depends on the initial distance between the eddy and the slope. The fact that reflects this dependence most is the change in the rate of cross-slope transport. Cases F1, F2 and F3 from table 3.1 are examined for their transport rates. In all three cases the total transport increases roughly linearly with time. But for the close interaction case F2, the transport process takes place in a relatively short period of time. The values of the total volume transport, the interaction time

(defined as the time from $t = 0$ to the first topographic eddy separation) and the rate of transport are listed in table 3.2 for these three cases. It is noted that the total transport across slope into the deep ocean does not vary greatly with the initial distance, but the rate of the transport does. When close to the slope, the eddy has a relatively stronger interaction with the slope water but the interaction lasts for a relatively short period of time; vice versa for an eddy initially far away from the slope. Since the cross-topography volume transport is mainly due to the eddy nonlinear advection, a weak advection in a long interaction time may transport across slope as much volume as a strong advection in a short interaction time. The difference is in the composition of the transported water mass. In a strong interaction, certain amount of fluid from the upper slope is advected off slope; while in a weak interaction only the fluid in the nearest vicinity of the slope boundary is transported into the deep ocean. Comparison of cross-slope transport for cases F1 and F2 shown in figure 3.7 and 3.9 indicates that F2 has about $10^{12}$ $m^3$ volume transported from upper slope area with depth shallower than 740 m and F1 virtually has none from that depth. This differs from the contour dynamics calculation shown in figure 2.26, where the volume transport increases as the initial distance between the eddy and the topography decreases and the interaction time is independent of the initial distance. The differences between the two are due to several factors, the most important due to the use of continuous slope in present study, which allows easy transport of near slope edge water and longer interaction time as the eddy moves away from the slope.

From the above analysis the strength of the interaction has a direct influence on topographic eddy generation. Careful examination shows that the circulation of the topographic eddy is indeed larger as the original eddy is initially closer to the slope. Table 3.3 lists the relevant numbers of the original eddy and the topographic eddies formed in three cases. The sizes of the topographic eddies are almost the same for all three cases. The interaction with the closest initial eddy-slope distance produces the strongest topographic eddy. This is not unexpected given the similar total volume transport but different origin of the eddy water from various depths of the slope for these cases.
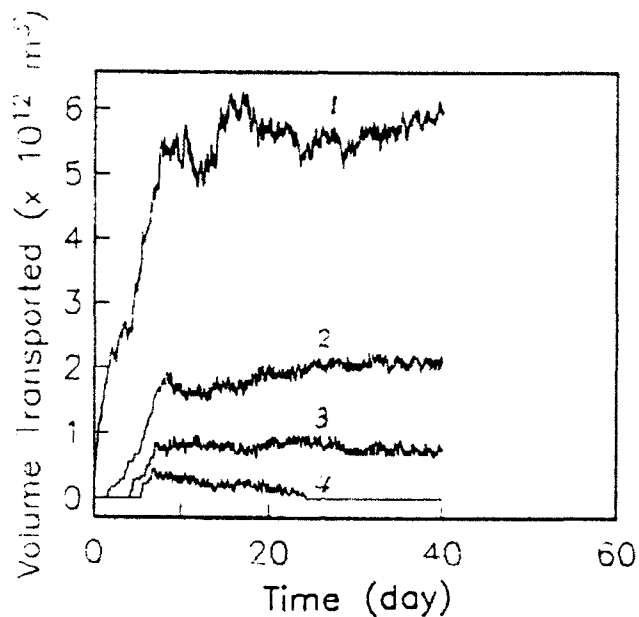
Figure 3.9: The accumulated cross-slope volume transport for case F2. The curves are (1) total volume transported; (2) volume transported from upper slope area 7.5 km away from the slope-deep ocean boundary; (3) volume transported from upper slope area 15 km away from the slope-deep ocean boundary; (4) volume transported from upper slope area 22.5 away from the slope-deep ocean boundary.

## Table 3.2

| Case | Total Volume Transported $(10^{12}m^3)$ | Length of Time (Days) | Rate of Transport $(10^6 m^3/s)$ |
|------|-----------------------------------------|-----------------------|----------------------------------|
| F1 | 5.6 | 12 | 5.4 |
| F2 | 5.8 | 8 | 8.4 |
| F3 | 5.6 | 20 | 3.2 |

Dependence of Volume Transport on Eddy Position

## Table 3.3

| Case | Circulation $(10^5 m^2)$ | Maximum Vorticity $(10^{-4}s^{-1})$ | Radius (km) |
|---|---|---|---|
| F1 | 0.65 | 0.32 | 38 |
| F2 | 0.80 | 0.54 | 39 |
| F3 | 0.40 | 0.11 | 38 |
| The Original Eddy | $-1.3$ | $-0.64$ | 50 |

The Characteristics of Topographic Eddies

It has been seen before that the eddy motion is dominated initially by the slope PV front disturbances and then by the dipolar advection. The eddy center trajectories for six cases are plotted in figure 3.10. According to the figure, the eddy propagation can be roughly divided into two stages. In first stage, the eddy is expelled from the slope due to the interaction with the cyclonic slope disturbance and the effect of topographic $\beta$ associated nonlinearity. The closer the eddy is initially to the slope, the farther it is expelled southeastward. The eddy trajectories at this stage agree qualitatively with that of the contour dynamics calculation shown in figure 2.23. In the second stage the cyclonic slope disturbance has separated from the slope and formed a topographic eddy, which forms a dipole-like structure with the original eddy. The propagation is mainly due to the dipolar advection. Depending upon the strength of the interaction, the eddies may propagate back to the slope and result in multiple interaction. Theoretically the multiple interaction is inevitable except only in the case in which the dipole is a symmetric one.

**Eddy Center Trajectory** (upper panel)

Legend
F1
F2
F3
F4
F5
F6

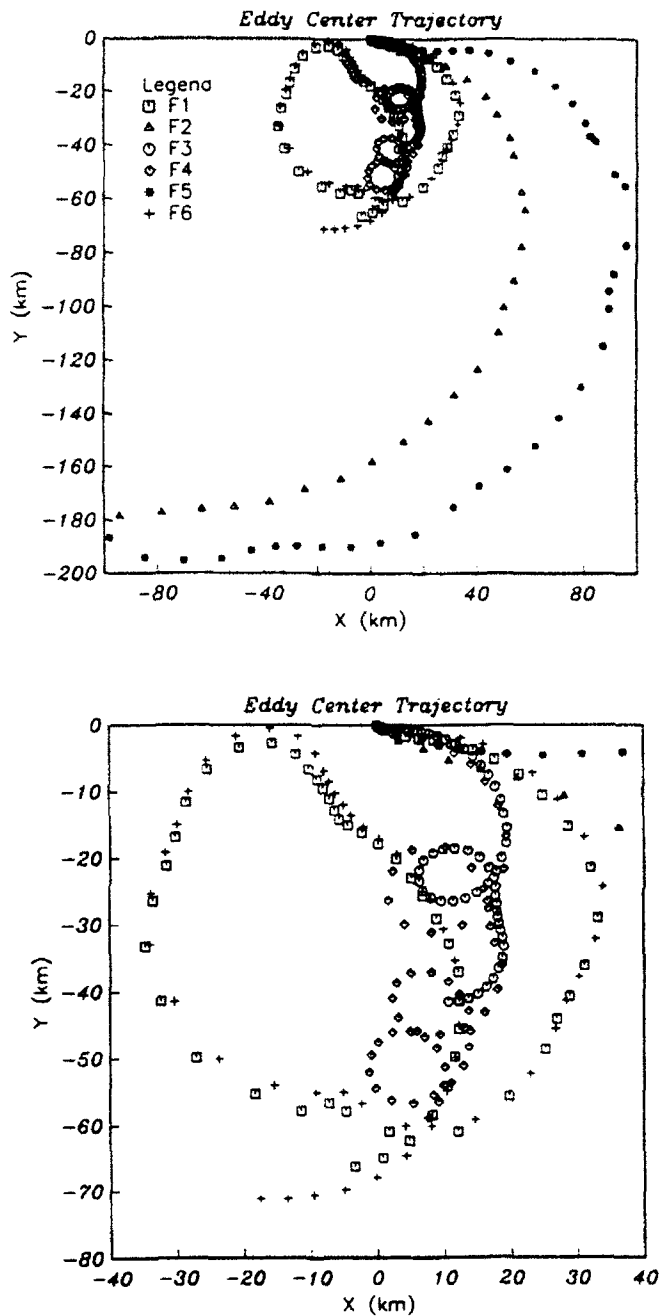**Eddy Center Trajectory** (lower panel)

Figure 3.10: Trajectories of the eddy centers for cases F1 to F6 listed in table 3.1. The marks represent the eddy center locations at the beginning of a day. The lower panel is a blowup of the center portion of the upper panel.

In reality the friction consumes momentum and the multiple interaction is conditional. Of the three cases here, F1 and F2 show multiple interaction and F3 is too weak to have it. One may expect that in the second stage, planetary $\beta$ effect will be effective, which will be investigated in the next section.

### 3.3.3 Dependence on Eddy Strength and Size

The eddy-topography interaction depends on the characteristics of the eddy. The dependence on the eddy strength and size will be the most interesting and relevant topics to this study. In this section, two cases F4 and F5 are examined and compared with case F3. In case F4, everything is the same as that in F3 except that the eddy in F4 has circulation and swirling transport twice as that of F3. The eddy e-folding radius in F5 is one and a half the the radius of the eddy in F3, while the eddy circulation and swirling transport are kept the same. Table 3.4 gives some results of the interaction.

Since the velocity field in case F4 is twice as strong as that of case F3, it seems likely to advect more fluid across the slope. The change is, however, very small. The volume transport in F4 increases only slightly. Due to the strong eddy velocity as well as the strong slope disturbance, the interaction in F4 takes only about half as long time as that in F3. The topographic eddies generated in these two cases have roughly the same size, but the circulation and maximum vorticity in F4 are more than doubled. This means that the cross-slope transport in F4 consists of more upper slope water due to the stronger eddy advective field. This result indicates that the strength of the cyclonic topographic eddy grows proportionally with the strength of the original eddy. The resulting eddy center trajectory is approximately the same as that in F3 but with the eddy in F4 moving twice as fast. It is seen from figure 3.10 that the two eddy trajectories are close before the topographic eddy separates from the slope. Upon the separation, a dipole structure forms and subsequently dominates the eddy propagation. The original eddy in F4 undergoes a larger loop trajectory and tends to move southward faster than

111

## Table 3.4

| Case | F3 | F4 | F5 |
|---|---|---|---|
| Total Volume Transported $(10^{12}m^3)$ | 5.6 | 6.5 | 8.8 |
| Length of Time (day) | 20 | 10 | 15 |
| Rate of Transport $(10^6 m^3/s)$ | 3.2 | 7.5 | 6.8 |
| Cyclonic Eddy Circulation $(10^5 m^2/s)$ | 0.40 | 0.90 | 1.02 |
| Maximum Vorticity $(10^{-4}s^{-1})$ | 0.11 | 0.20 | 0.65 |
| Cyclonic Eddy Radius (km) | 38 | 38 | 50 |

Influence of Eddy Strength and Size

the eddy in F3. This is due to the increase of the dipole strength in case F4, which is roughly doubled from that of F3.

The strongest influence comes from the variation of the size of the eddy. Starting from the same initial position, the eddy velocity field reaches farther onto the topography in F5 than that in F3. It also causes a larger size disturbance since the eddy spreads over a larger area. Potentially this can cause a larger cross-slope transport with more upper-slope fluid involved. Table 3.4 shows this is indeed the case. The volume transport and topographic eddy circulation increase by factors of 1.6 and 2.5 from that of F3, respectively. The maximum vorticity found at the center of the topographic cyclone is

now $0.65 \times 10^{-4}s^{-1}$, representing approximately the slope water from 600 meter depth isobath. As a comparison, the maximum vorticity found in the topographic eddies in cases F3 and F4 are those from 900 and 840 meter isobath, respectively. The interaction time lengths are also different among these three cases. It can be seen from table 3.4 that the strong interactions usually are shorter while the weak ones last longer; the strength of the interaction may be compensated by the change of interaction time, such as that in F3 and F4. Unlike the variation of eddy strength, the effect of wide-spread eddy velocity in F5 is not significantly compensated by the change in interaction time and results in a drastic increase in the total volume transport and the size of the topographic eddy. The rate of volume transport and eddy circulation are more than doubled with respect to F3. The eddy undergoes the largest excursion in a group of six cases (figure 3.10). Since the original eddy can not pull out a pool of slope water with circulation larger than its own, the limiting case of the interaction is a balanced dipole as mentioned before.

### 3.3.4 Dependence on Topography

The topographic effect is examined by comparing results of using topography A, B and C. For topography A and B the depths at the coast and at the deep ocean are roughly the same but the e-folding lengths $b^{-1}$ differ. Topography B has a flatter shelf and a steeper slope than topography A (figure 3.1). The topography A, used in all the previous cases, is always deeper than B at any given location on the shelf/slope. The topography C differs drastically from A and B by having a larger water depth at the coast (400 m). If a fluid column is moved across the slope into the deep ocean from the same starting location, the vortex tube stretching is largest in topography B and smallest in C. Therefore the amount of cyclonic circulation generated is also largest in B and smallest in C. On the other hand, if the same original eddy and initial position are used for these topographies, the amount of cyclonic vorticity generated due to advecting fluid across topography must be the same. Therefore in the case with topography B, i.e., F6 in table 3.1, there will be less fluid from upper slope moving into the deep ocean than that in case F1 with
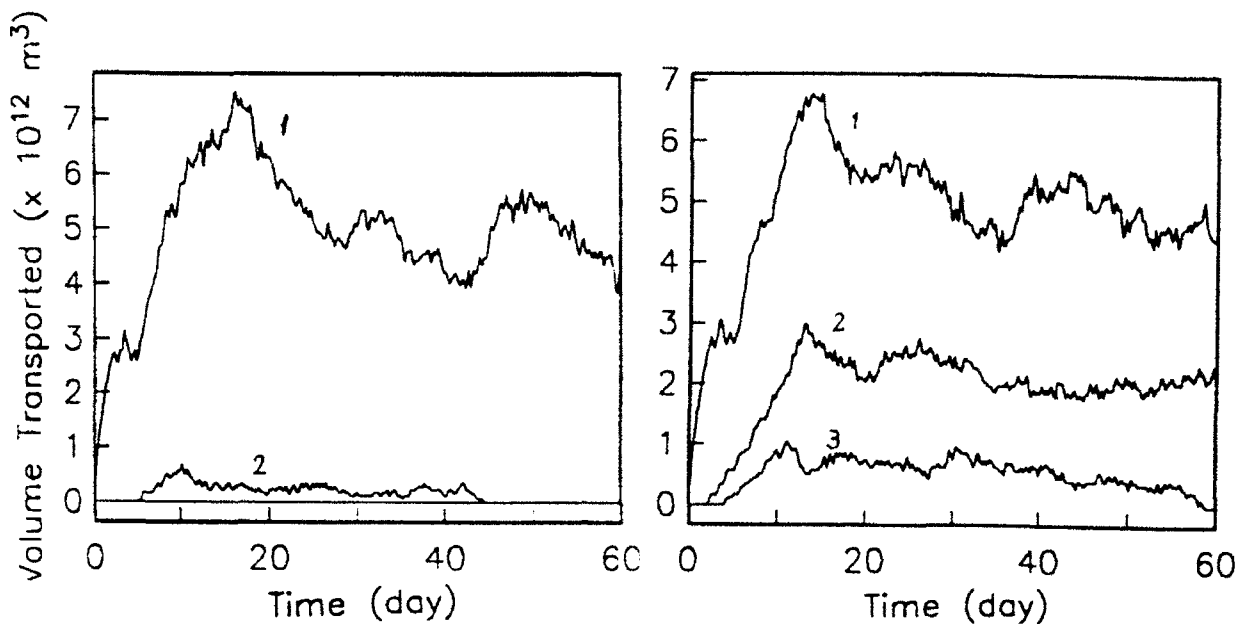
Figure 3.11: The accumulated cross-slope volume transport for cases F6 (left panel) and F7 (right panel). The curves are (1) total volume transported: (2) volume transported from upper slope area 7.5 km away from the slope-deep ocean boundary; (3) volume transported from upper slope area 15 km away from the slope-deep ocean boundary.

topography A, while the case with topography C, i.e., case F7, will have more fluid from upper slope. This is seen through comparing figures 3.7 and 3.11. The total volume transport of F6 and F7 is roughly the same as that of F1, but the transport in case F6 (F7) clearly consists of less (more) upslope fluid than that in case F1. This result differs from the contour dynamics results, where the cross-escarpment transport increases with decreasing topography height due to the step topography. Since the perturbation vorticity generated on the slope by the original eddy is not larger than the effective vorticity of the original eddy itself, the original eddy tends to generate an amount of perturbation cyclonic circulation proportional to its own anticyclonic circulation on the slope, regardless the size of the topography. In case F7 the eddy does not advect a large volume of low vorticity fluid from the edge of the slope due to the eddy size and interaction time limit. Instead it extracts fluid from upper slope area where the depth is shallow and the large vortex stretching provides the circulation. Unlike the sloping topography, the

114

volume transport across the escarpment in the contour dynamics calculation is equivalent to the circulation generated. To generate a given amount of perturbation circulation in the contour dynamics model the mechanism requires that a large volume transport must occur in a small escarpment case, and a small volume transport in a large escarpment case. For the present case of continuous slope, the large difference lies in the volume coming from the upper slope area, as shown in comparison of figures 3.7 and 3.11.

Similar eddy trajectories for case F1 and F6 are expected given only the slight difference in topographic eddy circulation and size and is seen from figure 3.10.

## 3.3.5   The Effect of Bottom Friction on Shelf/Slope Responses

To examine the effect of bottom friction on shelf/slope responses, case F11 is studied in this section. For the present barotropic problem, the bottom friction is treated as a body force acting on the whole water column. The friction is assumed linearly proportional to the velocity component in the same direction, for example, $r_f u$ in the $x$-momentum equation. The friction coefficient $r_f$ is dependent upon the local water depth and vanishes in the deep ocean. Therefore it only dampens the motion over the topography and does not affect the eddies in the deep ocean. $r_f$ is

$$r_f = - \begin{cases} r_D/h, & L - l < y < L \\ 0, & 0 < y < L - l \end{cases}, \tag{3.6}$$

where $r_D = 3 \times 10^{-4} \ m/s$.

Figure 3.12 shows the volume transport of this case and is compared with case F1. It is known that for steady flow the friction is ageostrophic and helps to increase the cross-isobath flow component. But here it weakens the time dependent cross-slope motion forced by the eddy and actually results in a slight decrease in cross-isobath transport. This in turn affects the eddy propagation and causes a small deviation from the eddy trajectory of F1. The major effect of bottom friction is the dampening of the shelf/slope waves caused by the eddy disturbance. Its discussion follows shortly below.
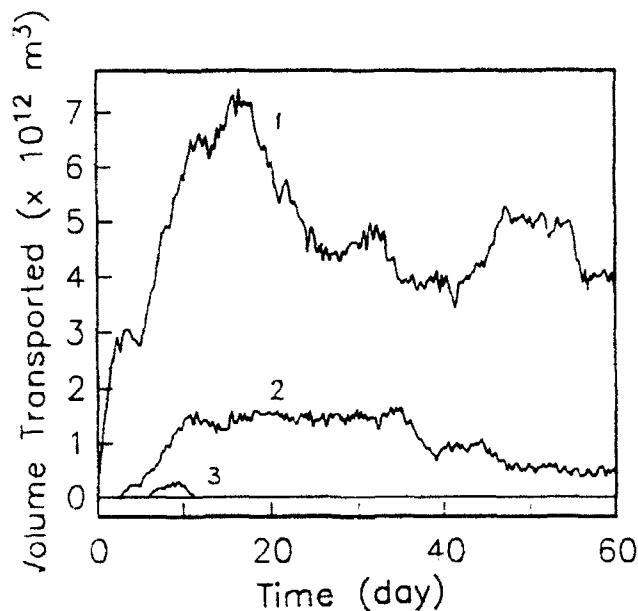
Figure 3.12: The accumulated cross-slope volume transport for case F11. The curves are (1) total volume transported; (2) volume transported from upper slope area 7.5 km away from the slope-deep ocean boundary; (3) volume transported from upper slope area 15 km away from the slope deep ocean boundary.

## 3.3.6 Cyclonic Eddy

It has been known that a cyclone behaves quite differently from an anticyclone when approaching a bottom topography. Contour dynamics calculations have shown that depending upon the strength of the PV front, a cyclonic vortex may either propagate onto or along a step topography. The cyclone-shelf/slope interaction will be investigated in this section.

Parameters of the cases to be examined are listed in table 3.1. The same eddy as in case F1 but with reverse circulation is used here. Figure 3.13 shows the evolution of streamfunction, vorticity and potential vorticity fields for case F9. Initially the cyclone moves towards the slope and perturbs the fluid on the slope. It disturbs the water column shoreward and induces a small anticyclonic structure on the slope. A dipole-like structure forms at the slope edge (day 16 and after in figure 3.13). The anticyclone on the slope will contribute to increase the westward propagation speed of
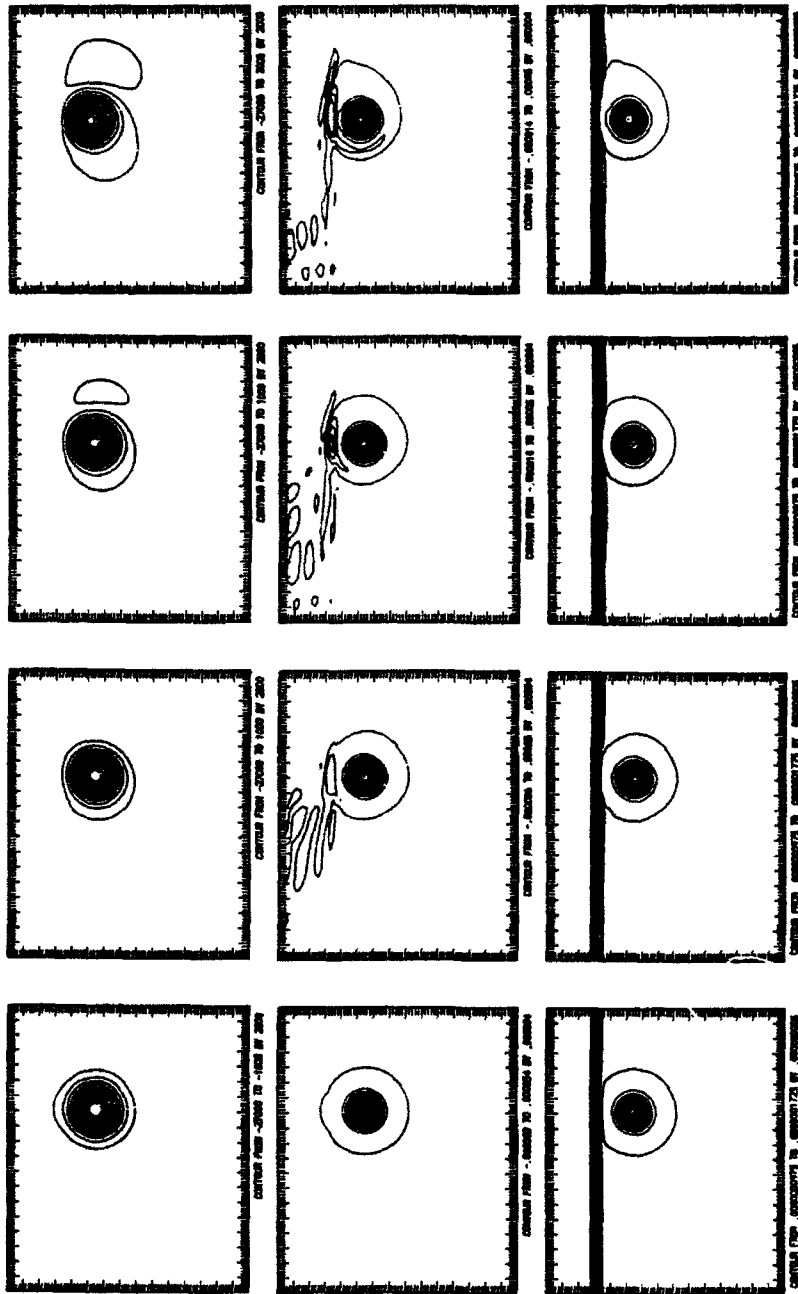
116

Figure 3.13: From top to bottom rows: contours of streamfunction, relative vorticity and potential vorticity. The columns are ordered from left to right, starting from day 0 with time increment of 8 days. Case F9.
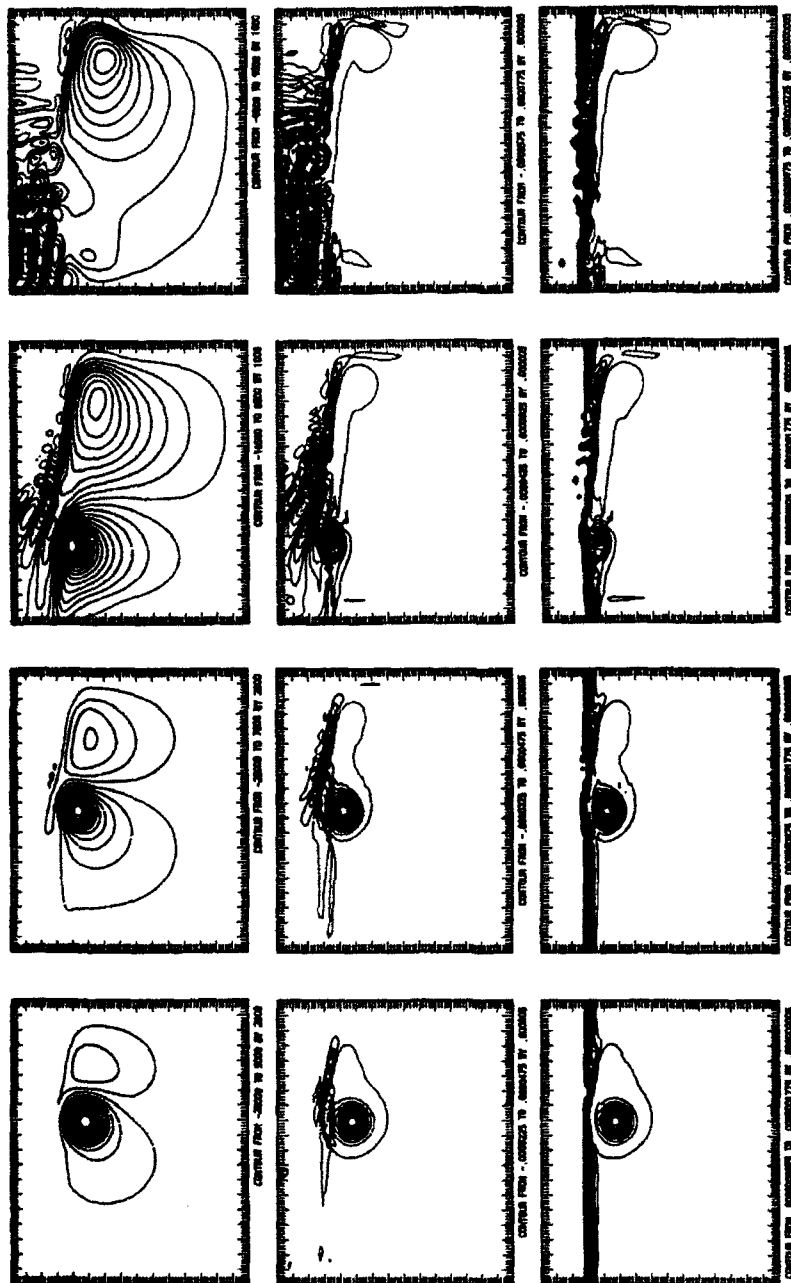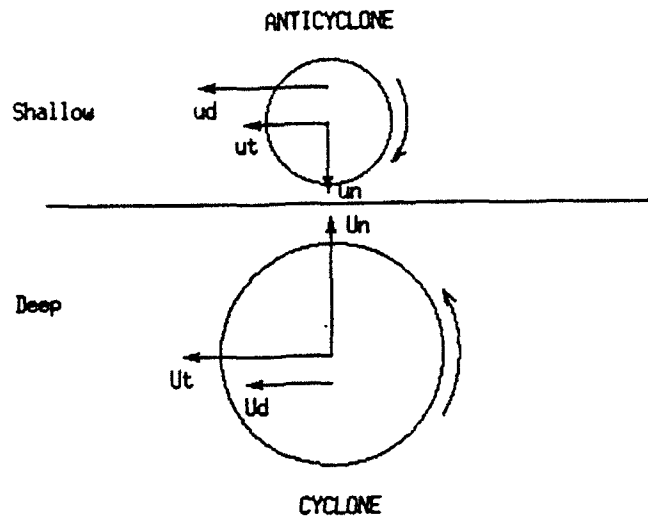
117

Figure 3.13: (continued)

Figure 3.14: Schematic illustration of eddy motion tendency for a dipole-like structure near the edge of a slope. $U_t$, $U_d$ and $U_n$ ($u_t$, $u_d$ and $u_n$) are velocity components of the original eddy (topographic eddy) due to topography $\beta$, dipole advection and nonlinear self-advection, respectively.

the cyclone. Figure 3.14 illustrates the motion tendency for both eddies. It is noted that the anticyclonic disturbance on the slope tends to adhere to the cyclone instead of being advected offshore. Under topographic $\beta$ and nonlinear effects the cyclone moves westward and onshore, and the anticyclone moves westward and offshore. Since the topographic $\beta$-induced velocity is proportional to both eddy strength and bottom slope, the cyclone, which is stronger and on a steeper lower slope, has a tendency to move westward faster than the anticyclone. On the other hand, the anticyclone is advected westward by the cyclone in this dipole-like structure at a rate faster than the motion of the cyclone due to the advection by the anticyclone. These two effects balance each other and the two eddies propagate westward roughly at the same speed. Meanwhile, the cyclone continues moving slopeward under the influence of nonlinear effect, against the slope eddy. There are two effects associated with the onslope anticyclonic disturbance: first, together with sloping bottom, it retards the upslope motion of the cyclone; second, it speeds up the westward propagation of the cyclonic eddy as two eddies get closer. Figure 3.15 shows
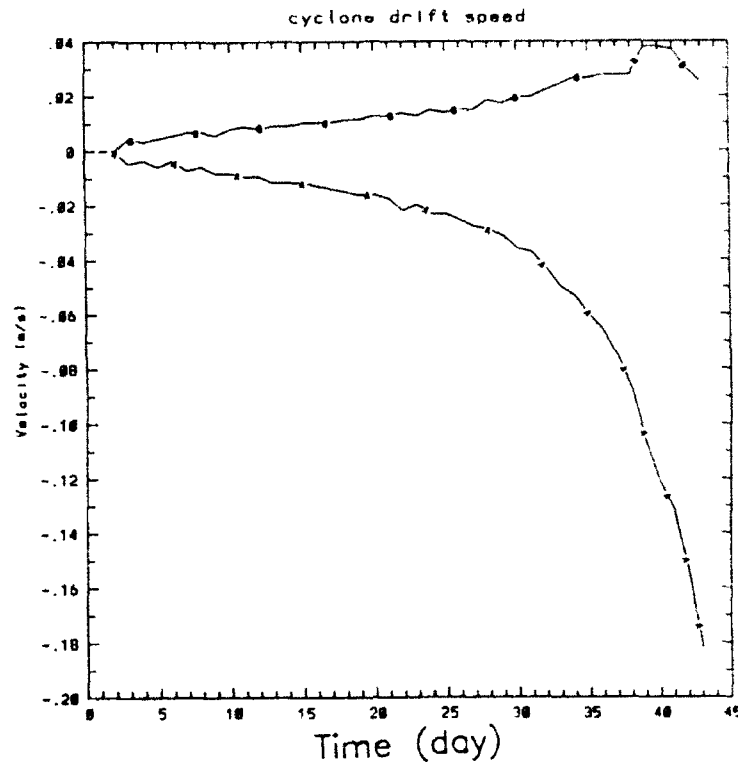
119

Figure 3.15: Propagation speed for the cyclonic eddy in case F9. Curve A is alongshore velocity and curve B is cross shore velocity.

the propagation speed of the cyclone. As the center of the cyclone gets very close to the slope, the westward propagation speed almost increases exponentially to 0.18 m/s, while the slopeward speed increases linearly and slowly, with value about 0.02 ∼ 0.03 m/s. The-cyclone will eventually move onto the slope with considerably weakened strength due to topographic Rossby wave radiation. It effectively causes large disturbances on shelf and slope.

An estimate (figure 3.16) shows that for case F9 between day 0 and day 35 when approaching the topography, both the KE density and the volume of the original eddy stay relatively constant. From day 35 to 45, the eddy area gradually decreases as part of the eddy reaches over the topography, but the eddy KE density is affected only slightly. The small increase in the eddy KE density in this period is due to the loss of part of the eddy volume that is less energetic than the average eddy KE. Between day 45 and 55, the eddy is moving quickly onto the slope and undergoes a drastic decrease in the eddy KE and volume. By day 56 almost the whole cyclonic eddy has moved onslope.
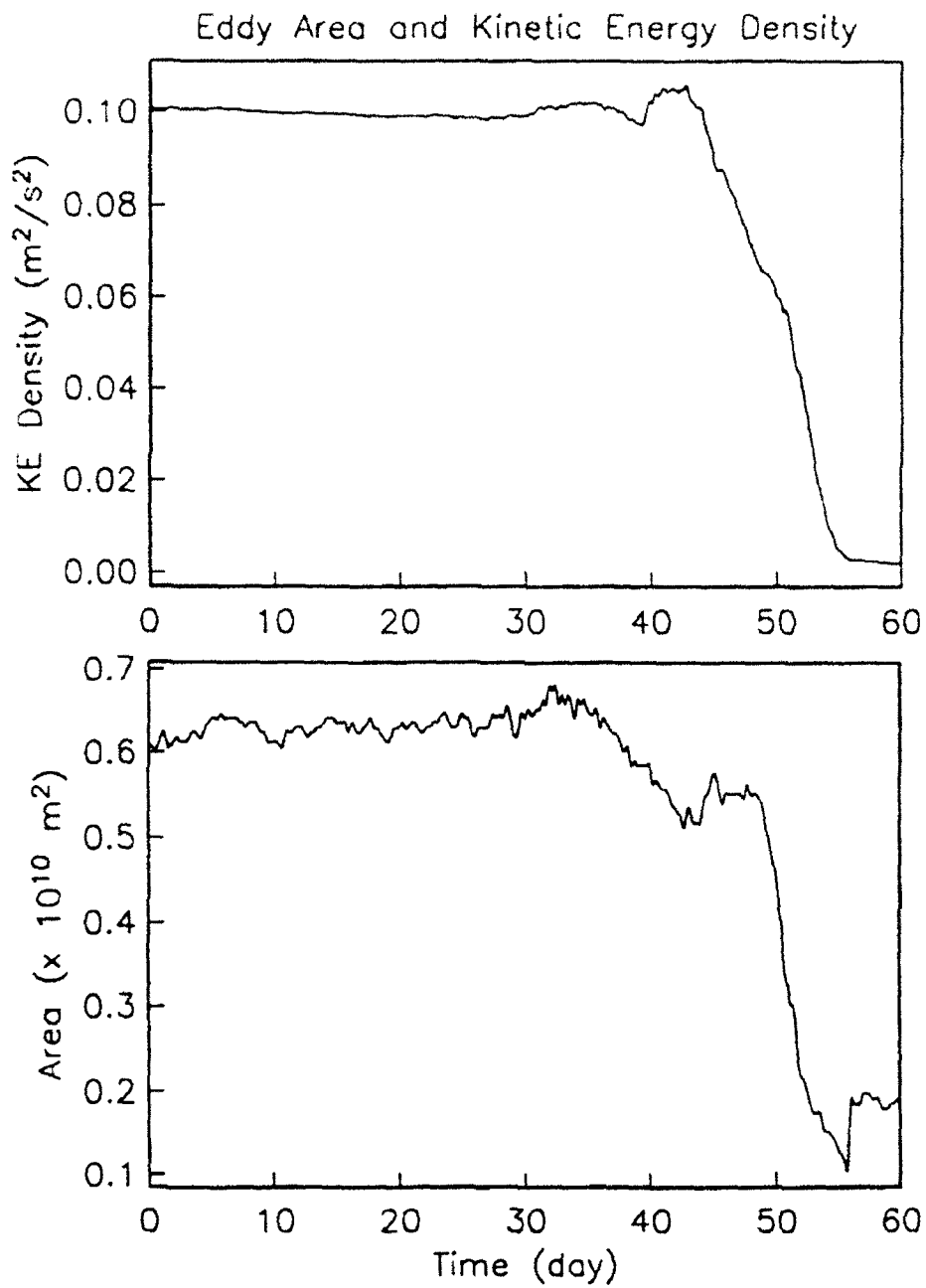
Figure 3.16: The time history of kinetic energy density of the original eddy (upper panel) and area of the original eddy (lower panel). Case F9
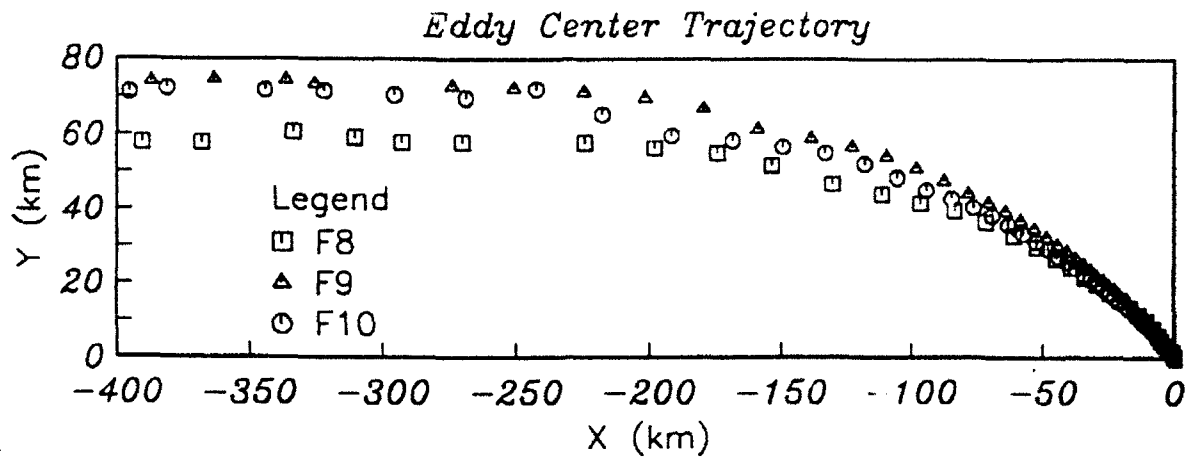
Figure 3.17: Cyclonic eddy center trajectories for cases F8, F9 and F10.

This is accompanied by strong topographic Rossby wave radiation on the slope after day 56 as seen from figure 3.13. Generally on an unbounded slope, the eddy that moves across isobaths will stop at the location (the arrest position) where the eddy rotation is balanced by the vortex stretching or compression. The eddy breaks apart quickly and radiates rapidly propagating Rossby Waves.

. The effect of a steeper topography is seen when comparing results of cases F9 (topography A) and F10 (topography B). For a given eddy the topography B has the arrest position farther downslope than topography A. The effect of this difference is reflected in the eddy center trajectories which are plotted in figure 3.17. The eddy center in case F9 reaches upslope a few kilometers more than that of case F10. As the eddy approaches the slope, the perturbations on the slope and the topographic $\beta$ effect strongly affect the eddy motion. When the eddy oscillates on (off) slope, its westward propagation speed accelerates (decelerates), as seen in figure 3.17.

Comparison between the results of F8 and F9 indicates that the change of initial eddy position does not cause any qualitative changes in the interaction process. The 15

km difference for the eddy positions in figure 3.17 is due to rearranging the eddy initial locations to the origin in the plot.

From continuity, an amount of slope water about the same size as the onslope portion of the original eddy must be displaced offslope. This volume exists mainly in the form of a small seaward displacement of the slope-deep ocean PV front and is not well resolved in the present grid resolution.

### 3.3.7 Generation of Waves on the Shelf/Slope

One of the most important features in the eddy-shelf/slope interaction is the generation of topographic waves. Observational evidence suggests that some of the velocity fluctuations on the continental slope and rise are related to the offshore mesoscale eddy activities (Hogg, 1981). Shoreward propagation of topographic waves was found to be associated with the radiation field of Gulf Stream warm-core rings (Louis et al, 1982; Ramp, 1989). Eddies in continental margins can cause seaward perturbations of the slope PV front, which subsequently propagate along isobaths in the same direction as continental shelf waves (Halliwell and Mooers, 1977). There have been many other observations that relate the offshore mesoscale eddy activities to the shelf/slope processes, but the topic of shelf wave generation by mesoscale eddies remains not well understood. The investigation in this section tries to shed some light on the problem.

Several studies have been proposed to address the shelf/slope responses to offshore eddy forcings. These studies can be roughly divided into two types according to their treatment of the offshore forcings. The first type treats the forcing like an isolated momentum source sitting on a sloping bottom and radiating topographic Rossby waves (Louis and Smith, 1982); or in a baroclinic case, an isolated eddy undergoes internal adjustment process of its density and velocity fields on a sloping bottom and generates topographic waves due to vertical density advection (Shaw and Divakar, 1991). The second type uses a boundary forcing. The forcing is prescribed on a given boundary of

123

the physical domain (usually parallel to the isobath) and is allowed to propagate along the boundary (Malanotte-Rizzoli, 1984; Chapman and Brink, 1987; Qiu, 1990). These studies show that the shelf/slope responses depend on the propagation speed and period of the forcing, stratification and friction.

In this section a different mechanism of topographic wave generation is explored. Based on the observations of Halliwell and Mooers (1979), the large seaward displacements of shelf/slope front caused by Gulf Stream warm-core rings usually move southwestward along isobaths. Their dominant interaction wave length ranges between 100 and 200 km, the period between three and seven weeks, and the propagation speed 2 $\sim$ 11 cm/s. The observations also indicate that the eddies do not force large shoreward perturbations of the slope front at their northwestern edge. Similar frontal perturbations were also observed by a hydrographic survey south of Cape May in the Mid-Atlantic Bight. Morgan and Bishop (1977) found that during the interaction between a Gulf Stream warm-core ring and a slope front, the water in the inner slope was displaced seaward from its mean position as the outer slope water was drawn across the slope into the deep ocean. According to the observations of Kirwan et al (1984), temporary offshore motion can occur after an anticyclone (the Loop Current eddy in their study) encounters the topography.

A question to be asked is how the forced displacement of slope water will behave after the eddy forcing relaxes. Unfortunately there have not been any direct observations on this subsequent shelf/slope adjustment process. However, observations do show some fast propagating frontal disturbances moving along the shelf/slope front (Halliwell and Mooers, 1979). They are possibly frontal trapped waves with unknown origin. A plausible mechanism for the evolution of shelf/slope disturbances after the relaxation of the eddy forcing is that the disturbances break apart and disperse as topographic waves.

Evidence supporting this mechanism is taken from the numerical results of present study. In figure 3.18 potential vorticity contours are plotted at day 4 and day 16 for the
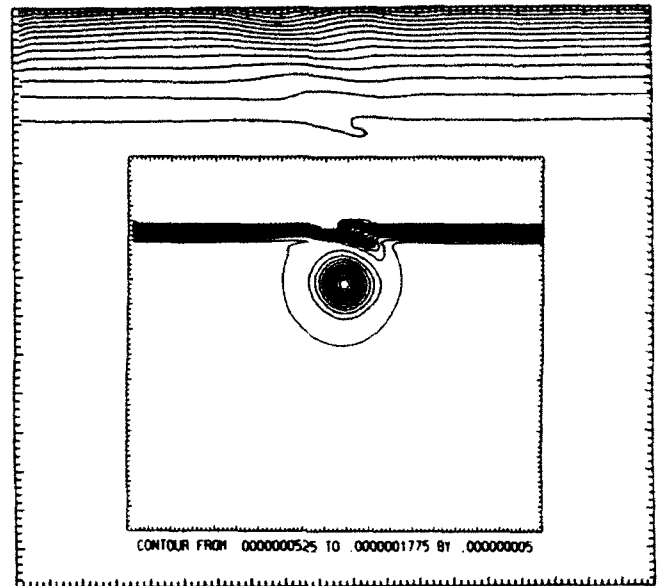
CONTOUR FROM .00000015 TO .00000175 BY .0000001
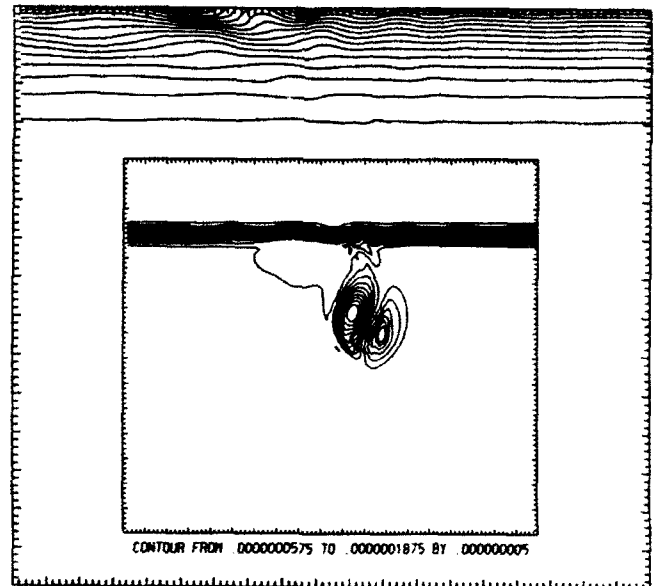


CONTOUR FROM .00000015 TO .00000185 BY .0000001

Figure 3.18: Potential vorticity (PV) contours at day 4 (upper panel) and day 16 (lower panel). The inner and outer plots show the potential vorticity contours at the same time but with different ranges and increments of the values. The outer plots illustrate the perturbation on the shelf and slope, while the inner plots focus on the slope PV front and the eddies.

eddy-topography interaction case F1. At day 4, a seaward disturbance develops northeast of the eddy, but no obvious shoreward displacement is seen on the opposite side. The disturbance is seen reaching the inner shelf. At day 16 the eddy moves offshore and the disturbance relaxes. Since potential vorticity is approximately conserved, the variation of PV contours represents the pattern of the dynamic field, similar to the previous contour dynamics. The contours clearly show patterns of oscillations and propagation. Another plot, figure 3.19a shows the time history of the alongshore velocity component at three cross shelf locations. The wave-like velocity oscillations are obvious and highly correlated at the three locations with a cross-shore phase lag for two adjacent locations of about six days. Shown in figure 3.19b is the alongshore velocity component along the 91 meter isobath contour. The horizontal axis shows along-isobath distance, and individual curves stacked vertically represent the alongshore velocity, plotted every six hours for the first 20 days. The along isobath wave propagation is observed. Even the wave dispersion can be seen in the plot: the fast-traveling long waves outpace the slow traveling short waves toward the left. The cross-shore velocity shows the same type of oscillations but with amplitude less than half of the alongshore velocity. Some questions are asked: Are these motions shelf/slope waves? What is their dispersion relation? What conditions do shelf/slope responses depend on? The answers will be sought as the following study focuses on the responses on the shelf/slope. In next section, the further explanations are sought to support the theory of the shelf wave generation and a momentum balance study will be performed to show that the shelf/slope responses are indeed governed by a set of linear wave equations.

## Free Shelf/Slope Trapped Waves

It is helpful to review first the properties of free shelf waves. Propagation of free waves over an exponential topography has been studied extensively in the past. It is well known that any straight continental shelf of monotonic depth profile supports a complete set of
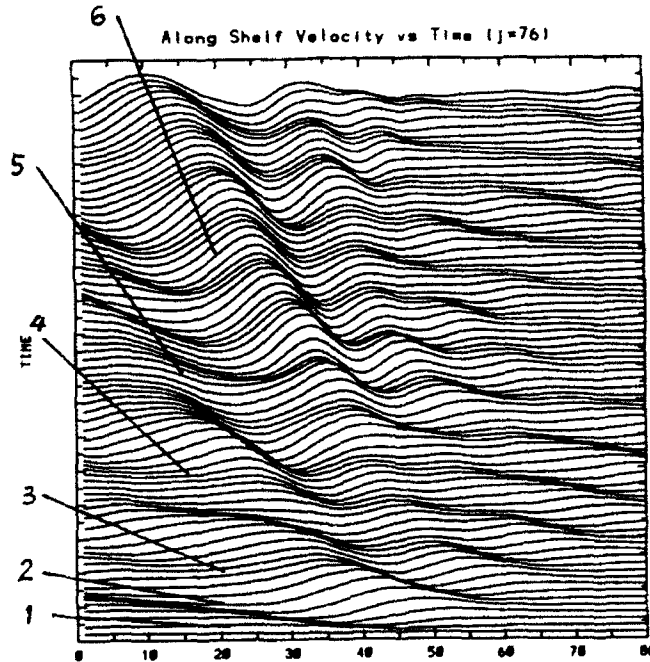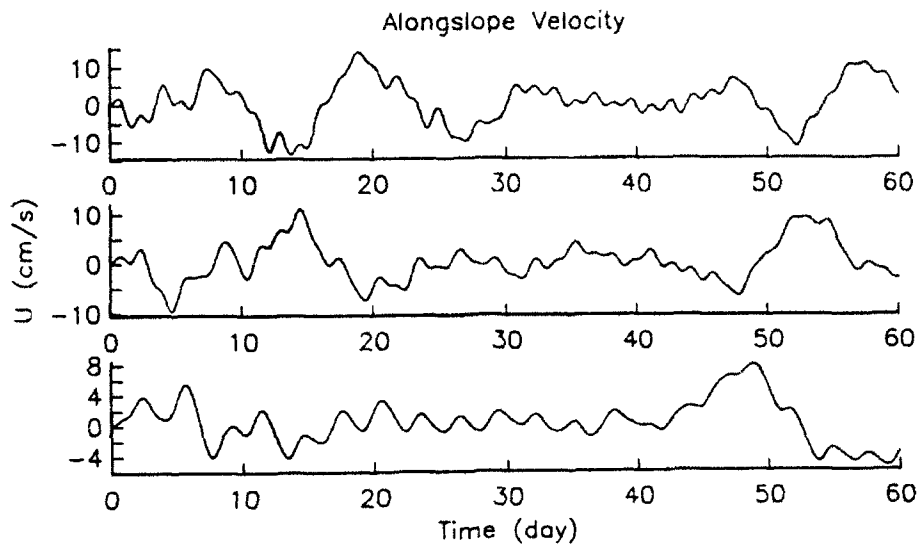
126

Figure 3.19: Upper panel: Alongshore velocity vs time at three cross-shelf locations 150 km away from the western basin boundary. From top to bottom the locations are: 30 km, 67.5 km and 105 km away from the coastal wall; Lower panel: snap shots of alongshore velocity on the 105 meter isobath contour (30 km away from the coastal wall) from day 0 to day 20 with interval of 6 hours. The horizontal axis is the alongshore distance in number of grids (it gives the distance in *km* if multiplied by 7.5 ), and the velocity at a given time is plotted as a curve stacked vertically with increasing time. The theoretical long wave phase speed is shown as straight lines extending out of the plotting frame. The numbers 1 to 6 near each straight line mark free shelf trapped modes 1 to 6, respectively.

127

barotropic trapped modes (Huthnance, 1975). The most relevant to the present study is the problem of a free wave propagating along an exponential slope by Buchwald and Adams (1968). For bottom profiles A and C given in the form of equation (3.2), the dispersion relation is given implicitly by following two equations,

$$m^2 + k^2 + b^2 + 2bfk/\sigma = 0, \tag{3.7a}$$

$$\tan ml = -m/(b+k), \tag{3.7b}$$

where the frequency $\sigma$ is a function of the alongshore wave number $k$, and $b$ and $l$ are defined the same as that in equation (3.2). The parameter $m$ can be eliminated to give a single relation for $\sigma$ and $k$. One important point regarding this dispersion relation is that for short waves ($kl >> 1$) the group velocity of each mode is in the opposite direction to the phase velocity. The group velocity changes sign when passing through an intermediate wave number. At this wave number the group velocity vanishes, and a resonant type of wave behavior may be expected.

## Generation of Shelf Waves

According to Huthnance (1975), the barotropic trapped modes on a monotonic slope with straight isobaths make a complete set. With external forcing applied, this implies that momentum transfer into slope wave modes is possible provided the forcing frequency is not specified (otherwise the shelf response has the same frequency as the forcing which may not be in the range of the shelf trapped waves), such as the forcing by an atmospheric disturbance traveling along the shelf (Gill and Schumann, 1974). In the case of an offshore eddy forcing, the momentum may either be radiated onshore (Louis and Smith, 1982) or transferred onshore through direct eddy-shelf/slope contact. In the present $f$-plane study, when the eddy drifts into the flat bottom region, the topographic wave radiation is suppressed. Therefore the shelf/slope response is due to direct eddy contact with the shelf/slope water. The eddy imparts energy and momentum to the shelf. The subsequent process is the adjustment of the shelf/slope water to this perturbation.

Assume that the velocity at a given shelf location can be expanded into a sum of harmonic waves

$$u(x,y,t) = \sum U_n(y)\cos(k_n x - \sigma_n t + \theta_n), \qquad (3.8)$$

where $U_n(y)$, $k_n$ and $\theta_n$ are, respectively, the amplitude, wave number, frequency and phase of the n-th mode of the wave. In order for it to represent shelf-trapped waves, $k_n$ and $\sigma_n$ must satisfy the shelf wave dispersion relation equation (3.7). Since the relation between $k_n$ and $\sigma_n$ is not known a priori, it is difficult to check $k_n$ and $\sigma_n$ directly against equation (3.7). Careful examination of figure 3.19 reveals that the alongshore velocity is not a wide band signal but rather is a mixture of a few dominant waves with distinct wave numbers and frequencies. For each given $k$ and $\sigma$, the energy density may be computed, which will give the distribution of energy which has been transferred into different wave modes. This can be further compared against the dispersion relation (3.7) to see if the peaks of wave energy lie in the $(k, \sigma)$ range of the shelf wave dispersion. For the observed motion to be linear shelf-trapped waves, its major energy peaks must lie on or close to the shelf wave dispersion curves.

This is done by calculating 2-D wave power spectral density in $(k, \sigma)$ space. The power spectrum for the alongshore velocity record shown in figure 3.19 (case F1 in table 3.1) is calculated and plotted in figure 3.20. This velocity record is observed on the inner shelf away from the eddy and therefore contains a very small direct eddy signal. The frequency and wave number bands for the spectrum are relatively narrow, mainly concentrated in the low frequency and small wave number region. Due to the finite alongshore distance (720 km) the velocity record is taken, the long wave energy may not be properly resolved in this spectral approach. This will be discussed in more detail later in this section. The spectrum is integrated over individual frequency and wave number bands to give the wave energy at a given $(k, \sigma)$ band. This is then divided by the total energy over the entire $(k, \sigma)$ space to yield the percentage power carried by the wave in that $(k, \sigma)$ band. The results are plotted on the theoretical dispersion diagram for free shelf trapped waves. Figure 3.21 shows the alongshore wave energy in $(k, \sigma)$
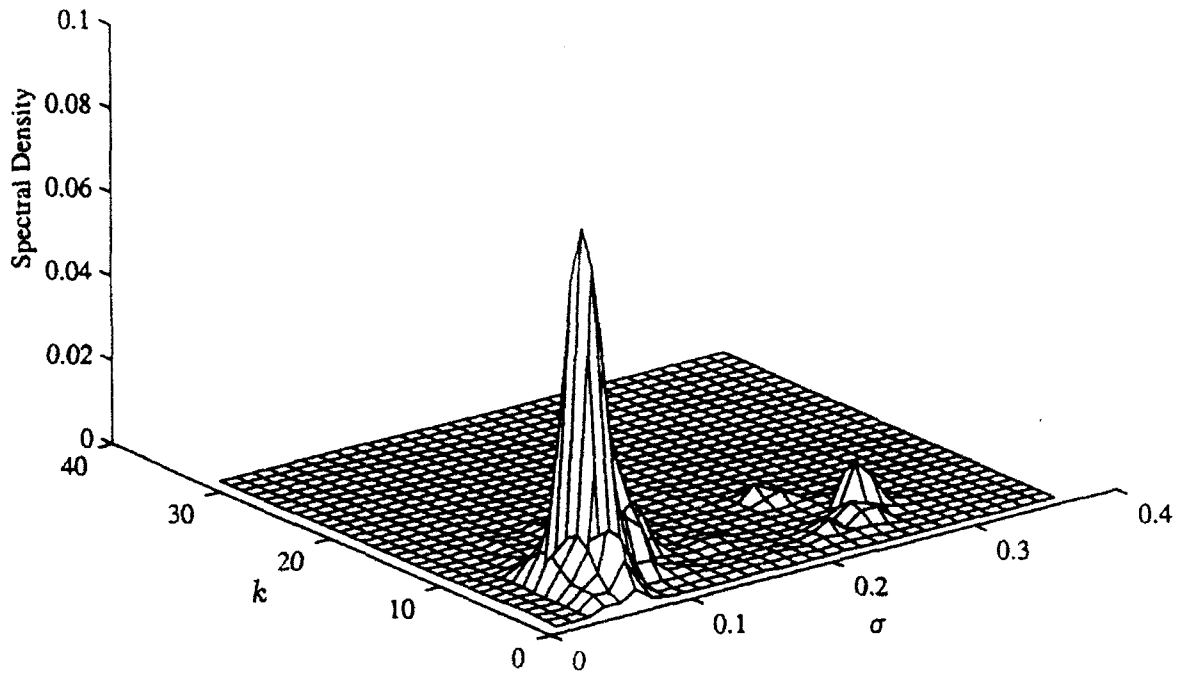
129

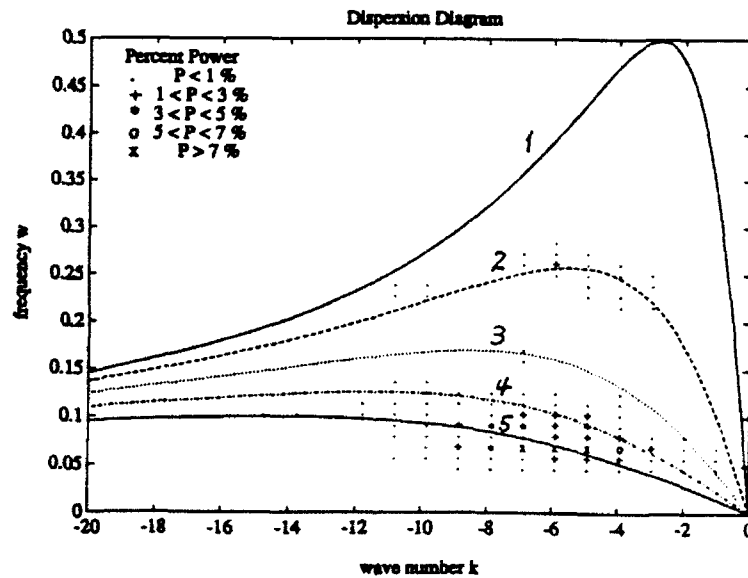Figure 3.20: 2-D power spectrum density of alongshore velocity for case F1.



Figure 3.21: Spectral energy density scatter plot on the shelf trapped wave dispersion diagram for Case F1. The curves are the theoretical solution of the dispersion relation equation (3.7) with $bl = 1.5$ for the first five shelf trapped wave modes excluding the Kelvin wave mode. From upper to lower curves in order, they are modes 1, 2 , 3, 4 and 5, respectively.
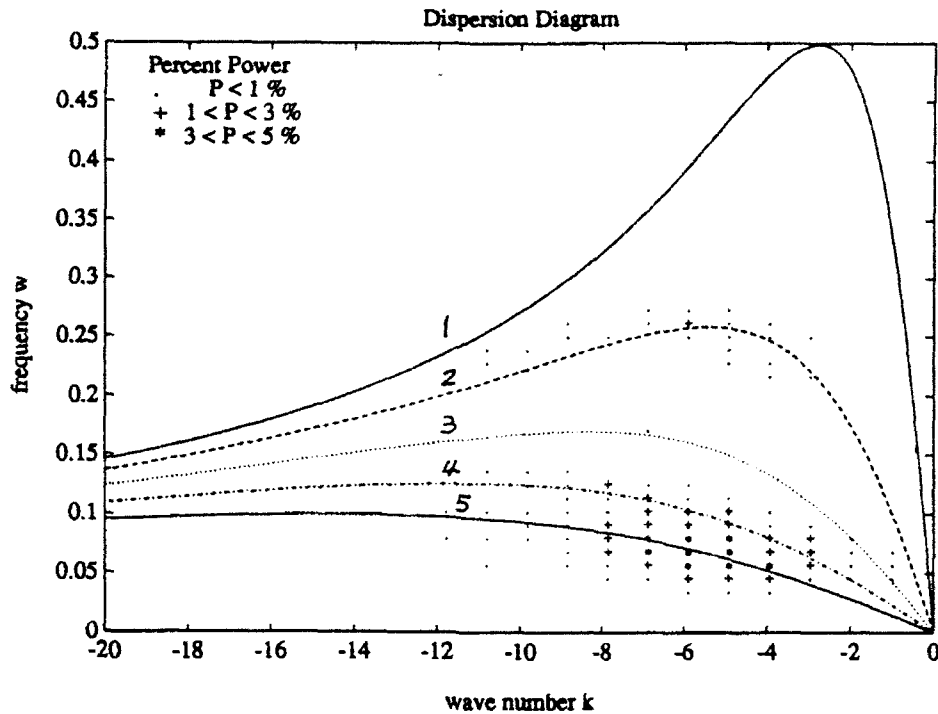
130

Figure 3.22: Spectral energy density scatter plot on the shelf trapped wave dispersion diagram the same as figure 3.21 for Case F3 (large initial distance between the eddy center and the topography).

space plotted on dispersion curves solved from equation (3.7) with $bl = 1.5$ (topography A). Only five free wave modes are shown and the zeroth mode, or Kelvin wave mode is not shown due to the use of a rigid lid. The major part of the wave energy ($\geq$ 80%) lies in a narrow frequency and wave number band ($0.05 \leq \sigma \leq 0.1$ and $3 \leq |k| \leq 9$), corresponding to dimensional values of wave period and wavelength ($7.3 \leq T \leq 14.5$ days and $105 \leq L \leq 314$ km). About 90% of the wave energy is distributed among modes 4, 5 and 6 (not shown), with mode 5 counting more than 50% of the total energy. The group velocities of these waves are in the same direction as the wave phase velocities.

The shelf response of case F3 is shown in figure 3.22. Except for the fact that the initial eddy-slope distance is larger in F3, the other conditions are exactly the same as that of F1. As discussed previously, the interaction of F3 is a weaker one in terms of the perturbation intensity and there is not a second interaction. But the interaction lasts twice as long as that of F1 (see table 3.2). The shelf responses show roughly the same

131

pattern as figure 3.21. The only difference is that the spectral density has a lower power level than case F1. The shelf/slope responses of case F4 are examined in the same way and their pattern of the modal energy distribution in $(k, \sigma)$ space is similar to that of F1 and F3.

A common feature observed in the above cases is the isolated energy peak on mode 2 curve around resonance $(k, \sigma)=(-6, 0.25)$, where the group velocity vanishes. Almost nothing is seen from mode 3. There are two possible explanations for this mode 2 response. The first, it is directly induced by the eddy disturbance through the resonant response of mode 2. The second is that the waves excited on mode 2 have group velocity in both directions. The positive propagating $c_g$ can be seen from figures 3.19b and 3.22, and the waves with negative group velocity reach the western sponge boundary and are partially reflected to give waves with positive $c_g$. The mode 2 responses are waves with fast phase speed and their energy accumulates around the $(k, \sigma)$ band of zero $c_g$. Therefore the waves with positive group velocity contain the artifact due to the boundary condition used. However, this artifact is unlikely to be dominant because the scattered waves are dampened significantly by the sr ＿₃e layers. The mode 2 energy is also very small, about less than 5% of the total wave energy.

To see if a larger size eddy can affect the pattern of the response, case F5 is examined. Figure 3.23 shows that mode 5 is still the most energetic wave mode, but its energy peak is slightly flattened. Corresponding to the weakened peak, more energy spreads over higher modes at a higher frequency band. The increase of mode 2 energy is clearly seen. There is also a tendency for the shelf response to shift toward longer wavelengths. This is directly a result of the larger size eddy in this case.

The topography effect is examined with case F7, which uses topography C with $bl = 0.46$ as given in section 3.2.1. The result, figure 3.24, shows that the most energetic response now moves slightly towards the lower modes. The modes (3 and 4) count for about 70% of the total energy. There is also more energy transfer into the two
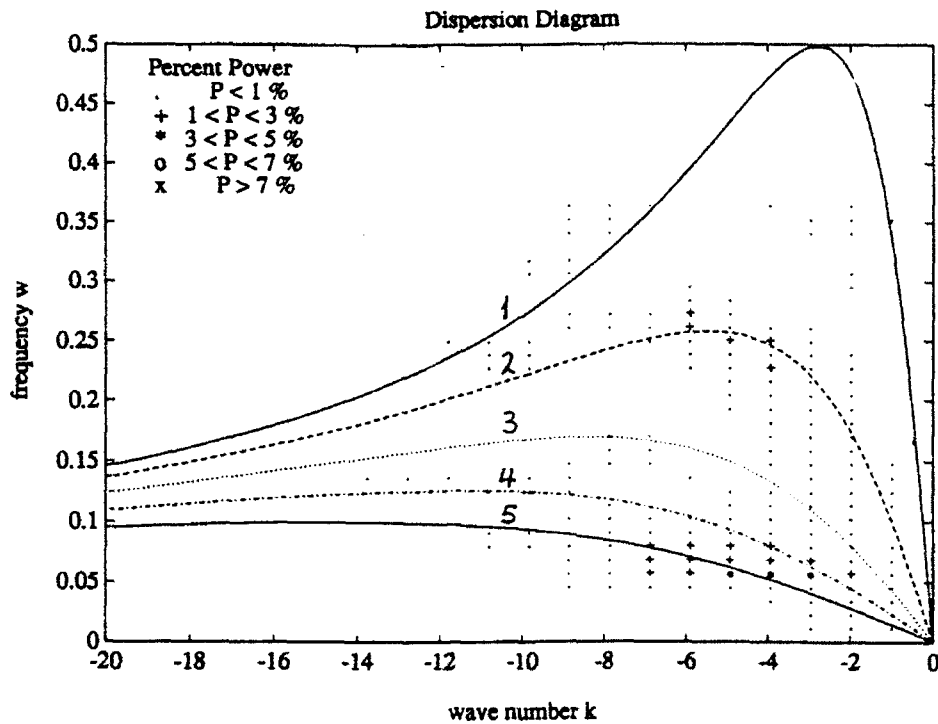
Figure 3.23: Spectral energy density scatter plot on the shelf trapped wave dispersion diagram the same as figure 3.21 for Case F5 (large size eddy).
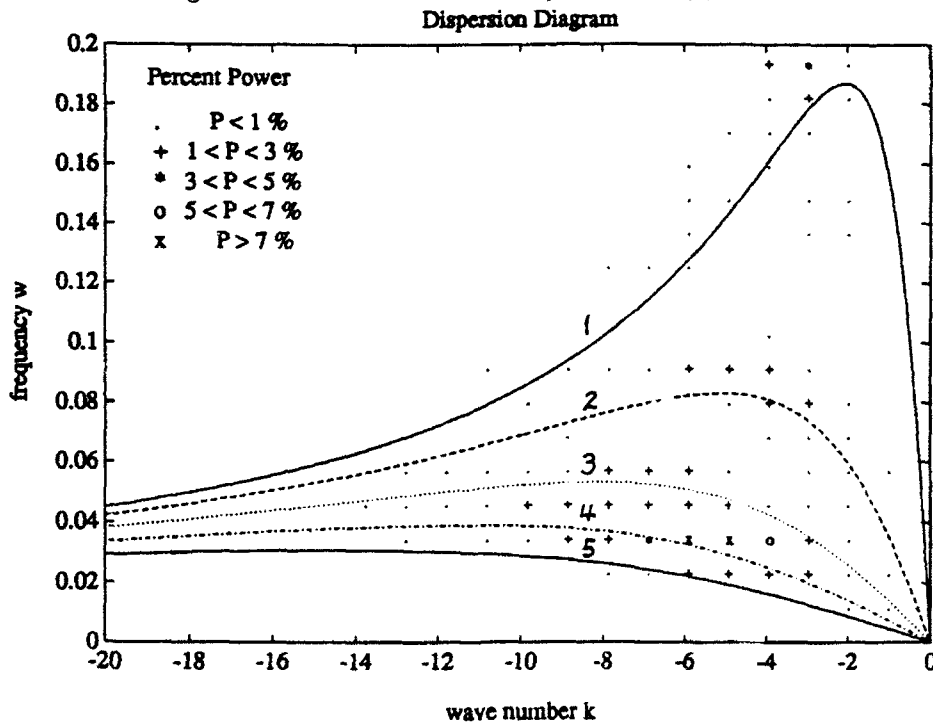


Figure 3.24: Spectral energy density scatter plot on the shelf trapped wave dispersion diagram for Case F7. The modes are 1 to 5 in order from upper to lower curves, respectively. The topography C is used where $bl = 0.46$.

lowest modes around the resonant band (where the group velocity is zero). However, the responses follow closely the dispersion curves of free shelf waves.

As seen from above cases, the lower modes (such as modes 1 and 2) appear to be much weaker than the higher modes in the energy spectra. This, however, does not necessarily mean the lack of lower mode response on the slope. The theoretical long wave speed is calculated for free shelf trapped modes and is plotted in figure 3.19 as a tilted line for each of the first six modes. It is seen that these long wave phase speeds represent fairly well the phase propagation observed in figure 3.19. The existence of the lower modes is obvious from the comparison of the theoretical and observed phase propagation. The reason that they do not show up strongly in the spectral plot is that the long waves (lower modes) propagate much faster than the short waves (higher modes). Most of the long wave energy exits the finite domain and is dissipated in the sponge boundary layer in a short period of time, while the energy of the slow propagating short waves stays in the domain. To demonstrate the existence of an energy source for the generation of long waves, the spectrum of the eddy forcing at the edge of the slope is also calculated in $k$-$\sigma$ space. It is found that 75% of the forcing energy lies within the long wave range of $0 < |k| < 2$, or in dimensional units, $L > 470$ km. This portion of the eddy forcing will excite long waves over the slope, and also transfer energy into higher modes. Even though the long wave is not properly resolved in the energy spectra due to the spatial limit, this does not affect the arguement that the shelf/slope responses are dominated by shelf trapped wave modes.

In all the above cases, the shelf/slope responses carry characteristics matching that of the shelf-trapped waves. To see how the responses vary across the shelf and slope, the alongshore velocity (the time history is shown in figure 3.19a) energy spectra of case FI at three cross-shelf locations west of the eddy disturbance are examined. The energy-frequency diagram is given in figure 3.25. Consistent with the previous results of the 2-D power spectrum, all three curves indicate the energy peaking in a narrow frequency band centered at $\sigma = 0.06$ and very small energy at high frequencies. The response amplitude
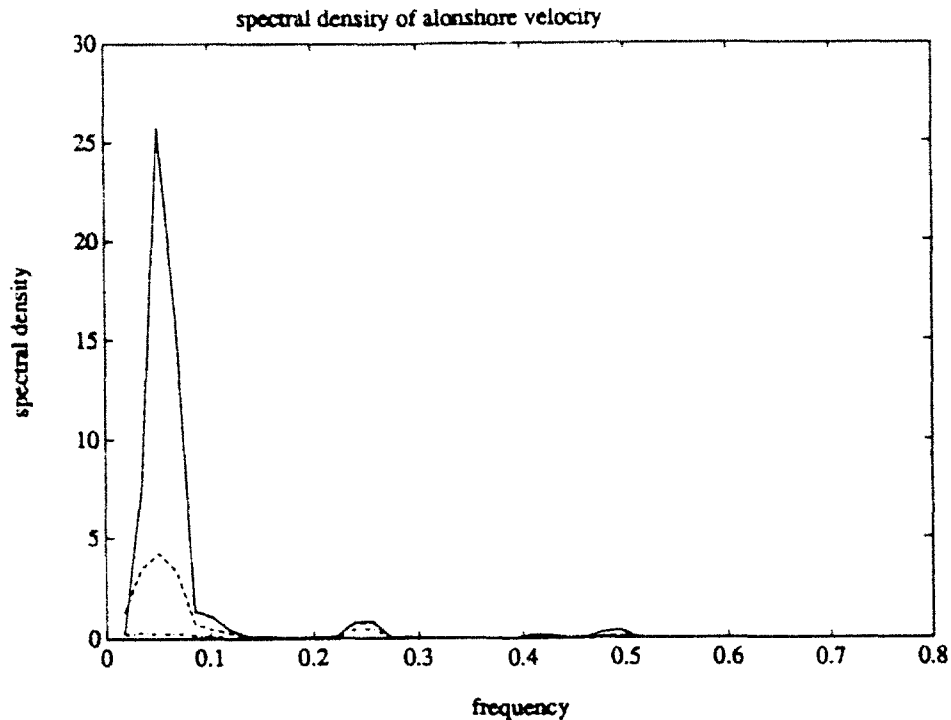
134

spectral density of alongshore velocity

Figure 3.25: Frequency domain alongshore velocity energy spectral density for case F1 at three locations as shown in figure 3.19a.

decreases exponentially seaward, an indication of shelf trapping. The alongshore velocity spectra at locations east of the eddy disturbance are also examined. The most energetic responses are short waves, and some of these waves have group velocity opposite to the direction of the phase speed. They are found to have amplitudes at least one order of magnitude smaller than the disturbance west of the eddy. This also serves as a good indication for small boundary reflection from the downstream sponge boundary layer.

The cross-shelf structure of the waves shown in figure 3.19 is examined using empirical orthogonal modes. Figure 3.26 shows the empirical eigenfunctions of the first three modes for the cross-shelf structure of the alongshore velocity. The velocity is from a cross-shelf section 210 km west of the initial location of the eddy, thus minimizing the direct eddy influence. The first mode accounts for about 51% of the total variance at this section. It displays clearly the exponential seaward amplitude decay and cross-shelf variation. The second and third modes account for 25% and 12% of the variance, respectively. Their cross-shelf variation decays toward outer slope, but with maximum
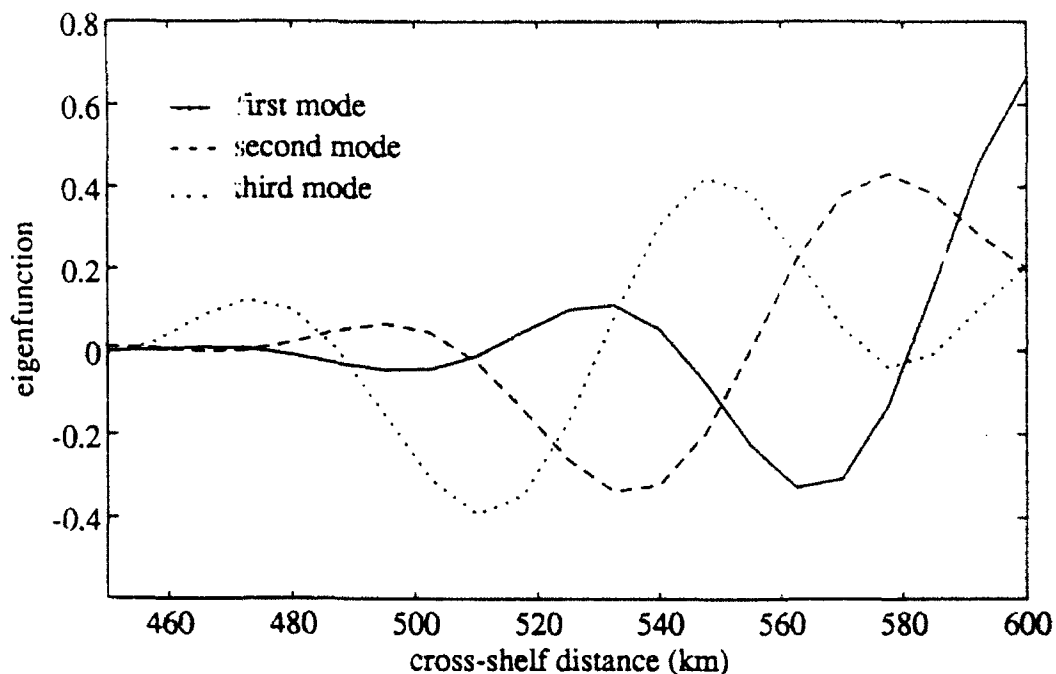
135

Figure 3.26: The eigenfunctions corresponding to the first three empirical eigen modes of alongshore velocity at a cross-shelf section west of the eddy. Case F1.

amplitude in the mid-shelf. These three modes combine to give 88% of the total variance observed at this section. They show the shelf-trapping effect for the responses on the shelf and slope, but by no means they represent the true cross-shelf structure of the theoretical shelf-trapped modes. The cross-shelf structure in equation (3.8) for the topography $A$ given by equation (3.2) has the following form:

$$U_n(y) = A_n e^{-b(L-y+l)} \{ bl \sin \frac{m_n}{l}(L-y) + m_n \cos \frac{m_n}{l}(L-y) \} \qquad (3.9)$$

where $A_n$ is the amplitude and $m$ is the parameter defined by equation (3.7). The first five cross-shelf modes are solved for $k = 6$ and plotted in figure 3.27. It is seen from the figure that all modal amplitudes (normalized) decay exponentially offshore and the third mode has amplitude close to zero at the location $y = 570km$. Since the previous spectral density are calculated using the alongshelf velocity at a location 30 km away from the coast, the weak mode three response in the figures of the spectral density can be attributed to this cross-shelf modal variation. The prominence of mode five can be explained in part by its first peak at this location. The relation between the dynamical
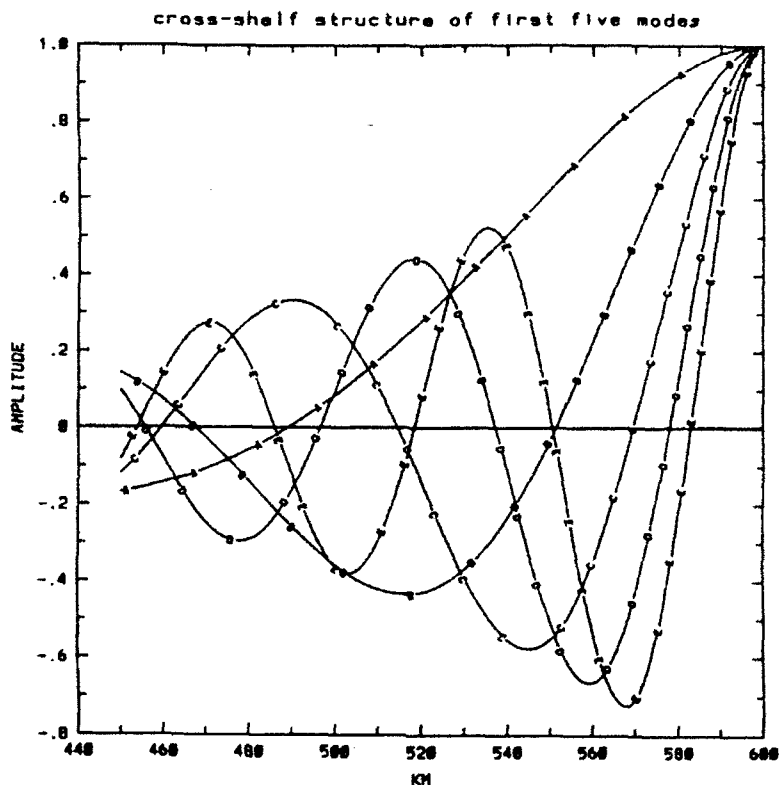
136

Figure 3.27: The normalized cross-shelf structure of the first five dynamic modes calculated from equations (3.7) and (3.9) for wave number $k = 6$. Letters $A$ to $E$ represent modes 1 to 5, respectively. The $x$-axis is in unit $km$.

modes and the empirical modes can also be seen by comparing figures 3.26 and 3.27. The large coastal amplitude seen in the first empirical mode corresponds to the positive amplitude for all five dynamical modes and the first negative peak near $y = 565km$ matches the large negative amplitude of three higher dynamical modes, while the lower modes propagate out of the domain and contributed less. The seaward decay of the first empirical mode is reflected by the cancellation of the positive and negative values of the dynamical modes. The high-order remnant from the combination of the dynamical modes is likely shown in the higher empirical modes, such as the mid-shelf amplitude peaks seen in the second and third empirical modes. It should be pointed out that the direct influence on the empirical modes from the original eddy is very small due to the large distance between the eddy and the location where the velocity record is taken.

The frictional effect on the shelf response is investigated with case F11. The energy-dispersion diagram shows the response has the same modal energy structure as

137

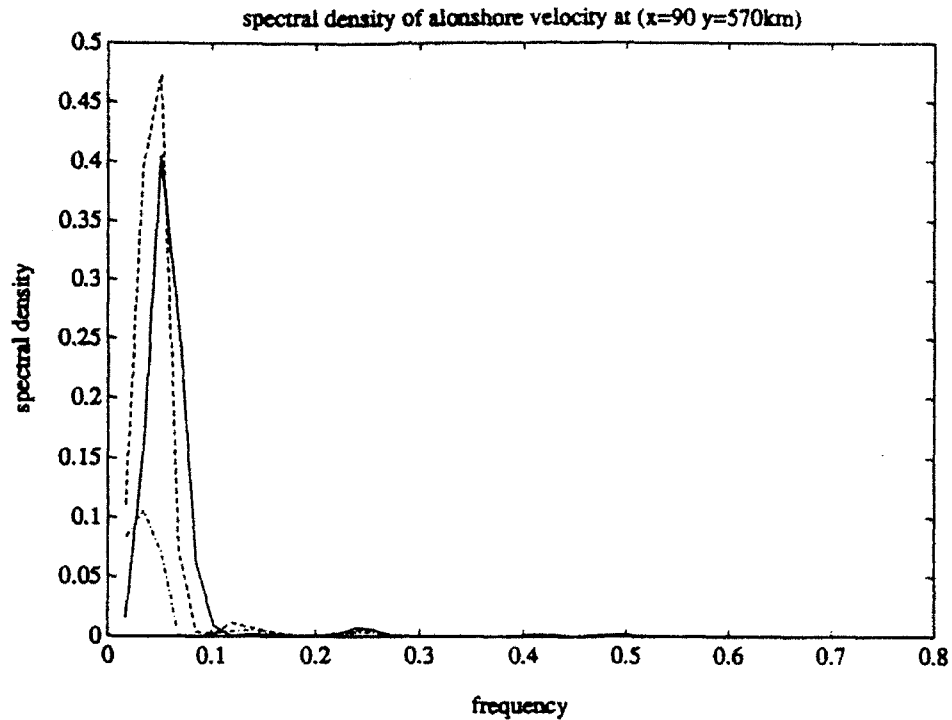spectral density of alongshore velocity at (x=90 y=570km)

Figure 3.28: Frequency domain spectral energy density for case F11 at three cross-slope locations the same as in figure 3.25. The solid, dashed and dot-dashed curves are in order from inner-shelf to outer-slope.

that of case F1 shown in figure 3.21, but the amplitude is significantly weaker. Figure 3.28 is a plot of energy spectra for case F11 similar to figure 3.25. The friction dampens the inner shelf response by a factor of 50 and causes the peak response to shift seaward.

In summary, the topographic waves are generated through eddy-shelf/slope interaction process. They are induced by the eddy forced shelf/slope disturbance. They propagate along isobaths with shallow water on the right and exhibit dispersion relations close to those of the free shelf-trapped waves. The peak response is centered in a narrow wave number and frequency band depending upon both the eddy structure and the topography. The excitation of shelf wave modes by eddy disturbance depends largely on the geometry of the shelf/slope profile and on the size of the eddy, and weakly on the eddy initial location and eddy strength.

## 3.4 Eddy-Shelf/Slope Interaction on a $\beta$-Plane

On the $\beta$-plane, an axially symmetric eddy will propagate westward and disperse rapidly as dispersive planetary Rossby waves (McWilliams and Flierl, 1979). As the longer wavelength Rossby wave components of the eddy propagate faster, the gradients on the leading western side are weakened and that on the trailing eastern side are steepened. This asymmetry results in an eddy self-advection tendency which is in the same direction as the flow on the strong gradient side. The resulting eddy propagation is southwestward (northwestward) for an anticyclone (cyclone) with a rate depending upon the size and strength of the eddy. The inclusion of the planetary $\beta$ will also increase the eddy decay rate over the purely frictional decay as seen in section 3.2.3. One of the important changes from previous $f$-plane study is that now the eddy may be initialized away from the topography and subsequently propagate toward it. This is considered more realistic than the previous field initialization. There are other changes associated with this. The Rossby wave dispersion and frictional decay will weaken the strength of the eddy before it reaches the slope. The fast propagating Rossby waves will arrive at the slope before the eddy and perturb the slope water. There will be other important changes due to the inclusion of planetary $\beta$, but no fundamental changes of shelf/slope responses are expected. This is because, as mentioned earlier, the topography control is dominant and the dynamic properties on shelf/slope are not altered at the lowest order by including $\beta$-effect. The resulting changes in the eddy propagation and strength may affect the duration of the interaction, and the subsequent processes of multiple interactions. These potentially important changes associated with $\beta$-effect no doubt deserve thorougl investigation.

The propagation tendency of an isolated eddy on a $\beta$-plane must be considered when the field is initialized. Since an anticyclone (cyclone) goes southwestward (northwestward) on a planetary $\beta$-plane, if initialized in a flat bottom ocean, an anticyclone will never reach a topography along the northern boundary. Therefore a western boundary or southern boundary topography will be used with water depth shallowing in the same
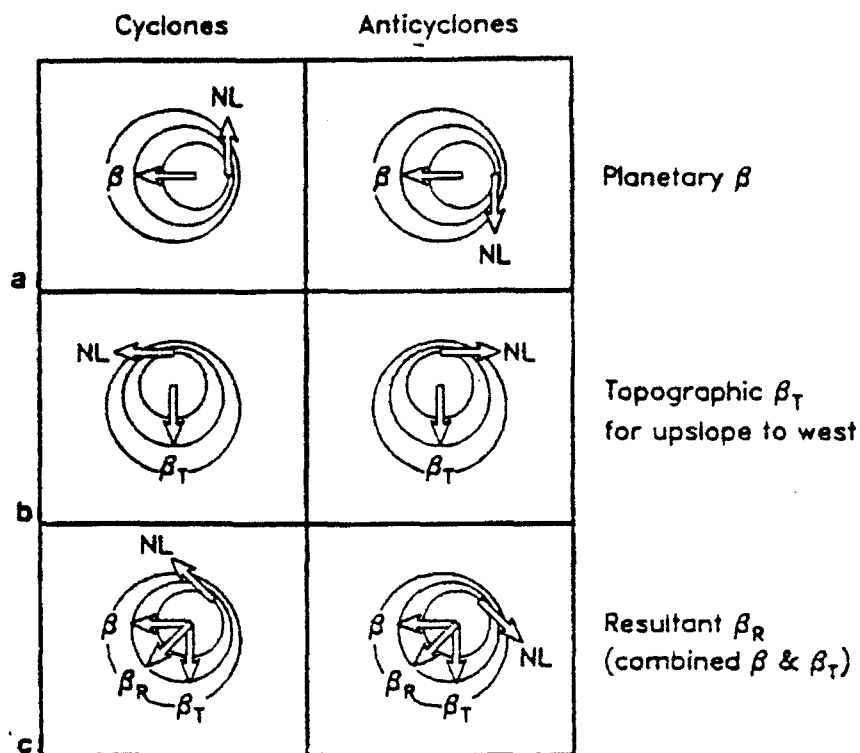
|  | Cyclones | Anticyclones |  |
|---|---|---|---|

Figure 3.29: Schematic propagation tendency diagram for cyclone and anticyclone: (a) planetary $\beta$-plane without topography; (b) $f$-plane with sloping bottom; (c) planetary $\beta$-plane with sloping bottom. The topography slopes up westward. After Smith and O'Brien (1983).

direction. This also makes the dynamics more interesting due to the existence of an angle between the planetary and the topographic $\beta$. By varying this angle we may study the effect of an eddy impinging on the slope from different directions. For a cyclone either a western boundary or northern boundary topography may be used.

Interesting combinations of the eddy propagation tendencies were discussed by Smith and O'Brien (1983). Their figure 3 is reproduced here in figure 3.29. The topography is upslope to west. The configuration of topographic $\beta$ and planetary $\beta$ produces the following results: the nonlinear advective tendency associated with the dispersive steepening on the wake side of the eddy acts meridionally in the planetary $\beta$-plane and zonally for prescribed topographic slope. The fact that nonlinear propagation has a zonal as well as a meridional component indicates that the topographic slope can significantly

alter the nonlinear propagation, especially when the nonlinear propagation is as large as the planetary $\beta$ and the topographic $\beta$ components.

In present study, the eddy is initialized in the deep flat-bottom ocean and subsequently propagates toward a west-bound topography. Upon reaching the topography, the simple scaling in the previous section shows that the topographic control is dominant over planetary $\beta$, and the anticyclone (cyclone) is expelled away from (trapped at) the topography. In the case of an anticyclone, the eddy will move on and off the topography under the influence of planetary and topographic $\beta$-effects. According to the propagation tendency shown in figure 3.29, the eddy will also move along slope. The eddy propagation is also influenced by the slope frontal disturbance and generation of topographic eddy. In addition, the eddy decay and volume change may also affect its propagation.

In this section the problem of eddy-topography interaction on a $\beta$-plane will be investigated. In the light of previous $f$-plane discussion, the emphases are on the differences between $f$ and $\beta$-plane interactions, especially the eddy propagation. In addition to the parameter range studied before, the effect of different incident angles as an eddy impinges on a slope will also be examined. In fact the study below will be divided into two groups according to the incident angle: oblique incidence and straight collision of a deep ocean eddy onto a topographic slope. Table 3.5 lists all the cases and parameters for the numerical experiments to be examined in this section.

## 3.4.1 An Anticyclone Impinging on a Slope at an Oblique Angle

The oblique incidence of an anticyclone onto a straight line slope is shown schematically in figure 3.30. This is an analog to many observed eddy-slope topography interactions. For example, in the North American continental slope and rise area, Gulf Stream warm-core rings often propagate southwestward near the edge of the slope and interact with shelf/slope waters (Smith, 1983; Churchill et al, 1986). In figure 3.30, the isobaths

141

## Table 3.5

| Cases | Eddy Rotation | Eddy Radius (km) | Initial Distance (km) | Topography | Comments |
|-------|---------------|------------------|-----------------------|------------|----------|
| B1  | −1 | 50 | 150 | A | Oblique Incident |
| B2  | −2 | 50 | 150 | A | Double Strength |
| B3  | −1 | 75 | 150 | A | Large Eddy |
| B4  | −1 | 50 | 100 | A | Small Distance |
| B5  | −1 | 50 | 150 | A | Bottom Friction |
| B6  | −1 | 50 | 150 | C | Topography C |
| B7  | −1 | 50 | 150 | A | Right Incident |
| B8  | −1 | 50 | 100 | A | Right Incident |
| B9  | −1 | 50 | 150 | C | Right Incident |
| B10 | 1  | 50 | 150 | A | Oblique Cyclone |
| B11 | 1  | 50 | 150 | A | Right Cyclone |

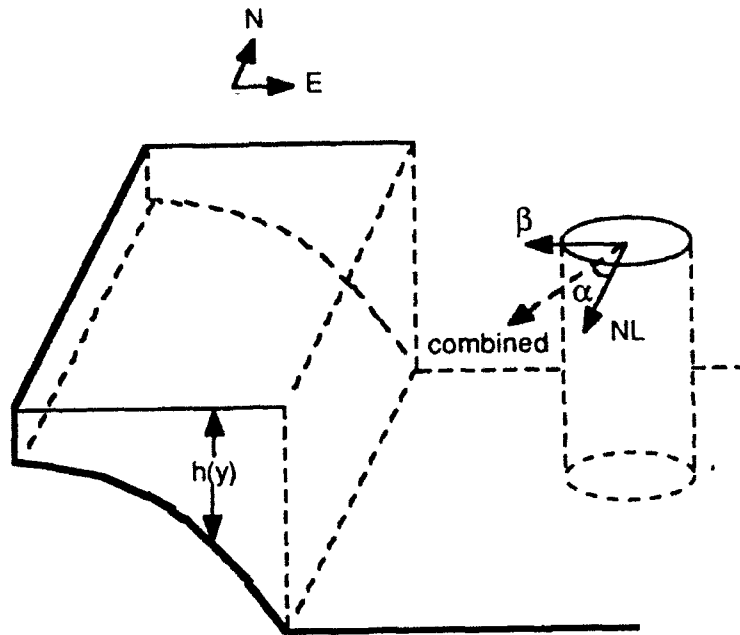$\beta$-Plane Eddy-Topography Interaction Experiments.

Figure 3.30: Schematic plot of anticyclonic eddy-slope interaction with an oblique incident angle. The isobath is north-south and the slope shallows monotonically to west. The arrows marked with $\beta$ and $NL$ represent the velocity components due to the planetary $\beta$ and nonlinear self-advection, respectively. Their combination gives the vector in between and has an angle $\alpha$ to the vector $NL$.

run strictly north-south, and the oblique incident angle $\alpha$ is the same angle defined by $\tan^{-1}(v_\beta/v_N)$, where $v_\beta$ and $v_N$ are the components of eddy propagation speed due to planetary $\beta$ and nonlinear self-advection, respectively. If $Q = V/\beta r_0^2$ is the ratio between nonlinearity and planetary $\beta$, $\alpha$ will increase as $Q$ decreases (McWilliams and Flierl, 1979). For linear case, $Q \sim 0$, the eddy will collide onto the slope at $\alpha = \pi/2$. In general, $Q$ is nonzero and large, and $0 < \alpha < \pi/2$.

Case B1 from table 3.5 will be examined first. It has the same topography and eddy as the case F1 in the previous $f$-plane study. The eddy center is initially 150 km away from the slope. For $\beta = 1.6 \times 10^{-11}$ and the parameter $Q = 12$, the nonlinearity is fairly dominant in this case. The results of flow field evolution are plotted in figure 3.31 for streamfunction, relative vorticity and potential vorticity contours. To minimize the change in the model formulation, the coordinates in the numerical model are arranged such that north is toward the right in figure 3.31. The topography shallows to the west.
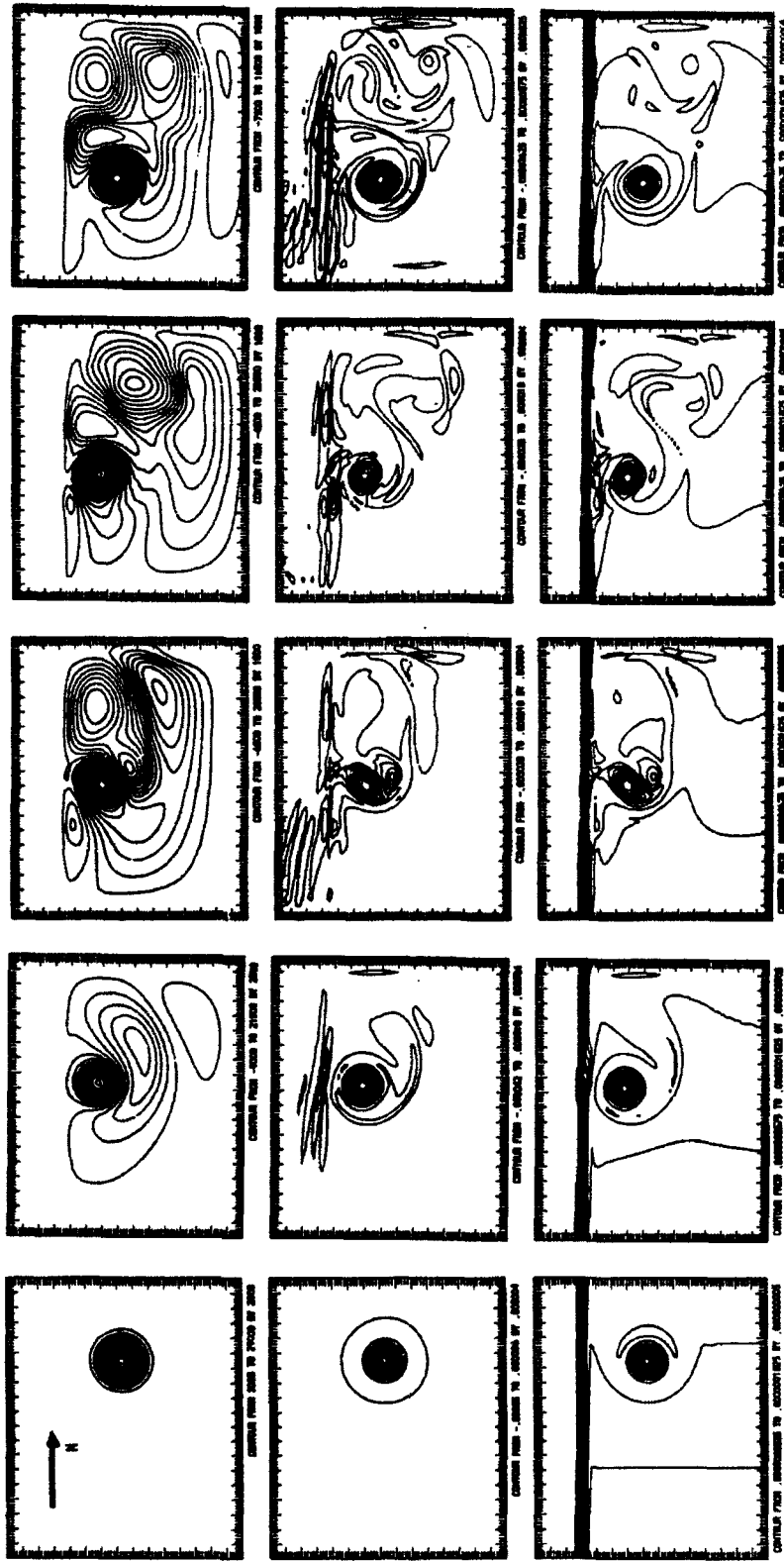
143

Figure 3.31: From top to bottom rows: contours of streamfunction, relative vorticity and potential vorticity. The columns from left to right are at days 0, 32, 56, 80 and 104. Case B1.

The no-flux condition is applied at the eastern and western walls. The sponge layer boundaries are now at the northern and southern ends of the domain and cross the topography. In figure 3.31 the eddy propagates westward due to the planetary $\beta$-effect. The subsequent Rossby wave dispersion flattens the gradient in the leading western side of the eddy and steepens the gradient in the trailing eastern side. The asymmetry is responsible for a southward nonlinear eddy self-advection. For this case, the rate of nonlinear propagation is almost twice that due to the $\beta$-effect only, resulting in an incident angle about $26°$. The familiar Rossby wave wake behind the moving eddy appears to the northeast. The eddy initially accelerates (figure 3.32a and b) and reaches the maximum speed $(-5.5, 2.8)$ $cm/s$ around day 25 before it starts to feel the influence of the topography. After that it decelerates. The development of a cyclonic slope disturbance together with the topographic $\beta$-effect causes a quick reversal of the eddy propagation to the east around day 45. Meanwhile a cyclonic topographic eddy separates from the slope and subsequently forms a dipole-like eddy pair with the original eddy and dominates its propagation. After the separation of the cyclone, the shape of the anticyclone is considerably distorted, and the long and thin streamers are formed at two longer ends of the eddy (figure 3.31 at day 56). About 20% of the eddy volume is lost through these streamers. This process of volume loss is similar to the f-plane situation discussed in the previous section.

The second interaction happens around day 70. The dipole breaks apart since the cyclone is trapped by the topography and moves away southward. In the second interaction only a small amount of the slope water (less than one third of that in the first interaction) is advected across the topography. However, due to the loss of cyclonic vorticity from the slope front by the eddy advection, a weak along-slope anticyclonic anomaly develops on the edge of the slope and propagates slowly along isobath toward left (figure 3.31 at day 104). Time history of this onslope anticyclonic anomaly shows that it is dispersive and propagates along-isobath to the south (the left in figure 3.31) under the effect of topographic $\beta$. After the second interaction, there is no intensive cyclone
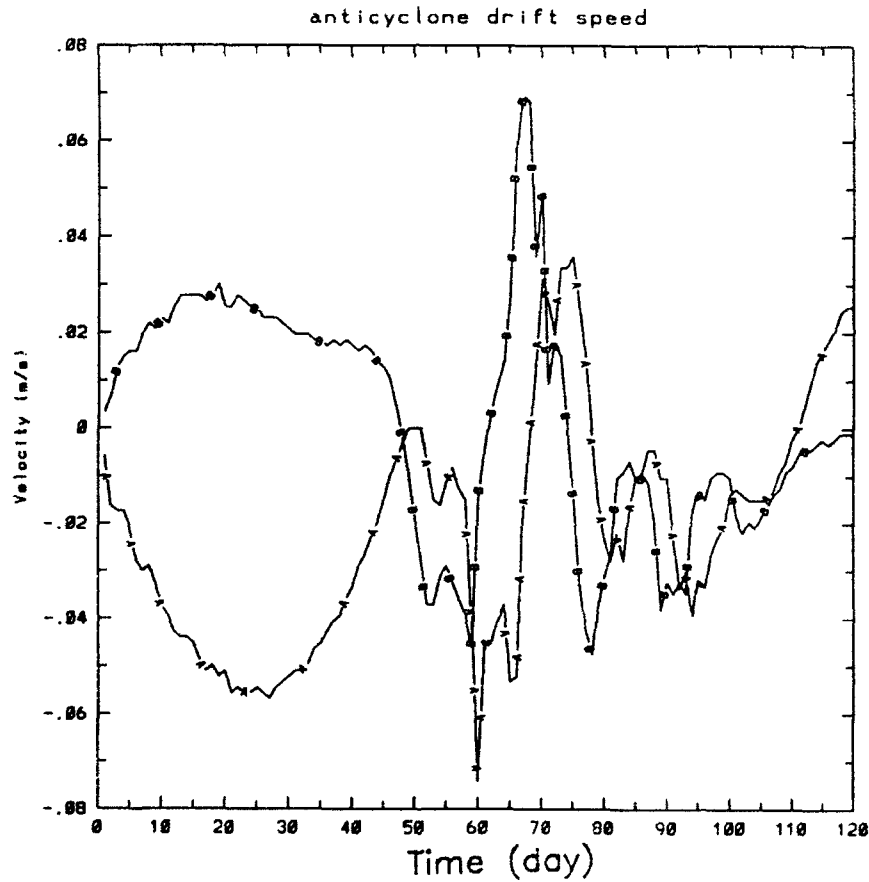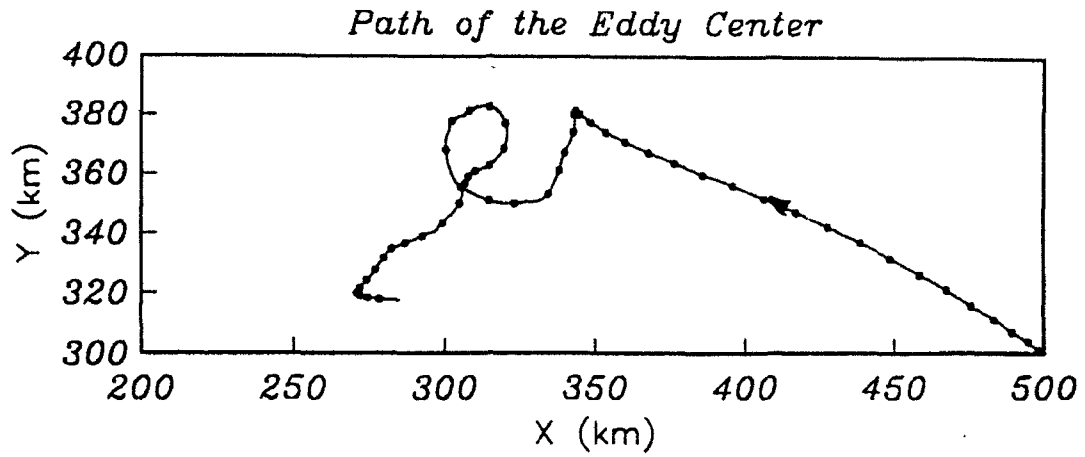
Figure 3.32: Eddy center trajectory (upper panel) and velocity components (lower panel) for case B1. In the upper panel, the dot marks represent the eddy positions at the beginning of every two days. In the lower panel, the curves $A$ and $B$ are the along- and across-shore velocity components, respectively.
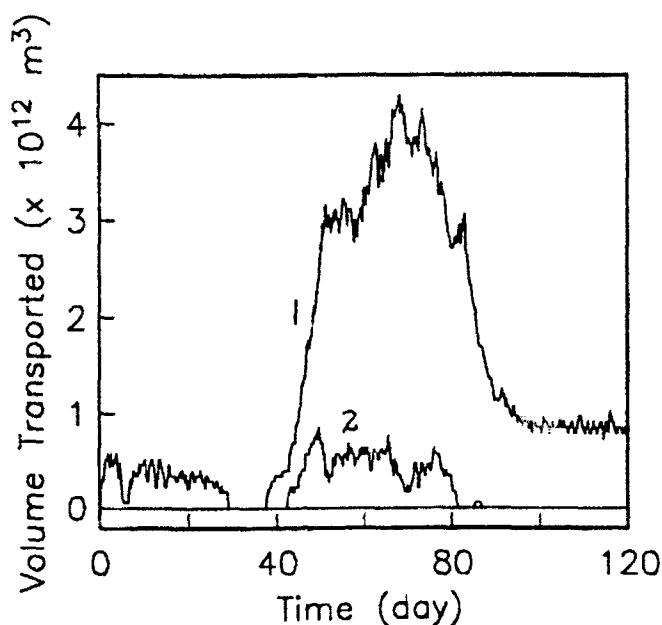
146

Figure 3.33: The accumulated cross-slope volume transport for case B1. The curves are (1) total volume transported; (2) volume transported from upper slope area 7.5 km away from the slope-deep ocean boundary.

formed on the periphery of the original eddy. The eddy motion is again controlled by the planetary $\beta$ and eddy self-advection. Surprisingly in figure 3.32a the eddy now moves southeastward against the planetary $\beta$-effect. The reason for this is the dominance of the nonlinearity in the eddy propagation. Comparing the streamfunction contours at day 32 with that at days 80 and 104 in figure 3.31, the long axis of the elliptically shaped anticyclone, due to the planetary wave dispersion, has rotated clockwise approximately $1.5\pi$, from the northwest orientation to the southwest orientation. The nonlinear self-advection that favors the steep gradient side of the eddy will overcome the planetary $\beta$-effect and cause the eddy to propagate southeastward. The planetary $\beta$ will eventually slow down the propagation and reverse it to the southwest direction.

Figure 3.33 gives the total cross-slope transported volume. It is seen that the first interaction produces about $3.5 \times 10^{12}$ $m^3$ transport at a rate of 2.9 $Sv$ (1 $Sv$ = $10^6$ $m^3/s$). The majority of the volume is from the vicinity of the slope edge. In the second interaction the first topographic eddy is released to the slope and accumulated volume transport actually decreases. By day 90 only about $10^{12}$ $m^3$ slope water is observed

to be transported into the deep ocean. This result indicates that multiple eddy-slope interactions may not contribute to increase the cross-slope volume transport, and in fact it may reduce the accumulated transport by transporting the water back onto the slope. The multiple interactions may cause quick decay of the original eddy strength, and thus result in weakened subsequent interactions. The strength of the interaction, indicated by the cross-topography volume transport, is dependent upon several factors. Among them are the eddy strength and size, the topography and the eddy incident angle. The average KE density and the area of the original eddy are shown in figure 3.34. It can be seen that on the way to the topography both the KE density and the area of the eddy decay at roughly constant rates, due to the Rossby wave radiation and internal friction. When the first interaction takes place, the eddy KE has dropped to 3/4 of the initial value in about 50 day period. Within the next ten days of the interaction, both the KE and the area undergo drastic decrease, corresponding to the volume loss discussed above. After this event, the KE and the area stay almost constant for the rest of the time. Other than the strong decay associated with the eddy-topography interaction, the planetary Rossby wave dispersion is the major source of eddy decay. The relatively small KE decay during the final 40 days in figure 3.34 indicates the planetary wave dispersion is suppressed during the period the eddy is propagating against the $\beta$-induced tendency.

In case B4, the eddy is 50 km closer to the topography than that in case B1. As expected a stronger interaction process follows. The first interaction starts around day 14 and the total volume transport increases to $5 \times 10^{12}$ $m^3$ during an interaction period about 10 days (figure 3.35). The volume transport also consists of more upslope fluid. Two interactions, having roughly equal strength, take place in case B4. The decrease of eddy strength during the two interactions combines to a total 50% loss in the original eddy circulation. After the second interaction, there is a strong dissipation process in the wake of the moving dipole structure, resulting sharp strength decrease in both the original and the topographic eddies. This process is shown in figure 3.36 using relative vorticity field at day 56, 64 and 72. As the original eddy tries to advect across-slope a
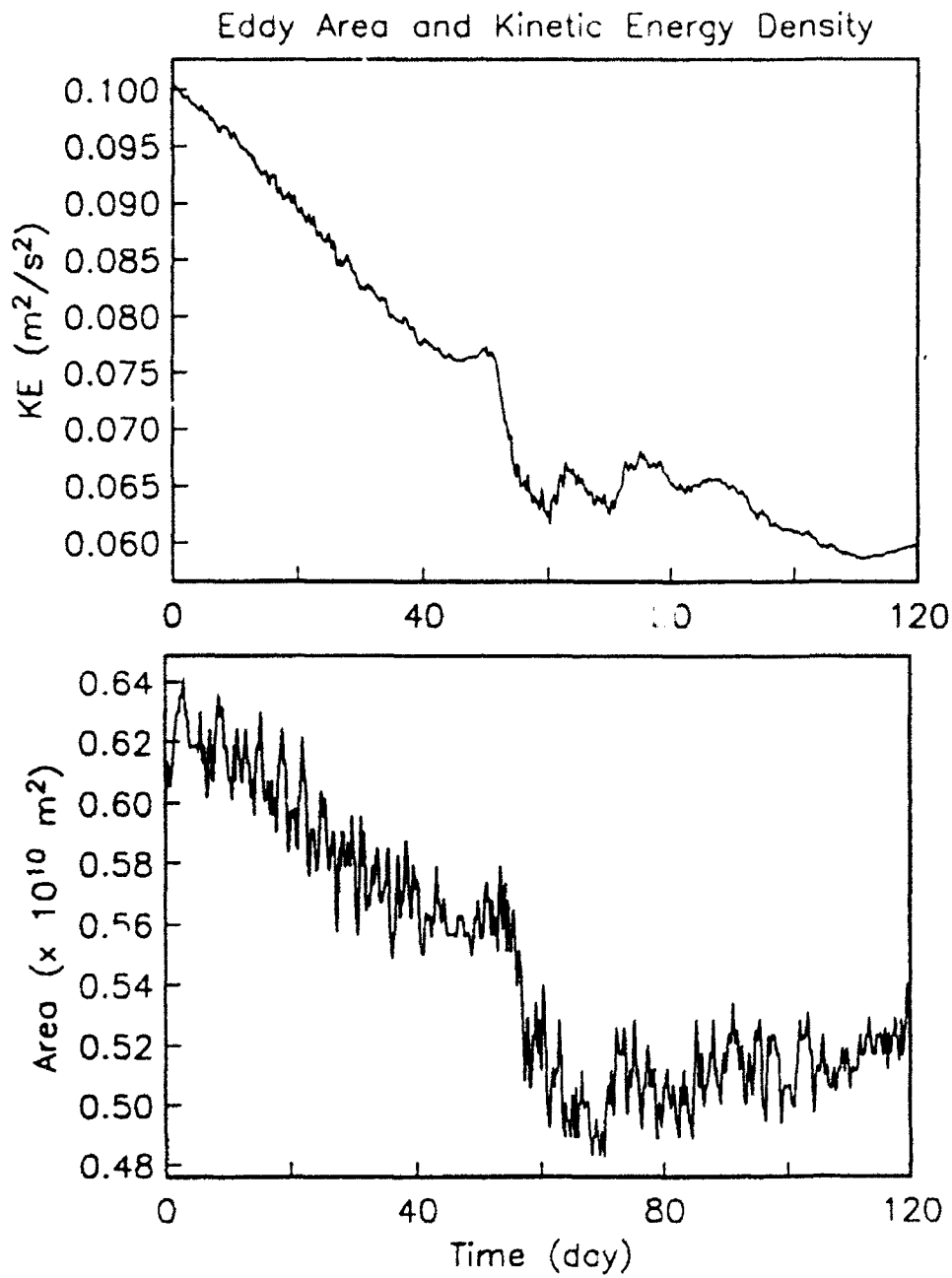
148

Figure 3.34: The time history of the average KE density (upper panel) and the area of the original eddy (lower panel, the eddy volume is the area multiplied by a constant depth) for case B1.

149

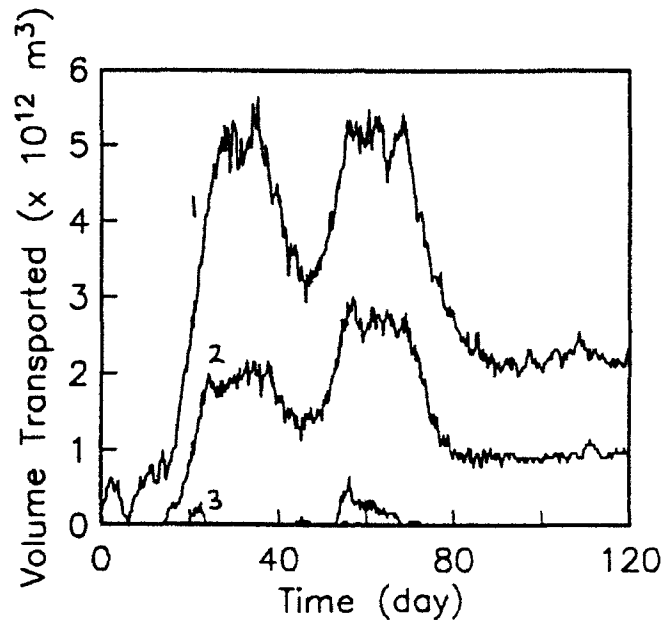Figure 3.35: The accumulated cross-slope volume transport for case B4. The curves are (1) total volume transported; (2) volume transported from upper slope area 7.5 km away from the slope-deep ocean boundary; (3) volume transported from upper slope area 15 km away from the slope-deep ocean boundary.
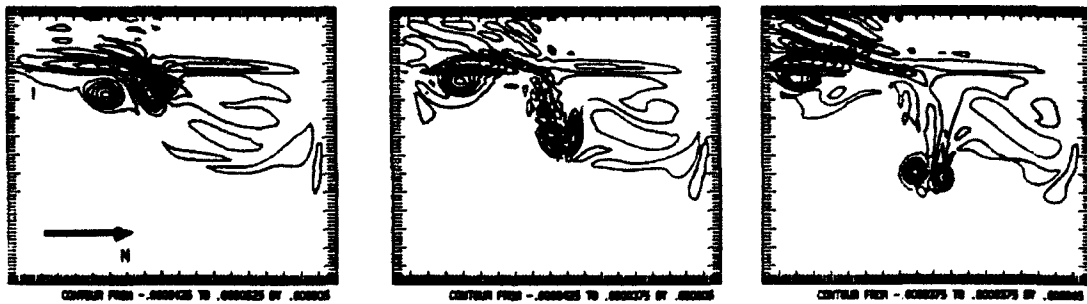


Figure 3.36: From left to right, the relative vorticity field at day 56, day 64 and day 72 for case B4.

150

pool of cyclonic slope water, it also releases the first cyclonic topographic eddy and sheds a portion of its own volume onto the slope (day 56). Forming a dipole-like structure, both the original eddy and the topographic eddy separate from the slope and leave behind a wake of mixture of water from both the original eddy and the slope (day 64). Strong dissipation takes place in the wake. By day 72, a well defined $\beta$-plane dipole has formed and propagates eastward. The final result is, therefore, very different from the one discussed previously. This is largely attributed to the difference in the eddy strength and the slight change of the eddy incident angle at the time of interaction. The original eddy in case B4 impinges on the topography at a larger incident angle and with a very small loss of its energy and volume (less than 10% of the total) to Rossby wave dispersion and frictional dissipation, compared with about 25% loss in case B4.

The importance of the eddy strength and size has been examined in the previous f-plane model. The results there indicate that the interaction time and the transport rate depend strongly upon the eddy strength, but their combination gives only weak change in total volume transport; while the total transport depends strongly upon the size of the eddy. It is interesting to see how these results change on the $\beta$-plane with an eddy impinging on the slope from a distance. The cases examined here are B1, B2 and B3, where the eddy in B2 has a swirling transport twice as that in B1, and the eddy in B3 has an e-folding radius one and a half the eddy radius in B1. The corresponding results are listed in table 3.6 for comparison.

Comparing with the $f$-plane results in table 3.4, the $\beta$-plane interactions are relatively weaker, with smaller total cross-slope volume transport. This is related to the eddy weakening due to planetary wave radiation. However, the general patterns of the responses are similar in both groups. The volume transport rate depends largely upon the eddy strength and the total volume transport depends largely upon the eddy size. The large size eddy causes more transport of upslope water than the smaller eddy with equal or twice the swirling transport. There are important differences between the interactions on $f$-plane and $\beta$-plane. The multiple interactions together with the

151

## Table 3.6

| Case | B1 | B2 | B3 |
|---|---|---|---|
| Total Volume Transported $(10^{12}m^3)$ | 3.5 | 4.8 | 5.2 |
| Length of Time (day) | 14 | 8 | 12 |
| Rate of Transport $(10^6 m^3/s)$ | 2.9 | 6.9 | 5.0 |
| Cyclonic Eddy Circulation $(10^5 m^2/s)$ | 0.3 | 0.5 | 0.9 |
| Maximum Vorticity $(10^{-4}s^{-1})$ | 0.1 | 0.20 | 0.6 |
| Cyclonic Eddy Radius (km) | 30 | 35 | 37 |

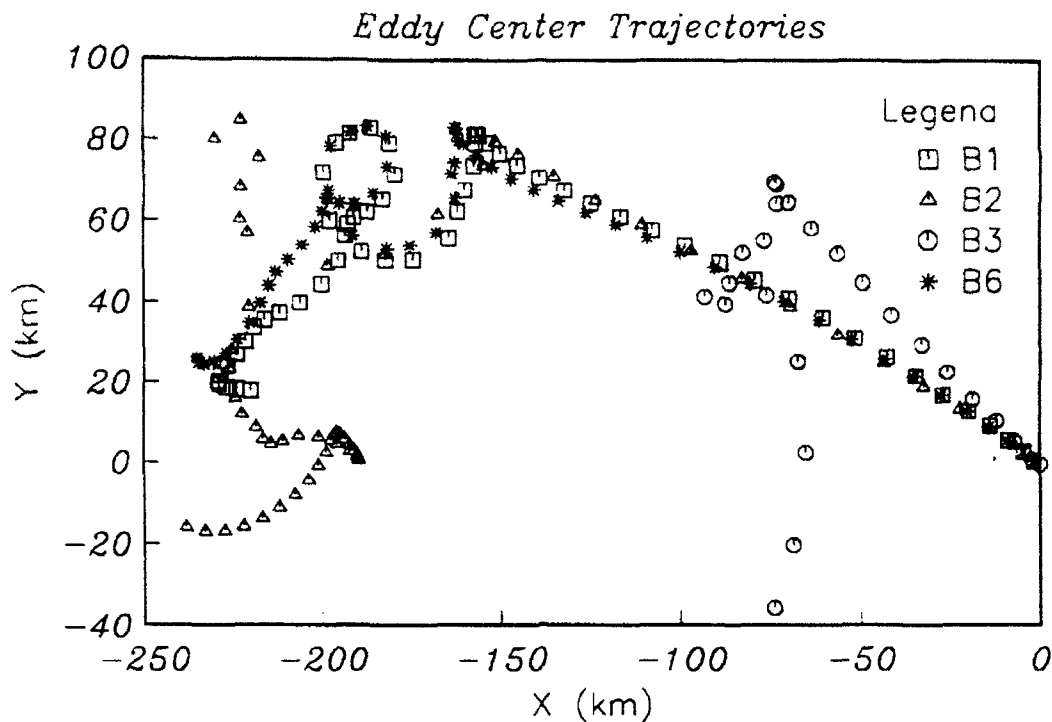The Effect of Eddy Strength and Size on $\beta$-Plane.

Figure 3.37: Trajectories of the eddy centers on the $\beta$-plane for cases B1, B2, B3 and B6 listed in table 3.5. The marks represent the eddy center locations at the beginning of every two days.

planetary $\beta$-effect can seriously alter the eddy propagation from that on the $f$-plane, which will affect directly the subsequent interactions. For example, the large portion of the cross-slope transported volume is released back to the slope during the subsequent interaction in most of the $\beta$-plane cases. In case B2, the transport resulting from the second interaction is less than 1/4 of the first one. The eddy propagation after the second interaction is therefore not controlled by the topographic eddy but by the nonlinear self-advection and the $\beta$-effect. Comparison of the eddy trajectories in cases B1 and B2 (figure 3.37) shows that they have roughly the same trajectory before the first interaction, but the eddy in B2 travels faster. After the second interaction, the eddies in both cases travel southeastward under nonlinear self-advection. Being initially stronger and spending less time in planetary dispersion, the eddy in B2 has a larger eastward drift than the eddy in B1. At the end of the calculation, the eddy in B2 has started to change its course back to the normal $\beta$-induced propagation. Comparing the eddy strength dependence on $f$

153

and $\beta$-planes, the volume transport processes are similar. This is not unexpected: the process of transporting water off the shelf depends only on $f$-plane dynamics; but the eddy propagation, a $\beta$ sensitive process, is very different for the two situations.

The effects of the eddy size change is more visible. The increase of the eddy size results in an increase of eddy westward propagation speed and a decrease in the southward speed (the nonlinear-self advection decreases when the eddy size increase). A large eddy will arrive at the west-bound slope quicker than a small eddy, provided they start from the same initial position. Therefore the large eddy retains a larger portion of its initial strength due to the shorter dissipation time. The large eddy also has a larger incident angle to the topography due to its faster westward speed and slower southward speed. This implies a stronger interaction between the large eddy and the topography. In case B3 a large cross-slope volume transport of about $5.2 \times 10^{12}$ $m^3$ is induced by the large eddy over a time period 12 days. The values of the maximum vorticity and the topographic eddy circulation indicate that a substantial amount of fluid is from the shallower water area. In fact the transported volume comes from as far as 25 $km$ upslope, which corresponds to a water depth 630 $m$. As discussed before, the strong eddy-slope interaction is accompanied by the generation of an intensive topographic eddy and the decrease of the original eddy size and strength. In figure 3.38 the flow field for B3 is shown at three times during the period of topographic eddy formation. At day 24 a strong cyclonic disturbance develops on the slope and subsequently moves across-slope into the deep ocean forced by the original eddy advection. The streamers are drawn from the enlongated original eddy at two longer ends by the intensive cyclone and the slope disturbance (day 32), resulting in a continuous loss of the eddy volume. Until about day 40 the original anticyclone has lost nearly half of its initial volume and KE in 12 days. The history of these changes are plotted in figure 3.39 for both the area and the average KE of the eddy. The sharp changes are obviously seen from the figure. After day 40 the circulations and the sizes of both the original eddy and the topographic eddy are almost equal, thus they form an approximately symmetric dipole structure and propagate
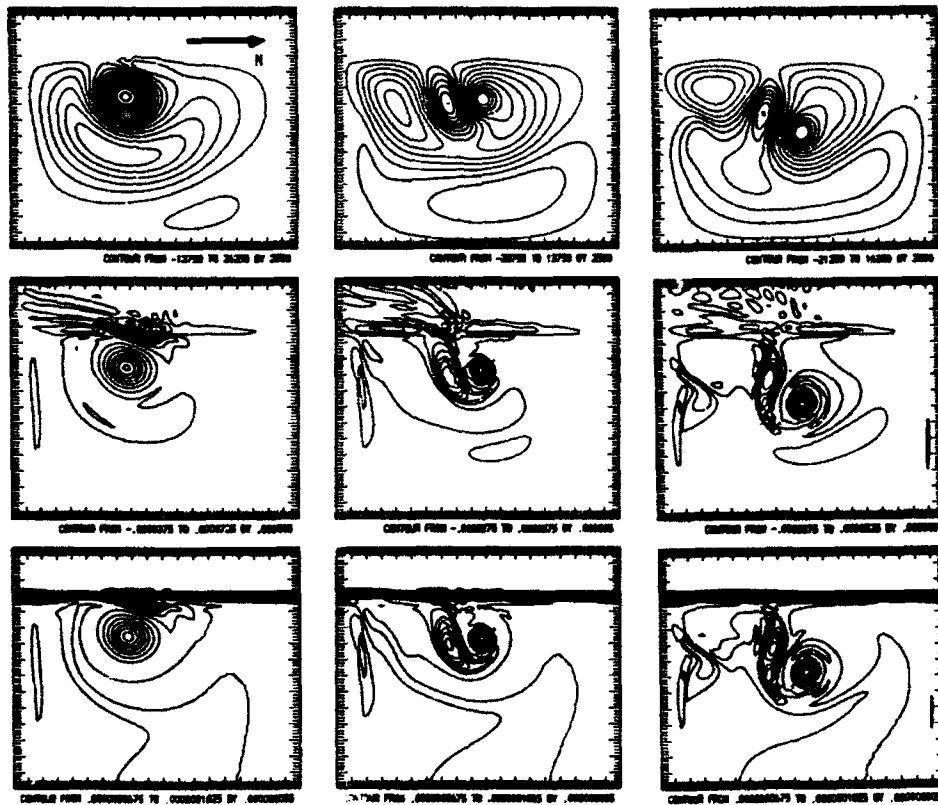
Figure 3.38: From top to bottom rows: contours of streamfunction, relative vorticity and potential vorticity. The columns from left to right are at day 24, 32 and 40. Case B3.
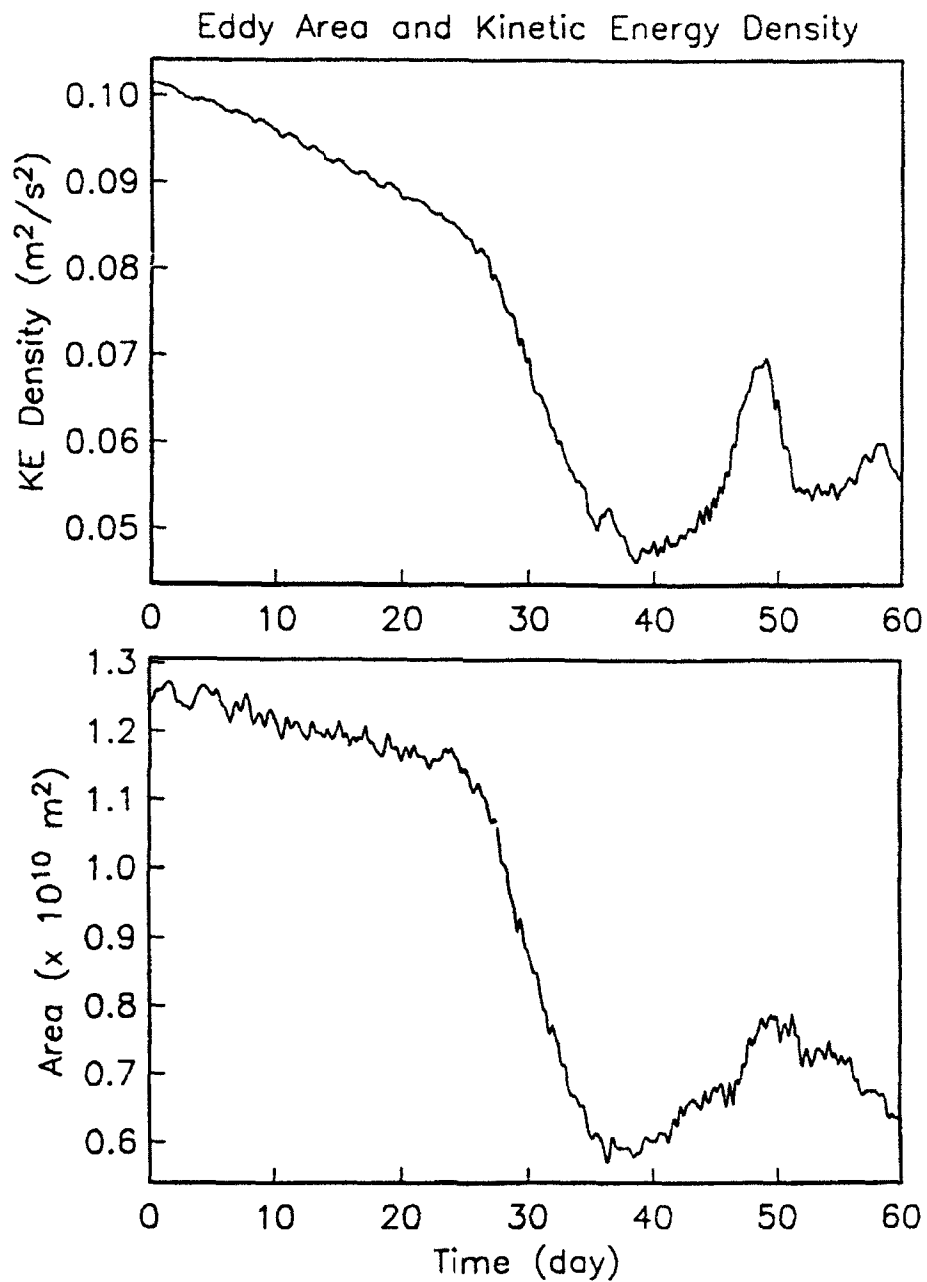
Figure 3.39: The time history of the average KE density (upper panel) and the area of the original eddy (lower panel, the eddy volume is the area multiplied by a constant depth) for case B3.

eastward away from the topography. This result differs completely from the results of both B1 and B2, where the majority of the volume transport is released back to the slope and the eddy propagation is under the influence of nonlinear eddy self-advection. As indicated by the eddy trajectory in figure 3.37, the eddy propagates eastward away from the topography.

In general the above results suggest that the cross-slope volume transport depends largely on the eddy size and weakly on the eddy strength. If the original eddy is much stronger than the topographic eddy, it may release the topographic eddy back to the slope and the accumulated volume transport may be much smaller. With equal swirling transport, the cross-slope volume transport is favored in the case of a larger radius eddy.

Comparisons between the results of B1 and B6 show the effect of different topography on the interaction. The interaction process of B6 is very similar to that of B1. Closer examination reveals that the cyclonic perturbation field extends farther upslope in B6 due to the smaller topography C used. After the topographic eddy separates from the slope, the two cases have not only the same structures and patterns in the streamfunction and vorticity fields, but also the same numerical values in the ranges of these fields. This may imply some simple intrinsic properties of the eddy-slope interaction regardless of the changes in topography size. The similarities persist for the rest of the interaction. Further comparison of the volume transport shows that the two cases have roughly equal total cross-slope volume transport, where 90% of the transport in B6 relative to about 15% of the transport in B1 is from the upper slope area, figures 3.33 and 3.40. The topographic eddies in these two cases have the same amount of circulations. This suggests that when interacting with bottom topography, an eddy tends to generate a fixed amount of vorticity perturbation, which is proportional to the eddy circulation and independent of the topographic slope. The same is also suggested by the previous contour dynamics study in chapter two. This is the intrinsic property in the eddy-topography interactions. For different topographies, the amount of the circulation generated is not necessarily proportional to the amount of cross-slope volume transport. For the cases
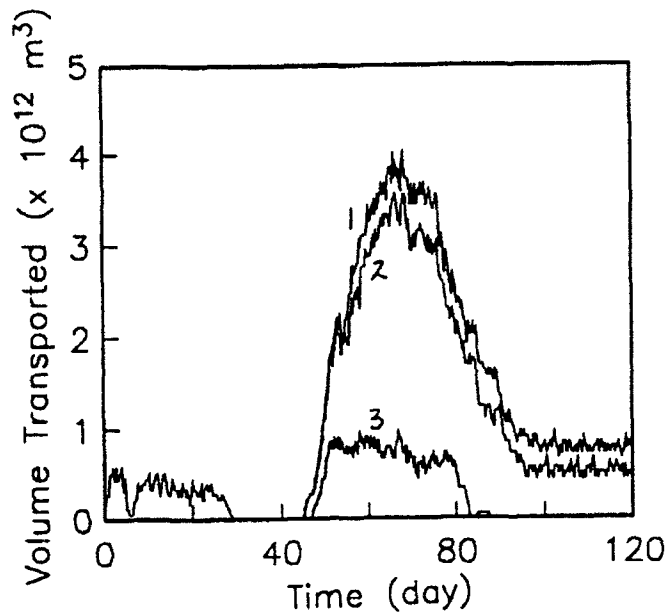
Figure 3.40: The accumulated cross-slope volume transport for case B6. The curves are (1) total volume transported; (2) volume transported from upper slope area 7.5 km away from the slope-deep ocean boundary; (3) volume transported from upper slope area 15 km away from the slope-deep ocean boundary.

discussed here, the volume transport is fairly constant, whereas the composition of the water mass varies with the size of the topography. The above results do not vary in general from the $f$-plane to the $\beta$-plane; recall the discussions in section 3.3.4. As expected the similarities in the eddy trajectories for cases B1 and B6 are observed in figure 3.37.

The same bottom friction defined by equation (3.6) is used in case B5, with the rest of the conditions exactly the same as those in case B2. Like the $f$-plane case F11, the results of B5 show a slight decrease in the total cross-slope volume transport from that of B2, largely due to the dampening of the perturbation momentum on the slope. Consequently the eddy center trajectories differ for these two cases; the eddy propagation in B2 is slightly more dominated by the topographic eddy process. The effect of frictional dampening of the shelf/slope responses has been discussed in the previous $f$-plane study; the result applies also to the $\beta$-plane situations.

## 3.4.2  An Anticyclone Impinging on a Slope at a Right Angle

If an eddy collides with a slope topography at a right angle, will the resulting interactions be the same as that with an oblique incident angle? If not, how do the results vary? This will be investigated in this subsection.

For the present configuration of the problem, the right angle incidence is achieved by rotating the coordinate system to a degree that the topography has a proper angle to the north. In such a coordinate system the eddy will propagate onto the slope at a $90^o$ angle to the isobath. On the $\beta$-plane the anticyclone propagation tendency has two components: a $\beta$-induced westward tendency and a resulting southward eddy self-advection. They combine to give a southwestward propagation tendency as shown in figure 3.29. Denoting the westward and southward propagation speed by $u_w$ and $u_s$, the counterclockwise angle between the north and the direction of the eddy propagation is given by $\theta = \pi/2 + \tan^{-1}(u_s/u_w)$. Therefore in the new coordinates if the topography is still given by the same expression as equation 3.2, north is then the direction with a clockwise angle $\theta$ with respect to the isobath contours. For the anticyclonic eddy used in the standard cases F1 and B1, this angle is approximately $\theta = \pi/2 + \tan^{-1}(15/7)$. After this coordinate rotation one should realize that not only the eddy incident angle changes, but also the resulting direction of the eddy propagation tendency relative to the topography changes. This configuration represent the collision of an anticyclonic eddy with a southwest-bound slope topography.

Case B7 from table 3.5 is studied first, which has comparable parameters to case B1. The interaction process is described by the picture of the eddy center trajectory, shown in figure 3.41. The eddy movements reveal that three strong interactions take place during the 120 day simulation. A topographic eddy forms in each of the interactions and subsequently dominates the original eddy propagation. Since the original eddy accelerates and approaches the slope, the increasing inertia enables the eddy to climb high onto the slope. Therefore the perpendicular interactions are most effective for the
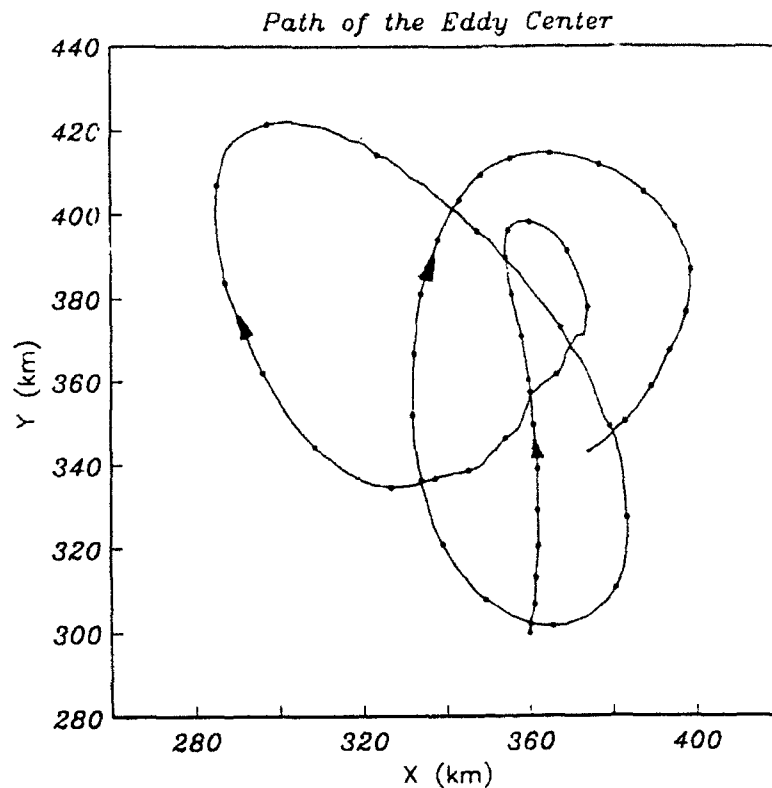
Figure 3.41: The trajectory of the eddy vorticity center for case B7. The dot marks represent the eddy positions at the beginning of every two days.

eddy penetration onto the slope. During the first interaction the original eddy reaches 20 km farther upslope than the eddy in case B1. The strong dipole motion resulting from the first interaction causes another straight eddy incidence onto the slope in the second interaction, in which the original eddy climbs even farther upslope. The subsequent interaction also shows similar behavior. The reversal of the eddy propagation direction from seaward to slopeward after the first and the second interactions occurs relatively abruptly, associated with a sharp increase in the curvature of the eddy trajectory. Besides the dipole propagation, the planetary $\beta$ and nonlinearity play important roles in regulating the eddy motion in the above processes. A few snap shots of the streamfunction and vorticity fields in figure 3.42 illustrate part of the interaction process. By day 24 the eddy is sufficiently close to the slope and induces a slope disturbance. The cyclonic slope disturbance is forced by the eddy advection and separates from the slope at day 32. The original eddy is also strongly perturbed from circular to elliptical shape by the flow induced by movements of the slope front and the formation of the topographic cyclone. As
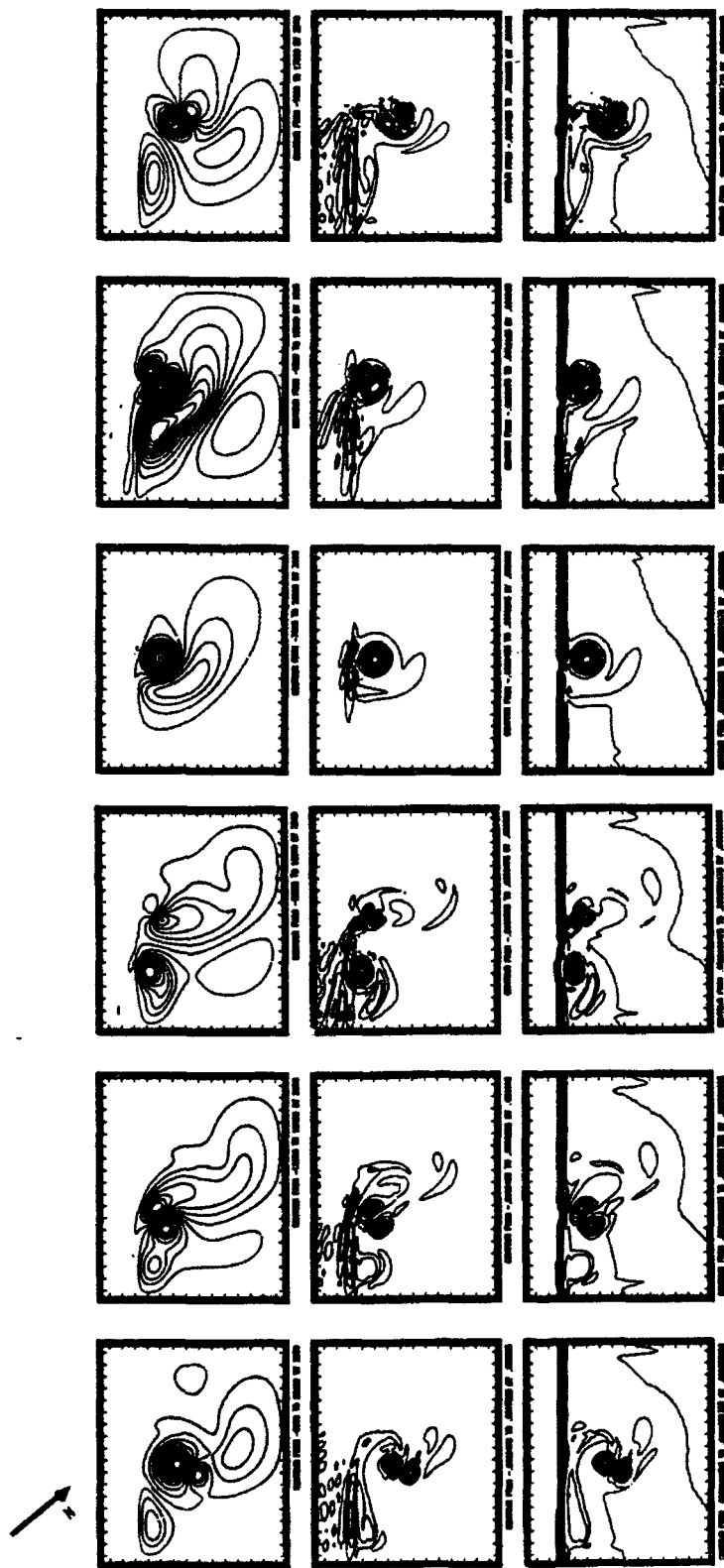
Figure 3.42: From top to bottom rows: contours of streamfunction, relative vorticity and potential vorticity. The columns from left to right are at days 24, 32, 40, 48, 56 and 64. Case B7.

161

the dipole-like eddy pair separates fro n the slope around day 40, the original eddy suffers a continuous loss of volume and momentum through the formation of streamers at the two longer ends of the eddy. As the eddy pair propagates through the flat bottom region in the basin (day 48), the planetary $\beta$ and nonlinear self-advection become important. Together with the eddy mutual advection, they speed up the eddy slopeward propagation to about 12 $cm/s$, which is twice the incident speed of the first interaction. Therefore the second interaction is particularly strong, as shown in figure 3.42 at days 56 and 64. By day 64, the eddy size is considerably smaller than the initial size. It is interesting to note that the cyclonic topographic eddy, trapped at the topography after breaking up with the original eddy, moves mainly along the outer slope edge due to the existence of an anticyclonic disturbance on the inner slope edge. The mechanism for this is the same as that discussed in section 3.3.6 for the cyclone-slope interaction process. The sharp changes of the eddy size and KE occur mainly in the first two interactions (figure 3.43). Compared with an oblique incidence case such as B1, the straight collision interactions in B7 result in much larger variations of the original eddy properties. For example, after the second interaction at day 80, both the strength and the size of the original eddy fall below 1/3 of the original values. The large changes take place during the first and second interactions, especially in the second interaction, with the eddy area decreasing by 50%. Corresponding to this sharp eddy volume decrease, there is an increase in the total cross-slope volume transport and the formation of the second topographic eddy as shown in figure 3.44 and in figure 3.42 at day 64. It can be seen from figure 3.44 that the initial cross-slope transport is from the immediate vicinity of the slope. After day 20, the eddy collides with the slope and causes a sharp increase in volume transport. As the second interaction takes place, the new transport adds to that from the first interaction and results in a large accumulated cross-slope volume. The average total transport for the first two interactions is approximately the same as that in case B1, shown in figure 3.33. However, the interaction in B7 is much stronger and involves more fluid from the upslope area.
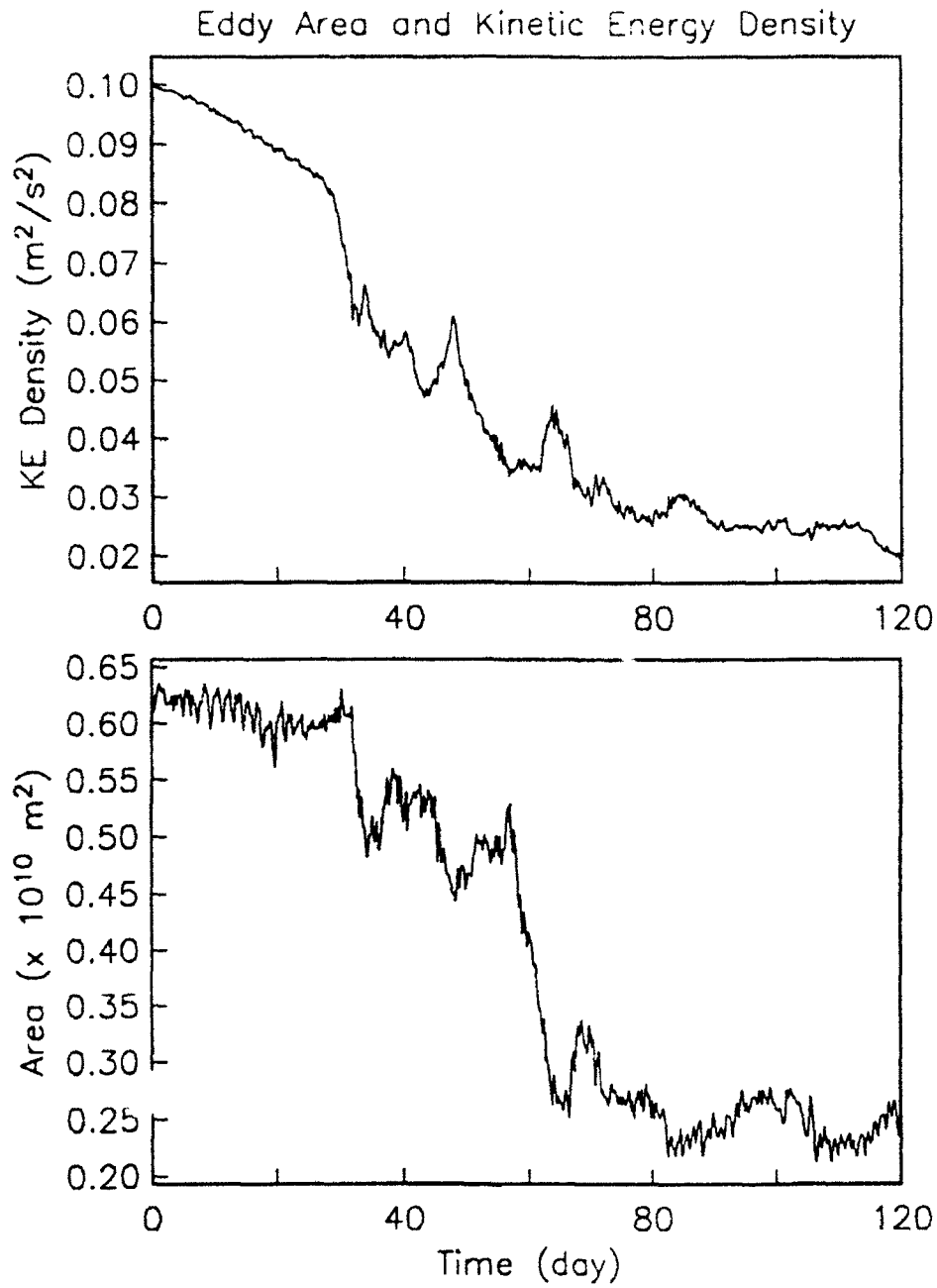
162

Figure 3.43: The time history of the average KE density (upper panel) and the area of the original eddy (lower panel, the eddy volume is the area multiplied by a constant depth) for case B7
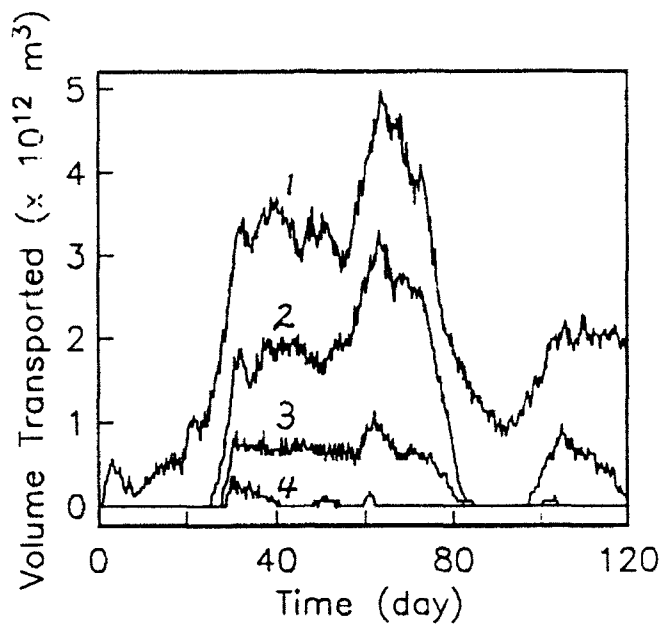
Figure 3.44: The accumulated cross-slope volume transport for case B7. The curves are (1) total volume transported; (2) volume transported from upper slope area 7.5 km away from the slope-deep ocean boundary; (3) volume transported from upper slope are? 15 km away from the slope-deep ocean boundary; (4) volume transported from upper slope area 22.5 km away from the slope-deep ocean boundary.

The interaction becomes stronger if the eddy is initially closer to the topography. In the case of oblique eddy incidence, such as case B4, this is attributed to the difference of the eddy strength and size at the time the interaction occurs. The Rossby wave dispersion and frictional dissipation weaken the eddy strength and reduce the eddy size. This decay is larger for the eddy initially farther away from the topography. Another effect related to this initial eddy location is the eddy incident speed at the time of collision. This effect is particularly important for the right angle eddy incidence. Figure 3.45 gives the eddy trajectory for case B8, where the eddy is initially 50 *km* closer to the slope than the eddy in B7. The eddy, having a short distance to accelerate, can not reach upslope as far as the eddy in B7 in the first interaction. and subsequently induces a cross-slope volume transport containing less upslope fluid as well. Calculations show that the average accumulated cross-slope volume is $5 \times 10^{12}$ $m^3$ for B8 relative to about $3.5 \times 10^{12}$ $m^3$ for B7. Thus there is more cross-topography volume transport generated in B8 than in B7. Since the differences in eddy size and strength are small in these
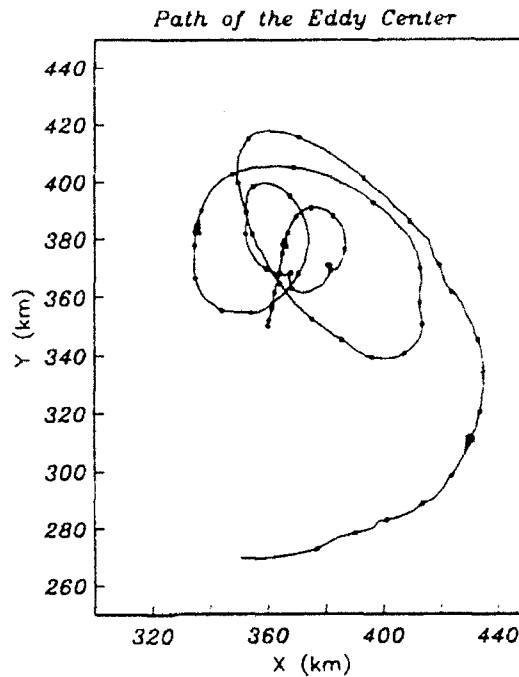
164

Figure 3.45: The trajectory of the eddy vorticity center for case B8. The dot marks represent the eddy positions at the beginning of every two days.

two cases at the time of collision (about 5% in strength and less in size), they can not explain the large differences in the total volume transports and the eddy trajectories. The plausible explanation is the difference of eddy incident speed, which results in the differences in the eddy upslope penetration distance and the interaction time. The eddy in B7 accelerates to a top slopeward speed of 6 $cm/s$ at day 18, while that in B8 reaches only 4 $cm/s$ at day 12 just before the collision. Upon collision, the topographic effect slows down the speed of eddy propagation and eventually turns it seaward. This slight difference in collision momentum enables the eddy in B7 to reach slightly higher upslope and to draw water across slope from shallower area. Examination of cases B7 and B8 shows that they contain approximately the same amount of total cyclonic perturbation circulation of $5.5 \times 10^5$ $m^2/s$, but have different interaction time, 8 days in B7 and 12 days in B8. The eddy in B8 stays close to the slope edge for a longer period of time and transport more lower slope water across the edge. Therefore the total volume transport in B8 is larger than that in B7, but the transport in B7 contains more upslope volume, which keeps the perturbation circulation in the two cases roughly the same.

A final case in this group is B9, which is similar to B7 but using topography C. In this case the anticyclonic eddy impinges on a smaller topography than the previous cases. From the previous discussion, the amount of the perturbation vorticity generated depends mainly on the strength and the size of the incident eddy at the time of collision. For the same anticyclone as that in B1 impinging on a smaller topography, there are two patterns of volume transport that enable the generation of an equal amount perturbation circulation. In the first case, more volume transport from lower slope is generated; in the second, there is less volume transport but it contains more upper slope water. Since the eddy more easily moves farther upslope onto a small topography, it is likely to advect more upper slope water across the topography. The results show that B9 and B7 have approximately the same circulation of $5.5 \times 10^4\ m^2/s$, and the total volume transport of $3.5 \times 10^{12}\ m^3$; but in B9 more than 50% of the volume is transported from upper slope area at least 15 $km$ away from the slope boundary compared with only 25% in B7. This result applies also to the oblique incident case. One important difference between cases B7 and B9 is the decay of the original eddy during the period of interaction. The average decay rate in B7 due to the eddy-topography interaction is much larger than that due to the radiation and frictional dissipation; while the interaction-induced decay rate in B9 is smaller than the corresponding planetary and frictional decay rate. This indicates that the eddy volume and KE loss during the interaction with a small topography is also small. This is because the front disturbance is relatively weak in strength for a small topographic slope. When it retreats from the slope after the collision, the original eddy is less distorted in its shape and does not form large streamers. This effectively reduces the eddy volume and KE loss through these streamers. The formation of the dipole-like structure acts to suppress the planetary long wave dispersion, since the dipole contains less long wave energy than the isolated eddy (Flierl, 1987). Furthermore, within the same 120 day time period, there are five interaction events taking place in B9 relative to three in B7. The changes of eddy volume and KE density in case B9 are plotted in figure 3.46, to be compared with figure 3.43. Approximately 60% KE density and 70% volume of
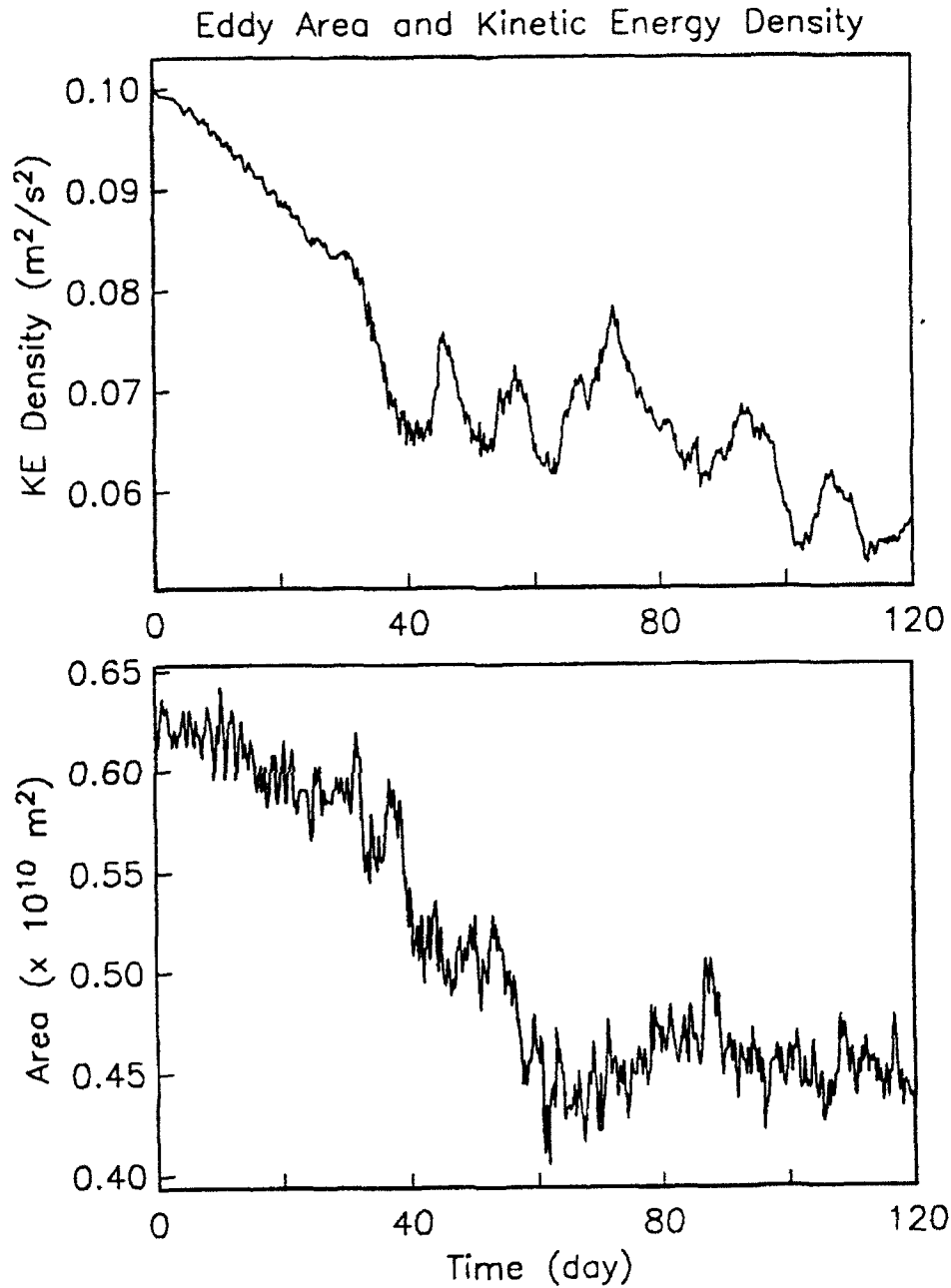
166

Figure 3.46: The time history of the average KE density (upper panel) and the area of the original eddy (lower panel, the eddy volume is the area multiplied by a constant depth) for case B9.

the original eddy are retained after five interactions in B9, relative to 20% KE and 40% volume retained after three interactions in B7.

### 3.4.3 Cyclone-Shelf/Slope Interactions

Two cases are examined in this subsection for collision of a cyclonic eddy with a slope topography, one oblique incidence and one straight collision. Since a cyclone moves northwestward on a planetary $\beta$-plane, the straight collision case requires that the topography is to the northwest of the eddy, with isobath running southwest to northeast. For the eddy similar to the one used in case B1 but with opposite circulation, the coordinate rotation is approximately $\theta = \pi/2 - \tan^{-1}(15/7)$ for case B11.

For the oblique eddy incident case B10, the topography is west-bound. The streamfunction, relative vorticity and potential vorticity fields are plotted in figure 3.47. The original eddy center trajectories are plotted in figure 3.48. Once it feels the influence of the topography, after about 40 days of propagation, the eddy starts to change its course of propagation. Its northward (along slope) speed slows down and westward (slopeward) speed accelerates due to the topographic $\beta$ and associated nonlinear effect, respectively. If the streamfunction fields at day 40 and 56 are compared, it can be seen that the longer axis of the elliptical eddy has rotated counterclockwise about $\pi/2$. The eddy nonlinear self-advection is now slopeward, causing the slopeward eddy acceleration. The average slopeward speed before day 40 is approximately 2.5 $cm/s$, that jumps to 4.8 $cm/s$ averaged over next 20 days. After day 64 the eddy moves quickly onto the slope. It breaks apart on the slope due to strong topographic Rossby wave radiation and vortex tube compression (day 72). Strong shelf disturbances are observed across the slope to the coastal wall, which are dispersing into topographic waves. The small scale structures are observed seaward along the edge of the slope to balance the onslope eddy fluxes. It is expected that the original eddy will undergo a drastic change in its volume and energy level during the interaction. Figure 3.49 illustrates this process. Starting around day
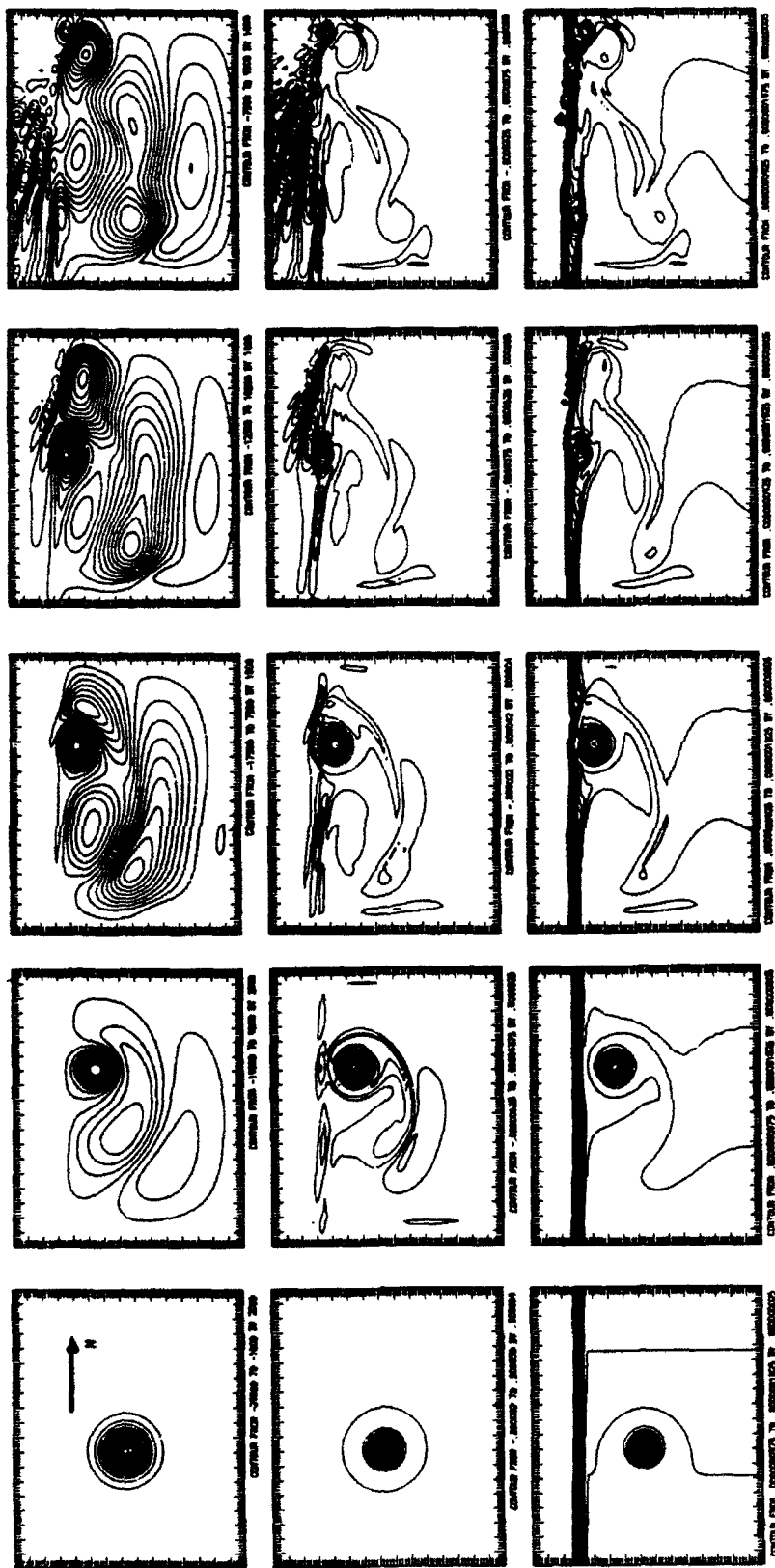
168

Figure 3.47: The streamfunction (upper panels), relative vorticity (middle panels) and potential vorticity (lower panels) field at days 0, 40, 56, 64 and 72 for case B10.
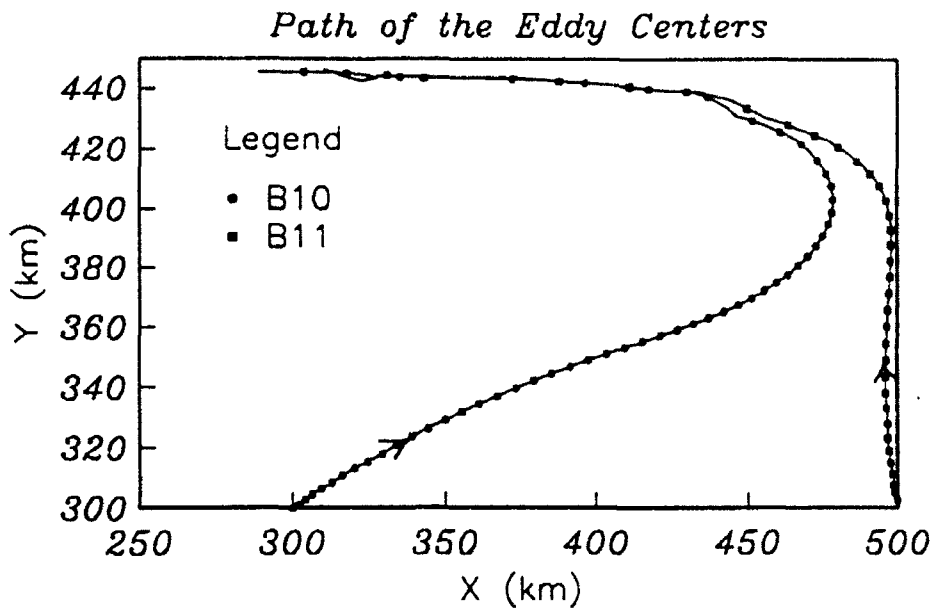
169

Figure 3.48: The trajectories of the eddy vorticity center for cases B10 and B11. The dot marks represent the eddy positions at the beginning of each day.

56, both the KE density and the volume of the original eddy diminish virtually to zero within about 10 day period. Not surprisingly no major seaward transport is produced by this strong slopeward flux of mass and momentum.

The straight eddy-slope collision case B11 shows no qualitative difference from case B10. Its eddy trajectory is also shown in figure 3.48. After the eddy moves into the distance within which the topographic influence becomes dominant, the rest of the interaction process is roughly the same as that of B10. There are, however, slight quantitative differences between them and can be seen by comparing the eddy center trajectories. First, upon collision with the slope, the eddy in B11 has an impinging speed larger than that in B10, due to the fact the nonlinear advection speed is slopeward and approximately twice as fast as the $\beta$-induced eddy speed; second, less eddy decay has occurred in B11 than in B10 before it reaches the slope; thus the eddy is stronger in B11. These result in a slightly stronger interaction in B11, seen from the fast along-slope eddy propagation represented by the space between the dot marks in figure 3.48. This is
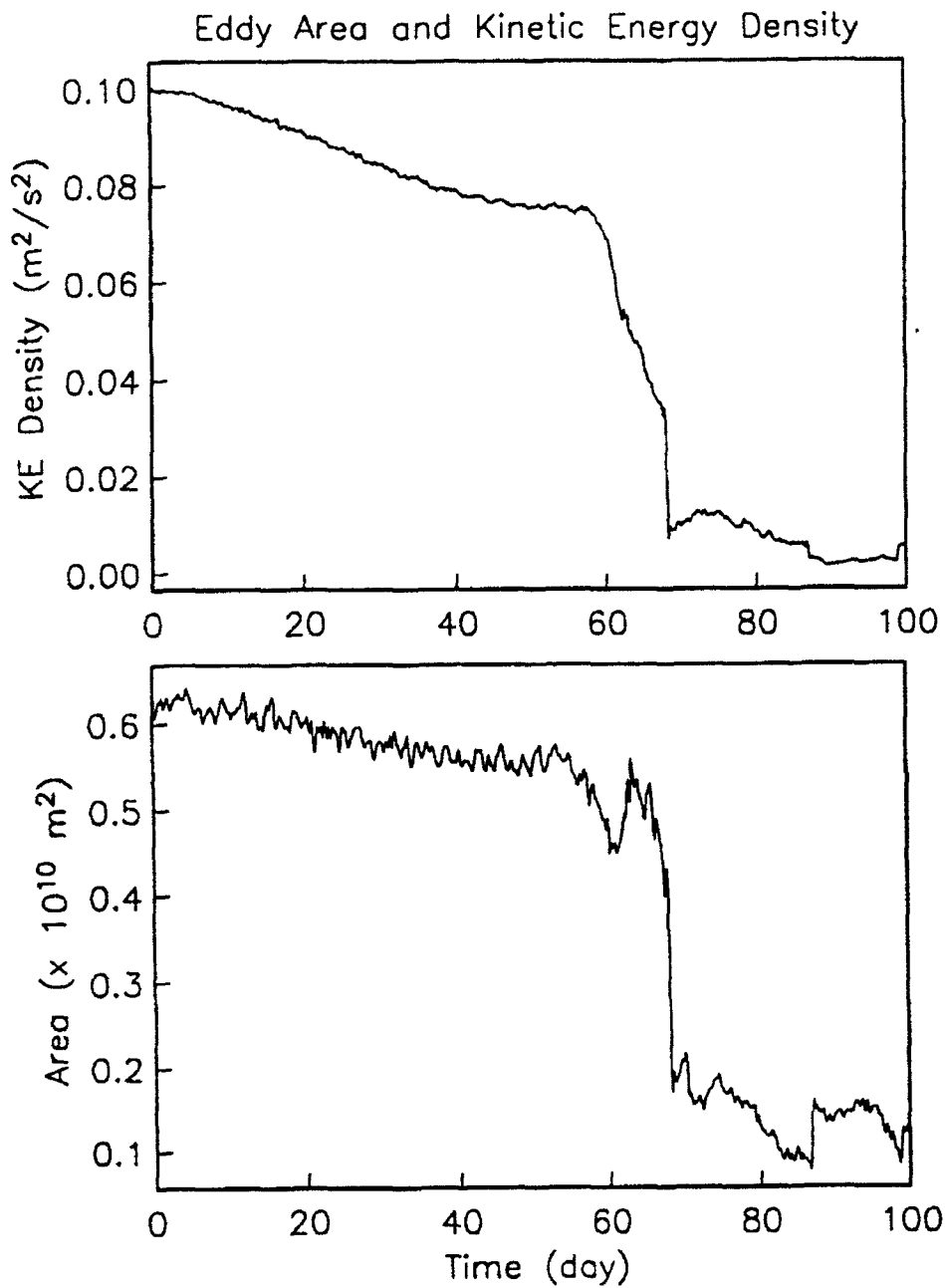
170

Figure 3.49: The time history of the average KE density (upper panel) and the area of the original eddy (lower panel, the eddy volume is the area multiplied by a constant depth) for case B10.

consistent with the f-plane results shown in figure 3.17. The slope front oscillations are the cause of the uneven eddy propagation speed near the slope boundary.

The cyclone-topography interactions have no qualitative difference whether they are defined on $f$-plane or $\beta$-plane. The reason is that the cyclone is trapped at the slope and the topographic $\beta$-effect is always dominant over the planetary $\beta$-effect as long as the ratio $\beta_T/\beta$ is large, where $\beta_T = f_0 h_y/h$ is the parameter of topographic $\beta$.

## 3.4.4 Velocity Field and Momentum Balance

Close examination of the streamfunction field such as the one shown in figure 3.31 indicates that the perturbation flow field induced by the eddy tends to be insulated from the shelf/slope area. This is not unexpected due to the topographic constraint on the current (Wang, 1982; Csanady and Shaw, 1983; Vennell, 1988). One the other hand, the momentum perturbation penetrates the slope to reach the inner shelf and excites wave motions. It is interesting to examine the eddy-induced perturbation flow field and to relate it with the different stages of the interaction and the cross-slope processes.

Since the original eddy field itself is perturbed, it is difficult to separate it from the so called eddy-induced or perturbation field. This, however, does not affect the far field seriously, since the eddy field decays exponentially in space. To examine the development of the perturbation velocity field, case B1 (shown in figure 3.31) is considered. As the eddy approaches the slope, the Rossby wave wake formed behind the eddy also moves toward the topography. By day 56, a pair of the counter rotating cells has formed from the trailing Rossby wave wake. The cyclonic cell pushes against the steep slope edge and causes the crowding of streamlines there. The corresponding vector velocity field is shown in figure 3.50. It can be seen from the figure that the double cell structure north of the original eddy drives a slopeward flow with velocity roughly $5 \sim 8 \ cm/s$. Due to the topographic insulation this slopeward transport is unable to reach upslope and thus turns into a narrow along-isobath current flowing south at the edge of the slope. This current

172

VELOCITY(Z = -10.0,DAY = 56.0)
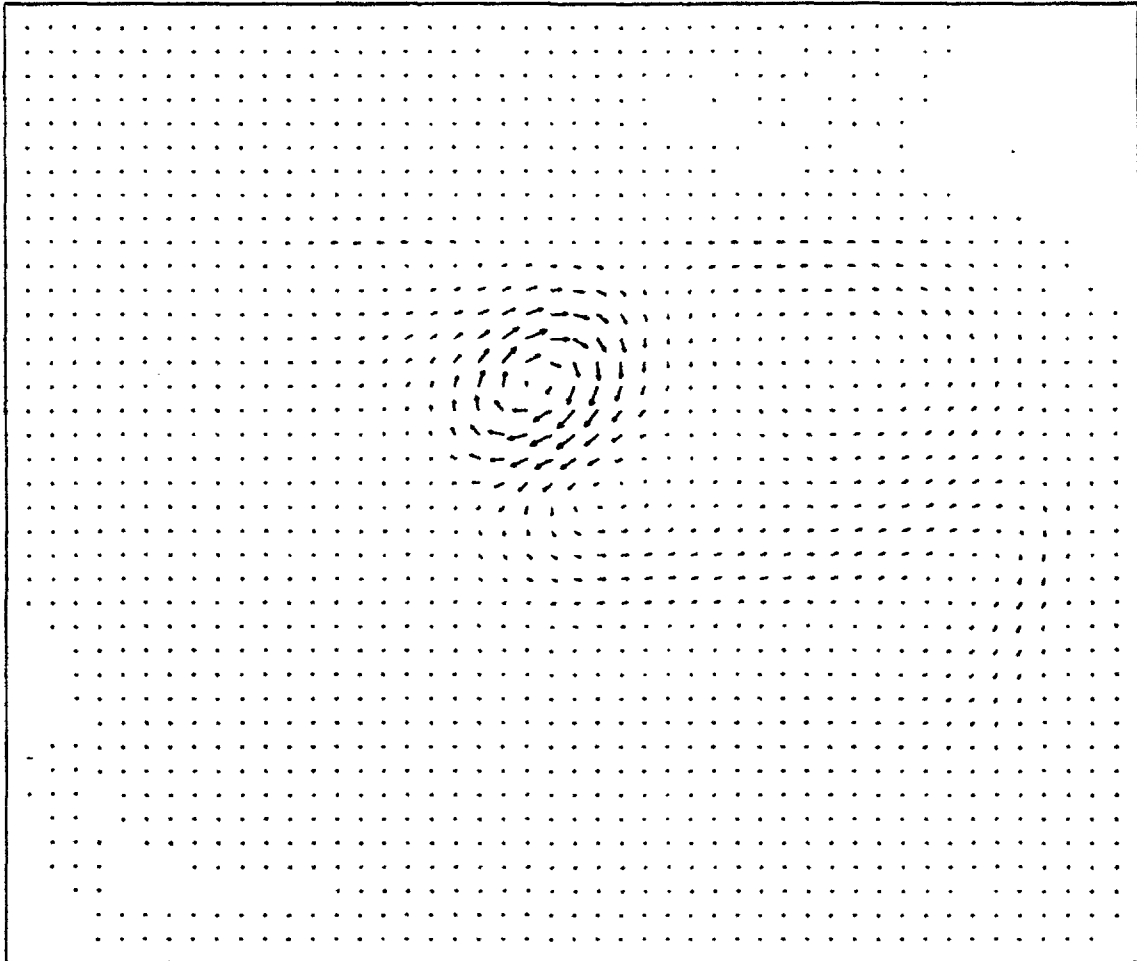


0.524E+00
MAXIMUM VECTOR

Figure 3.50: The instantaneous velocity field at day 56 for case B1.

173

is seen extending downstream across the edge of the original eddy field. It is called here the eddy-induced slope current. The size and the strength of this current vary in space and time depending upon the interaction process. It is relatively persistent throughout the remaining interaction and shifts slowly downstream along the slope. This should be dependent on the individual case with regard to the eddy incident angle and strength of the interaction, etc. In the straight collision case, the trailing Rossby wave wake now pushes the slope from the left side of the original eddy. The slopeward flow associated with the cyclonic cell circulation turns into an along-slope current similar to the case just discussed. For the cyclone-slope interaction, there is a similar development of the eddy-induced slope current from the evolving Rossby wave wake. The current is in the opposite direction to the previous anticyclone-slope interaction cases and lasts only as long as the original eddy is not totally on the slope. After the eddy moves fully onto the slope, the eddy breaks apart into strong topographic waves and the eddy-induced slope current disappears. This along-slope current is first pointed out by Chapman and Brink (1987). When studying the shelf and slope responses to a translating offshore eddy, they found a narrow jet-like feature on the slope ahead of the eddy (to the left of an anticyclone when facing shoreward) with alongshore velocity in the opposite direction to that in the eddy. They suggest that this jet is the offshore edge of the shelf circulation cell which feeds into the original eddy. The present study shows agreement in the eddy-induced alongshore current and further suggests that the current may extend to the eddy trailing edge on a $\beta$-plane. The circulation pattern shown in figure 3.50 tends to suggest that the jet is part of the outer-slope circulation cell. This does not exclude the possibility that the shelf circulation also feeds into the jet as in Chapman and Brink (1987), but the shelf circulation may simply be too weak to be seen.

The eddy induced perturbation current was also observed in the previous contour dynamics investigation. In that case the perturbation PV front and the cyclonic topographic eddy tend to generate a residual current in the deep water between the escarpment and the eddy. The strength of the current is dependent on the magnitude of

174

the perturbation for the given topography, since the current is driven by the vorticity anomaly. It is difficult to detect if such a current exists in the present study, because the amplitude of the PV frontal deformation is small and the influence from the original eddy is dominant and not easily separated. The eddy-induced slope current discussed in this section is clearly different from the vorticity anomaly driven residual current. The slope current is caused by the eddy momentum radiation and the blocking by the topographic slope. It should be noted that, though all the cases studied in this chapter show the existence of the eddy induced slope current at various stages of the interaction, none show a permanent current.

In the study of the $f$-plane interaction problems, it is shown that linear dynamics prevails except when the strong eddy advection is involved. The cross-slope transport process tends to be dominated by the nonlinear dynamics. This property must not change from the $f$ to the $\beta$-plane, since the inclusion of the $\beta$-effect does not affect the dynamic balance of the momentum equations. On a $\beta$-plane it remains to be seen if the condition of an eddy impinging on a slope from a distance can result in any change. An experiment like case B4 but with only linear momentum equations is performed. Without nonlinear advection the eddy will move westward over a flat-bottom ocean, and impinges upon a western boundary topography at a right angle. Due to the lack of advection, cross-slope volume transport is virtually none. As the eddy presses against the slope under the planetary $\beta$-effect, it undergoes an interaction process very different from case B4. The contours of streamfunction, relative vorticity and potential vorticity are potted in figure 3.51 at various times. There is no north-south (along slope) excursion of the eddy center. The part of the eddy reaching on the slope leaks mass and momentum through strong topographic wave radiation. This affects the shape and strength of the eddy and causes strong slope disturbances. The results again strongly suggest that nonlinearity is a key mechanism to the eddy-slope interactions. It may only be numerically large for certain processes, such as in cross-slope volume transport and eddy propagation, but the consequent interaction and field evolution are fundamentally affected.
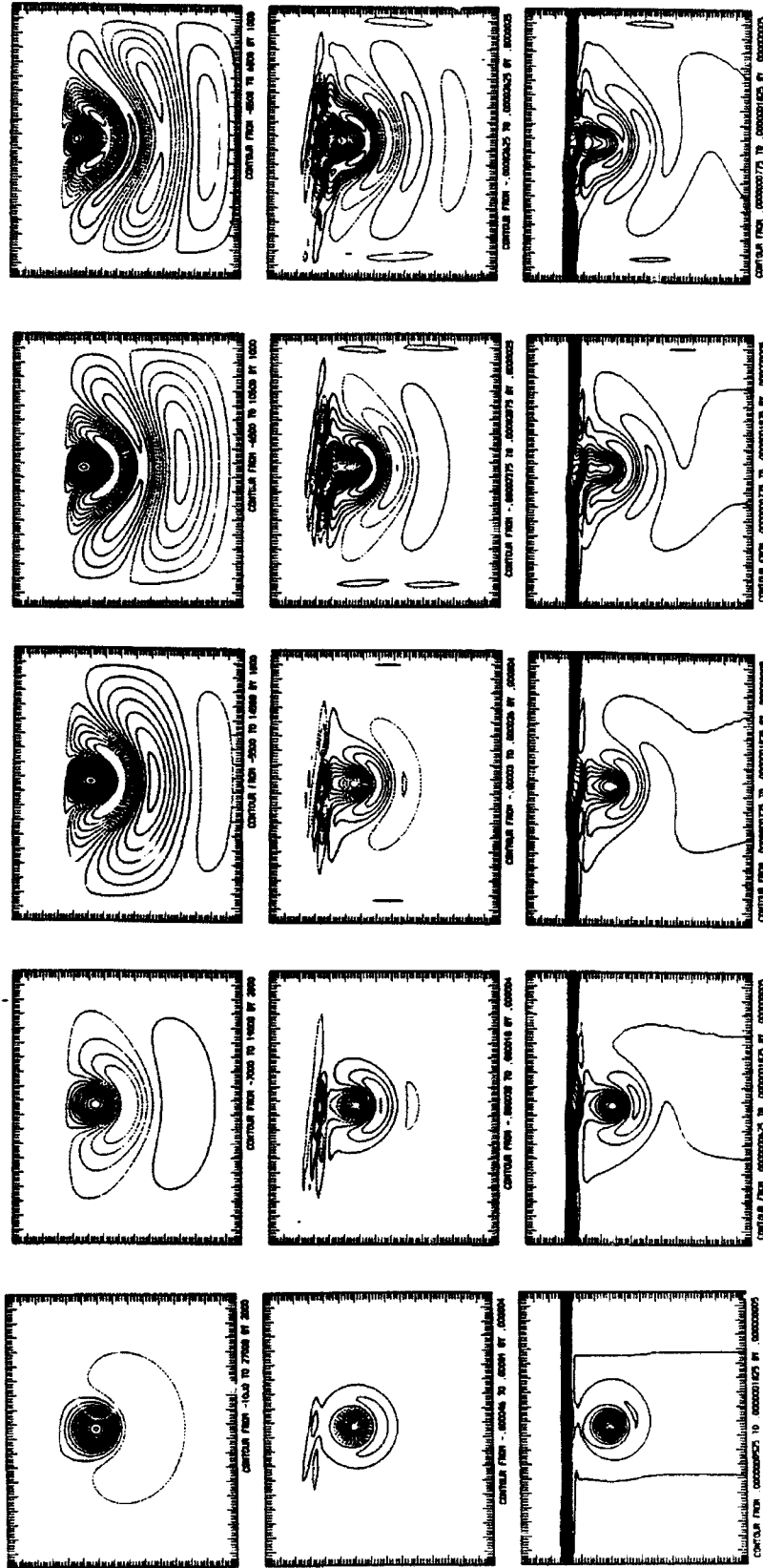
Figure 3.51: From top to bottom rows: contours of streamfunction, relative vorticity and potential vorticity. The columns from left to right are at days 8, 32, 56, 80 and 104. Case B7.

Figure 3.52: Time variation of the individual terms in equation (3.1a) at a location 7.5 km upslope, ie $(x, y) = (345, 458)$ km for case B1. The legends are: (A) $u_t$, (B) $uu_x$, (C) $vu_y$, (D) $-fv$, (E) $-p_x$ and (F) $\nu_4\nabla^4 u$.

The variations of the individual terms in the $x$ momentum equation at a fixed slope location are plotted in figure 3.52 for case B1. The lowest order balance is between $-fv$ and $-p_x$, except during the two interaction processes. The sharp increase in the magnitude of $uu_x$ and $vu_y$ indicates the strong advection associated with the eddy velocity field. The friction term $\mu_4\nabla^4 u$ stays small during the entire interaction.

Both $x$ and $y$ momentum balances are shown in figure 3.53 for case B7. Two of the three interaction events are seen at this location. During the interaction period, the nonlinear terms are important at the lowest order in the $x$- momentum equation, but not in the $y$ momentum equation. The large values of $vu_y$ in figure 3.53a indicate strong cross-slope eddy momentum fluxes associated with the interaction events. For anticyclonic eddy-slope interaction the result is always $-fv \sim -p_x$ since $-fv$ and $vu_y$
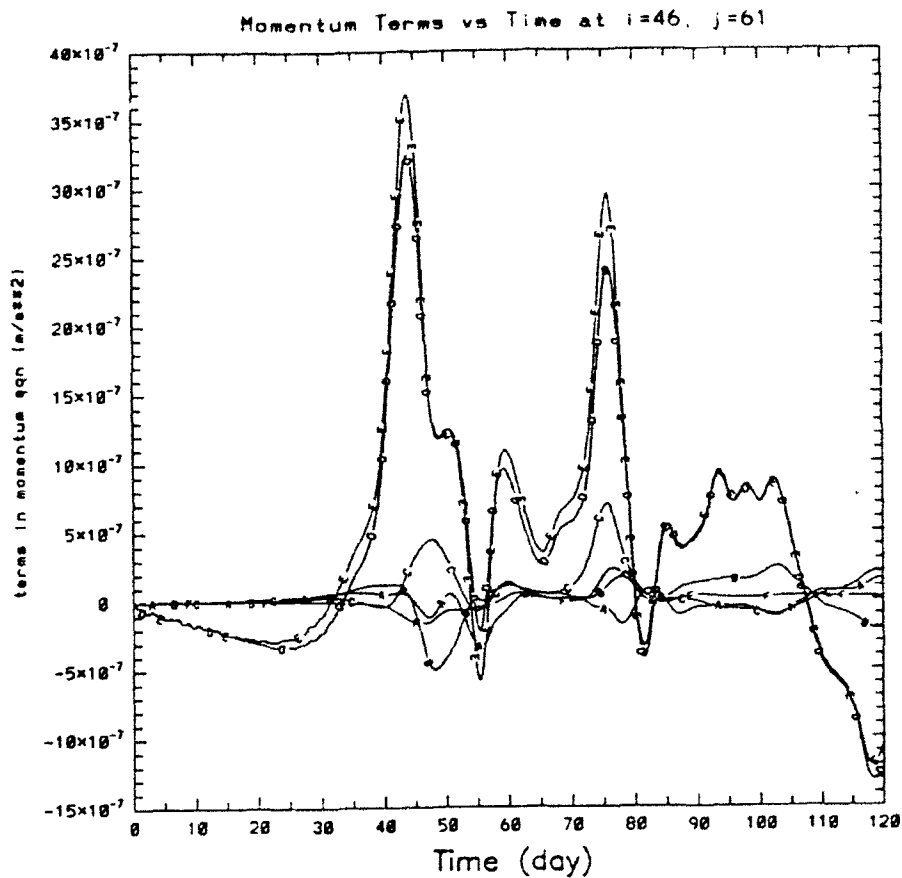
Figure 3.53: Time variation of the individual terms in equations (3.1a) and (3.1b) at a location 15 km upslope, ie $(x, y) = (360, 465)$ km for case B7. (a) Upper panel for $x$ momentum equation, the legends are: (A) $u_t$, (B) $uu_x$, (C) $vu_y$, (D) $-fv$, (E) $-p_x$ and (F) $\nu_4\nabla^4 u$. (b) Lower panel for $y$ momentum equation, the legends are: (A) $v_t$, (B) $uv_x$, (C) $vv_y$, (D) $fu$, (E) $-p_y$ and (F) $\nu_4\nabla^4 v$.

178

have the same sign; it will be seen shortly this situation reverses for cyclonic eddy-slope interaction. The $y$ momentum balance shows that to a good approximation the cross-slope momentum balance is always geostrophic, even during the period of interaction. Comparison between figure 3.53a and b also indicates that the along-slope velocity contains more lower frequency components than the cross-slope velocity. At this location, it is likely due to the influence from the propagating original eddy field, which is seen to cause the persistent positive $u$ there.

The final example, B10, concerns the interaction between a cyclone and a slope. The previous results show that the original eddy dissipates quickly once the interaction starts and the associated cross-slope volume transport is very small. Figure 3.54 gives the change of the individual terms in the $u$ momentum equation. Immediately after the eddy reaches the location around day 61, all terms except the biharmonic friction term increase sharply. The antisymmetry of the time history indicates the passing of the cyclonic eddy. The reversal of the cross-slope velocity at this location also implies the smallness in cross-slope transport. The velocity in the trailing side of the eddy is larger than the leading side, because the topographic wave radiation causes the nonlinear steepening on the trailing side. As already mentioned before, now $|-fv| > |-p_x|$ when nonlinearity is important. After the passing of the eddy, the perturbed slope front oscillates. The magnitude of individual terms in both $u$ and $v$ momentum equation suggests the balance among the linear terms except the friction term. The flow field after the eddy passing can be described by following linear momentum equation:

$$u_t - fv = -p_x \tag{3.10a}$$

$$v_t + fu = -p_y \tag{3.10b}$$

These are the same equations describing the free continental shelf waves studied by Buchwald and Adams (1968). It is natural from this result that one would explain the shelf/slope responses in terms of the shelf-trapped waves. The eddy forcing generates a strong slope disturbance, which disperses into a series of shelf wave components after the
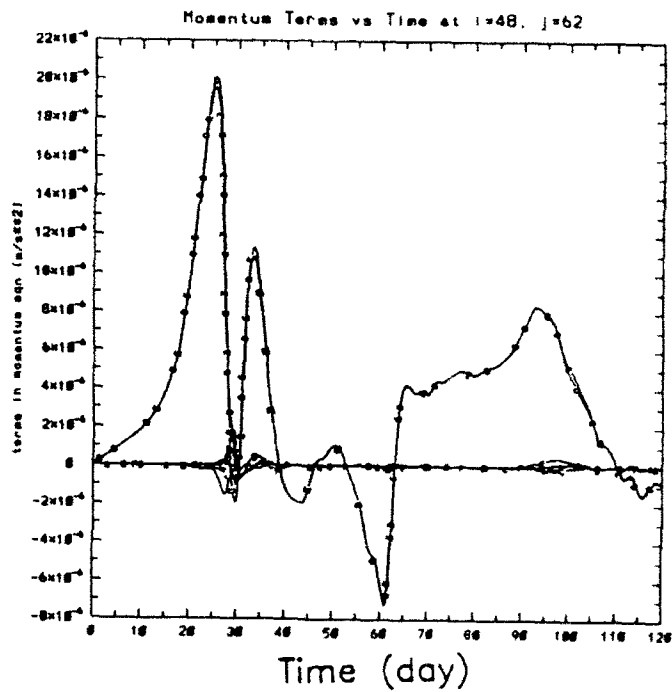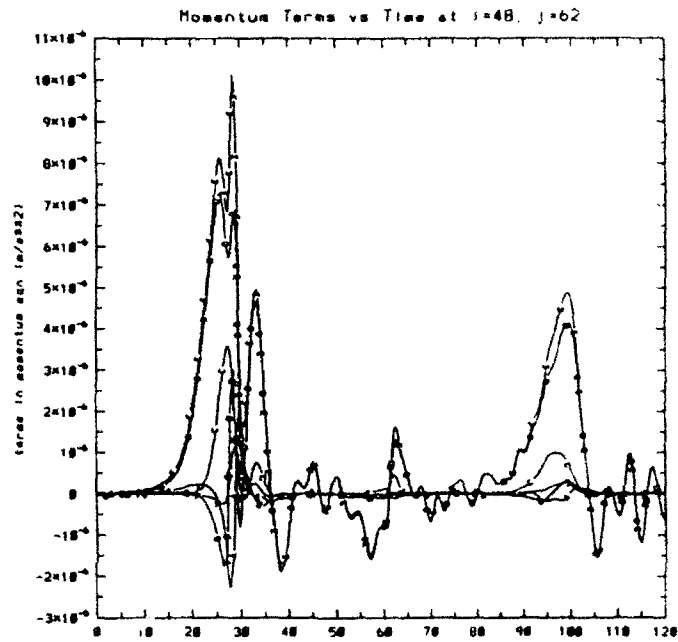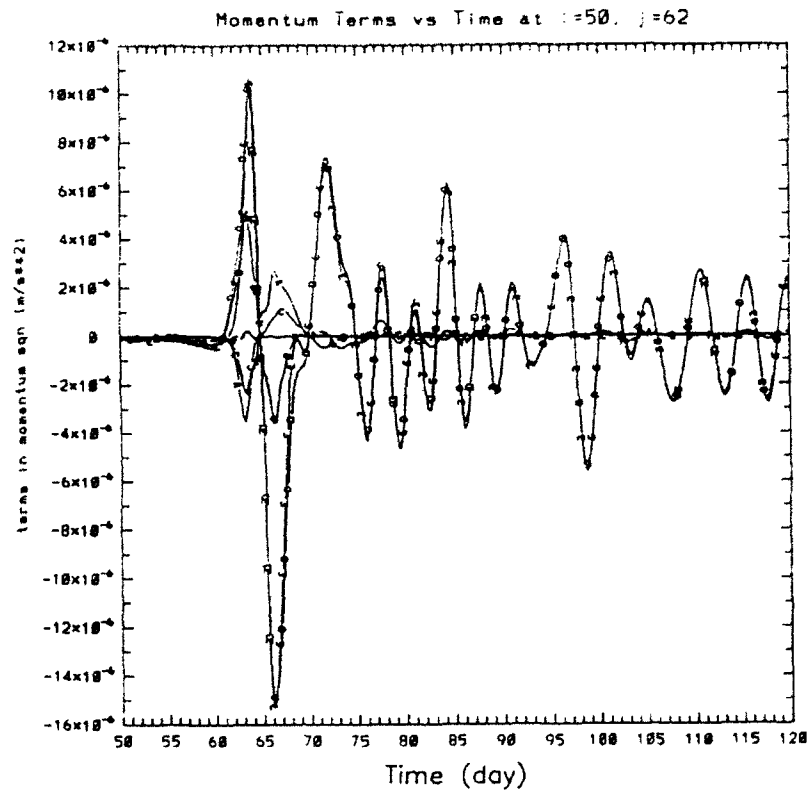
179

Figure 3.54: Time variation of the individual terms in equation (3.1a) at a location 15 km upslope, ie $(x, y) = (375, 465)$ km for case B10. The legends are: (A) $u_t$, (B) $uu_x$, (C) $vu_y$, (D) $-fv$, (E) $-p_x$ and (F) $\nu_4 \nabla^4 u$.

relaxation of the eddy forcing. This has been discussed in the previous $f$-plane study and will be discussed more below.

### 3.4.5 Topographic Waves on the Shelf/Slope

It has been shown in the previous section that on the $f$-plane shelf waves are excited through the interaction of an eddy with shelf/slope water. The estimate in section 3.3 shows that the topographic $\beta$ is about one to two orders of magnitude larger than the planetary $\beta$ for the topography and the parameter range of this study. Since shelf waves are vorticity waves, the topographic control being dominant over the planetary $\beta$ on the shelf and slope suggests that the planetary $\beta$-effect is negligible there. Therefore the discussion of shelf waves in the previous section applies also to the situation on the planetary $\beta$-plane. With an eddy impinging on a slope, it remains to see how this change and the different incident angles can affect the excitation of shelf waves.

Due to the planetary wave dispersion on the $\beta$-plane, the long wave components of the original eddy propagate faster than the eddy center does. Thus before the eddy reaches the topography, the fast long waves will arrive.

The velocity field perturbation on the slope due to this planetary Rossby wave radiation is, however, rather small. The record from three locations downstream to the Rossby wave propagation shows that the velocity is oscillatory with amplitude less than $1\ cm/s$. The velocity increases sharply and the oscillation frequencies go up as the interaction occurs. These are seen from the alongshore velocity record plotted in figure 3.55 for case B1. The large change in the amplitude starts around day 40 when the topographic waves excited by eddy-slope interaction propagate through these locations. The similar patterns of velocity variations are observed in other cases as well. The pre-interaction Rossby wave signals are always weak in the velocity record and are overwhelmed by the succeeding strong topographic waves. Their contribution to the shelf energy spectra is

Figure 3.55: Alongshore velocity vs time at three cross-shelf locations 150 km away from the left boundary for case B1. From top to bottom the locations are: 30 km, 67.5 km and 105 km away from the coastal wall.

not the same as the radiation loss of the eddy energy since the latter spreads over the entire space.

The dispersion relations of the waves caused by an eddy impinging on topography are examined and compared against the theoretical shelf wave dispersion relations. This is done in the same way as in the previous section. In figure 3.56 the wave spectral energy as a function of frequency and wave number is plotted on the shelf wave dispersion diagram for case B1. It is known from the previous $f$-plane study that long wave energy may not be properly resolved by this spectrum if the the domain size, over which the velocity record is taken, is not large enough. This, however, does not affect the arguement that the observed responses are dominated by shelf trapped waves. It can be seen that the waves with modes 5 and lower contain approximately 70% of the total energy in the spectrum. The frequency and wave number bands for the most energetic waves are close to those from the previous $f$-plane cases, such as that shown in figure 3.21. The near-

Figure 3.56: Spectral energy density scatter plot on the shelf trapped wave dispersion diagram for Case B1. The curves are the theoretical solution of the dispersion relation equation (3.7) with $bl = 1.5$ for the first five shelf trapped wave modes excluding the Kelvin wave mode. From upper to lower curves in order, they are modes 1, 2 , 3, 4 and 5, respectively.

Figure 3.57: Spectral energy density scatter plot on the shelf trapped wave dispersion diagram for Case B7. The dispersion curves are the same as those in figure 3.56

resonant responses seen in some of the $f$-plane cases are too weak to be observed in case B1. The general patterns of the shelf responses on the $\beta$-plane are consistent with the $f$-plane dynamics that governs the shelf/slope responses.

With the eddy impinging on a slope at a right angle, the resulting waves tend to shift slightly toward higher frequency and wave number bands. Figure 3.57 is for case B7. The most energetic waves now have wave number and frequency centered around $(-7, 0.07)$ instead of $(-5, 0.05)$ in figure 3.56 for case B1. The case with right angle incidence also has larger wave amplitudes due to less eddy energy loss and faster incident speed at the time of the collision. The straight incidence eddy tends to generate slope perturbations with smaller alongshore scale than the oblique incidence due to the near zero alongshore eddy propagation speed in the former case. This is likely to be the reason that the most energetic wave numbers in case B7 shift toward larger wave numbers compared with that of case B1.
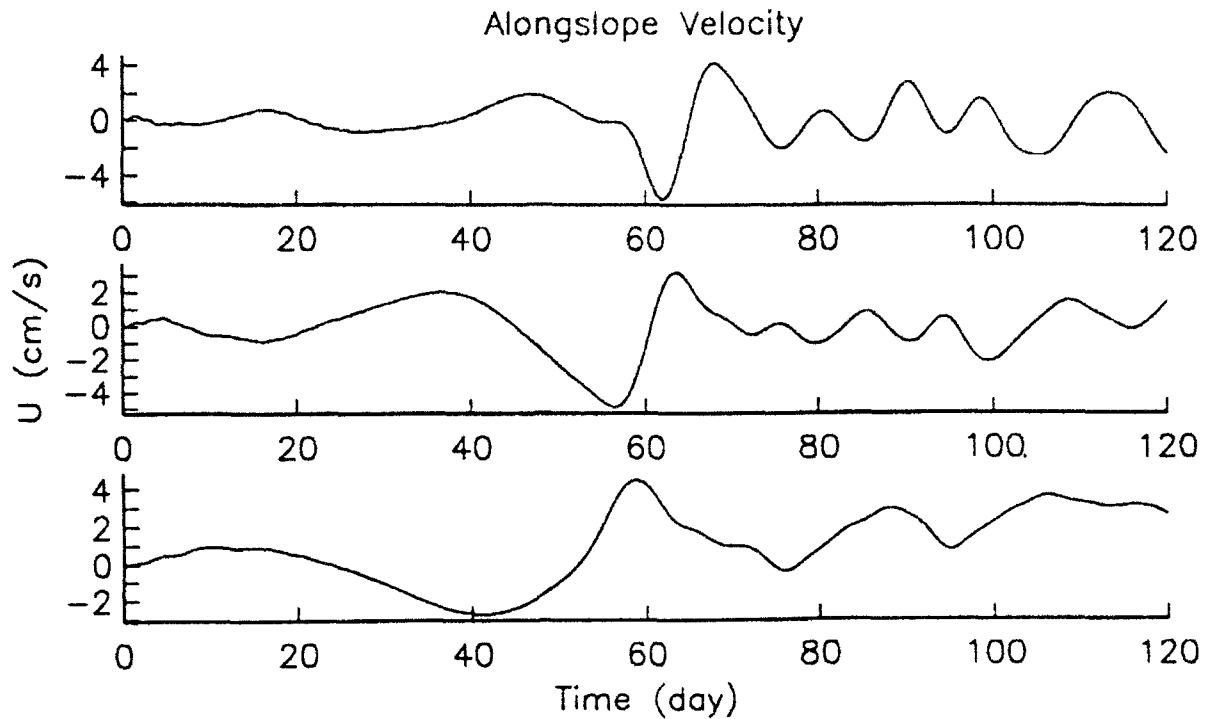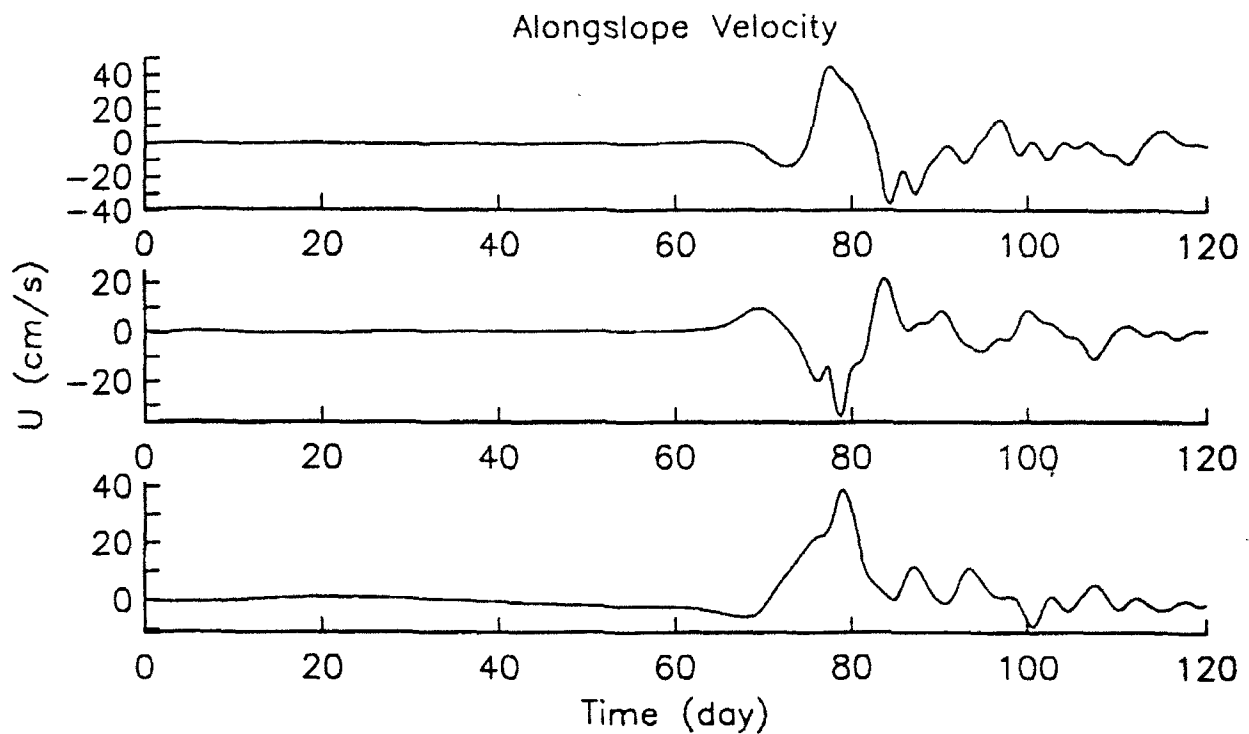
Figure 3.58: Alongshore velocity vs time for case B10 at three cross-shelf locations 150 km away from the left boundary. From top to bottom the locations are: 30 km, 67.5 km and 105 km away from the coastal wall.

The results of the cyclone-slope interaction are shown in figure 3.58 for case B10. It has been seen already from figure 3.47 that the original eddy moves onto the slope after day 64 and strongly radiates topographic waves. The perturbation velocity on the slope is exceptionally strong, close to 40 cm/s at inner shelf. as shown in figure 3.58 at three downstream locations across the slope. At all three locations the strong influences of the eddy passing through the lower slope are clearly seen as the large velocity events occurring between day 70 and 85. These are not the direct original eddy velocity field, but the strong wave-like and rapidly propagating perturbations generated by the impinging original cyclone. The slower propagating shelf/slope waves subsequently propagate through these locations shown as smaller amplitude oscillations following the eddy events. The alongshore velocity along the 105 meter isobath contour (37.5 km away from the coast wall) is plotted in figure 3.59 from day 65 to 95. The large amplitude waves are seen to propagate rapidly to the left and then are followed by the smaller amplitude waves.

185
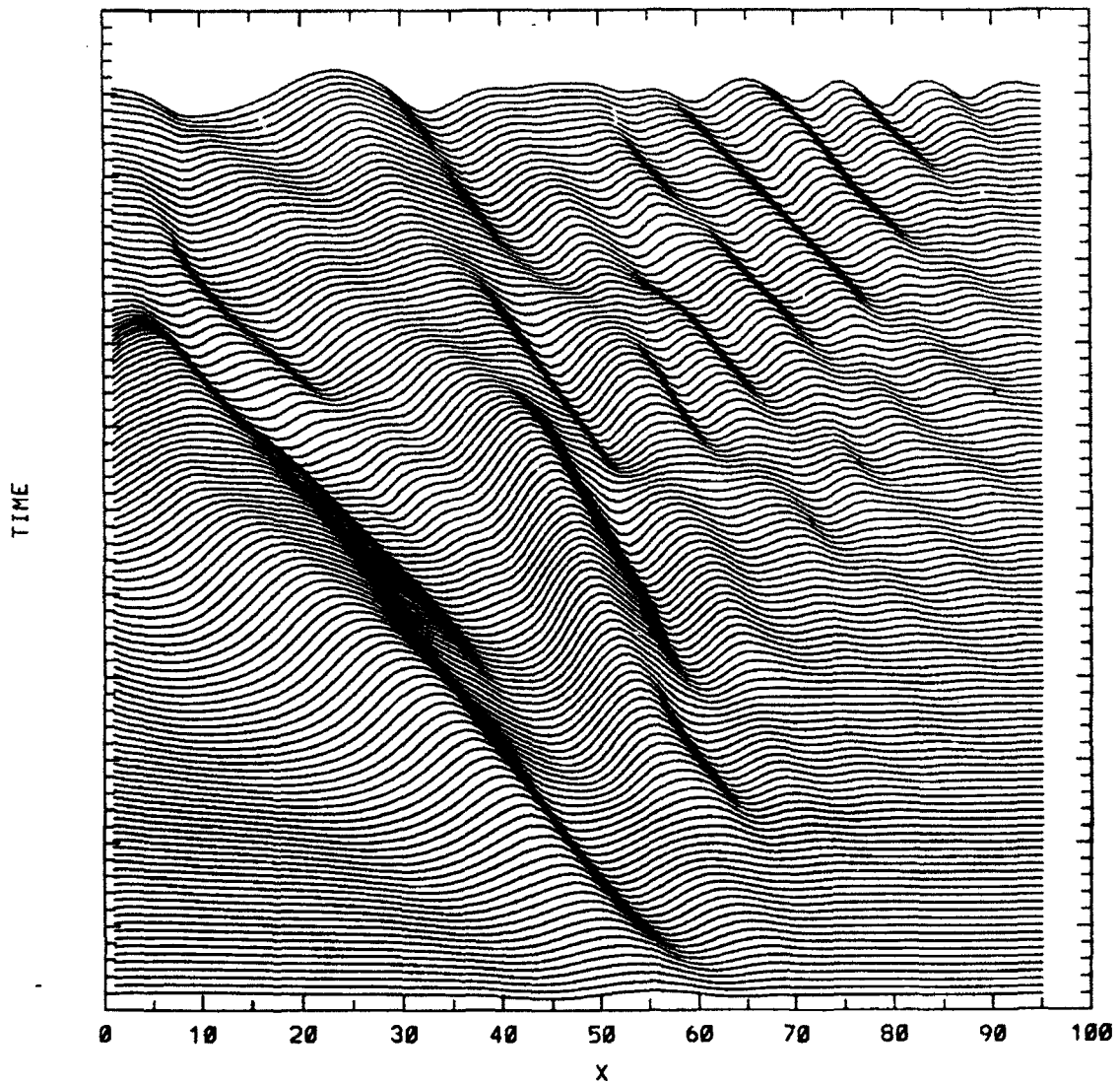
Figure 3.59: Snap shots of alongshore velocity on the 91 meter isobath contour (30 km away from the coastal wall) from day 0 to day 20 with interval of 6 hours. The horizontal axis is the alongshore distance (.5km) and the velocity at a given time is plotted as a curve stacked vertically with increasing time.
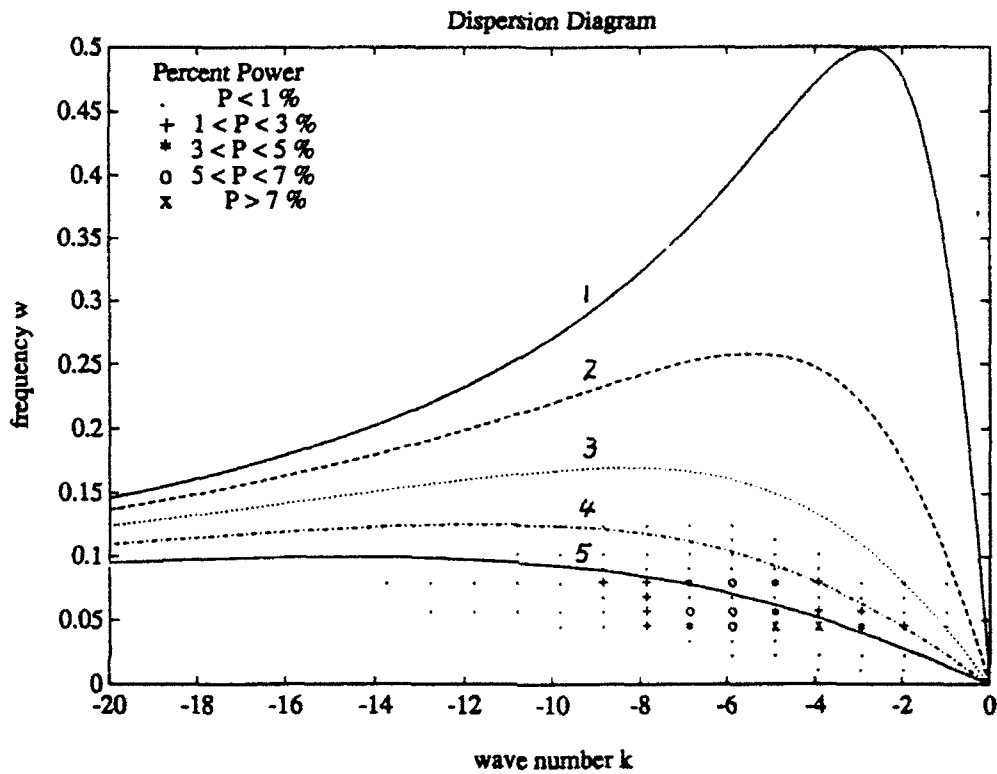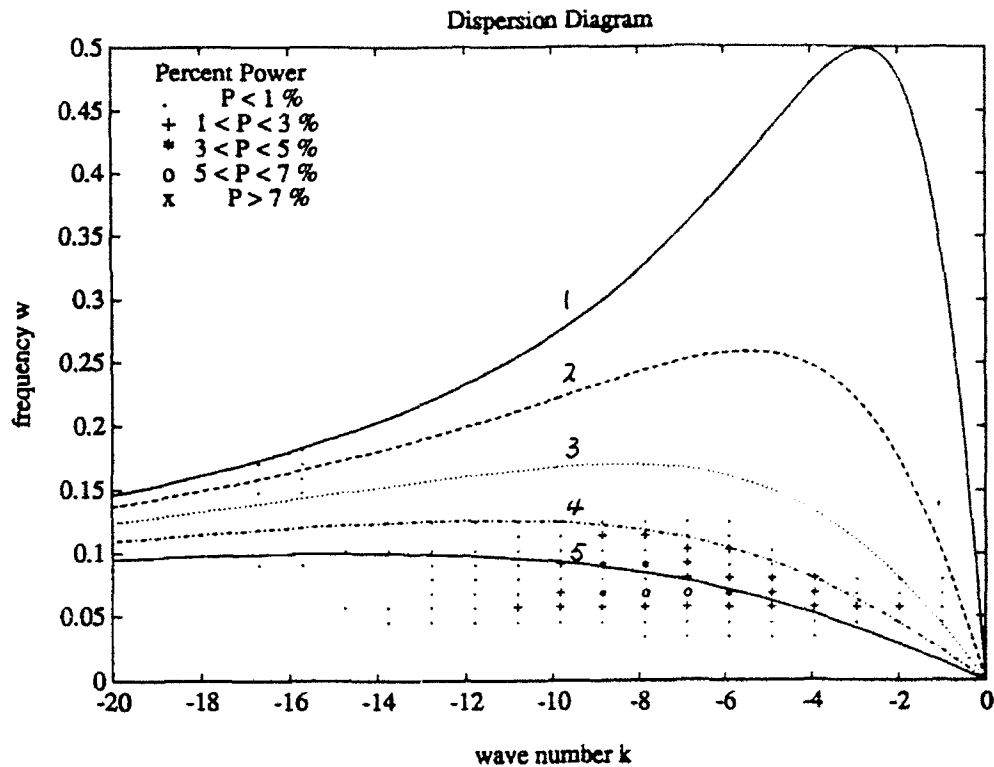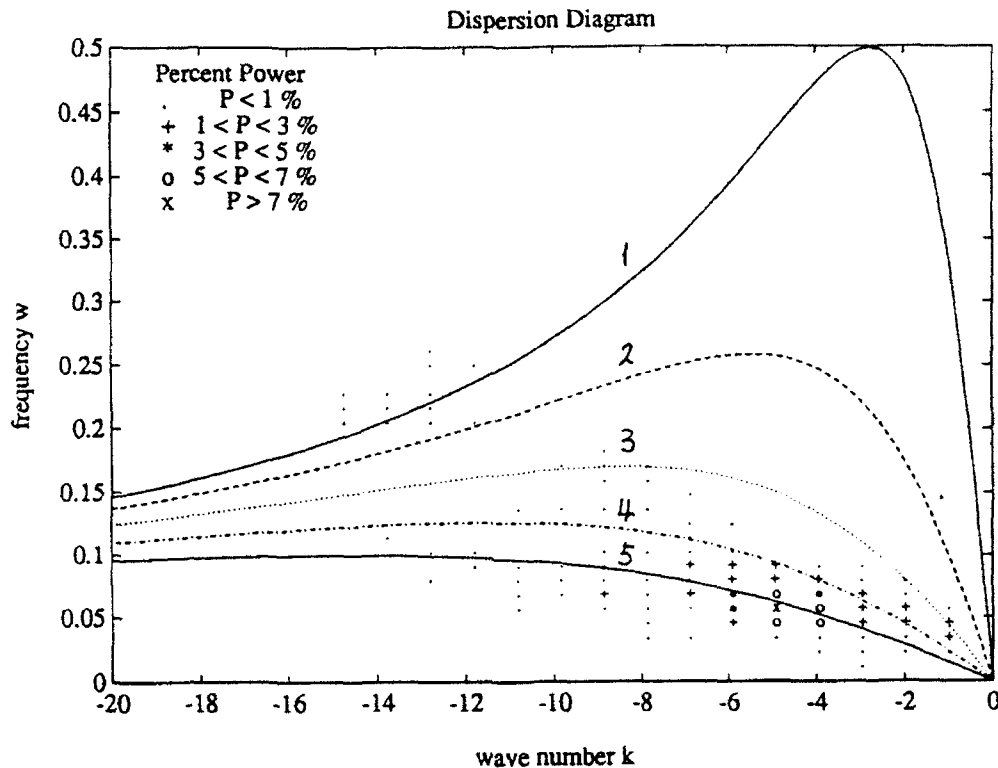
Figure 3.60: Spectral energy density scatter plot on the shelf trapped wave dispersion diagram for Case B10. The dispersion curves are the same as the figure 3.56

A series of short waves with right-going group velocity is also observed. These possibly consist of the short wave disturbances and the short wave components of the original eddy. The amplitudes of these short waves are small compared with those left-going long waves. The corresponding alongshore velocity energy scatter plot for the velocity record of in figure 3.59 is shown in figure 3.60. The basic structure of the energy distribution among different wave modes are the same as the two cases discussed previously. A small amount of short-wave energy with right-going group velocity is seen to follow the mode 1 dispersion curve. The major responses are in high mode waves with $(k, \sigma)$ centered around $(-5, 0.05)$.

The shelf/slope responses on the $\beta$-plane caused by the eddy-topography interaction are similar to the $f$-plane situation. The transfer of the eddy perturbation energy into shelf wave modes is governed by the $f$-plane dynamics. Therefore, the results from the previous section on the dependence of shelf response upon various other parameters will apply directly to the $\beta$-plane situation.

## 3.5 Summary and Conclusions

In this chapter the interactions of a mesoscale eddy with a shelf/slope topography are studied. Due to the different dynamics governing the motion of the isolated eddy, the problem is investigated separately on the $f$-plane and the planetary $\beta$-plane. The major differences exist in the eddy movements and its time dependent decay. Some quantitative changes in the interaction processes are observed as the consequences of the $\beta$-dependent activities. There are, however, no fundamental differences in shelf/slope responses and cross-slope exchanges between the results of these two models. Therefore some of the $f$-plane results may apply directly to the corresponding $\beta$-plane problem. Particularly the results of the cyclone-topography interactions are similar on both the $f$-plane and the $\beta$-plane, due to the fact the eddy is trapped to the topography and topographic $\beta$ is always dominant over planetary $\beta$.

The most important results of this chapter are summarized below.

1. The cross-slope exchanges are determined by the strength and the size of the eddy, and the penetration of the eddy onto the slope. For given penetration distance, the strong or large eddy will cause the upper-slope fluid to cross the topography and result in a strong interaction; while the weak or small eddy will mainly advect across topography the fluid from the immediate vicinity of the slope boundary. The large onslope penetration will cause volume transport from upper-slope and perturb the shelf water more effectively.

2. The properties of the topographic eddy are strongly dependent on the strength of the interaction. The size of the topographic eddy does not vary much with the interaction strength, but the circulation and intensity of the topographic eddy depend strongly on it.

3. Multiple eddy-topography interactions are possible for an anticyclone interacting with a shallowing slope. The multiple interactions may not contribute to increase

the cross-topography volume transport. On the other hand, they may reduce the accumulated volume transport by transporting the water back onto the slope.

4. On the $\beta$-plane the interaction is dependent upon the eddy incident angle. The perpendicular eddy incidence is the most effective for eddy penetration onto the slope.

5. The eddy-topography interaction may result in the losses of eddy volume and momentum. In general it also increases the eddy decay rate over the radiation and frictional decay rate. But the formation of the topographic eddy and the subsequent dipole-like eddy pair may suppress the planetary decay and thus reduce the eddy decay rate.

6. The cyclone is trapped to the slope and consequently breaks apart quickly on the slope due to the intense topographic wave radiation. It is, therefore, more effective in inducing motions on the shelf. It does not, however, cause large offslope volume transport.

7. The continental shelf waves are generated through eddy-slope interactions. These waves are intermittent, and propagate along isobath contours with the coast on the right.

8. An eddy-induced residual current on the $\beta$-plane is observed. The current is part of the offshore circulation cell and is opposite to the direction of the original eddy circulation.

In particular, the major differences and similarities between the $f$-plane and $\beta$-plane eddy-topography interactions are summerized and compared against each other.

| $f$-plane | $\beta$-plane |
|---|---|
| **Anticyclone** | **Anticyclone** |
| **Volume Transport** | **Volume Transport** |
| It is dependent on the size and strength of the original eddy, the distance between the eddy and the topography, and the geometry of the topography. | It is slightly smaller than the corresponding $f$-plane case due to the eddy decay. It is also dependent on the eddy incident angle. |
| **Topographic Eddy** | **Topographic Eddy** |
| Formed due to vortex stretching of the slope water advected seaward by the original eddy, the topographic eddy is cyclonic and may be transported back to the slope. | Similar to the $f$-plane eddies. The results vary slightly depending upon the incident angle of the original eddy. |
| **Motion and Decay of the Original Eddy** | **Motion and Decay of the Original Eddy** |
| Multiple eddy-slope interactions are possible. A net westward alongslope drift (facing the coast) result. Eddy-slope interaction produces a quick loss of eddy kinetic energy and mass at rates much larger than frictional decay. | Both differ from $f$-plane case due to the planetary $\beta$-effect. The results depend strongly on the eddy incident angle. Both eddy-slope interaction and planetary Rossby wave radiation cause the eddy to decay. The dipole suppresses the radiation decay. |
| **Shelf/Slope Waves** | **Shelf/Slope Waves** |
| They are shelf/slope trapped modes. | Similar to the $f$-plane case. |
| **Residual Current** | **Residual Current** |
| It is not observed explicitly. | It is observed near the edge of the slope and is opposite to the direction of the original eddy circulation. |
| **Cyclone** | **Cyclone** |
| It is trapped at the topography and does not induce much transport. Effective in causing shelf/slope perturbations. | Virtually similar to the $f$-plane case. The eddy decays slightly faster due to the planetary $\beta$ effect. |

It is recognized that the barotropic assumption of this study puts a strong constraint on the applicability of the model results to the realistic oceanic situation. In the light of this study, future investigations will focus on the effects of stratification and density fronts in the eddy-topography system. It is expected that three-dimensional field evolutions will add new aspects into the system, such as the frontal instabilities, upwelling and density driven currents. The present study achieves, however, important progress in understanding the fundamental dynamics of the eddy-slope interaction and the responses of both the eddy and the shelf/slope. The results enable some direct comparisons with the oceanic observations. In next chapter, the observations from some areas of the world ocean are discussed and compared with the present model results.

# Chapter 4

# Comparison of Model Results with Oceanic Observations

Observations in many of the world continental margins show that mesoscale eddies frequently interact with bottom topography. In particular eddy-topography interactions are often observed near oceanic western boundaries, where mesoscale eddies form due to unstable current meanders and baroclinic instability processes. In this chapter the interaction processes observed on the eastern continental margins of the United States and in the Gulf of Mexico will be examined and compared with the model results from the previous chapters. It is hoped that the model-observation comparisons will provide physical insight into complex, real world eddy-topography interactions and enable a better understanding of the interaction processes.

## 4.1 Gulf Stream Ring and Topography Interactions

There is a persistent frontal boundary separating shelf and slope water near the continental shelf break in the Mid-Atlantic Bight. Frequently this front is perturbed by Gulf Stream warm-core rings (WCRs here after) incident on the slope region. The frontal disturbances can develop into unstable wave-like distortions (Halliwell and Mooers, 1979; Ramp et al, 1983) and form shelf water streamers which extend seaward and sometimes spiral around the ring (Morgan and Bishop, 1977; Bisagni, 1983; Evans et al, 1985; Joyce et al, 1992). The seaward disturbances may detach parcels of shelf water and form smaller cyclonic eddies in the slope region (Cresswell, 1967; Wright, 1976; Kennelly et al, 1985).
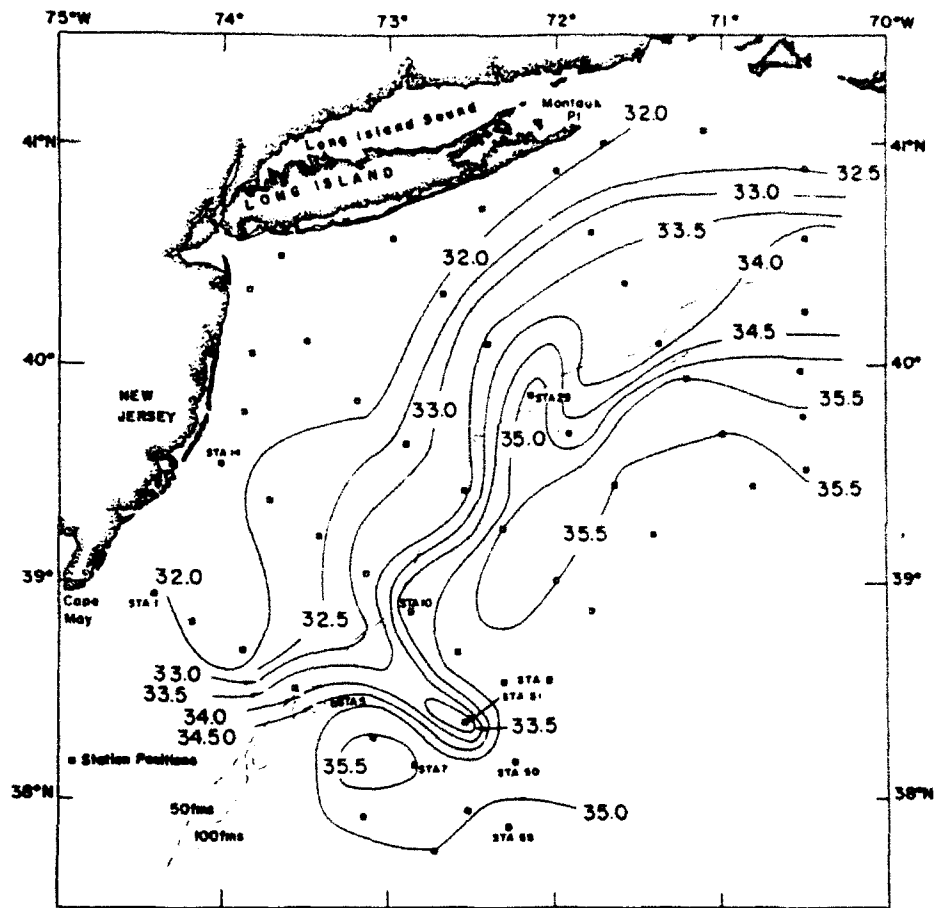
Figure 4.1: Salinity field at 10 m depth. After Morgan and Bishop (1977).

A significant amount of cross-shelf/slope exchange is attributed to these ring-induced events (Morgan and Bishop, 1977; Smith, 1978; Churchill et al, 1986; Joyce et al, 1992).

Figure 4.1 shows an instantaneous salinity field at 10 m depth in the Mid Atlantic Bight adapted from a paper of Morgan and Bishop (1977). A tongue of fresher shelf water is drawn across the shelf/slope front by a Gulf Stream WCR (characterized by salinity higher than 35 psu) drifting close to 200m isobath, though the spatial resolution of the hydrographic stations is somehow coarse compared with the dimension of the tongue. The size of the tongue is roughly 80 km long, 30 km wide and 50 m thick, extending seaward due to the advection of the anticyclonic ring induced velocity field. This feature is similar to the initial field development of the anticyclone-topography interaction from the model simulation, such as that shown in figure 3.18a, the potential vorticity field for case F1 at day 4. However, the observed shelf water tongue extends seaward approximately perpendicular to the isobath contour, while the model result shows that the offshore flow

is tangential to the eddy perimeter and intersects the isobath contour at an angle. This is likely due to the strong perturbation velocity field caused by barotropic vortex stretching, which tends to advect the original eddy to the right against the cyclonic tongue.

Generally the observations suggest that these tongues are caused by a ring advecting shelf water around its perimeter. The tongues are usually connected to their origins as they encircle the WCRs. Further evidence is given by Churchill et al (1986). They find that in a cross shelf-slope temperature section the same water mass appears on both sides of the WCR 83D. They show that it is a band of middle or outer shelf water drawn seaward by the WCR. Instead of extending from surface to bottom, the tongues usually have thickness of 50 to 100 meters in the upper water column. In the model, as the tongue is drawn from shallow water to deep water, the vortex stretching effect is exaggerated due to the barotropic assumption. The stretching generates strong velocity shear in the tongue, which affects the propagation of the original vortex. The original eddy advects the cyclonic tongue away from the front, and then the tongue tends to separate from its origin and evolve into a cyclonic topographic eddy. This process is also described in chapter two on topographic eddy formation during vortex-escarpment interaction.

Similar to the formation of topographic cyclones in the model results, observations also show the existence of small cyclones in the vicinity of Gulf Stream WCRs (Kennelly et al, 1985; Evans et al, 1985). Possibly formed in the slope region, these cyclones are approximately 40 to 50 km in diameter and have lifetimes of several weeks. The study by Kennelly et al (1985) indicates that the water mass in the cyclones is formed north of the ring center and is of shelf origin, containing a mixture of both shelf and slope water. The velocity of the cyclone is fairly barotropic over a depth range of upper 1000 m of the water column and with a maximum value about 60% of that of the WCR. Some formation mechanisms for these small cyclones have been proposed. Kennelly et al (1985) cite baroclinic instability and the tendency for the original eddy to spin up a barotropic modon as possible mechanism. The present model results suggest that vortex stretching

Figure 4.2: Satellite image of WCR 82B during May 5, 1982. High-resolution image highlighting a ringlet adjacent to 82B with acoustic-Doppler-obtained velocity vectors superimposed. Adapted from Kennelly et al (1985).

of the shelf water tongue is another possible mechanism for cyclonic eddy generation. From figure 4.2, adapted from Kennelly et al (1985) , one can clearly see the formation of a small cyclone off the head of a shelf water tongue drawn seaward by WCR 82B. Another cyclonic feature to the southeast of 82B can also be seen. The two cyclones are advected clockwise around the WCR. This is very similar to the interaction process shown in figure 3.34 at day 56 for case B4. Figure 3.34 shows the flow field during the second eddy-topography interaction. A cyclonic topographic eddy is forming from the seaward flowing shallow water tongue. The interaction perturbs the shape of the original eddy elliptically. The cyclone from the first interaction is still seen to the left of the original eddy. The comparison shows that even the orientation of the elliptical eddy is roughly in the same direction as observed by Kennelly et al (1985). The small cyclones in the model usually end up moving back onto the slope and being destroyed there.

Their lifetime, about 20 to 30 days, is close to the lifetime of the cyclones observed by Kennelly et al (1985). The fate of the cyclones observed by Kennelly et al (1985) is not clear. Presumably they are either entrained into WCRs, absorbed by the Gulf Stream, or dissipated and mixed on the slope as occurs in the model. According to Kennelly et al (1985) detached cyclones are found throughout the slope water, with observed lifetimes of 1 to 2 weeks. The mechanism causing the separation of these cyclones from the perimeter of a WCR is not known. Several possibilities are proposed here. Firstly, it may be due to the ring interacting with the shelf/slope front. The cyclones tend to be trapped at the front and dissipate there. Secondly, it may be affected by the ring-ring or ring-stream interactions. Finally baroclinic instabilities may cause the ringlet to detach. Only the first mechanism can be studied with the present model.

The seaward flowing shelf water tongues and small cyclones are important features of cross shelf/slope transport. They play a significant role in the maintenance of shelf and slope water mass properties. Wright (1976) indicates that in the Mid Atlantic Bight about 2400 $km^3/year$ of shelf water must be transported offshelf to maintain the salt balance due to a fresh water runoff about 157 $km^3/year$ onto the shelf. The ring-shelf/slope interactions may be responsible for a significant portion of the total exchanges. The estimates of the ring-induced transport for a single interaction event vary greatly from available observations. They strongly depend on two factors: the rate of transport and the duration of the interaction. A reasonable estimate of the duration is the time length of ring-induced shelf streamer events. According to Evans et al (1985), the average duration of such events is approximately two weeks. Using this and available observations, the measured rate of seaward transport and the net total transport in a single interaction event are shown in table 4.1. No corrections are made about shelf and slope water mixing or transport back to the shelf. The estimates in this table are prone to different sources of errors and are considered only as orders of magnitude. The transport varies for different eddies and interaction strength, as suggested already by the numerical calculations. The barotropic model results tend to give larger transport rates than observations. If the

## Table 4.1

| Authors | Rate of Transport $(10^6 m^3/s)$ | Net Transport $(10^{12} m^3)$ |
|---|---|---|
| Morgan and Bishop (1977) | 0.0089 | 0.011 |
| Smith (1978) | 0.19 | 0.23 |
| Bisagni (1983) | 0.15 | 0.18 |
| Churchill et al (1986) | 0.048 | 0.058 |
| Joyce et al (1992) | 0.87 | 1.1 |
| This study | 2.9 | 3.5 |

Estimated eddy induced volume transport from different sources.

model transport of a slab-like seaward flowing tongue with just upper 100 meters is considered, the transport rate and total transport become $0.3 \times 10^6 \ m^3/s$ and $0.35 \times 10^{12} \ m^3$, respectively. These are close to the average values of the observed transport. The major uncertainty here is the total time of the model interaction compared with that in the observations. The former is about two weeks, while the latter is obscure and is commonly assumed to be about two weeks (Evans et al, 1985; Churchill et al, 1986) to two months (Smith, 1978). In addition, the present numerical results suggest that the occurrence of multiple eddy-topography interactions acts to transport water back onto the shelf. The total accumulated transport is effectively reduced by this mechanism. In observations it is difficult to resolve the occurrence of multiple interaction events, since instability processes, eddy-eddy or eddy-stream interactions and external forcing can strongly affect eddy propagation.

The movement of Gulf Steam Rings can be monitored by freely drifting buoys or identified from satellite images. Recent measurements enable very accurate tracking of rings, especially warm-core rings, through their surface thermal signatures. The general results agree with the historical data that rings propagate on average southwestward with speeds ranging from several to a few tens of centimeters per second. The ring trajectories and speeds vary as they encounter bottom topography and interact with the Gulf Stream. Warm-core ring 82B was studied using satellite-derived AVHRR thermal images for about a half year time period in 1982 by Evans et al (1985). During that period 82B propagated southwestward in the Mid Atlantic slope region and finally merged with the Gulf Stream near Cape Hatteras. Figures 4.3a and b are adapted from Evans et al (1985). On average the ring propagates southwestward roughly following the isobath contours. When it encounters the irregular bottom topography at the Hudson Canyon in J.D. (Julian Days) 109–123, the ring turns westward and its speed increases from 2.5 cm/s to about 7 cm/s. The subsequent event resembles an eddy incident onto a shallow topography with an oblique angle. The eddy center experiences a depth change of about 400 m. As in the model results, the ring is expelled southeastward from the topography
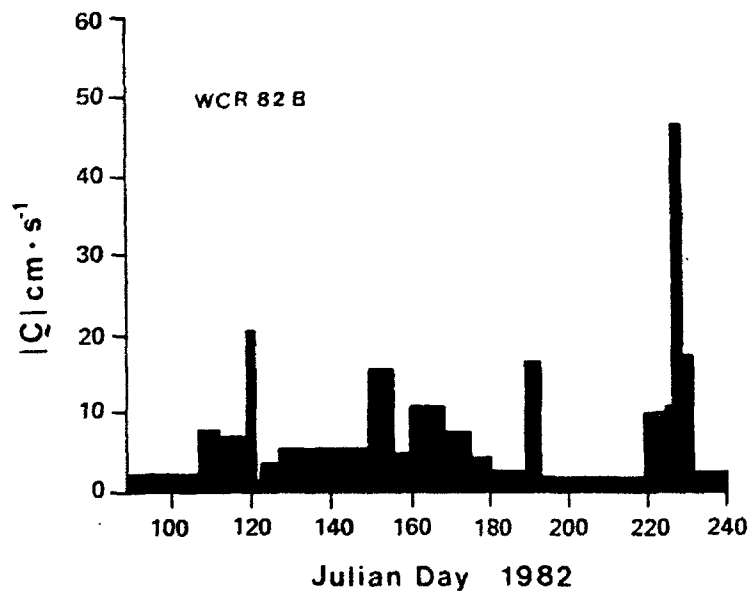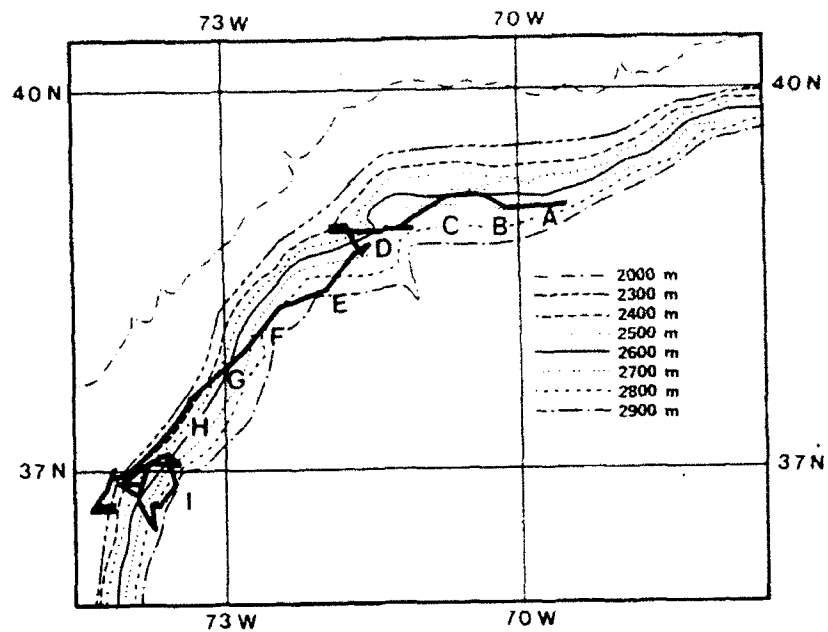
Figure 4.3: Upper panel: The location of ring center track for 82B relative to bottom topography. Letters are placed to major event locations: A, ring formation (Julian days 39–56, J.D. here after); B, 82B and the Gulf Stream encounter (J.D. 77); C, cold shelf water entrainment (J.D. 85–95); D, Hudson Canyon passage (J.D. 109–123); E, cold shelf water entrainment (J.D. 132–139) ; F, the Gulf Stream streamer entrained into 82B; G, start of Wilmington-Delaware Canyon passage (J.D.153); H, cold entrainment period (J.D. 168); I, Cape Hatteras area, the Gulf Stream encounters with 82B (J.D. 183–238). Lower panel: WCR 82B absolute translation speed versus time. After Evans et al (1985).

199

into the deep water. At the same time a cross-shelf volume transport is induced by the ring velocity field and shelf water entrainment is observed. The ring ellipticity increases and its major axis orientation rotates from north-south to east-west. Meantime a cyclonic vortex to the northeast of 82B is seen and is associated with a strong streamer that wraps cold shelf water around the east side of 82B. After J.D. 123 (position D) the planetary and topographic $\beta$-effects again apparently dominate the ring's motion, which is back towards southwestward with a speed of about 5 cm/s. Evans et al (1985) notice that as a ring moves toward shallow topography such as in the ring-topography interaction during J.D. 109–123, there are often cyclonic vortices generated to the northeast of the ring. These vortices are usually advected clockwise around the ring and cause entrainment into the WCR. Ring-topography interaction and cyclone formation also affect the size and the shape of WCR 82B. These features are qualitatively similar to the present model results.

A case of a Gulf Steam cold-core ring (CCR) impinging on a shallow topography is reported by Cheney and Richardson (1976). Their figures 6 and 7 are adapted here as figure 4.4a and b. In a series of hydrographic surveys, they find that a CCR encounters the Blake Plateau in the western Sargasso Sea, where the water depth shallows from 5000 m to less than 1000 m. The ring undergoes large changes as it climbs onto the Blake Plateau. The decay rates of the ring's available potential energy, kinetic energy and azimuthal transport increase four fold. There is a significant loss of ring volume and its radius shrinks from 75 km to less than 30 km. As the ring moves onto the Blake Plateau, it loses part of the lower ring structure and the ring bottom is squashed. The model results indicate strong Rossby wave radiation taking place in such a situation, thereby weakening the strength of the CCR and contributing to the increased ring energy decay rate. According to Cheney and Richardson, the topography had little effect on the movement of the ring. In contrast, the model results show accelerated eddy propagation toward the topography. This may be due to the baroclinic structure of the ring, which presumably decouples the strong topographic influence from the upper layer ring motion.

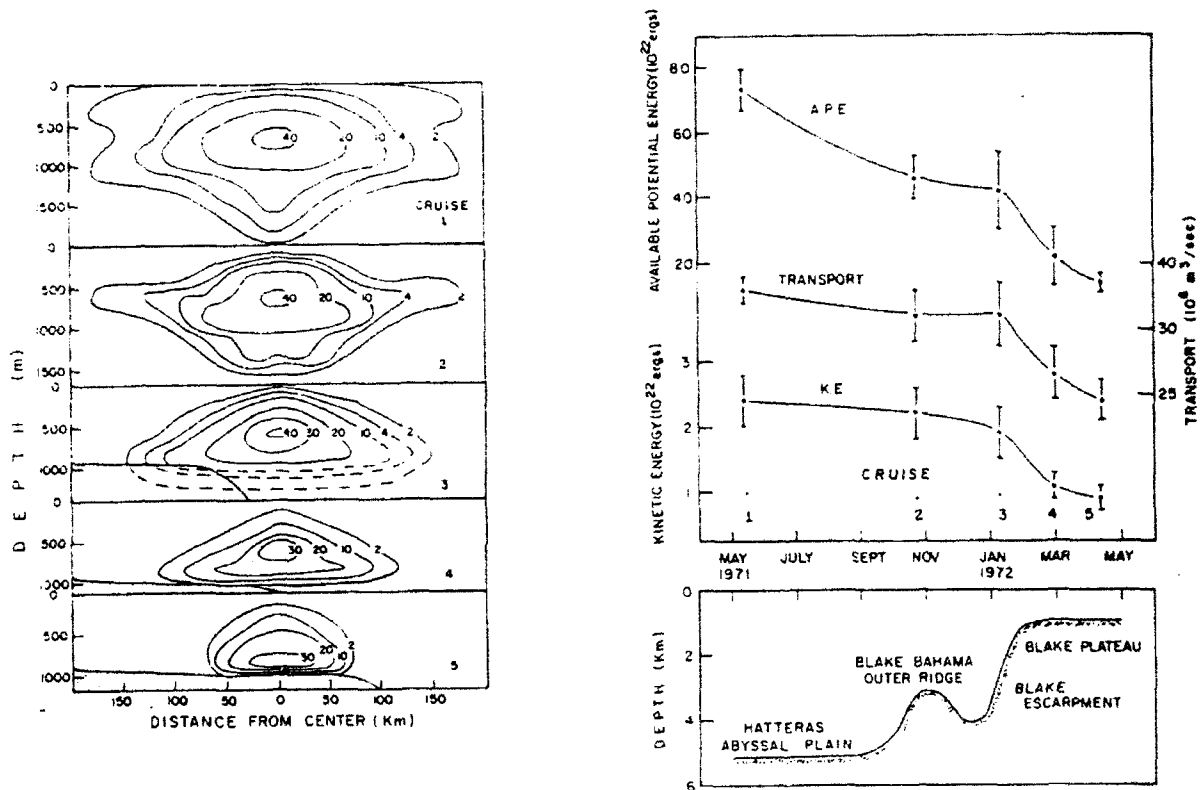Figure 4.4: Left panel: Decay sequence described by contours of available potential energy density. Contours are in units of $10^3$ ergs/g. Bottom depth is shown for the passage of the ring onto the Blake Plateau. Right panel: Decay of available potential energy, transport and kinetic energy relative to 1000 m. Variation of the depth under the center of the ring is shown below. After Cheney and Richardson (1976).

201

Direct observation of shelf waves induced by mesoscale eddies is difficult, though some limited evidence is available in the work of Halliwell and Mooers (1979), Louis et al (1982) and Ramp (1989). Basically, eddy-induced topographic waves are divided into two types: across-shore propagating topographic Rossby waves and alongshore propagating shelf-trapped waves. Shoreward propagating topographic Rossby waves originating from a nearby source have been studied by a number of investigators: Hogg (1981), Louis and Smith (1982), Shaw and Peng (1987), Ramp (1989) and Shaw and Divakar (1991). Since the slope is an excellent insulator of energy transmission at longer time scales (> 10 days), topographic Rossby waves originating from the deep ocean or the lower continental rise can not readily penetrate the continental slope. Shaw and Peng (1987) and Shaw and Divakar (1991) show that for sources on the upper rise, some of the energy can reach onto the shelf. Ramp (1989) provides observational evidence for onshore-propagating topographic Rossby waves due to a nearby warm-core ring on the slope. His calculation gives group velocities of −11 and −40 km/day at the shelf break region near Georges Bank for across-shore and alongshore propagation, respectively. The alongshore-propagating shelf-trapped waves are generated by a shelfward flux of momentum and forced water column perturbation due to direct eddy-shelf contact. Unlike shoreward propagating topographic Rossby waves, continental shelf waves are coastally trapped and propagate only along isobath contours with amplitude generally decreasing offshore. Ramp's (1989) results show both alongshore and across-shore wave propagation. He calculated an alongshore wave propagation of 40 km/day (or .46m/s), though no cross-shore wave amplitude information is given. These alongshore wave components may contain both the waves directly excited by the eddy forcing and the shoreward propagating topographic waves that are refracted to alongshore direction as they shoal. However, given the proximity of the source location and increasing dissipation near coast, the wave refraction effect must be relatively small. Ramp (1989) also argues that the shelf and slope waves so generated cannot travel very far alongshore due to strong frictional dissipation in shallow water. Since the shelf and slope responses are fairly barotropic (Louis et al, 1982; Chapman

and Brink, 1987; Ramp, 1989), bottom friction can be modeled as a body force on the entire water column. Ramp estimates that on the 325 m isobath, using bottom drag $C_D = 2 \times 10^{-3}$ and water particle velocity $V_b = 20$ cm/s, the alongshore dissipation length scale for the wave is about 325 km. This length scale is even smaller in shallower water. This result basically agrees with the results of frictional shelf/slope model experiment. The model results further indicate that the location of the maximum shelf response shifts seaward. Since eddy-topography interaction is intermittent, the shelf and slope waves also show intermittency. This property can used as an indicator to detect such waves in a time series observation (Louis et al, 1982).

## 4.2 Loop Current Eddy in the Gulf of Mexico

The unstable Gulf of Mexico Loop Current can detach anticyclones with radii of about 100 km into the Gulf of Mexico. These eddies are known to propagate southwestward into the western gulf where they collide with the continental shelf and slope. The western gulf is bounded to the north and south by continental boundaries. The collision of a Loop Current Eddy (LCE) with the western gulf boundary is physically similar to the present model study of an anticyclone colliding against a western boundary.

Kirwan et al (1984) use satellite-tracked drifters deployed in a LCE to study eddy evolution and propagation. Their results indicate that the southwestward propagation of an LCE slows down as it encounters the western gulf slope. The eddy shape is perturbed elliptically during its interaction with the shelf and slope. After reaching its maximum shelfward penetration distance, the eddy moves temporarily northeastward. According to the present study, this is likely due to the combined effects of the cyclonic shelf/slope perturbation velocity and topography-induced nonlinear self-advection of the LCE. The east-west orientation of the elliptical eddy also agrees with the model results. It is difficult to detect whether or not the eddy's long axis rotates during the interaction.

In another study, Vidal et al (1992) examine the collision of a LCE against the western gulf shelf and slope. Upon colliding, the anticyclonic LCE sheds approximately one third of its volume (about $2 \times 10^4$ $km^3$) and its strength is considerably weakened. Their observation tends to indicate that the lost momentum and relative vorticity of the eddy due to the collision probably support the shear flow to the north and south along the western gulf shelf break. Similar behaviors are found in the present numerical study. In the model, the along-topography current is observed during the eddy-slope collision. It is usually associated with a weak cyclone to the northeast of the original anticyclone for the case of eddy impinging a west-bound slope. The strength of the cyclone is enhanced through close interaction with the original anticyclone. The near-slope portion of the cyclone is squashed against the slope and thus intensifies a jet-like along slope current (such as that shown in figure 3.29 at t=56 days). A smaller temporary cyclonic feature can also be seen to the south of the original eddy. During this interaction the anticyclone also loses a portion of its volume and energy as shown in figure 3.32, and transports a certain amount of slope water into the deep ocean.

Cyclonic eddies to the north of slope-colliding LCE's in the western Gulf of Mexico have been observed quite frequently (Merrell and Morrison, 1981; Hamilton, 1992). Figures 4.5a and b show two examples. Merrell and Morrison estimated a net eastward (offshore) transport of $29.7 \times 10^6$ $m^3/s$ between the centers of the cyclone and anticyclone. The transported fluid consists of mixtures of LCE water (i.e., Subtropical Underwater) and Gulf Common Water. The anticyclone is greatly enlongated in east-west direction. The influence of this eddy pair on the exchange between the shelf and the western gulf is not known for this event. According to the present model results, the cross-shelf transport may be enhanced and the eddy pair may have a tendency to move offshore. This is unlikely to be true for the case observed by Merrell and Morrison (1981) because of the large eddy size. In figure 4.5b from Hamilton (1992), two cyclonic features are seen north of the anticyclonic eddy. The one to the northeast can be explained as a trailing cyclone due to the Rossby wave dispersion mechanism discussed previously. The cyclone north
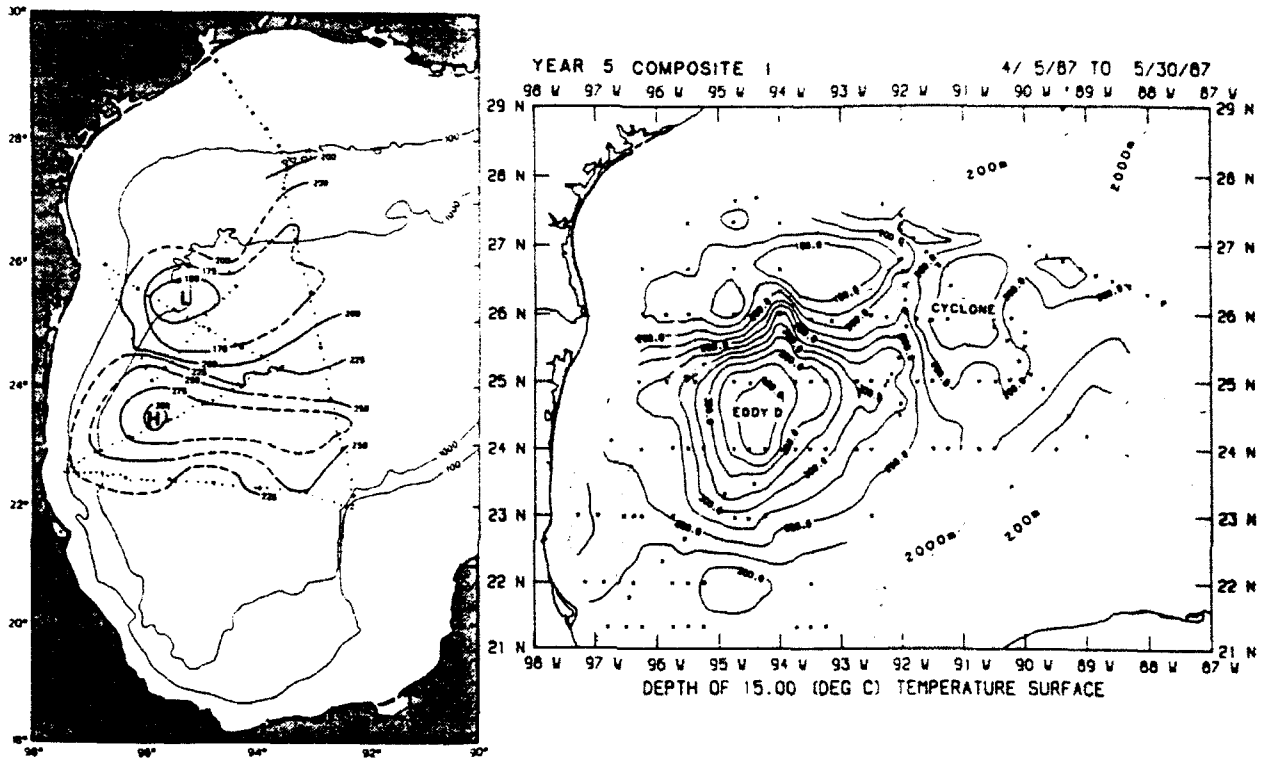
Figure 4.5: Left panel: Depth contours in meters of the 15°C isotherms as observed in April 1978. Centers of the anticyclonic and cyclonic circulation features are denoted by H and L, respectively. After Merrell and Morrison, 1981. Right panel: Depth contours in meters of the 15°C isotherms composited from observation during April 5 to May 30, 1987. After Hamilton, 1992.

of the anticyclone is on the slope and is likely generated by the velocity perturbation of the anticyclone-cyclone eddy pair. But Hamilton (1992) found that both cyclones have stronger deep signals in 8°C isotherm than the anticyclone, which implies that the anticyclone may not play an important role in the formation of the northern cyclone in the early stage. Another possible interpretation also exists that the anticyclone may influence the formation of the cyclones when its lower portion contacts with the slope. As the anticyclone is expelled seaward, its lower portion may be weakened by bottom friction and topographic wave radiation. The process is likely baroclinic and is beyond the scope of this study. Hamilton (1992) also finds that after six months the anticyclone moves northward alongshore and that there is only one cyclone observed to the north on Louisiana slope. It is not known if this cyclone is the remnant from one of the two previous cyclones. In the model, alongshore eddy propagation in the opposite direction to shelf waves may occur temporarily as the eddy is expelled away from the slope. The topographic $\beta$-effect tends to cause the anticyclone to move in the same direction as the shelf waves. Due to the fact that the LCE becomes more surface intensified as it drifts into the western gulf (Vidal et al, 1992), the interactions between LCE and continental slope are more baroclinic than the previous Gulf Stream ring cases, the comparison here is somewhat more problematic. Usually the shelf/slope responses are more barotropic, while the eddy propagation is more baroclinic.

## 4.3 Summary

The comparison between the model results and observations shows that they are qualitatively consistent. Due to the complicated nature of observed eddy-topography interaction processes, the comparison has to be made using different events to highlight the particular features contained in the observation. Some encouraging agreement is found for the most important processes produced by the model, such as cross-topography exchange, topographic eddy formation, eddy decay, and to a lesser degree, eddy propagation. Evi-

dence is taken from Gulf Stream rings and Loop Current Eddies, and more can be found from other shelf and slope regions where mesoscale eddies are active. It is realized that the effect of stratification is lacking in the model and that other mechanisms may also contribute to the above mentioned processes. For example, baroclinic instability may also assist the formation of observed small cyclones in the real ocean, where the cross shelf or slope volume transport is mainly confined to the upper 100 m depth. However, the model results provide some clear physical insight into the problem, highlight dynamic mechanisms for certain important features and shed light on the complicated eddy-topography interaction processes.

# Concluding Remarks

Through a simple to relatively complicated modeling effort, some fundamental aspects of the eddy-topography interaction process are investigated, such as the eddy-induced cross-topography exchange, topographic eddy formation, eddy propagation and topographic wave generation. The contour dynamics approach in chapter two, though having simple structure, produces the basic features of the interaction and sets up the framework for subsequent study. The primitive equation modeling, inheriting the same fundamental dynamics, recasts the important features of eddy-topography interaction and provides more realistic picture for both the eddy evolution and the shelf/slope responses. The comparison between the model results and the observations shows good qualitative agreement in many aspects and provides dynamical interpretations to some important features, such as the formation of topographic cyclone, the variation of the size, shape and strength of the eddy and the responses on the shelf and slope. Rough quantitative comparison for cross-slope volume transport seems possible allowing some margin of error due to the mechanisms not included in the model.

The model is limited by some assumptions, and the most important ones are the density homogeneity, the exponential topography with no alongshore variation and the idealized bottom friction. Other factors which may be important in influencing oceanic eddy-topography interaction but are not an intrinsic part of the modeled interaction process are currents, wind and thermal forcing. The model would be greatly improved by the inclusion of stratification, which would enable a more realistic treatment of the eddy as well as the shelf/slope density front. It would also introduce density adjustment processes into the interaction, reduce the vortex stretching compared to the purely barotropic case, and permit baroclinic instability processes. Observations show that most of the cross-shelf/slope exchange takes place in the upper 100 to 200 meters depth, and that the cyclonic eddies formed around the ring perimeter are not as intense as the topographic eddies found in the present study. Eddy propagation in a baroclinic ocean will

also be different from that in a barotropic model ocean (McWilliams and Flierl, 1979), and so will the planetary dispersion of the eddy components. The use of more realistic topography may alter extensively the model responses on the shelf and slope. The improved model would probably produce some results that are more quantitatively comparable with observations, such as volume of cross-topography transport and strength of topographic eddies. Other results, such as topographic waves on the shelf/slope, may become more obscure.

The restrictions on the study in chapter three can be relaxed readily in the numerical model. However, care must be taken to ensure that the numerical computation properly resolves the flow field in the presence of both large topography and density stratification using the vertical sigma-coordinate. Future work will investigate the role of density stratification in eddy-topography interaction processes and study the evolution of shelf and slope density fronts and cross-frontal exchanges. The focus will still be on the same important dynamical features identified by the simple contour dynamics model, but possible new mechanisms will be sought to better interpret the results.

# APPENDIX A

It can be shown for small amplitude escarpment waves that the correct dispersion relationship can be derived using either linear or nonlinear matching condition. Since the linear condition is valid only at small amplitude limit, it is a special case of the nonlinear condition. The nonlinear matching condition, equation (2.7), is the exact condition that a cross escarpment flow has to satisfy and is valid regardless of the amplitude limit.

## Nonlinear condition

We consider equations (2.16) and (2.17) without point vortex. The small amplitude limit allows us to approximate $\nabla^2 \psi$ by only $\psi_{yy}$ in the region between the interface and the escarpment. The potential vorticity interface is assumed to be sinusoidal $\eta_1 = a_1 \sin k(x - ct)$ for $y < 0$ and $\eta_2 = a_2 \sin k(x - ct)$ for $y > 0$, respectively. Integrating $\psi_{yy}$ on each side of the escarpment over the small interval between the interface and $y = 0$, we can get

$$u|_{0_-} = u|_{\eta_1} + \alpha h_1 \eta_1 \qquad (A.1a)$$

$$u|_{0_+} = u|_{\eta_2} - \alpha h_2 \eta_2 \qquad (A.1b)$$

where $\alpha = f\Delta h/h_1 h_2$. Now we consider the interface over one wave length, with $\eta_2 > 0$ in $x < x_0$ and $\eta_1 < 0$ in $x > x_0$. The stream function for small amplitude wave takes the form

$$\psi = \begin{cases} Ae^{ky} \sin k(x - ct), & y < 0 \\ Be^{-ky} \sin k(x - ct), & y > 0 \end{cases} \qquad (A.2)$$

For $x < x_0$, substituting $\psi$ and $\eta$ into (A.1) and matching $u|_{0_-} = u|_{0_+}$, we get

$$k(A + B) = \alpha h_2 a_2. \qquad (A.3)$$

Similarly, we can obtain

$$k(A + B) = \alpha h_1 a_1. \qquad (A.4)$$

(A.3) and (A.4) give $h_1 a_1 = h_2 a_2$. Substituting (A.2) into (2.7a) yields $h_1 A = h_2 B$. Applying these results to (A.4) for $y < 0$, we get

$$A = \frac{f}{k} \frac{h_1 - h_2}{h_1 + h_2} a_1. \qquad (A.5)$$

From $\eta_t = \psi_x$, we get the contour equation $\psi + c\eta = constant$. Substituting $\psi$ and $\eta_1$ into this equation, and letting the constant be zero, we obtain

$$A = -ca_1. \qquad (A.6)$$

Compare (A.5) with (A.6), we immediately get

$$c = -\frac{f}{k} \frac{h_1 - h_2}{h_1 + h_2}. \qquad (A.7)$$

The same result can be obtained by considering the contour on $y < 0$ side.

## Linear condition

The matching conditions obtained from linearized version of equation (2.1) are

$$[u_t] = f[v] \qquad (A.8a)$$

$$[p] = 0 \qquad (A.8b)$$

$$[vh] = 0 \qquad (A.8c)$$

Substituting (A.2) into (A.8a) to yield

$$c = -\frac{f}{k} \frac{A - B}{A + B},$$

and using (A.8c), we end up with (A.7).

# APPENDIX B

When the escarpment is finite, the flow across it experiences finite jump in velocity. For a particle crossing the escarpment within a given time step, the velocity used in contour dynamics calculation is taken to be an average of the velocity on both side of the escarpment. This average velocity can be calculated to an accuracy of order $O(\Delta h/h)$

If the particle travels a distance $\Delta y$ in a time interval $\Delta t$,

$$\Delta y = v_1 \Delta t_1 + v_2 \Delta t_2 = \bar{v} \Delta t$$

where $v_1$, $v_2$ and $\Delta t_1$, $\Delta t_2$ are the velocity and travelling time in the region of water depth $h_1$ and $h_2$, respectively; $\bar{v}$ is the average velocity in the whole time interval $\Delta t$, and $\Delta t_1 + \Delta t_2 = \Delta t$. Using equation (2.7a), for particle crossing the escarpment from $h_2$ to $h_1$ we obtain

$$\bar{v}_+ = \frac{\Delta y_2}{\Delta t} + \frac{h_2}{h_1} \left( v_2 - \frac{\Delta y_2}{\Delta t} \right)$$

where $\Delta y_2$ is the distance the particle travelled at $y > 0$ side during the time interval $\Delta t_2$, it is of the same sign as $v_2$. Similarly, for particle crossing the escarpment from $h_1$ to $h_2$, we obtain

$$\bar{v}_- = \frac{\Delta y_1}{\Delta t} + \frac{h_1}{h_2} \left( v_1 - \frac{\Delta y_1}{\Delta t} \right)$$

with $\Delta y_1$ being the distance the particle travelled at $y < 0$ side during the time interval $\Delta t_1$, and of the same sign as $v_1$.

# References

Bell, G. I., 1990: Interaction between vortices and waves in a model of geophysical flow, *Phys. Fluids, A, 2*, 575–586

Bell,. G. I., and L. J. Pratt, 1991: The interaction of an eddy with a unstable jet, submitted to *J. Phys. Oceanogr.*

Bell,. G. I., and L. J. Pratt, 1992: Eddy mean flow interaction theorems for piecewice constant potential vorticity flows, submitted to *J. Fluid Mech.*

Bisagni, J. J., 1983: Lagrangian current measurements within the eastern margin of a warm-core Gulf-Stream ring, *J. Phys. Oceanogr., 13,* 709–715

Brink, K. H., 1991: Coastal-trapped waves and wind-driven currents over the continental shelf, *Ann. Rev. Fluid Mech., 23*, 389–412

Buchwald, V. T., and J. K. Adams, 1968: The propagation of continental shelf waves, *Proc. Roy. Soc., A, 305*, 235–250

Carton, X. J., and J. C. McWilliams, 1989: Barotropic and baroclinic instabilities of axisymmetric vortices in a quasi-geostrophic model, Mesoscale/Synoptic Coherent Structures in Geostrophic Turbulence, ed. by J. C. J. Nihoul and B. M. Jamart, Elsevier

Chapman, D. C., and K. H. Brink, 1987: Shelf and slope circulation induced by fluctuating offshore forcing, *J. Geophys. Res., 92*, 11,741–11,759

Cheney, R. E., and P. L. Richardson, 1976: Observed decay of a cyclonic Gulf Stream ring, *Deep Sea Res., 23*, 143–155

Churchill, J. H., P. C. Cornillon, and G. W. Milkowski, 1986: A cyclonic eddy and shelf-slope water exchanges associated with a Gulf Stream warm-core ring, *J. Geophys. Res., 91*, 9615–9623

Cresswell, G. H., 1967: Quasi-synoptic monthly hydrography of the transition region between coastal and slope water south of Cape Cod, Massachusetts, Ref. 67-35, WHOI

Csanady, G. T. and P. T. Shaw, 1983: The insulating effect of a steep continental slope, *J. Geophys. Res., 88*, 7519–7524

Dritschel, D., 1988: Nonlinear stability bounds for inviscid, two-dimensional, parallel or circular flows with monotonic vorticity and the analogous three-dimensional quasigeostrophic flows, *J. Fluid Mech., 191*, 575–581

Evans, R. E., K. S. Baker, O. B. Brown, and R. C. Smith, 1985: Chronology of warm-core ring 82B, *J. Geophys. Res., 90*, 8803–8813

Flierl, G. R., 1987: Isolated eddy models in geophysics, *Ann. Rev. Fluid Mech.*, *19*, 493–530

Gill, A. E and E. H. Schumann, 1974: The generation of long shelf waves by the wind, *J. Phys. Oceanogr.*, *4*, 83–90

Gill, A. E., M. K. Davey, E. R. Johnson, and P. F. Linden, 1986: Rossby adjustment over a step, *J. Mar. Res.*, *44*, 713–738

Grimshaw, R, and Z. Yi, 1990: Finite amplitude long waves on coastal currents, *J. Phys. Oceanogr.*, *20*, 3–18

Haidvogel, D. B., J. L. Wilkin, and R. E. Young, 1991a: A semi-spectral primitive equation ocean circulation model using vertical sigma and orthogonal curvilinear horizontal coordinates, *J. Comput. Phys.*, *94*, 151–185

Haidvogel, D. B., A. Beckmann, K. S. Hedström, 1991b: Dynamical simulations of filament formation and evolution in the coastal transition zone, *J. Geophys. Res.*, *96*, 15,017–15,040

Halliwell, G. R., and C. N. K. Mooers, 1979: The space time structure and variability of the shelf water-slope water and Gulf Stream surface temperature fronts and associated warm-core eddies, *J. Geophys. Res.*, *84*, 7707–7725

Hamilton, P. 1992: Lower continental slope cyclonic eddies in the central Gulf of Mexico, *J. Geophys. Res*, *97*, 2185-2200

Hedström, K., 1986: Interaction of a point vortex and a shear flow, Summer study program in GFD, WHOI-86-45, 142–152

Hogg, N., 1981: Topographic waves along 70°W on the continental rise, *J. Mar. Res.*, *39*, 627–649

Huthnance, J. M., 1975: On trapped waves over a continental shelf, *J. Fluid Mech.*, *69*, 689–704

Joyce, T. M., J. K. B. Bishop, and O. B. Brown, 1992: Observation of offshore shelf-water transport induced by a warm-core ring, *Deep-Sea Res.*, *39, Suppl. 1*, 97-113

Kennelly, M., R. H. Evans, and T. Joyce, 1985: Small scale cyclones on the periphery of a Gulf Stream warm-core ring, *J. Geophys. Res.*, *90*, 8845–8857

Kirwan, A. D., W. J. Merrell, J. K. Lewis, and R. E. Whitaker, 1984: Lagrangian observations of an anticyclonic ring in the western Gulf of Mexico, *J. Geophys. Res.*, *89*, 3417–3424

Louis, J., and P. C. Smith, 1982: The development of the barotropic radiation field of an eddy over a slope, *J. Phys. Oceanogr.*, *12*, 56–73

214

Louis, J., B. Petrie, and P. C. Smith, 1982: Observation of topographic Rossby waves on the continental margin off Nova Scotia, *J. Phys. Oceanogr.*, *12*, 47–55

Longuet-Higgins, M. S., 1968: On the trapping of waves along a discontinuity of depth in a rotating ocean, *J. Fluid Mech.*, *31*, 417–434

McWilliams, J. G., and G. R. Flierl, 1979: On the evolution of isolated nonlinear vortices, *J. Phys. Oceanogr.*, *9*, 1155–1182

Malanotte-Rizzoli, P., 1984: Boundary-forced nonlinear planetary radiation, *J. Phys. Oceanogr.*, *14*, 1032–1046

Meacham, S. P., 1991: Meander evolution on piecewise-uniform, quasi-geostrophic jets. *J. Phys. Oceanogr.*, *21*, 1139–1170

Merrell, W. J., and J. M. Morrison, 1981: On the circulation of the western Gulf of Mexico with observations from April 1978, *J. Geophys. Res.*, *86*, 4181–4185

Morgan, C. W., and J. M. Bishop, 1977: An example of Gulf Stream eddy-induced water exchange in the Mid-Atlantic Bight, *J. Phys. Oceanogr.*, *7*, 472–479

Mysak, L. A., 1980: Recent advance in shelf wave dynamics, *Rev. Geophys. Space Phys.*, *18*, 211–241

Nof, D, 1988: The propagation of "streamers" along the periphery of warm-core rings. *Deep-Sea Res.*, *35*, 1483–1498

Pedlosky, J., 1979: Geophysical Fluid Dynamics, Springer-Verlag, New York, 624pp

Polvani, L., 1988: Geostrophic Vortex Dynamics, Ph.D. Thesis, MIT/WHOI, WHOI-88-48. 221pp

Pratt, L. J. and M. E. Stern, 1986: Dynamics of potential vorticity fronts and eddy detachment, *J. Phys. Oceanogr.*, *16*, 1099–1118

Pullin, D. I., 1992: Contour dynamics methods, *Ann. Rev. Fluid Mech.*, *24*, 89–115

Qiu, B., 1990: Low-frequency shelf/slope responses induced by localized offshore forcings, *J. Geophys. Res.*, *95*, 9447–9459

Ramp, S. R., 1989: Moored observations of current and temperature on the shelf and upper slope near ring 82B, *J. Geophys. Res.*. *94*, 18,071–18087

Robinson, A. R. (editor), 1983: Eddies in Marine Science, Springer-Verlag, Berlin, 609pp

Shaw, P. T., and S. Divakar, 1991: Generation of topographic waves over the continental margin, *J. Phys. Oceanogr.*, *21*, 1032–1042

Shaw, P. T., and C. Y. Peng, 1987: A numerical study of the propagation of topographic Rossby waves, *J. Phys. Oceanogr.*, *17*, 538-366

Smith, D. C., IV, 1986: A numerical study of Loop Current eddy interaction with topography in the western Gulf of Mexico, *J. Phys. Oceanogr.*, *16*, 1260-1272

Smith, D. V., IV, and J. J. O'Brien, 1983: The interaction of a two-layer isolated mesoscale eddy with bottom topography. *J. Phys. Oceanogr.*, *13*, 1681-1697

Smith, P. C., 1978: Low frequency fluxes of momentum, Heat, salt, and nutrients at the edge of the Scotian Shelf, *J. Geophys. Res.*, *83*, 4079-4096

Spitz and Nof, D., 1991: Separation of boundary currents due to bottom topography, *Deep-Sea Res.*, *38*, 1-20

Stern, M. E., 1991: Entrainment of an eddy at the edge of a jet, *J. Fluid Mech.*, *228*, 342-360

Stern, M. E. and G. R. Flierl, 1987: On the interaction of a vortex with a shear flow, *J. Geophys. Res.*, *92*, 10733-10744

Swatters, G. E., and G. R. Flierl, 1991: Dynamics of ventilated coherent cold eddies on a sloping bottom, *J. Fluid Mech.*, *223*, 565-587

Thompson, L., 1991: Flow over Finite Isolated Topography, Ph.D. Thesis, MIT/WHOI, WHOI-91-05. 222pp

Thompson, L. and G. R. Flierl, 1992: Barotropic flow over finite isolated topography: steady solutions on the beta-plane and the initial value problem, submitted to the *J. Fluid Mech.*

Vennell M. R., 1988: The influence of a steady baroclinic deep ocean on the shelf. Ph.D. thesis, MIT/WHOI Joint Program in Oceanography, 198pp.

Vidal, V. M., F. V. Vidal and J. M. Pérez-Molero, 1992: Collision of a Loop Current anticyclonic ring against the continental shelf slope of the western Gulf of Mexico, *J. Geophys. Res.*, *97*, 2155-2172

Wang, D. P., 1982: Effect of slope on the mean shelf circulation, *J. Phys. Oceanogr.*, *12*, 1524-1526

Wright, W. R., 1976: The limit of shelf water south of Cape Cod, 1941 to 1972, *J. Mar. Res.*, *34*, 1-14

# DOCUMENT LIBRARY

March 11, 1991

*Distribution List for Technical Report Exchange*

Attn: Stella Sanchez-Wade
Documents Section
Scripps Institution of Oceanography
Library, Mail Code C-075C
La Jolla, CA 92093

Hancock Library of Biology &
    Oceanography
Alan Hancock Laboratory
University of Southern California
University Park
Los Angeles, CA 90089-0371

Gifts & Exchanges
Library
Bedford Institute of Oceanography
P.O. Box 1006
Dartmouth, NS, B2Y 4A2, CANADA

Office of the International
    Ice Patrol
c/o Coast Guard R & D Center
Avery Point
Groton, CT 06340

NOAA/EDIS Miami Library Center
4301 Rickenbacker Causeway
Miami, FL 33149

Library
Skidaway Institute of Oceanography
P.O. Box 13687
Savannah, GA 31416

Institute of Geophysics
University of Hawaii
Library Room 252
2525 Correa Road
Honolulu, HI 96822

Marine Resources Information Center
Building E38-320
MIT
Cambridge, MA 02139

Library
Lamont-Doherty Geological
    Observatory
Columbia University
Palisades, NY 10964

Library
Serials Department
Oregon State University
Corvallis, OR 97331

Pell Marine Science Library
University of Rhode Island
Narragansett Bay Campus
Narragansett, RI 02882

Working Collection
Texas A&M University
Dept. of Oceanography
College Station, TX 77843

Library
Virginia Institute of Marine Science
Gloucester Point, VA 23062

Fisheries-Oceanography Library
151 Oceanography Teaching Bldg.
University of Washington
Seattle, WA 98195

Library
R.S.M.A.S.
University of Miami
4600 Rickenbacker Causeway
Miami, FL 33149

Maury Oceanographic Library
Naval Oceanographic Office
Stennis Space Center
NSTL, MS 39522-5001

Marine Sciences Collection
Mayaguez Campus Library
University of Puerto Rico
Mayaguez, Puerto Rico 00708

Library
Institute of Oceanographic Sciences
Deacon Laboratory
Wormley, Godalming
Surrey GU8 5UB
UNITED KINGDOM

The Librarian
CSIRO Marine Laboratories
G.P.O. Box 1538
Hobart, Tasmania
AUSTRALIA 7001

Library
Proudman Oceanographic Laboratory
Bidston Observatory
Birkenhead
Merseyside L43 7 RA
UNITED KINGDOM

Mac 90-32

50272-101

| REPORT DOCUMENTATION PAGE | 1. REPORT NO. WHOI-92-40 | 2. | 3. Recipient's Accession No. |
|---|---|---|---|

**4. Title and Subtitle**

Interaction of an Eddy with a Continental Slope

**5. Report Date**
September 1992

**6.**

**7. Author(s)**
Xiaoming Wang

**8. Performing Organization Rept. No.**
WHOI 92-40

**9. Performing Organization Name and Address**

The Woods Hole Oceanographic Institution
Woods Hole, Massachusetts 02543

**10. Project/Task/Work Unit No.**

**11. Contract(C) or Grant(G) No.**

(C)

(G)

**12. Sponsoring Organization Name and Address**

**13. Type of Report & Period Covered**

Ph.D. Thesis

**14.**

**15. Supplementary Notes**

This thesis should be cited as: Xiaoming Wang, 1992. Interaction of an Eddy with a Continental Slope.
Ph.D. Thesis. MIT/WHOI, WHOI-92-40.

**16. Abstract (Limit: 200 words)**

This study concerns the barotropic interactions between a mesoscale eddy and a straight monotonic bottom topography. Through simple to relatively complicated modeling effort, some of the fundamental properties of the interaction are investigated.

In chapter two, the fundamental aspects of the interaction are examined using a simple contour dynamics model. With the simplest model configuration of an ideal vortex and a step topography, the basic dynamical features of the observed oceanic eddy-topography interaction are qualitatively reproduced. The results consist of eddy-induced cross-topography exchange, formation of topographic eddies, eddy propagation and generation of topographic waves. In chapter three, a more complicated primitive equation model is used to investigate a mesoscale eddy interacting with an exponential continental shelf/slope topography on both $f$ and $\beta$-planes. The $f$-plane model recasts the important features of chapter two in more details. On the $\beta$-plane, the problem of eddy colliding onto a continental shelf/slope from a distance with straight or oblique incident angles is investigated. The eddy evolution and shelf/slope responses are examined in detail. Model-observation comparisons in chapter four show favorable qualitative agreement of the model results with some of the observed events in the eastern U.S. continental margins and in the Gulf of Mexico. The model results give dynamical interpretations to some observed features of the observed oceanic eddy-topography interactions and provide enlightening insight into the problem.

**17. Document Analysis    a. Descriptors**

1. eddy
2. topography
3. interaction

**b. Identifiers/Open-Ended Terms**

**c. COSATI Field/Group**

| 18. Availability Statement | 19. Security Class (This Report) UNCLASSIFIED | 21. No. of Pages 220 |
|---|---|---|
| Approved for publication; distribution unlimited. | 20. Security Class (This Page) | 22. Price |